Large-scale real-space Kohn-Sham density functional theory calculations using adaptive finite-element discretization

by

Phani Motamarri

A dissertation submitted in partial fulfillment
of the requirements for the degree of
Doctor of Philosophy
(Mechanical Engineering)
in The University of Michigan
2014

Doctoral Committee:

Associate Professor Vikram Gavini, Chair
Professor Selim Esedoglu
Professor Krishnakumar. R. Garikipati
Jaroslaw Knap, U. S. Army Research Laboratory

© Phani Motamarri 2014
All Rights Reserved

For my beloved parents

TABLE OF CONTENTS

DEDICATION ii

LIST OF FIGURES v

LIST OF TABLES vii

LIST OF APPENDICES viii

ABSTRACT ix

CHAPTER

I. Introduction 1

II. Electronic structure theories 9

2.1 The many-body Schrödinger equation 9
2.1.1 Born-Oppenheimer approximation: 10
2.2 Hartree-Fock method 13
2.3 Density-functional theory 16
2.3.1 Existence of a functional of density 16
2.3.2 The Kohn-Sham approach 18
2.3.3 Kohn-Sham eigenvalue problem 21

III. Real-space finite-element formulation of Kohn-Sham density functional theory 25

3.1 Formulation 32
3.1.1 Kohn-Sham saddle-point formulation 32
3.1.2 Kohn-Sham self-consistent formulation 37
3.1.3 Discrete Kohn-Sham problem 41
3.2 A-*priori* mesh adaption 44
3.2.1 Estimate of energy error 45

3.2.2 Optimal coarse-graining rate . . . 51
3.3 Numerical implementation . . . 52
3.3.1 Higher-order finite-element discretizations . . . 53
3.3.2 Spectral finite-element basis . . . 53
3.3.3 Self-consistent field iteration . . . 55
3.4 Numerical results . . . 64
3.4.1 Rates of convergence . . . 64
3.4.2 Computational cost . . . 75
3.4.3 Scalability of finite-element basis: . . . 90
3.5 Summary . . . 90

IV. Subquadratic-scaling subspace projection method for Kohn-Sham density functional theory . . . 92

4.1 Mathematical Formulation . . . 96
4.1.1 Projection of the Hamiltonian into a finite-dimensional subspace . . . 97
4.1.2 Reprojection into a non-orthogonal basis . . . 98
4.1.3 Density Matrix . . . 100
4.2 Subspace-projection algorithm using finite-element basis . . . 102
4.2.1 Eigenvalue problem in orthonormalized FE basis . . . 102
4.2.2 Chebyshev filtered subspace iteration . . . 104
4.2.3 Localization and truncation . . . 107
4.2.4 Subspace projection in the non-orthogonal basis . . . 111
4.2.5 Electron density computation . . . 112
4.3 Results and discussion . . . 116
4.3.1 Aluminum nano-clusters: Pseudopotential study . . . 118
4.3.2 Alkane chains: Pseudopotential study . . . 124
4.3.3 Silicon nano-clusters: All-electron study . . . 127
4.4 Summary . . . 132

V. Configurational force approach to atomic relaxations using Kohn-Sham density functional theory . . . 133

5.1 Hellmann-Feynman theorem . . . 134
5.2 Configurational force approach . . . 137

VI. Conclusions . . . 149

6.1 Summary . . . 149
6.2 Future work and directions . . . 154

APPENDICES . . . 157

BIBLIOGRAPHY . . . 174

LIST OF FIGURES

Figure

3.1	Convergence rates for the finite-element approximation of boron atom. .	71
3.2	Convergence rates for the finite-element approximation of methane molecule.	71
3.3	Electron density contours of methane molecule.	73
3.4	Electron density contours of barium $2 \times 2 \times 2$ BCC cluster.	73
3.5	Convergence rates for the finite-element approximation of barium cluster.	74
3.6	Convergence rates for the finite-element approximation of bulk FCC calcium.	74
3.7	Computational efficiency of various orders of finite-element approximations. Case study: boron atom.	79
3.8	Computational efficiency of various orders of finite-element approximations. Case study: methane molecule.	79
3.9	Computational efficiency of various orders of finite-element approximations. Case study: barium $2 \times 2 \times 2$ BCC cluster.	80
3.10	Computational efficiency of various orders of finite-element approximations. Case study: bulk calcium FCC crystal.	80
3.11	Electron density contours of $3 \times 3 \times 3$ FCC aluminum cluster.	83
3.12	Electron density contours of $5 \times 5 \times 5$ FCC aluminum cluster.	83
3.13	Electron density contours of $7 \times 7 \times 7$ FCC aluminum cluster.	85
3.14	Electron density contours of a graphene sheet containing 100 atoms. . .	87
3.15	Schematic of Tris(bipyridine) ruthenium complex.	89
3.16	Electron density contours of Tris (bipyridine) ruthenium complex.	89
3.17	Relative speedup as a function of the number of processors.	91
4.1	Total computational times for the proposed method and ChFSI-FE. Case study: Aluminum nano-clusters.	122
4.2	Average computational times per SCF iteration for the proposed method and ChFSI-FE. Case study: Aluminum nano-clusters.	122
4.3	Electron density contours on the mid-plane of $9 \times 9 \times 9$ fcc aluminum nano-cluster.	123
4.4	Total computational times for the proposed method and ChFSI-FE. Case study: Alkane chains.	128
4.5	Average computational times per SCF iteration for the proposed method and ChFSI-FE. Case study: Alkane chains.	128
4.6	Electron density isocontours of $C_{900}H_{1802}$.	129

4.7 Total computational times for the proposed method and ChFSI-FE. Case study: Silicon nano-clusters. 130
4.8 Average computational times per SCF iteration for the proposed method and ChFSI-FE. Case study: Silicon nano-clusters. 130
4.9 Electron density contours on the mid-plane of $3 \times 3 \times 3$ silicon nano-cluster. 131
C.1 Convergence of the finite-element approximation for Hydrogen atom using GLL quadrature rule for overlap matrix. 165
D.1 Average computational times per SCF iteration for individual components of the proposed method. Case Study: Aluminum nano-clusters. 167
D.2 Average computational times per SCF iteration for individual components when sparse data-structures are active. Case Study: Aluminum nano-clusters. 167
D.3 Average computational times per SCF iteration for individual components of the proposed method. Case Study: Alkane chain. 171
D.4 Average computational times per SCF iteration for individual components when sparse data-structures are active. Case Study: Alkane chain. . . . 171
D.5 Variation of density fraction with SCF iteration showing where the sparse data-structures (brown line) and dense data-structures are used. Case Study: Aluminum 7x7x7 nano-cluster and Alkane chain $C_{900}H_{1802}$. . . . 172
D.6 Relative change in ground-state energy with SCF iteration. Case Study:Aluminum 7x7x7 nano-cluster and Alkane chain $C_{900}H_{1802}$. 172
D.7 Average computational times per SCF iteration for individual components of the proposed method. Case Study: Silicon nano-clusters. 173

LIST OF TABLES

Table

3.1	Comparison of Generalized vs Standard eigenvalue problems.	59
3.2	Comparison of Standard eigenvalue problem vs Chebyshev filtered subspace iteration (ChFSI).	61
3.3	Convergence with finite-element basis for a $3\times3\times3$ FCC aluminum cluster using HEX125SPECT element.	81
3.4	Comparison of higher-order finite-element (FE) basis with plane-wave basis for a $3 \times 3 \times 3$ FCC aluminum cluster.	82
3.5	Convergence with finite-element basis for a $5 \times 5 \times 5$ FCC cluster using HEX125SPECT element.	84
3.6	Comparison of higher-order finite-element (FE) basis with plane-wave basis sets for a $5 \times 5 \times 5$ FCC aluminum cluster.	84
3.7	100 atom graphene sheet (600 electrons).	87
3.8	Tris(bipyridine)ruthenium (290 electrons).	89
4.1	Convergence of the finite-element discretization (HEX125SPECT element) for a $3 \times 3 \times 3$ fcc aluminum cluster.	119
4.2	Ground-state energies per atom (eV) for the various sizes of aluminum nano-clusters computed using the proposed subspace projection algorithm technique and ChFSI-FE [1].	124
4.3	Convergence of the finite-element discretization for $C_{33}H_{68}$ using HEX125SPECT element.	125
4.4	Comparison of ground-state energies (eV per atom) for various alkane chains.	126
4.5	Comparison of ground-state energies (Ha per atom) for various sizes of silicon clusters.	132
A.1	Convergence of $E^h_{\text{electrostatic}}$ for "HEX27" element	160
A.2	Convergence of $E^h_{\text{electrostatic}}$ for "HEX125SPECTRAL" element	160
B.1	Computational cost per iteration. Case study: Barium	161
C.1	Computed ground-state energies of Hydrogen atom by employing GLL quadrature rules for overlap matrix.	164
C.2	Comparison between GLL rule and GQ rule	165

LIST OF APPENDICES

Appendix

A. Discrete formulation of electrostatic interactions in all-electron calculations 158

B. Trade-offs in higher-order elements: Source of diminishing returns with increasing order 161

C. Accuracy of Gauss-Lobatto-Legendre quadrature 163

D. Scaling performance of individual components of the subspace projection technique 166

ABSTRACT

Large-scale real-space Kohn-Sham density functional theory calculations using adaptive finite-element discretization

by

Phani Motamarri

Chair: Vikram Gavini

Past few decades have seen an increasingly important role played by quantum mechanical calculations based on Kohn-Sham density functional theory (DFT) in the investigation of wide variety of materials properties. However, large-scale DFT calculations are computationally very demanding and hence have been primarily associated with either plane-wave basis or atomic-orbital basis sets, imposing severe restrictions on the permissible boundary conditions and the type of materials systems simulated. Furthermore, these basis sets exhibit poor parallel scalability. On the other hand, finite-element (FE) discretization of Kohn-Sham DFT, among the real-space techniques is versatile and is amenable for unstructured coarse-graining, allows for consideration of complex geometries and boundary conditions, and is scalable on parallel computing platforms. However, the inherent shortcomings in the use of finite-element discretization for DFT have made it less attractive for large scale calculations restricting the materials system sizes to few hundreds of electrons. This thesis tries to address the inherent shortcomings and presents the development of new computationally efficient and robust parallel algorithms to enable large-scale

DFT calculations using finite-element basis (DFT-FE). The proposed DFT-FE enabled for the first time, simulation of electronic structure of materials systems as large as 7000 atoms ($\sim$ 14000 valence electrons) using finite-element basis.

The key ideas in the development of DFT-FE include (i) an adaptive higher-order spectral finite-element based self-consistent framework which can handle all-electron and pseudopotential calculations with complex boundary conditions on a single footing, (ii) a subspace projection method using higher-order spectral finite-element discretization to reduce the computational complexity of DFT calculations while treating metallic and insulating materials in a single framework and (iii) a configurational force approach to efficiently compute forces on atoms to find the geometry of a given materials system in the most stable state.

The numerical investigations conducted with DFT-FE on representative benchmark examples show that computational efficiency of finite-element basis is competing with commercial codes using plane-wave basis (smooth pseudopotential calculations), and compares well with atomic-orbital basis (all-electron calculations with singular potentials) and show excellent parallel scalability. Furthermore, the benchmark studies involving pseudopotential calculations on metallic aluminum nano-clusters (up to 3500 atoms) and on insulating alkane chains (up to 7000 atoms) as well as all-electron calculations on semi-conducting silicon nano-clusters (up to 4000 electrons), reveal that the proposed subspace projection algorithm exhibits subquadratic-scaling behavior with system size along with accuracies commensurate with chemical accuracy. Significant computational savings have been realized with $\sim$ 10 fold speedups observed for the largest systems with respect to previous reference calculations.

CHAPTER I

Introduction

Electronic structure calculations have played a significant role in predicting various aspects of materials behavior over the past few decades. The success stories of electronic structure calculations range from the accurate prediction of phase transformations in a wide range of materials to providing various insights into mechanical, electronic, magnetic, and optical properties of materials and compounds. In particular, the Kohn-Sham approach to density functional theory (DFT) [2] has made quantum-mechanically informed calculations on ground-state materials properties computationally tractable, and has provided many important insights into a wide range of materials properties.

The Kohn-Sham approach to DFT is based on the key result of Hohenberg & Kohn [3] that the ground-state properties of a materials system can be described by a functional of electron density. Though, the existence of an energy functional has been established by the Hohenberg-Kohn result, its functional form is not known to date. The work of Kohn & Sham [2] addressed this challenge in an approximate sense, and has laid the foundations for the practical application of DFT to materials systems by reducing the many-body problem of interacting electrons into an equivalent problem of non-interacting electrons in an effective mean field that is governed by the electron density. This effective single-electron description is exact in principle for ground-

state properties, but is formulated in terms of an unknown exchange-correlation term that includes the quantum-mechanical interactions between electrons. This exchange-correlation term is approximated using various models—commonly modeled as an explicit functional of electron density—and these models have been shown to predict a wide range of materials properties across various materials systems.

Despite the reduced computational complexity of Kohn-Sham approach in comparison to the original many-body Schrödinger problem, simulations of large-scale material systems with DFT are still computationally very demanding and has been historically associated with the computation of bulk properties of materials using plane-wave basis. Plane-wave basis provides an efficient computation of the electrostatic interactions arising in Kohn-Sham DFT naturally through Fourier transforms. Further, the plane-wave basis provides variational convergence in the ground-state energy with exponential convergence rates. However, one often encounters the need for understanding materials properties influenced by defects–vacancies, dopants, dislocations, interfaces, free surfaces–in small concentrations which can potentially generate long range fields that are often incompatible with periodic boundary conditions. Furthermore, the plane-wave basis provides a uniform spatial resolution which can be inefficient in the investigation of materials systems involving large nano-clusters, amorphous materials etc., or materials properties which require all-electron calculations, where higher basis resolution is often required in some spatial regions and a coarser resolution suffices elsewhere. Moreover, the plane-wave basis is non-local in real space, which significantly affects the scalability of computations on parallel computing platforms. On the other hand, atomic-orbital-type basis sets [4, 5, 6] have been been widely used for studying materials systems such as molecules and clusters. However, these basis sets are well suited only for isolated systems and cannot handle arbitrary boundary conditions. Furthermore, using these basis functions, it is difficult to achieve a systematic basis-set convergence for all materials

systems. Due to the non-locality of these basis functions the efficiency of parallel scalability on a large number of processors is also affected. Thus, the development of systematically improvable and scalable real-space techniques for electronic structure calculations has received significant attention over the past decade, and we refer to [7, 8, 9, 10, 11, 12, 13, 14] and references therein for a comprehensive overview. Among the real-space techniques, the finite-element basis presents some key advantages—it is amenable to unstructured coarse-graining, allows for consideration of complex geometries and boundary conditions, and is scalable on parallel computing platforms. We refer to [15, 16, 17, 18, 19, 20, 21, 22, 23, 24, 25, 26, 27, 28, 29, 30], and references therein, for a comprehensive overview of the past efforts in developing real-space electronic structure calculations based on a finite-element discretization. However, the inherent shortcomings in the use of finite-element discretization for Kohn-Sham DFT have made it less attractive for large scale calculations and the largest materials system simulated using finite-elements is less than few hundreds of electrons. *The central theme of this thesis focuses on the development of new computationally efficient and robust finite-element based parallel algorithms to enable large-scale Kohn-Sham DFT calculations.* We subsequently demonstrate these methods to simulate materials systems as large as 7000 atoms($\sim$14000 electrons) for the first time ever using finite-element basis. Further, the new computational techniques developed as a part of this thesis can be readily extended to study crucial aspects of energetics of defects in materials with long range fields which is beyond the scope of existing DFT codes and thereby help in devising better macroscopic material models.

While the finite-element basis is more versatile than the plane-wave basis [15, 19], prior investigations have shown that linear finite-elements require a large number of basis functions—of the order of $100,000$ basis functions per atom—to achieve chemical accuracy in electronic structure calculations (cf. e.g. [23, 31]), and this compares very poorly with plane-wave basis or other real-space basis functions. However, the

use of higher-order elements increases the per basis-function computational cost due to the need for higher-order accurate numerical quadrature rules. Furthermore, the bandwidth of the matrix increases cubically with the order of the finite-element, which in turn increases the computational cost of matrix-vector products. In addition, since a finite-element basis is non-orthogonal, the discretization of the Kohn-Sham DFT problem results in a generalized eigenvalue problem, which is more expensive to solve in comparison to a standard eigenvalue problem resulting from using an orthogonal basis (for e.g. plane-wave basis). Thus, the computational efficiency afforded by using a finite-element basis in electronic structure calculations, and its relative performance compared to plane-wave basis and atomic-orbital-type basis functions (for e.g Gaussian basis), has remained an open question to date and forms the subject of the first part of my thesis. To this end, we develop: (i) a unified real-space self-consistent framework which can handle all-electron and pseudopotential calculations with both non-periodic and periodic boundary conditions on a similar footing (ii) an *a priori* mesh adaption technique to construct a close to optimal finite-element discretization of the problem; (iii) an efficient solution strategy for solving the discrete eigenvalue problem by using higher-order spectral finite-elements (6th order) in conjunction with Gauss-Lobatto quadrature, and a Chebyshev acceleration technique for computing the occupied eigenspace. We subsequently study the numerical aspects of the finite-element discretization of the formulation, investigate the computational efficiency afforded by higher-order finite-elements, and compare the performance of the finite-element basis with plane-wave and Gaussian basis on representative benchmark problems. Our studies show that staggering computational savings of the order of 1000-fold can be realized by using higher-order finite-element discretization, in comparison to linear finite-elements used previously in the literature. A comparative study of the computational efficiency of the proposed higher-order spectral finite-element discretization show that the performance of finite-element basis is compet-

ing with commercial codes using plane-wave discretization for non-periodic calculations involving smooth potentials (pseudo-potentials) where valence electrons are only treated, and Gaussian basis for all-electron calculations involving singular potentials. Furthermore, we demonstrate the capability of the proposed approach by computing the electronic structure of an aluminum nano-cluster containing 1688 atoms with Kohn-Sham DFT using modest computational resources. Good scalability of the implementation up to a few hundred processors is also demonstrated.

However, we note that the self-consistent approach to DFT formulated in the first part of this thesis scales as $\mathcal{O}(M\,N^2)$ where M denotes the number of basis functions and N denotes the system size (number of atoms or number of electrons in the system). As $M \propto N$, the algorithm scales as $\mathcal{O}(N^3)$ asymptotically, thus limiting accessible systems to a few thousand atoms. Infact, this computational cost becomes prohibitively expensive as the system size becomes larger with M being high in the context of grid-based methods like finite-element discretizations. Numerous efforts have been focused in the literature to reduce the computational complexity and to have improved-scaling behavior for DFT calculations. A comprehensive review of these methods has been provided by Göedecker [32], and more recently by Bowler and Miyazaki [33]. Majority of these methods, which rely on the locality of the Wannier functions or the exponential decay of the density matrix in real-space, have been demonstrated to work well for insulating systems, exhibiting linear-scaling with system size. However, for metallic systems, due to the slower decay of the density matrix, the computational complexity of these approaches can deviate significantly, in practice, from linear-scaling. The Fermi-operator expansion method [34, 35, 32], which is equally applicable to both insulating and metallic systems, computes the finite-temperature density-matrix through a Chebyshev polynomial approximation of the Fermi distribution function (also referred to as Fermi function) of the Kohn-Sham Hamiltonian. The accuracy of such an expansion depends on the smearing parameter

($\sigma = k_B T$) in the Fermi distribution and the width of the eigenspectrum (ΔE) of the discretized Hamiltonian. In fact, the number of polynomial terms required to achieve a prescribed accuracy [35] is $\mathcal{O}(\frac{\Delta E}{\sigma})$. Though numerous recent efforts have focused towards developing alternate approximations to the Fermi function, or approximations to its spectral representation which aim to reduce the number of terms used in the expansion to approximate the Fermi function, a major drawback with these methods is that they are not efficient for local real-space basis functions like finite-elements, where, typically, more refined discretizations are needed for chemical accuracy resulting in very large width of the eigenspectrum of the finite-element discretized Hamiltonian. A reduced-scaling technique which is well-suited for finite-element discretizations that treats both metallic and insulating systems on a similar footing has not been attempted before and forms the subject of the second part of my thesis. To this end, we borrow localization ideas from Garcia et. al. [36] and develop a sub-quadratic scaling subspace projection technique which is equally applicable to pseudopotential and all-electron calculations. The main ideas used in our approach are: (i) employ Chebyshev filtered subspace iteration to compute the occupied eigenspace; (ii) employ a localization procedure to generate non-orthogonal localized wavefunctions spanning the Chebyshev filtered subspace; (iii) use adaptive tolerances to truncate the wavefunctions, with looser tolerances being employed in initial self-consisted field (SCF) iterations and progressively tightening as the SCF iteration approaches convergence, and (iv) employ Fermi-operator expansion in terms of the projected Hamiltonian expressed in the non-orthogonal localized basis to compute the density matrix, electron density and band energy. We subsequently demonstrate the accuracy, efficiency and scaling of the proposed approach on benchmark systems involving pseudopotential calculations on metallic aluminum nano-clusters up to 3430 atoms and on insulating alkane chains up to 7052 atoms, as well as all-electron calculations on semi-conducting silicon nano-clusters up to 3920 electrons.

The benchmark studies revealed that accuracies commensurate with chemical accuracy can be obtained with the proposed method, and a subquadratic-scaling with system size was observed for the range of materials systems studied. In particular, for the alkane chains—representing an insulating material—close to linear-scaling is observed, whereas, for aluminum nano-clusters—representing a metallic material—the scaling is observed to be $\mathcal{O}(N^{1.46})$. For all-electron calculations on silicon nano-clusters, the scaling with the number of electrons is computed to be $\mathcal{O}(N^{1.75})$. In all the benchmark systems, significant computational savings have been realized with the proposed approach, with $\sim 10-$fold speedups observed for the largest systems with respect to previous reference calculations.

An important aspect of electronic structure calculations using DFT is the efficient computation of forces on atoms to find the geometry of a given materials system in the most stable state and this forms the subject of the third part of this thesis. A crucial step to evaluate forces on atoms in most DFT codes is to use Hellmann-Feynman theorem [37] which relates the derivatives of the total energy with respect to position of atoms to the expectation value of the derivative of the Hamiltonian with respect to position of atoms. However these atomic forces are usually corrected for incomplete-basis-set error, non-self-consistency error which are not accounted in the atomic forces evaluated using the Hellmann-Feynman theorem. The incomplete-basis-set error [38, 39, 40] often arises when finite number of basis functions are used to represent the electronic wavefunction which is the case in any numerical calculations and these basis functions themselves depend on nuclear positions in a given materials system. The non self-consistency error [40, 41] arises due to the difference between the self-consistent("exact") potential and its non-self-consistent (approximate) counterpart which is usually non-zero for any self-consistent DFT calculation performed on any finite numerical precision computer. Furthermore, Hellmann-Feynman theorem fails to capture stress in the cell as it produces zero force for any affine deformation of

the system and this Pulay stress contributions are explicitly accounted later in the DFT calculations [42, 43]. The real-space finite-element formulation proposed in this thesis has atomic nuclei coincident with finite-element nodes and must account for all the three errors discussed above when evaluating the forces using Hellmann-Feynman theorem and hence needs a careful treatment. In this thesis we adopt an alternate route and propose the use of configurational force (Eshelby) approach for efficient computation of forces on atoms in Kohn-Sham DFT calculations and derive the relevant expressions in a more general setting by using the non-orthogonal formulation of Kohn-Sham DFT. We note that the proposed Eshelby formulation for atomic relaxations provides a unified framework that captures atomic forces due to Hellmann-Feynman theorem, incomplete-basis-sets and non-self-consistency, and furthermore accounts for elastic stresses on periodic-cells on a single footing.

The remainder of this thesis is organized as follows. Chapter 2 provides an overview of the electronic-structure theories. Chapter 3 describes the real-space self-consistent formulation of the Kohn-Sham DFT problem and subsequently discusses the computational aspects of the proposed adaptive higher-order spectral finite-element discretization of the problem. This chapter further shows that the performance of the proposed approach is competing with plane-wave basis for pseudopotential calculation and compares to Gaussian basis for all-electron calculations. Chapter 4 describes the subspace projection technique built on the formulation described in Chapter 3 and demonstrates the subquadratic scaling behavior of the proposed algorithm on representative benchmark examples involving large-scale DFT simulations. Chapter 5 develops the Eshelby form of forces using the real-space non-orthogonal Kohn-Sham DFT formulation to perform atomic relaxations in a finite-element based setting. Finally we conclude in Chapter 6 with a short discussion and consider the scope for future work.

CHAPTER II

Electronic structure theories

2.1 The many-body Schrödinger equation

The most fundamental governing equation for conducting quantum mechanically informed calculations of materials properties involves the computation of electronic-wavefunctions by solving the time-independent Schrödinger equation [44] which assumes the form of an eigenvalue problem given by

$$\mathcal{H}\Psi = E\Psi, \tag{2.1}$$

$$\begin{aligned}\mathcal{H} = &-\frac{1}{2}\sum_{i=1}^{N_e}\nabla_i^2 - \frac{1}{2}\sum_{I=1}^{N_a}\frac{1}{m_I}\nabla_I^2 - \sum_{i=1}^{N_e}\sum_{I=1}^{N_a}\frac{Z_I}{|\mathbf{r}_i - \mathbf{R}_I|} + \frac{1}{2}\sum_{\substack{i,j=1\\ i\neq j}}^{N_e}\frac{1}{|\mathbf{r}_i - \mathbf{r}_j|} \\ &+ \frac{1}{2}\sum_{\substack{I,J=1\\ I\neq J}}^{N_a}\frac{Z_I Z_J}{|\mathbf{R}_I - \mathbf{R}_J|}\end{aligned}$$

$$\Psi = \Psi(\mathbf{x}_1, \mathbf{x}_2, \cdots, \mathbf{x}_{N_e}, \mathbf{R}_1, \mathbf{R}_2, \cdots, \mathbf{R}_{N_a}) \tag{2.2}$$

where the operator $\mathcal{H}$ is the sum of operators for the total kinetic energy of N_e electrons, kinetic energy of N_a nuclei, electrostatic interaction energy between electrons and nuclei and the repulsive energy of the nuclei and further the operator $\mathcal{H}$ acts on Ψ, the many body electronic wavefunction. If $\mathbf{r}_i \in \mathbb{R}^3$ denotes the spatial coordinate of i^{th} electron and s_i denotes the spin of i^{th} electron then $\mathbf{x}_i = (\mathbf{r}_i, s_i)$ and $\mathbf{R}_I \in \mathbb{R}^3$

represents the nuclear position of I^{th} nuclei. Further, the electronic wavefunction Ψ has a functional dependence on $\mathbf{x}_i$ and $\mathbf{R}_I$ and is antisymmetric in $(\mathbf{x}_1, \mathbf{x}_2, \cdots \mathbf{x}_{N_e})$ i.e Ψ changes sign if any pair of coordinates $\mathbf{x}_i$ and $\mathbf{x}_j$ are interchanged. In other words

$$\Psi(\mathbf{x}_1, \cdots, \mathbf{x}_i, \cdots \mathbf{x}_j \cdots \mathbf{x}_{N_e}, \mathbf{R}_1, \cdots, \mathbf{R}_{N_a}) = -\Psi(\mathbf{x}_1, \cdots, \mathbf{x}_j, \cdots \mathbf{x}_i \cdots \mathbf{x}_{N_e}, \mathbf{R}_1, \cdots, \mathbf{R}_{N_a}).$$

2.1.1 Born-Oppenheimer approximation:

When we rewrite equation (2.1) as an eigenvalue problem to compute the ground-state electronic energy for a given configuration of nuclei $\mathbf{R} = \{\mathbf{R}_I\}$ neglecting the effect of motion of nuclei (c.f equation (2.3)), we are making the so called Born-Oppenheimer approximation (c.f [45]). This approximation requires that the total energy of the system is a unique function of positions of the nuclei, independent of their velocities or history. Hence for a given positions of nuclei, the ground state energy of the materials system can be computed by solving the following equation for its lowest energy eigenvalue:

$$\mathcal{H}_e \Psi_e = E_e \Psi_e \tag{2.3}$$

where

$$\mathcal{H}_e = -\frac{1}{2} \sum_{i=1}^{N_e} \nabla_i^2 + V(\mathbf{r}_1, \cdots, \mathbf{r}_{N_e}, \mathbf{R}_1, \cdots, \mathbf{R}_{N_a}) \tag{2.4}$$

with

$$V(\mathbf{r}_1, \cdots \mathbf{r}_{N_e}, \mathbf{R}_1, \cdots, \mathbf{R}_{N_a}) = \sum_{i=1}^{N_e} V_{\text{ext}}(\mathbf{r}_i, \mathbf{R}) + V_{\text{ee}}(\mathbf{r}_1, \cdots, \mathbf{r}_{N_e}) + V_{\text{nn}}(\mathbf{R}_1, \cdots, \mathbf{R}_{N_a})$$

$$\Psi_e = \Psi_e(\mathbf{x}_1, \mathbf{x}_2, \cdots \mathbf{x}_{N_e}) \tag{2.5}$$

where

$$V_{\text{ext}}(\mathbf{r}, \mathbf{R}) = -\sum_{I=1}^{N_a} \frac{Z_I}{|\mathbf{r} - \mathbf{R}_I|}$$

$$V_{\text{ee}}(\mathbf{r}_1, \cdots, \mathbf{r}_{N_e}) = \frac{1}{2} \sum_{\substack{i,j=1 \\ i \neq j}}^{N_e} \frac{1}{|\mathbf{r}_i - \mathbf{r}_j|}$$

$$V_{\text{nn}}(\mathbf{R}_1, \cdots, \mathbf{R}_{N_a}) = \frac{1}{2} \sum_{\substack{I,J=1 \\ I \neq J}}^{N_a} \frac{Z_I Z_J}{|\mathbf{R}_I - \mathbf{R}_J|}$$

Since V_{nn} is a fixed constant which depends on the given positions of nuclei $\mathbf{R} = \{\mathbf{R}_I\}$, the eigenvalue problem (2.3) can be solved without V_{nn}, however it needs to be added to compute the ground-state energy E_e^0 under Born-Oppenheimer approximation. Further, the wavefunction Ψ_e is anti-symmetric for electronic degrees of freedom and can be scaled by any constant since it is the solution of the eigenvalue problem (2.3). The scaling constant by convention is chosen such that the wavefunction Ψ_e is normalized to unity.

$$\int |\Psi_e|^2 \, d\mathbf{x}_1 \, d\mathbf{x}_2 \cdots \, d\mathbf{x}_{N_e} = 1. \tag{2.6}$$

Hence the expression for the density of electrons at a position $\mathbf{r}_1$ is given by the marginal probability distribution:

$$\rho(\mathbf{r}_1) = N \int |\Psi_e|^2 \, d\boldsymbol{s}_1 \, d\mathbf{x}_2 \cdots \, d\mathbf{x}_{N_e} \tag{2.7}$$

The expectation values of the operators corresponding to the kinetic energy and the electrostatic interaction energy between electrons and nuclei of the Hamiltonian $\mathcal{H}_e$ in equation (2.3) can be computed to be kinetic energy T, electron-electron interaction energy E_{ee} and the electron-nuclei interaction energy E_{eZ} in the following way:

$$T = \int \Psi_e^* \left(-\frac{1}{2} \sum_i \nabla_i^2 \right) \Psi_e \, d\mathbf{x}_1 \cdots \, d\mathbf{x}_{N_e} \tag{2.8}$$

$$E_{ee} = \int \Psi_e^* \left(\frac{1}{2} \sum_i {\sum_j}' \frac{1}{|\mathbf{r}_i - \mathbf{r}_j|} \right) \Psi_e \, d\mathbf{x}_1 \cdots \, d\mathbf{x}_{N_e} \tag{2.9}$$

$$E_{eZ} = \int \Psi_e^* \left(\sum_i \sum_I \frac{-Z_I}{|\mathbf{r}_i - \mathbf{R}_I|} \right) \Psi_e \, d\mathbf{x}_1 \cdots d\mathbf{x}_{N_e} = \int \Psi_e^* \left(-\sum_i V_{\text{ext}}(\mathbf{r}_i, \mathbf{R}) \right) \Psi_e \, d\mathbf{x}_1 \cdots d\mathbf{x}_{N_e} \tag{2.10}$$

Using the expression for electron density in equation (2.7), we have

$$E_{eZ} = \sum_i \int \frac{1}{N_e} \rho(\mathbf{r}_i) V_{\text{ext}}(\mathbf{r}_i, \mathbf{R}) \, d\mathbf{r}_i = \int \rho(\mathbf{r}) V_{\text{ext}}(\mathbf{r}, \mathbf{R}) \, d\mathbf{r} \tag{2.11}$$

The above expression is clearly the classical electrostatic interaction energy between the electrons and the nuclei of a given materials system.

It is to be noted that the eigenvalue problem (2.3) admits a variational problem with the functional defined to be the expectation value of $\mathcal{H}_e$

$$E(\Psi_e) = \langle \Psi_e | \, \mathcal{H}_e \, | \Psi_e \rangle \tag{2.12}$$

and hence the variational problem to compute the ground-state materials properties is given by

$$E_e^0 = \inf_{\Psi_e} E(\Psi_e) \tag{2.13}$$

subject to the following normalization and antisymmetry constraints:

$$\int |\Psi_e|^2 \, d\mathbf{x}_1 \, d\mathbf{x}_2 \cdots d\mathbf{x}_{N_e} = 1,$$

$$\Psi_e(\mathbf{x}_1, \cdots, \mathbf{x}_i, \cdots \mathbf{x}_j \cdots \mathbf{x}_{N_e}) = -\Psi_e(\mathbf{x}_1, \cdots, \mathbf{x}_j, \cdots \mathbf{x}_i \cdots \mathbf{x}_{N_e}).$$

It is worthwhile to note from equation (2.5) that the many-body electronic wave-function Ψ_e maps a vector in $\mathbb{R}^{3N_e}$ to $\mathbb{C}$ and belongs to an infinite-dimensional physical Hilbert space $\mathbb{H}$ on $(\mathbb{R}^{3N_e})$. This translates into huge computational complexity in solving the eigenvalue problem (2.3) which makes ab-initio computation of ground-state materials properties almost impossible. In otherwords, one needs to diagonalize

a matrix of astronomical dimension $I^{3N_e} \times I^{3N_e}$ where I denotes the number of intervals corresponding to the discretization of the real line and N_e denotes the number of electrons in the materials system and this problem is computationally intractable. Hence approximate methods of quantum mechanics which can explain the main features of the complex atomic systems with less computation are highly desirable [46] and these methods have been developed over a period of last 50 years and are often termed as electronic structure theories in the literature. Here we discuss the most widely used theories namely Hartree-Fock method and the density-functional theory. We use the Dirac notation bra $\langle . |$ and ket $| . \rangle$ to represent abstract vectors henceforth in this thesis.

2.2 Hartree-Fock method

The Hartree-Fock approximation [47] assumes that electrons in a given materials system interact with each other only through a mean-field potential created by other electrons and the nuclei and thus does not account for electron-correlations. Here the many-body wavefunction Ψ_e is approximated as a Slater determinant which obeys the anti-symmetric nature of the many-body electronic wavefunction.

$$\Psi_e(\mathbf{x}_1, \cdots, \mathbf{x}_{N_e}) \approx \Psi_{\mathrm{HF}}(\mathbf{x}_1, \cdots, \mathbf{x}_{N_e}) = \frac{1}{\sqrt{N_e!}} \det \begin{pmatrix} \psi_1(\mathbf{x}_1) & \psi_1(\mathbf{x}_2) & \cdots & \psi_1(\mathbf{x}_{N_e}) \\ \psi_2(\mathbf{x}_1) & \psi_2(\mathbf{x}_2) & \cdots & \psi_2(\mathbf{x}_{N_e}) \\ . & . & . & . \\ . & . & . & . \\ \psi_{N_e}(\mathbf{x}_1) & \psi_{N_e}(\mathbf{x}_2) & \cdots & \psi_{N_e}(\mathbf{x}_{N_e}) \end{pmatrix} \tag{2.14}$$

where $\{\psi_1, \cdots, \psi_{N_e}\}$ is assumed to be set of orthonormal single-particle wavefunctions:

$$\int \psi_i^*(\mathbf{x})\psi_j(\mathbf{x})\, d\mathbf{x} = \delta_{ij}. \tag{2.15}$$

The Slater-determinant approximation of Ψ_e reduces the wavefunction in $\mathbb{H}(\mathbb{R}^{3N_e})$ to N_e single-particle wavefunctions belonging to $\mathbb{H}(\mathbb{R}^3)$ thus making the electronic-structure problem computationally tractable. Now substituting Ψ_e from (2.14) in (2.12) we obtain the Hartree-Fock functional:

$$E_{\text{HF}}(\{\psi_i\}) = \langle \Psi_{\text{HF}} | \, \mathcal{H}_e \, | \Psi_{\text{HF}} \rangle = \sum_{i=1}^{N_e} H_i + \frac{1}{2} \sum_{i,j=1}^{N_e} (J_{ij} - K_{ij}) \tag{2.16}$$

where

$$H_i = \int \psi_i^*(\mathbf{x}) \left[-\frac{1}{2}\nabla^2 + V_{\text{ext}}(\mathbf{r}, \mathbf{R}) \right] \psi_i(\mathbf{x})\, d\mathbf{x} \tag{2.17}$$

$$J_{ij} = \int \int \psi_i(\mathbf{x})\psi_i^*(\mathbf{x}) \frac{1}{|\mathbf{r} - \mathbf{r}'|} \psi_j^*(\mathbf{x}')\psi_j(\mathbf{x}')\, d\mathbf{x}\; d\mathbf{x}' \tag{2.18}$$

$$K_{ij} = \int \int \psi_i^*(\mathbf{x})\psi_j(\mathbf{x}) \frac{1}{|\mathbf{r} - \mathbf{r}'|} \psi_i(\mathbf{x}')\psi_j^*(\mathbf{x}')\, d\mathbf{x}\; d\mathbf{x}' \tag{2.19}$$

Here J_{ij} and K_{ij} are called Coulomb integrals and exchange integrals respectively. Further $J_{ii} = K_{ii}$ in the above equations. Hence the variational problem in Hartree-Fock approximation is given by:

$$\inf_{\{\psi_i\}} E_{\text{HF}}(\{\psi_i\}) \tag{2.20}$$

subject to the orthonormality constraint (2.15). The Euler-Lagrange equations of the functional in (2.20) give rise to Fock differential equations and is solved self-consistently for the ground-state properties. Further the electron density is computed

using the following expression after the self-consistency is achieved:

$$\rho(\mathbf{r}) = \sum_{i=1}^{N_e} |\psi_i(\mathbf{x})|^2 \tag{2.21}$$

It is clear from the variational structure of the Hartree-Fock problem that the ground-state energy of a materials system computed from the Hartree-Fock approximation provides an upper bound to the actual ground-state energy of the system. Though the Hartree-Fock approximation makes electronic-structure calculations computationally tractable, this method does not account for electron-correlation energy. Hence, the development of more accurate and reliable electronic structure methods has been the focus over the past few decades. One of the refined electronic-structure theories which is a generalization of the Hartree-Fock approximation is the "multi-configuration" approach. Here, the variational structure (2.12) is exploited and the many-body wavefunction is approximated as a linear combination of a number of Slater-determinants and it is shown that the space spanned by the basis of Slater determinants is dense in the complete Hilbert space thus reproducing the exact quantum mechanical equations [48, 49]. Another method which has gained immense popularity over the course of last few decades is the density-functional theory of Hohenberg, Kohn and Sham [50, 44]) which expresses the ground-state properties of a materials system just by a functional of electron density. Density functional theory has played a significant role in providing many important insights into a wide range of materials properties for a long time and is known for its accuracy, reliability and feasibility of electronic structure calculations. We discuss Density-functional theory in the next section.

2.3 Density-functional theory

Density-functional theory is based on a remarkable result of Hohenberg and Kohn [3, 2] which states that there is a one-to-one correspondence between the ground-state electronic wave-function Ψ_e of a quantum mechanical system with N interacting electrons and the ground-state electron density. Infact, Hohenberg and Kohn showed that ground-state electron density is uniquely determined by the external potential of an electronic system provided the ground-state is nondegenerate. Since the external potential determines the entire electronic system, the ground state wavefunction and hence the ground state energy is uniquely determined by the ground-state electron density. This powerful result reduces the many-body Schrödinger problem of interacting electrons into an equivalent problem of non-interacting electrons in an effective mean field that is governed by electron density. We now show that the ground-state properties of materials depend only on electron density, following the Levy-Lieb constrained search approach [51]:

2.3.1 Existence of a functional of density

The variational statement (2.12) makes it obvious that the energy of the materials system is always greater than or equal to its ground-state energy. Denoting the ground-state energy by E_e^0, we have

$$\langle \Psi_e | \, \mathcal{H}_e \, | \Psi_e \rangle \geq E_e^0. \tag{2.22}$$

Substituting equations (2.4) and (2.5) in (2.22), we get the following:

$$\left\langle \Psi_e \right| T + \frac{1}{2} \sum_i \sum_j{}' \frac{1}{|\mathbf{r}_i - \mathbf{r}_j|} \left| \Psi_e \right\rangle + \int \rho(\mathbf{r}) V_{\text{ext}}(\mathbf{r}, \mathbf{R}) \, d\mathbf{r} \geq E_e^0 \tag{2.23}$$

The first term in equation (2.23) which includes the kinetic energy of interacting electrons and the electron-electron interactions depends on the electronic wave-function whereas the second term which denotes the interaction of the external-field with the electrons in the system is independent of the electronic wave-function and depends only on electron density. The equality in (2.22) holds when the wavefunction Ψ_e is the exact ground-state wavefunction and ρ is the exact ground state density. Now, the dependence of the first term on the wavefunction is removed by defining a functional:

$$F(\rho) = \min_{\Psi_e \to \rho} \left\langle \Psi_e \middle| T + \frac{1}{2} \sum_i \sum_j{}' \frac{1}{|\mathbf{r}_i - \mathbf{r}_j|} \middle| \Psi_e \right\rangle \tag{2.24}$$

where $\Psi_e \to \rho$ indicates the minimization over all possible anti-symmetric wavefunctions Ψ_e which generates a particular electron density ρ. Thus it follows that the ground-state energy and hence the ground-state materials properties depend only on electron density. The ground-state energy is given by

$$E_e^0 = \min_{\rho \in \mathcal{K}} \left(F(\rho) + \int \rho(\mathbf{r}) V_{\text{ext}}(\mathbf{r}, \mathbf{R})\, d\mathbf{r} \right) + \frac{1}{2} \sum_{I=1}^{N_a} \sum_{\substack{J=1 \\ J \neq I}}^{N_a} \frac{Z_I Z_J}{|\mathbf{R}_I - \mathbf{R}_J|} \tag{2.25}$$

where the last term in the above equation is the electrostatic repulsive energy between the nuclei which is independent of the electron density ρ. We also remark that the space of minimization of the electron density $\mathcal{K}$ consists of $\rho(\mathbf{r})$ which are non-negative, continuous and normalized. Further, any such $\rho(\mathbf{r})$ is obtained from an antisymmetric wavefunction Ψ_e describing N_e electrons given by equation (2.7) (because of the constraint $\Psi_e \to \rho$ in (2.24)). Such a density $\rho(\mathbf{r})$ is termed as 'N-representable'. In addition, the anti-symmetric wavefunction giving rise to $\rho(\mathbf{r})$ may be the solution of the Schrödinger equation for the above N-electron system moving in an external potential. Such a density $\rho(\mathbf{r})$ is termed as 'v-representable'. Hence the space of minimization ϱ consists of both v -representable and N-representable

densities $\rho(\mathbf{r})$. So far, the existence of unique functional of electron density $F(\rho)$ is discussed but a prescription to exactly evaluate of $F(\rho)$ is an open-question and is even more harder problem than the original variational problem (2.12). However, a practical method to compute $F(\rho)$ is proposed by Kohn and Sham [2] which lies at the heart of Kohn-Sham DFT and is discussed below:

2.3.2 The Kohn-Sham approach

An important step taken by Kohn and Sham [2] is to make use of the properties of a reference system of non-interacting electrons with density ρ to write the function $F(\rho)$ as

$$F(\rho) = T_{\mathrm{s}}(\rho) + E_{\mathrm{H}}(\rho) + E_{\mathrm{xc}}(\rho) \tag{2.26}$$

The first term in the expression for $F(\rho)$ denotes the kinetic energy of a non-interacting system of N_e electrons denoted by $T_s(\rho)$ and the second term denotes the classical electrostatic energy between the electrons denoted by $E_H(\rho)$ while the third term $E_{\mathrm{xc}}(\rho)$ denotes the exchange and correlation energy. The error made by approximating the kinetic energy and electron-electron interaction energy of the interacting electrons with the kinetic energy $T_{\mathrm{s}}(\rho)$ and classical electrostatic Hartree energy $E_{\mathrm{H}}(\rho)$ of the reference system of non-interacting electrons is lumped into the exchange-correlation energy $E_{\mathrm{xc}}(\rho)$ which is amenable to rather good approximations [2].

Hence the Kohn-Sham functional of electron density is given by

$$E_{\mathrm{KS}}(\rho) = T_{\mathrm{s}}(\rho) + E_{\mathrm{H}}(\rho) + E_{\mathrm{xc}}(\rho) + E_{\mathrm{eZ}}(\rho) + E_{\mathrm{ZZ}} \tag{2.27}$$

where

$$E_{\mathrm{eZ}}(\rho) = \int \rho(\mathbf{r}) V_{\mathrm{ext}}(\mathbf{r}, \mathbf{R})\, d\mathbf{r} \tag{2.28}$$

$$E_{\mathrm{ZZ}} = \frac{1}{2} \sum_{\substack{I,J=1 \\ I \neq J}}^{N_a} \frac{Z_I Z_J}{|\mathbf{R}_I - \mathbf{R}_J|} \tag{2.29}$$

We note that the equation (2.27) is just a reformulation of the functional in (2.25) when exact E_{xc} is known and hence E_{KS} equals E_e^0 at the ground-state. The ground state is infact obtained by rendering the Kohn-Sham functional $E_{\mathrm{KS}}(\rho)$ stationary with respect to ρ subject to the constraint that the total number of electrons is N_e. Hence

$$\frac{\delta E_{\mathrm{KS}}}{\delta \rho} = \frac{\delta}{\delta \rho} \left[T_{\mathrm{s}}(\rho) + E_{\mathrm{H}}(\rho) + E_{\mathrm{xc}}(\rho) + E_{\mathrm{eZ}}(\rho) + E_{\mathrm{ZZ}} \right] = \mu \tag{2.30}$$

$$\implies \frac{\delta T_{\mathrm{s}}}{\delta \rho} + V_{\mathrm{H}}(\rho) + V_{\mathrm{xc}}(\rho) + V_{\mathrm{ext}}(\rho) = \mu \tag{2.31}$$

where μ denotes the Lagrange multiplier associated with the constraint.

Kohn and Sham noticed that the solution of equation (2.31) for ground state electron density is identical to that of the equation for the ground state electron density of a reference system of non-interacting electrons in an effective potential V_{eff} i.e.

$$\frac{\delta T_{\mathrm{s}}}{\delta \rho} + V_{\mathrm{eff}}(\rho) = \mu \tag{2.32}$$

with

$$V_{\mathrm{eff}}(\rho) = V_{\mathrm{H}}(\rho) + V_{\mathrm{xc}}(\rho) + V_{\mathrm{ext}}(\rho) \tag{2.33}$$

In principle, equation (2.32) involves solving the Schrödinger equation associated with a non-interacting system consisting of N_e electrons in an effective mean field,

$$\left(-\frac{1}{2}\nabla^2 + V_{\mathrm{eff}}(\rho) \right) \psi_n(\mathbf{x}) = \epsilon_n \psi_n(\mathbf{x}) \tag{2.34}$$

and from its solutions $\psi_n(\mathbf{x})$, one can compute the kinetic energy just as in Hartree-Fock theory

$$T_{\mathrm{s}} = \sum_{i=1}^{N_e} \int \psi_n^*(\mathbf{x}) \left(-\frac{1}{2}\nabla^2 \right) \psi_n(\mathbf{x})\, d\mathbf{x} \tag{2.35}$$

and the electron density is computed using

$$\rho(\mathbf{r}) = \sum_{i=1}^{N_e} |\psi_i(\mathbf{x})|^2 \tag{2.36}$$

The above single-particle Schrödinger equations are known as the Kohn-Sham equations. The formulation presented so far does not involve any approximation so far. However this is only true if the exact functional form of $E_{\mathrm{xc}}(\rho)$ is known. This exchange-correlation term is approximated using various models—commonly modeled as an explicit functional of electron density—and these models have been shown to predict a wide range of materials properties across various materials systems.

The popular form of exchange-correlation energy functional is the local-density approximation (LDA) [52]

$$E_{\mathrm{xc}}(\rho) = \int \epsilon_{\mathrm{xc}}(\rho(\mathbf{r}))\, d\mathbf{r} \tag{2.37}$$

where $\epsilon_{\mathrm{xc}}(\rho(\mathbf{r}))$ is a local functional of ρ which is to be modeled. The most widely used model is that of homogeneous free electron gas. Further, local density gradients can also be used to improve the exchange-correlation approximations which are often referred to as generalized gradient approximations (GGA) [53, 54, 52].

$$E_{\mathrm{xc}}(\rho) = \int \epsilon_{\mathrm{xc}}(\rho(\mathbf{r}), \nabla\rho(\mathbf{r}))\, d\mathbf{r} \tag{2.38}$$

Hybrid exchange-correlation functionals [55] have also been used in the recent past which involves using the one-body wavefunctions in the exchange term and are found to be better approximations in predicting accurate band-gaps of semi-metals and

semi-conductor materials. Finally under the approximation for exchange-correlation energy, the problem of computing the ground-state electron density for a given position of nuclei $\mathbf{R}$ in Kohn-Sham DFT involves minimizing the Kohn-Sham energy functional $E_{\mathrm{KS}}(\{\psi_i\}, \mathbf{R})$ with respect to single particle wavefunctions $\{\psi_i\}$ and the functional is given by:

$$E_{\mathrm{KS}}(\{\psi_i\}, \mathbf{R}) = \sum_{i=1}^{N_e} \int \psi_i^*(\mathbf{x}) \left(-\frac{1}{2}\nabla^2\right) \psi_i(\mathbf{x})\, d\mathbf{x} + \int \rho(\mathbf{r}) V_{\mathrm{ext}}(\mathbf{r}, \mathbf{R})\, d\mathbf{r} + E_{\mathrm{xc}}(\rho) + \frac{1}{2} \int \int \frac{\rho(\mathbf{r})\rho(\mathbf{r}')}{|\mathbf{r} - \mathbf{r}'|}\, d\mathbf{r}\, d\mathbf{r}' + \frac{1}{2} \sum_{I=1}^{N_a} \sum_{\substack{J=1 \\ J \neq I}}^{N_a} \frac{Z_I Z_J}{|\mathbf{R}_I - \mathbf{R}_J|} \tag{2.39}$$

subject to the following orthonormal constraints given by

$$\int \psi_i(\mathbf{x}) \psi_j(\mathbf{x})\, d\mathbf{x} = \delta_{ij} \tag{2.40}$$

and the electron density is computed using $\rho(\mathbf{r}) = \sum_{i=1}^{N_e} |\psi_i(\mathbf{x})|^2$. We note that the Kohn-Sham energy functional presented above treats all-electrons explicitly and is often referred to as all-electron calculation. However, the tightly bound core electrons close to the nucleus of an atom may not influence the chemical bonding, and may not play a significant role in governing many material properties. Hence, it is a common practice to adopt the pseudopotential approach [56], where only the wavefunctions for the valence electrons are computed in response to the pseudopotential providing the effective electrostatic potential of the nucleus and core electrons.

2.3.3 Kohn-Sham eigenvalue problem

We now discuss the equivalence of the DFT variational and eigenvalue problems in this subsection in greater detail. Using Lagrange multipliers λ_{ij} to enforce the orthonormality constraints in equation (2.40) , we obtain the following functional to

be minimized:

$$E_{\text{cons}}(\{\psi_i\}, \mathbf{R}, \Lambda) = E_{\text{KS}}(\{\psi_i\}, \mathbf{R}) - \sum_{i=1}^{N_e}\sum_{j=1}^{N_e} \lambda_{ij} \left(\int \psi_i^*(\mathbf{x})\psi_j(\mathbf{x})\, d\mathbf{x} - \delta_{ij} \right) \tag{2.41}$$

and $\Lambda = (\Lambda_{ij})_{1\leq i,j\leq N_e}$ is $N_e \times N_e$ matrix with entries λ_{ij}. Rendering E_{cons} stationary, with respect to $\psi_i(\mathbf{x})$ and λ_{ij}, we obtain the following equations

$$\left(-\frac{1}{2}\nabla^2 + V_{\text{eff}}(\rho, \mathbf{R}) \right) \psi_i(\mathbf{x}) = \sum_{j=1}^{N_e} \lambda_{ij}\psi_j(\mathbf{x}) \tag{2.42}$$

$$\left(-\frac{1}{2}\nabla^2 + V_{\text{eff}}(\rho, \mathbf{R}) \right) \psi_i^*(\mathbf{x}) = \sum_{j=1}^{N_e} \lambda_{ji}\psi_j^*(\mathbf{x}) \tag{2.43}$$

$$\int \psi_i^*(\mathbf{x})\psi_j(\mathbf{x})\, d\mathbf{x} = \delta_{ij} \tag{2.44}$$

where

$$V_{\text{eff}}(\rho, \mathbf{R}) = V_{\text{ext}}(\rho, \mathbf{R}) + \frac{\delta E_{\text{H}}(\rho)}{\delta\rho} + \frac{\delta E_{\text{xc}}(\rho)}{\delta\rho}. \tag{2.45}$$

Taking the complex conjugate of (2.42), then subtracting it from (2.43), we obtain the relation

$$\sum_{j=1}^{N_e} (\lambda_{ij} - \lambda_{ij}^*)\psi_j(\mathbf{x}) = 0 \tag{2.46}$$

Since the ψ_j are linearly independent it follows that $\lambda_{ij} = \lambda_{ij}^*$, proving that the matrix Λ is indeed Hermitian. Expressing equation (2.42) in matrix form we get

$$\mathcal{H}\boldsymbol{\Psi} = \boldsymbol{\Psi}\Lambda \ \ , \ \ \mathcal{H} = -\frac{1}{2}\nabla^2 + V_{\text{eff}}(\rho, \mathbf{R}) \ \ , \ \ \boldsymbol{\Psi} = [\psi_1(\mathbf{x})\ \psi_2(\mathbf{x}) \cdots \psi_{N_e}(\mathbf{x})] \tag{2.47}$$

Since the matrix Λ is Hermitian, there exists an unitary matrix Q such that $\hat{\Lambda} = Q^*\Lambda Q$ where $\hat{\Lambda}$ is a real diagonal matrix. Further, we subject the wavefunctions to an unitary transformation with Q i.e $\hat{\boldsymbol{\Psi}} = \boldsymbol{\Psi}\, Q$. Since unitary transformations are norm-conserving, the electron density remains invariant, hence $\mathcal{H}$ remains invariant.

Using the above relations, Equation (2.47) can be rewritten as

$$\mathcal{H}\hat{\mathbf{\Psi}} = \hat{\mathbf{\Psi}}\hat{\Lambda} \tag{2.48}$$

The above equation is nothing but an eigenvalue problem of the form

$$\mathcal{H}\hat{\psi}_i = \epsilon_i\hat{\psi}_i, \quad i = 1, 2....N_e \tag{2.49}$$

where ϵ_i is the diagonal element of $\hat{\Lambda}$ matrix and $\hat{\psi}_i(\mathbf{x})$ are said to be canonical wavefunctions. Dropping the hat notation for the canonical wavefunctions, the Kohn-Sham variational problem is equivalent to solving the following eigenvalue problem for smallest N_e eigenvalues:

$$\left(-\frac{1}{2}\nabla^2 + V_{\text{eff}}(\rho, \mathbf{R})\right)\psi_i = \epsilon_i\,\psi_i, \quad i = 1, 2....N_e \tag{2.50}$$

and the choice of one over the other is strictly a matter of convenience. Further, the electron density in terms of the canonical wavefunctions is given by

$$\rho(\mathbf{r}) = \sum_{i=1}^{N_e} f(\epsilon_i, \mu)|\psi_i(\mathbf{x})|^2 \ , \tag{2.51}$$

where $f(\epsilon_i, \mu)$ is the orbital occupancy function, whose range lies in the interval $[0, 1]$, and μ represents the Fermi-energy. In ground-state calculations, the orbital occupancy function $f(\epsilon, \mu)$ is given by the Heaviside function

$$f(\epsilon, \mu) = \begin{cases} 1 & \text{if } \epsilon < \mu, \\ 0 & \text{otherwise .} \end{cases} \tag{2.52}$$

The Fermi-energy μ is computed from the constraint on the total number of electrons in the system $\int \rho(\mathbf{r})\, d\mathbf{r} = \sum_i f(\epsilon_i, \mu) = N_e$. Further, the kinetic energy of the non-

interacting electrons T_s can be written using the orbital occupancy factor and the Kohn-Sham eigenvalues in the following way:

$$T_s(\{\psi_i\}) = \sum_{i=1}^{N_e} \int \psi_i^*(\mathbf{x}) \left(-\frac{1}{2}\nabla^2\right) \psi_i(\mathbf{x})\, d\mathbf{x} = \sum_{i=1}^{N_e} f(\epsilon_i, \mu)\epsilon_i - \int V_{\text{eff}}(\mathbf{r})\, \rho(\mathbf{r})\, d\mathbf{r} \quad (2.53)$$

In the case of a periodic crystal, the effective potential V_{eff} has the periodicity of the lattice and the solutions of the Kohn-Sham eigenvalue problem are given by the Bloch theorem [57]. For periodic systems, it is computationally efficient to compute the Bloch solutions directly. The formulation in (2.50) represents a nonlinear eigenvalue problem which has to be solved self-consistently, and forms the major part of discussion in the subsequent chapters.

We remark that the above discussion of density functional theory inherently assumes absolute zero temperature. Extensions to finite temperatures (c.f [50]) is possible by introducing the Helmholtz free energy $\mathcal{F} = E_{KS} - T\,\mathcal{S}$ where E_{KS} is the ground-state energy obtained in Kohn-Sham DFT by introducing the finite temperature T while S denotes the entropy. The orbital occupancy function $f(\epsilon, \mu)$ can now take the fractional values between 0 and 1 as defined by the Fermi-Dirac distribution given by

$$f(\epsilon, \mu) = \frac{1}{1 + \exp\left(\frac{\epsilon - \mu}{\sigma}\right)}, \quad (2.54)$$

where $\sigma = k_B\, T$, k_B, being the Boltzmann constant. The entropy is given by the following expression:

$$\mathcal{S} = -k_B \sum_i \left[f(\epsilon_i, \mu) \log f(\epsilon_i, \mu) + (1 - f(\epsilon_i, \mu) \log(1 - f(\epsilon_i, \mu)))\right] \quad (2.55)$$

CHAPTER III

Real-space finite-element formulation of Kohn-Sham density functional theory

The enormous computational effort associated with Kohn-Sham DFT calculations has restricted investigations on material system sizes ranging from hundreds to a maximum of thousand atoms and hence has been primarily associated with the computation of bulk properties of materials using plane-wave basis[58, 59, 60]. However, plane-waves restrict simulation domains to periodic boundary conditions that are not suited for most material systems containing defects, nano-clusters, amorphous materials and so on. On the other hand, there are atomic-orbital-type basis sets [4, 5, 6] which are well suited only for isolated systems and cannot handle arbitrary boundary conditions. The efficiency of parallel scalability is significantly affected in both the cases due to nonlocality of basis functions. Thus, there has been an increasing thrust on systematically improvable and scalable real-space techniques [7, 8, 9, 10, 11, 12, 13, 14] for electronic-structure calculations over the past decade. The finite-element (FE) discretization of Kohn-Sham DFT, among the real-space techniques presents some key advantages–it is amenable to unstructured coarse-graining, allows for consideration of complex geometries and boundary conditions, and is scalable on parallel computing platforms. Thus, there has been an increasing thrust on systematically improvable and scalable real-space techniques for electronic-

structure calculations over the past decade. The finite-element (FE) discretization of Kohn-Sham DFT [15, 16, 17, 18, 19, 20, 21, 22, 23, 24, 25, 26, 27, 28, 29, 30], among the real-space techniques presents some key advantages–it is amenable to unstructured coarse-graining, allows for consideration of complex geometries and boundary conditions, and is scalable on parallel computing platforms.

While the finite-element basis is more versatile than the plane-wave basis [15, 19], it is not without its shortcomings. Prior investigations have shown that linear finite-elements require a large number of basis functions—of the order of $100,000$ basis functions per atom—to achieve chemical accuracy in electronic structure calculations (cf. e.g. [23, 31]), and this compares very poorly with plane-wave basis or other real-space basis functions. It has been demonstrated that higher-order finite-element discretizations can alleviate this degree of freedom disadvantage of linear finite-elements in electronic structure calculations [24, 31, 61]. However, the use of higher-order elements increases the per basis-function computational cost due to the need for higher-order accurate numerical quadrature rules. Furthermore, the bandwidth of the matrix increases cubically with the order of the finite-element, which in turn increases the computational cost of matrix-vector products. In addition, since a finite-element basis is non-orthogonal, the discretization of the Kohn-Sham DFT problem results in a generalized eigenvalue problem, which is more expensive to solve in comparison to a standard eigenvalue problem resulting from using an orthogonal basis (for e.g. plane-wave basis). Thus, the computational efficiency afforded by using a finite-element basis in electronic structure calculations, and its relative performance compared to plane-wave basis and atomic-orbital-type basis functions (for e.g Gaussian basis), has remained an open question to date. Hence, in the present work, we conduct a numerical investigation on the Kohn-Sham DFT problem and attempt to establish the computational efficiency afforded by higher-order finite-element discretizations in electronic structure calculations. To this end, we develop: (i) a unified

self-consistent formulation which can handle all-electron and pseudopotential calculations in a non-periodic and periodic setting on a similar footing (ii) an *a priori* mesh adaption technique to construct a close to optimal finite-element discretization of the problem; (iii) an efficient solution strategy for solving the discrete eigenvalue problem by using spectral finite-elements in conjunction with Gauss-Lobatto quadrature, and a Chebyshev acceleration technique for computing the occupied eigenspace. We subsequently study the numerical aspects of the finite-element discretization of the formulation, investigate the computational efficiency afforded by higher-order finite-elements, and compare the performance of the finite-element basis with plane-wave and Gaussian basis on benchmark problems.

The *a priori* mesh adaption technique proposed in this chapter is based on the ideas in [62, 63], and closely follows the recent development of the mesh adaption technique for orbital-free DFT [64]. This is based on minimizing the discretization error in the ground-state energy, subject to a fixed number of elements in the finite-element mesh. To this end, we first develop an estimate for the finite-element discretization error in the Kohn-Sham ground-state energy as a function of the characteristic mesh-size distribution, $h(\mathbf{r})$, and the exact ground-state electronic fields comprising of wavefunctions and electrostatic potential. We subsequently determine the optimal mesh distribution for the chosen representative solution by determining the $h(\mathbf{r})$ that minimizes the discretization error. The resulting expressions for the optimal mesh distribution are in terms of the degree of the interpolating polynomial and the exact solution fields of the Kohn-Sham DFT problem. Since the exact solution fields are *a priori* unknown, we use the asymptotic behavior of the atomic wavefunctions [65] away from the nuclei to determine the coarse-graining rates for the finite-element meshes used in our numerical study. Though the resulting finite-element meshes are not necessarily optimal near the vicinity of the nuclei, the mesh coarsening rate away from the nuclei provides an efficient way of resolving the vacuum in non-periodic

calculations.

We next implement an efficient solution strategy for solving the finite-element discretized eigenvalue problem, which is crucial before assessing the computational efficiency of the basis. We note that the non-orthogonality of the finite-element basis results in a discrete generalized eigenvalue problem, which is computationally more expensive than the standard eigenvalue problem that results from using an orthogonal basis like plane-waves. We address this issue by employing a spectral finite-element discretization and Gauss-Lobatto quadrature rules to evaluate the integrals which results in a diagonal overlap matrix, and allows for a trivial transformation to a standard eigenvalue problem. Further, we use the Chebyshev acceleration technique for standard eigenvalue problems to efficiently compute the occupied eigenspace (cf. e.g. [66] in the context of electronic structure calculations). Our investigations suggest that the use of spectral finite-elements and Gauss-Lobatto rules in conjunction with Chebyshev acceleration techniques to compute the eigenspace gives a $10-20$ fold computational advantage, even for modest materials system sizes, in comparison to traditional methods of solving the standard eigenvalue problem where the eigenvectors are computed explicitly. Further, the proposed approach has been observed to provide a staggering $100-200$ fold computational advantage over the solution of a generalized eigenvalue problem that does not take advantage of the spectral finite-element discretization and Gauss-Lobatto quadrature rules. In our implementation, we use a self-consistent field (SCF) iteration with Anderson mixing [67], and employ the finite-temperature Fermi-Dirac smearing [58] to suppress the charge sloshing associated with degenerate or close to degenerate eigenstates around the Fermi energy.

We next study various numerical aspects of the finite-element discretization of the Kohn-Sham DFT problem on benchmark problems involving both all-electron and pseudopotential calculation. Among pseudopotential calculations, we restrict ourselves to local pseudopotentials as a convenient choice to demonstrate our ideas.

We begin our investigation by examining the numerical rates of convergence of higher-order finite-element discretizations of Kohn-Sham DFT. We remark here that optimal rates of convergence have been demonstrated for quadratic hexahedral and cubic serendipity elements in pseudopotential Kohn-Sham DFT calculations [21, 27], and mathematically proved for Kohn-Sham DFT for the case of smooth pseudopotential external fields [68]. We also note that there have been several works on the mathematical analysis of optimal rates of convergence for non-linear eigenvalue problems [69, 70, 71]. However, the mathematical analysis of optimal rates of convergence of higher-order finite-element discretization of Kohn-Sham DFT problem involving Coulomb-singular potentials is an open question to date, to the best of our knowledge. In the present study, we compute the rates of convergence of the finite-element discretization of Kohn-Sham DFT for a range of finite-elements including linear tetrahedral element, hexahedral spectral-elements of order two, four and six. Two sets of benchmark problems are considered in this study: (i) all-electron calculations on boron atom and methane molecule; (ii) local pseudopotential calculations on a non-periodic barium cluster consisting of $2 \times 2 \times 2$ body-centered cubic (BCC) unit cells and a periodic face-centered cubic (FCC) calcium crystal. We note that our restriction in the present study to local pseudopotentials for pseudopotential calculations does not affect our conclusions on convergence rates, as demonstrated in [21, 27] where non-local pseudopotentials were employed. In these benchmark studies, as well as those to follow, the proposed *a priori* mesh adaption scheme is used to construct the meshes. These studies show rates of convergence in energy of $O(h^{2k})$ for a finite-element whose degree of interpolation is k, which denote optimal rates of convergence as demonstrated in [21, 68]. An interesting aspect of this study is that optimal rates of convergence have been observed even for all-electron calculations involving Coulomb-singular potentials, which, to the best of our knowledge, have not been analyzed or reported heretofore for the Kohn-Sham problem. We note that,

for Coulomb-singular potentials, in the context of orbital-free DFT optimal rates of convergence have been demonstrated in [71] for $k = 1$, 2 and have been demonstrated numerically for up to $k = 4$ in [64]. While the electrostatic interactions are common for both Kohn-Sham DFT and orbital-free DFT, the Kohn-Sham problem presents a more complex case as the approximation errors are governed by the entire occupied eigenspace of the Kohn-Sham problem as opposed to just the lowest eigenstate in the case of the orbital-free DFT problem.

We finally turn towards assessing the computational efficiency afforded by higher-order finite-element discretizations in Kohn-Sham DFT calculations. To this end, we use the same benchmark problems and measure the CPU-time for the solution of the Kohn-Sham DFT problem to various relative accuracies for all the finite-elements considered in the present study. We observe that higher-order elements can provide a significant computational advantage in the regime of chemical accuracy. The computational savings observed are about 1000-fold upon using higher-order elements in comparison with a linear finite-element for both all-electron as well as local pseudopotential calculations. We observe that a point of diminishing returns is reached at the sixth-order for the benchmark systems we studied and for accuracies commensurate with the chemical accuracy—i.e., no significant improvements in the computational efficiency was observed beyond this point. The degree of freedom advantage of higher-order finite-elements is nullified by the increasing per basis-function costs beyond this point. To further assess the effectiveness of higher-order finite-elements, we conduct local pseudopotential calculations on large aluminum clusters ranging from $3 \times 3 \times 3$ to $5 \times 5 \times 5$ FCC unit cells using the hexic spectral finite-element, and compare the computational times with that of plane-wave basis discretization using the ABINIT package [60]. We note that similar relative accuracies in the ground-state energies are achieved using the hexic finite-element with a lower computational cost in comparison to the plane-wave basis. Furthermore, we compute the electronic structure

of an aluminum cluster of $7 \times 7 \times 7$ FCC unit cells, containing 1688 atoms, with the finite-element basis using modest computational resources, which could not be simulated in ABINIT due to huge memory requirements.

We also investigate the efficiency of higher-order elements in the case of all-electron calculations on a larger materials systems and compare it with the Gaussian basis using the GAUSSIAN package [72]. In this case, the benchmark systems considered are a graphene sheet with 100 atoms and a tris (bipyridine) ruthenium complex with 61 atoms. We find that the solution times using the finite-element basis is larger by a factor of around 10 in comparison to Gaussian basis and we attribute this difference to the highly optimized Gaussian basis functions for specific atom types that resulted in the far fewer basis functions required to achieve chemical accuracy. While this difference in the performance can be offset by the better scalability of finite-element discretization on parallel computing platforms, there is also much room for further development and optimization in the finite-element discretization of the Kohn-Sham DFT problem. Finally, we assess the parallel scalability of our numerical implementation. We demonstrate the strong scaling up to 192 processors (limited by our access to computing resources) with an efficiency of 91.4% using a 172 atom aluminum cluster discretized with 3.91 million degrees of freedom as our benchmark system.

The remainder of the chapter is organized as follows. Section 3.1 describes the variational formulation of the Kohn-Sham DFT problem followed by a discussion on the discrete Kohn-Sham DFT eigenvalue problem. Section 3.2 develops the error estimates for the finite-element discretization of Kohn-Sham DFT, and uses these estimates to present an *a priori* mesh adaption scheme. Section 3.3 describes our numerical implementation of the self-consistent field iteration of the Kohn-Sham eigenvalue problem, and, in particular, discusses the efficient methodologies developed to solve the Kohn-Sham DFT problem using the finite-element basis. Section 3.4 presents a

comprehensive numerical study demonstrating the computational efficiency afforded by higher-order finite-element discretizations in electronic structure calculations, and also provides a performance comparison of finite-element basis with plane-wave and Gaussian basis. We finally conclude with a short discussion and summary of the chapter in Section 3.5.

3.1 Formulation

3.1.1 Kohn-Sham saddle-point formulation

In this section, we recall the Kohn-Sham DFT energy functional from Chapter II and present the saddle-point formulation arising out of the local reformulation of electrostatic energy. We subsequently review the equivalent self-consistent formulation of the Kohn-Sham eigenvalue problem, and present the discretization of the formulation using a finite-element basis and discuss how the present formulation provides a unified framework for both non-periodic, periodic, all-electron and psuedopotential calculations.

We recall from chapter II, the spinless Kohn-Sham energy functional describing a materials system consisting of N_e electrons and N_a nuclei is given by

$$E(\boldsymbol{\Psi}, \mathbf{R}) = T_{\mathrm{s}}(\boldsymbol{\Psi}) + E_{\mathrm{xc}}(\rho) + E_{\mathrm{H}}(\rho) + E_{\mathrm{ext}}(\rho, \mathbf{R}) + E_{\mathrm{zz}}(\mathbf{R}), \tag{3.1}$$

where

$$\rho(\mathbf{r}) = \sum_{i=1}^{N_e} |\psi_i(\mathbf{x})|^2 \tag{3.2}$$

represents the electron density. In the above expression, we denote the spatial coordinate by $\mathbf{r}$, whereas $\mathbf{x} = (\mathbf{r}, s)$ includes both the spatial and spin degrees of freedom with $\mathbf{r} = (x, y, z) = (r_1, r_2, r_3)$. Further $\boldsymbol{\Psi} = \{\psi_1(\mathbf{x}), \psi_2(\mathbf{x}), \cdots, \psi_{N_e}(\mathbf{x})\}$ denotes the vector of orthonormal single electron wavefunctions, where each wavefunction

$\psi_i \in \mathbb{X} \times \{\alpha, \beta\}$ can in general be complex-valued, and comprises of a spatial part belonging to a suitable function space $\mathbb{X}$ (elaborated subsequently) and a spin state denoted by $\alpha(s)$ or $\beta(s)$. We further denote by $\mathbf{R} = \{\mathbf{R}_1, \mathbf{R}_2, \cdots \mathbf{R}_{N_a}\}$ the collection of all nuclear positions. The first term in the Kohn-Sham energy functional in (3.1), $T_s(\{\mathbf{\Psi}\})$, denotes the kinetic energy of non-interacting electrons and is given by

$$T_{\rm s}(\mathbf{\Psi}) = \sum_{i=1}^{N_e} \int \psi_i^*(\mathbf{x}) \left(-\frac{1}{2}\nabla^2\right) \psi_i(\mathbf{x})\, d\mathbf{x} \ , \tag{3.3}$$

where ψ_i^* denotes the complex conjugate of ψ_i. E_{xc} in the energy functional denotes the exchange-correlation energy which includes the quantum-mechanical many body interactions. In the present work, we model the exchange-correlation energy using the local density approximation (LDA) [73, 74] represented as

$$E_{\rm xc}(\rho) = \int \varepsilon_{\rm xc}(\rho)\rho(\mathbf{r})\, d\mathbf{r} \ , \tag{3.4}$$

where $\varepsilon_{\rm xc}(\rho) = \varepsilon_{\rm x}(\rho) + \varepsilon_{\rm c}(\rho)$, and

$$\varepsilon_{\rm x}(\rho) = -\frac{3}{4}\left(\frac{3}{\pi}\right)^{1/3} \rho^{1/3}(\mathbf{r}) \ , \tag{3.5}$$

$$\varepsilon_c(\rho) = \begin{cases} \frac{\gamma}{(1+\beta_1\sqrt{(r_s)}+\beta_2 r_s)} & r_s \geq 1, \\ A\, \log r_s + B + C\, r_s \log r_s + D\, r_s & r_s \ < \ 1, \end{cases} \tag{3.6}$$

and $r_s = (3/4\pi\rho)^{1/3}$. Specifically, we use the Ceperley and Alder constants as given in [74]. We remark that we have restricted the present formulation and study to LDA exchange-correlation functionals solely for the sake of clarity, and the formulation can be trivially extended (cf. e.g. [25]) to local spin density approximation (LSDA) and generalized gradient approximation (GGA) exchange-correlation functionals.

The electrostatic interaction energies in the Kohn-Sham energy functional in (3.1)

are given by

$$E_{\mathrm{H}}(\rho) = \frac{1}{2}\int\int \frac{\rho(\mathbf{r})\rho(\mathbf{r}')}{|\mathbf{r}-\mathbf{r}'|}\, d\mathbf{r}\; d\mathbf{r}'\,, \tag{3.7}$$

$$E_{\mathrm{ext}}(\rho,\mathbf{R}) = \int \rho(\mathbf{r})V_{\mathrm{ext}}(\mathbf{r},\mathbf{R})\, d\mathbf{r} = \sum_J \int \rho(\mathbf{r})V_J(\mathbf{r},\mathbf{R}_J)\, d\mathbf{r}\,, \tag{3.8}$$

$$E_{\mathrm{zz}} = \frac{1}{2}\sum_{I,J\neq I} \frac{Z_I Z_J}{|\mathbf{R}_I-\mathbf{R}_J|}\,, \tag{3.9}$$

where E_{H} is the Hartree energy representing the classical electrostatic interaction energy between electrons, E_{ext} is the interaction energy between electrons and the external potential induced by the nuclear charges given by $V_{\mathrm{ext}} = \sum_J V_J(\mathbf{r},\mathbf{R}_J)$ with V_J denoting the potential (singular Coulomb potential) contribution from the J^{th} nucleus, and E_{zz} denotes the repulsive energy between nuclei with Z_I denoting the charge on the I^{th} nucleus. We note that in a non-periodic setting, representing a finite atomic system, all the integrals in equations (3.3)-(3.8) are over $\mathbb{R}^3$ and the summations in (3.8)-(3.9) include all the atoms I and J in the system. In the case of an infinite periodic crystal, all the integrals over $\mathbf{r}$ in equations (3.3)-(3.8) extend over the unit cell, whereas the integrals over $\mathbf{r}'$ extend in $\mathbb{R}^3$. Similarly, in (3.8)-(3.9) the summation over I is on the atoms in the unit cell, and summation over J extends over all lattice sites. We note that, in the context of periodic problems, the above expressions assume a single k-point ($\Gamma-$point) sampling. The computation of the electron density and kinetic energy in (3.2) and (3.3) for multiple k-point sampling involves an additional quadrature over the k-points in the Brillouin zone (cf. e.g [57]).

The electrostatic interaction terms as expressed in equations (3.7)-(3.9) are non-local in real-space, and, for this reason, evaluation of electrostatic energy is the computationally expensive part of the calculation. Following the approach in [75, 25], the electrostatic interaction energy can be reformulated as a local variational problem in electrostatic potential by observing that $\frac{1}{|\mathbf{r}|}$ is the Green's function of the Laplace operator. To this end, we represent the nuclear charge distribution by $b(\mathbf{r},\mathbf{R}) =$

$\sum_{I=1}^{N_a} b_I(\mathbf{r}, \mathbf{R}_I) = -\sum_{I=1}^{N_a} Z_I \tilde{\delta}_{\mathbf{R}_I}(\mathbf{r})$, where $Z_I \tilde{\delta}_{\mathbf{R}_I}(\mathbf{r})$ represents a bounded smooth charge distribution centered at $\mathbf{R}_I$, corresponding to the regularization of a point charge having a support in a small ball around $\mathbf{R}_I$ with charge Z_I. The nuclear repulsion energy can subsequently be represented as

$$E_{\text{zz}}(\mathbf{R}) = \frac{1}{2} \int \int \frac{b(\mathbf{r}, \mathbf{R}) b(\mathbf{r}', \mathbf{R})}{|\mathbf{r} - \mathbf{r}'|} \, d\mathbf{r} \, d\mathbf{r}' - E_{\text{self}}. \tag{3.10}$$

where

$$E_{\text{self}} = \frac{1}{2} \sum_{I=1}^{N_a} \int \int \frac{b_I(\mathbf{r}, \mathbf{R}_I) b_I(\mathbf{r}, \mathbf{R}_I)}{|\mathbf{r} - \mathbf{r}'|} \, d\mathbf{r} \, d\mathbf{r}' \tag{3.11}$$

We remark that, the first term in the equation (3.10) differs from the expression in equation (3.9) by the self-energy of the nuclei E_{self}, which is an inconsequential constant depending only on the nuclear charge distribution. Subsequently, the electrostatic interaction energy, up to a constant self-energy, is given by the following variational problem:

$$\begin{aligned} &\frac{1}{2} \int \int \frac{\rho(\mathbf{r}) \rho(\mathbf{r}')}{|\mathbf{r} - \mathbf{r}'|} \, d\mathbf{r} \, d\mathbf{r}' + \int \rho(\mathbf{r}) V_{\text{ext}}(\mathbf{r}) \, d\mathbf{r} + \frac{1}{2} \int \int \frac{b(\mathbf{r}, \mathbf{R}) b(\mathbf{r}', \mathbf{R})}{|\mathbf{r} - \mathbf{r}'|} \, d\mathbf{r} \, d\mathbf{r}' \\ &= -\inf_{\varphi \in \mathcal{Y}} \left\{ \frac{1}{8\pi} \int |\nabla \varphi(\mathbf{r})|^2 \, d\mathbf{r} - \int (\rho(\mathbf{r}) + b(\mathbf{r}, \mathbf{R})) \varphi(\mathbf{r}) \, d\mathbf{r} \right\}, \end{aligned} \tag{3.12}$$

where $\varphi(\mathbf{r})$ denotes the trial function for the total electrostatic potential due to the electron density and the nuclear charge distribution and $\mathcal{Y}$ is a suitable function space discussed subsequently. Similarly the computation of self-energy in equation (3.11) is reformulated as a local-variational problem in self-potentials $\boldsymbol{\nu} = \{\nu_1(\mathbf{r}), \nu_2(\mathbf{r}), \cdots\}$ associated with N_a nuclei:

$$E_{\text{self}} = E_{\text{self}}(\boldsymbol{\nu}, \mathbf{R}) = \sup_{\boldsymbol{\nu}\in\mathcal{V}}\Big(\sum_{I=1}^{N_a}\Big[-\frac{1}{8\pi}\int\limits_{\Omega_I} |\nabla\nu_I(\mathbf{r})|^2\, d\mathbf{r} + \int\limits_{\Omega_I} b_I(\mathbf{r})\nu_I(\mathbf{r})\, d\mathbf{r} + \frac{1}{8\pi}\int\limits_{\partial\Omega_I} \bar{\nu_I}(\mathbf{r})(\nabla\bar{\nu_I}(\mathbf{r}).\boldsymbol{n})\, d\Gamma_I\Big]\Big) \tag{3.13}$$

where $\bar{\nu_I}(\mathbf{r})$ denotes the boundary condition $\frac{Z_I}{|\mathbf{r}-\mathbf{R}_I|}$ applied on the boundary $d\Gamma_I$ of the domain Ω_I on which $\nu_I(\mathbf{r})$ is computed and $\mathcal{V} = \{\mathcal{V}_1, \cdots, \mathcal{V}_{N_a}\}$ is the set of appropriate function spaces discussed subsequently. Using the above local reformulations of electrostatic interactions, the Kohn-Sham energy functional (3.1) can be rewritten as

$$E(\boldsymbol{\Psi}, \mathbf{R}) = \sup_{\varphi\in\mathcal{Y}}\inf_{\boldsymbol{\nu}\in\mathcal{V}} L(\varphi, \boldsymbol{\nu}, \boldsymbol{\Psi}, \mathbf{R}) \ , \tag{3.14}$$

where

$$L(\varphi, \boldsymbol{\nu}, \boldsymbol{\Psi}, \mathbf{R}) = T_{\text{s}}(\boldsymbol{\Psi}) + E_{\text{xc}}(\rho) - \frac{1}{8\pi}\int |\nabla\varphi(\mathbf{r})|^2\, d\mathbf{r} + \int (\rho(\mathbf{r}) + b(\mathbf{r}, \mathbf{R}))\varphi(\mathbf{r})\, d\mathbf{r} + \sum_{I=1}^{N_a}\Big[\frac{1}{8\pi}\int\limits_{\Omega_I} |\nabla\nu_I(\mathbf{r})|^2\, d\mathbf{r} - \int\limits_{\Omega_I} b_I(\mathbf{r})\nu_I(\mathbf{r})\, d\mathbf{r} - \frac{1}{8\pi}\int\limits_{\partial\Omega_I} \bar{\nu_I}(\mathbf{r})(\nabla\bar{\nu_I}(\mathbf{r}).\boldsymbol{n})\, d\Gamma_I\Big] \ . \tag{3.15}$$

Subsequently, the problem of determining the ground-state energy and electron density for given positions of nuclei can be expressed as the following variational problem:

$$\inf_{\boldsymbol{\Psi}\in\mathcal{X}} E(\boldsymbol{\Psi}, \mathbf{R}) \ , \tag{3.16}$$

where $\mathcal{X} = \big\{\boldsymbol{\Psi} \,|\, \langle\psi_i, \psi_j\rangle_{\mathbb{X}\times\{\alpha,\beta\}} = \delta_{ij}\big\}$ with $\langle\ ,\ \rangle_{\mathbb{X}\times\{\alpha,\beta\}}$ denoting the inner product defined on $\mathbb{X}\times\{\alpha, \beta\}$. $\mathbb{X}$ denotes a suitable function space that guarantees the existence of minimizers. We note that bounded domains are used in numerical computations, which in non-periodic calculations corresponds to a large enough domain containing

the compact support of the wavefunctions and in periodic calculations correspond to the supercell. We denote such an appropriate bounded domain, subsequently, by Ω. For formulations on bounded domains, $\mathbb{X} = \mathcal{Y} = H_0^1(\Omega)$ in the case of non-periodic problems and $\mathbb{X} = \mathcal{Y} = H_{per}^1(\Omega)$ in the case of periodic problems are appropriate function spaces which guarantee existence of solutions (cf. e.g. [25]). Further we also note that the appropriate functional space for the self-potential $\nu_I(\mathbf{r})$ is given by $\mathcal{V}_I = H^1(\Omega_I)$. Mathematical analysis of the Kohn-Sham DFT problem proving the existence of solutions in the more general case of $\mathbb{R}^3$ ($\mathbb{X} = H^1(\mathbb{R}^3)$) has recently been reported [76].

3.1.2 Kohn-Sham self-consistent formulation

The stationarity condition corresponding to the Kohn-Sham variational problem is equivalent to solving the non-linear Kohn-Sham eigenvalue problem given by:

$$\mathcal{H}\psi_i = \epsilon_i \psi_i, \tag{3.17}$$

where

$$\mathcal{H} = \left(-\frac{1}{2}\nabla^2 + V_{\text{eff}}(\rho, \mathbf{R}) \right) \tag{3.18}$$

is a Hermitian operator with eigenvalues ϵ_i, and the corresponding orthonormal eigenfunctions $\psi_i(\mathbf{r})$ denote the spatial part of canonical wavefunctions. As discussed in Chapter II, the electron density in terms of the spatial part of canonical wavefunctions is computed using

$$\rho(\mathbf{r}) = 2 \sum_i f(\epsilon_i, \mu) |\psi_i(\mathbf{r})|^2 \ , \tag{3.19}$$

where the factor 2 in the above equation represents the case of spin independent system where each orbital is occupied by two electrons. The effective single-electron

potential in equation (3.18), $V_{\text{eff}}(\rho, \mathbf{R})$, in (3.18) is given by

$$V_{\text{eff}}(\rho, \mathbf{R}) = \varphi(\mathbf{r}, \mathbf{R}) + \frac{\delta E_{\text{xc}}}{\delta \rho} = \varphi(\mathbf{r}, \mathbf{R}) + V_{\text{xc}}(\rho) \tag{3.20}$$

where $\varphi(\mathbf{r}, \mathbf{R})$ is the total electrostatic potential comprising of both Hartree potential and nuclear potential contribution which is computed through the solution of a Poisson equation

$$-\frac{1}{4\pi}\nabla^2 \varphi(\mathbf{r}, \mathbf{R}) = \rho(\mathbf{r}) + b(\mathbf{r}, \mathbf{R}) \ .$$

However in the case of a pseudopotential approach where only the wavefunctions for the valence electrons are computed, $b(\mathbf{r}, \mathbf{R})$ corresponds to the regularization of a point charge having a support in a small ball around $\mathbf{R}_I$ with valence charge Z_I. Further, the single-electron potential $V_{\text{eff}}(\rho, \mathbf{R})$ in (3.18) now consists of an effective electrostatic potential of the nucleus and core electrons and is often defined by an operator

$$\mathcal{V}_{\text{PS}} = \mathcal{V}_{\text{loc}} + \mathcal{V}_{\text{nl}} \, , \tag{3.21}$$

where $\mathcal{V}_{\text{loc}}$ is the local part of the pseudopotential operator and $\mathcal{V}_{\text{nl}}$ is the non-local part of the operator. If we use the norm-conserving Troullier-Martins pseudopotential [77] in the Kleinman-Bylander form [78], the action of these operators on a Kohn-Sham wavefunction in the real-space is given by

$$V_{\text{loc}}(\mathbf{r}, \mathbf{R})\psi(\mathbf{r}) = \sum_{J=1}^{N_a} V_{\text{loc}}^J(\mathbf{r} - \mathbf{R}_J)\psi(\mathbf{r}) \, , \tag{3.22}$$

$$V_{\text{nl}}(\mathbf{r}, \mathbf{R})\psi(\mathbf{r}) = \sum_{J=1}^{N_a} \sum_{lm} C_{lm}^J V_{lm}^J \zeta_{lm}^J(\mathbf{r} - \mathbf{R}_J) \Delta V_l{}^J(\mathbf{r} - \mathbf{R}_J) \, , \tag{3.23}$$

where

$$\Delta V_l^J(\mathbf{r}-\mathbf{R}_J) = V_l^J(\mathbf{r}-\mathbf{R}_J) - V_{\text{loc}}^J(\mathbf{r}-\mathbf{R}_J)\,,$$
$$C_{lm}^J = \int \zeta_{lm}^J(\mathbf{r}-\mathbf{R}_J)\Delta V_l^J(\mathbf{r}-\mathbf{R}_J)\psi(\mathbf{r})\,d\mathbf{x}\,,$$
$$\frac{1}{V_{lm}^J} = \int \zeta_{lm}^J(\mathbf{r}-\mathbf{R}_J)\Delta V_l^J(\mathbf{r}-\mathbf{R}_J)\zeta_{lm}^J(\mathbf{r}-\mathbf{R}_J)\,d\mathbf{x}\ .$$

In the above, $V_l^J(\mathbf{r}-\mathbf{R}_J)$ denotes the pseudopotential component of the atom J corresponding to the azimuthal quantum number l, $V_{\text{loc}}^J(\mathbf{r}-\mathbf{R}_J)$ is the corresponding local potential, and $\zeta_{lm}^J(\mathbf{r}-\mathbf{R}_J)$ is the corresponding single-atom pseudo-wavefunction with azimuthal quantum number l and magnetic quantum number m. Hence the single-electron potential $V_{\text{eff}}(\rho,\mathbf{R})$ in (3.18) in the case of pseudopotential approach is given by

$$V_{\text{eff}}(\rho,\mathbf{R}) = \varphi(\mathbf{r},\mathbf{R}) + V_{\text{xc}}(\rho) + V_{\text{loc}}(\mathbf{R}) + V_{nl}(\mathbf{R}) - \sum_{J=1}^{N_a}\nu_J(\mathbf{r}) \tag{3.24}$$

Finally, the system of equations corresponding to the Kohn-Sham eigenvalue problem is given by

$$\left(-\frac{1}{2}\nabla^2 + V_{\text{eff}}(\rho,\mathbf{R})\right)\psi_i = \epsilon_i\psi_i, \tag{3.25a}$$
$$2\sum_i f(\epsilon_i,\mu) = N_e; \quad \rho(\mathbf{r}) = 2\sum_{i=1} f(\epsilon_i,\mu)|\psi_i(\mathbf{r})|^2, \tag{3.25b}$$
$$-\frac{1}{4\pi}\nabla^2\varphi(\mathbf{r},\mathbf{R}) = \rho(\mathbf{r}) + b(\mathbf{r},\mathbf{R}); \quad -\frac{1}{4\pi}\nabla^2\nu_I(\mathbf{r},\mathbf{R}) = b_I(\mathbf{r},\mathbf{R}). \tag{3.25c}$$

which have to be solved with appropriate boundary conditions based on the problem under consideration. In the case of a periodic crystal, the effective potential V_{eff} has the periodicity of the lattice and the solutions of the Kohn-Sham eigenvalue problem are given by the Bloch theorem [57]. Thus, for periodic systems, it is computationally efficient to compute the Bloch solutions directly and further the sum over the atoms

in equations (3.22) and (3.24) runs over all the atoms in the crystal. The formulation in (3.25a) represents a nonlinear eigenvalue problem which has to be solved self-consistently and is subsequently discussed in section 3.3. Upon self-consistently solving (3.25a), the ground-state energy of the materials system in our real space formulation is computed using

$$E^0_{\text{tot}} = E_{\text{band}} \; + \int (\varepsilon_{\text{xc}}(\rho) - V_{\text{xc}}(\rho))\, \rho \, d\mathbf{r} \; + \frac{1}{2} \int (b(\mathbf{r}, \mathbf{R}) - \rho(\mathbf{r}))\varphi(\mathbf{r}, \mathbf{R}) \, d\mathbf{r} \\ - \frac{1}{2} \sum_{J=1}^{N_a} \int_{\Omega_I} b_I(\mathbf{r}) \nu_I(\mathbf{r}) \, d\mathbf{r} \tag{3.26}$$

where E_{band}, denotes the band energy, is given by

$$E_{\text{band}} = 2 \sum_i f(\epsilon_i, \mu) \epsilon_i \, . \tag{3.27}$$

We note that the expression for the computation of ground-state energy given in equation (3.26) can be used for both all-electron and pseudopotential calculations. The domain of integration in (3.26) corresponds to a large enough domain containing the compact support of the wavefunctions in the case of non-periodic calculations while in the case of periodic calculations, E^0_{tot} represents the energy per periodic unit-cell and hence the domain of integration corresponds to a periodic unit-cell. The energy per periodic unit-cell computed using the expression in (3.26) involves E_{band} and the electron density $\rho(\mathbf{r})$ which inturn involves an integral over the Brillouin zone and is usually evaluated using an additional quadrature rule over the k-points in the Brillouin zone (cf. e.g [57]). Next we turn to the discrete formulation of the above Kohn-Sham eigenvalue problem.

3.1.3 Discrete Kohn-Sham problem

If $\mathbb{V}_h^M$ represents the finite-dimensional space with dimension M, the finite-element approximation of the various field variables (spatial part of the wavefunctions and the electrostatic potential) in the Kohn-Sham eigenvalue problem (3.25a) are given by

$$\psi_i^h(\mathbf{r}) = \sum_{j=1}^{M} N_j(\mathbf{r})\psi_i^j \ , \tag{3.28}$$

$$\varphi^h(\mathbf{r}) = \sum_{j=1}^{M} N_j(\mathbf{r})\varphi^j \ , \tag{3.29}$$

where $N_j : 1 \leq j \leq M$ denote the basis of $\mathbb{V}_h^M$. Subsequently, the discrete eigenvalue problem corresponding to (3.25a) is given by

$$\mathbf{H}\tilde{\boldsymbol{\Psi}}_i = \epsilon_i^h \mathbf{M}\tilde{\boldsymbol{\Psi}}_i \ , \tag{3.30}$$

where H_{jk} denotes the discrete Hamiltonian matrix, M_{jk} denotes the overlap matrix (or commonly referred to as the mass matrix in finite-element literature), and ϵ_i^h denotes i^{th} eigenvalue corresponding to the eigenvector $\tilde{\boldsymbol{\Psi}}_i$. The expression for the discrete Hamiltonian matrix H_{jk} for a non-periodic problem with $\mathbb{X} = \mathcal{Y} = H_0^1(\Omega)$ as well as a periodic problem on a supercell with $\mathbb{X} = \mathcal{Y} = H_{per}^1(\Omega)$ is given by

$$\mathrm{H}_{jk} = \mathrm{H}_{jk}^{\mathrm{loc}} + \mathrm{H}_{jk}^{\mathrm{nl}} \, , \tag{3.31}$$

where

$$\mathrm{H}_{jk}^{\mathrm{loc}} = \frac{1}{2}\int \nabla N_j(\mathbf{r}).\nabla N_k(\mathbf{r}) \, d\mathbf{r} + \int V_{\mathrm{eff,loc}}^h(\mathbf{r},\mathbf{R}) N_j(\mathbf{r}) N_k(\mathbf{r}) \, d\mathbf{r} \ . \tag{3.32}$$

We refer to [21] for the expression of H_{jk} in the case of a periodic problem on a unit-cell using the Bloch theorem. Note that in (3.32), $V_{\mathrm{eff,loc}}^h$ denotes the local part

of the effective single-electron potential computed in the finite-element basis (the discretized effective single-electron potential). In the case of all-electron calculations, $V^h_{\text{eff,loc}} = V^h_{\text{xc}} + \varphi^h$ with φ^h denoting the discretized all-electron total elecrostatic potential comprising of external Coulomb potential from all nuclei and the Hartree potential from all-electron density while in the case of pseudopotential calculations, $V^h_{\text{eff,loc}} = \varphi^h + V^h_{\text{xc}} + V^h_{\text{loc}} - \sum_{J=1}^{N_a} \nu^h_J$, where V^h_{loc} denotes the discretized local part of the pseudopotential (cf. equations (3.22) and (3.24)). Here φ^h denotes the discretized total electrostatic potential comprising of external Coulomb potential from all nuclei with valence charge and the Hartree potential from the valence electron density and ν^h_J denotes the discretized self-potential arising out of the J^{th} nuclear charge. As noted in the set of equations (3.25a) to (3.25c), φ^h and ν^h_J are computed as solutions of the Poisson's equation in the finite-element basis. In the case of all-electron calculations, the term H^{nl}_{jk} in (3.31) is zero, while in the case of pseudopotential calculations it is given by

$$\mathrm{H}^{\text{nl}}_{jk} = \sum_{J=1}^{N_a} \sum_{lm} C^J_{lm,j} V^J_{lm} C^J_{lm,k} \,, \tag{3.33}$$

where

$$C^J_{lm,j} = \int \zeta^J_{lm}(\mathbf{r} - \mathbf{R}_J) \Delta V_l{}^J(\mathbf{r} - \mathbf{R}_J) N_j(\mathbf{r}) \, d\mathbf{r} \,. \tag{3.34}$$

Finally, the matrix elements of the overlap matrix $\mathbf{M}$ are given by

$$\mathrm{M}_{jk} = \int N_j(\mathbf{r}) N_k(\mathbf{r}) \, d\mathbf{r}. \tag{3.35}$$

We note that the matrices $\mathbf{H}^{\text{loc}}$ and $\mathbf{M}$ are sparse as the finite-element basis functions are local in real space and have a compact support (a finite region where the function is non-zero and zero elsewhere). Further, the vectors $C^J_{lm,j}$ in $\mathbf{H}^{nl}$ are also sparse since both $\zeta^J_{lm}(\mathbf{r} - \mathbf{R}_J)$ and $\Delta V_l{}^J(\mathbf{r} - \mathbf{R}_J)$ have a compact support, thus rendering a sparse structure to the discrete Hamiltonian $\mathbf{H}$.

It is now desirable to transform the generalized eigenvalue problem (3.30) into a

standard eigenvalue problem for which a wide range of efficient solution procedures can be employed. Since the matrix $\mathbf{M}$ is positive definite symmetric, there exists a unique positive definite symmetric square root of $\mathbf{M}$, and is denoted by $\mathbf{M}^{1/2}$. Hence, the following holds true:

$$\begin{aligned} & \mathbf{H}\hat{\boldsymbol{\Psi}}_i = \epsilon_i^h \mathbf{M}\hat{\boldsymbol{\Psi}}_i \\ \Rightarrow \quad & \mathbf{H}\hat{\boldsymbol{\Psi}}_i = \epsilon_i^h \mathbf{M}^{1/2}\mathbf{M}^{1/2}\hat{\boldsymbol{\Psi}}_i \\ \Rightarrow \quad & \widetilde{\mathbf{H}}\widetilde{\boldsymbol{\Psi}}_i = \epsilon_i^h \widetilde{\boldsymbol{\Psi}}_i \,, \end{aligned} \tag{3.36}$$

where

$$\begin{aligned} \widetilde{\boldsymbol{\Psi}}_i &= \mathbf{M}^{1/2}\hat{\boldsymbol{\Psi}}_i \\ \widetilde{\mathbf{H}} &= \mathbf{M}^{-1/2}\mathbf{H}\mathbf{M}^{-1/2} \,. \end{aligned}$$

We note that $\widetilde{\mathbf{H}}$ is a Hermitian matrix, and (3.36) represents a standard Hermitian eigenvalue problem. The actual eigenvectors are recovered by the transformation $\hat{\boldsymbol{\Psi}}_i = \mathbf{M}^{-1/2}\tilde{\boldsymbol{\Psi}}_i$.

Furthermore, we note that the transformation to a standard eigenvalue problem (3.36) is computationally advantageous if the matrix $\mathbf{M}^{-1/2}$ can be evaluated with modest computational cost and the matrix $\widetilde{\mathbf{H}}$ has the same sparsity structure as the matrix $\mathbf{H}$. This is immediately possible by using a spectral finite-element basis which is discussed in detail in the subsequent section. The convergence of finite-element approximation for the Kohn-Sham DFT model was shown in [25] using the notion of $\Gamma-$convergence. We also refer to the recent numerical analysis carried out on finite dimensional discretization of Kohn-Sham models [68], which also provides the rates of convergence of the approximation for pseudopotential calculations. We remark that in the present work we use the same finite-element discretization for

both electronic wavefunctions and electrostatic potential, as is evident from equations (3.28)-(3.29). Since the electrostatic potential has similar discretization errors as compared to the electronic wavefunctions and since the Kohn-Sham DFT problem is a saddle-point problem in electronic wavefunctions and electrostatic potential (see equations (3.14)-(3.16), also cf. [25]) the convergence of the finite-element discretization error is non-variational in general. We note, however, that by using a more refined discretization (h-refinement) or by using a higher-order polynomial (p-refinement) as in [30] for the discretization of electrostatic fields in comparison to the discretization of electronic wavefunctions, this drawback can be mitigated. Next, we derive the optimal coarse-graining rates for the finite-element meshes using the solution fields in the Kohn-Sham DFT problem.

3.2 A-*priori* mesh adaption

We propose an *a priori* mesh adaption scheme in the spirit of [63, 62] by minimizing the error involved in the finite-element approximation of the Kohn-Sham DFT problem for a fixed number of elements in the mesh. The proposed approach closely follows the *a priori* mesh adaption scheme developed in the context of orbital-free DFT [64]. In what follows, we first derive a formal bound on the energy error $|E-E_h|$ as a function of the characteristic mesh-size h, and the distribution of electronic fields (wavefunctions and electrostatic potential). We note that, in a recent study, error estimates for a generic finite dimensional approximation of the Kohn-Sham model have been derived [68]. However, the forms of these estimates are not useful for developing mesh-adaption schemes as the study primarily focused on proving the convergence of the finite-dimensional approximation and determining the convergence rates. We first present the derivation of an error bound in terms of the canonical wavefunctions and the electrostatic potential, and subsequently develop an *a priori* mesh adaption scheme based on this error bound.

3.2.1 Estimate of energy error

In the present section and those to follow, we demonstrate our ideas on a system with no spin-polarization consisting of $N_e = 2N$ electrons for the sake of simplicity and notational clarity. Let ($\bar{\mathbf{\Psi}}^h = \{\bar{\psi}_1^h\,,\, \bar{\psi}_2^h \cdots \bar{\psi}_N^h\}\,, \bar{\varphi}^h\,, \bar{\epsilon}^h = \{\bar{\epsilon}_1^h\,, \bar{\epsilon}_2^h \cdots \bar{\epsilon}_N^h\}$) and ($\bar{\mathbf{\Psi}} = \{\bar{\psi}_1\,,\, \bar{\psi}_2 \cdots \bar{\psi}_N\}, \bar{\varphi}\,, \bar{\epsilon} = \{\bar{\epsilon}_1\,, \bar{\epsilon}_2 \cdots \bar{\epsilon}_N\}$) represent the solutions (spatial part of canonical wavefunctions, electrostatic potential, eigenvalues) of the discrete finite-element problem (3.30) and the continuous problem described in (3.25a)- (3.25c) respectively. In the following derivation and henceforth in this article, we consider all wavefunctions to be real-valued and orthonormal. We note that it is always possible to construct real-valued orthonormal wavefunctions for both non-periodic problems as well as periodic problems on the supercell. The wavefunctions are complex-valued for periodic problems on a unit-cell (with multiple k-points using the Bloch theorem), and the following approach is still valid, but results in more elaborate expressions for the error bounds. Using the local reformulation of electrostatic interactions in the Kohn-Sham energy functional (equations (3.14)-(3.15)), the ground-state energy in the discrete and the continuous problem can be expressed as:

$$E_h(\bar{\mathbf{\Psi}}^h, \bar{\varphi}^h) = 2\sum_{i=1}^{N} \int\limits_{\Omega} \frac{1}{2}|\nabla \bar{\psi}_i^h|^2 \, d\mathbf{r} + \int\limits_{\Omega} F(\rho(\bar{\mathbf{\Psi}}^h))\, d\mathbf{r} - \frac{1}{8\pi}\int\limits_{\Omega} |\nabla \bar{\varphi}^h|^2 \, d\mathbf{r} + \int\limits_{\Omega} (\rho(\bar{\mathbf{\Psi}}^h) + b)\bar{\varphi}^h \, d\mathbf{r}\,, \tag{3.37}$$

$$E(\bar{\mathbf{\Psi}}, \bar{\varphi}) = 2\sum_{i=1}^{N} \int\limits_{\Omega} \frac{1}{2}|\nabla \bar{\psi}_i|^2 \, d\mathbf{r} + \int\limits_{\Omega} F(\rho(\bar{\mathbf{\Psi}}))\, d\mathbf{r} - \frac{1}{8\pi}\int\limits_{\Omega} |\nabla \bar{\varphi}|^2 \, d\mathbf{r} + \int\limits_{\Omega} (\rho(\bar{\mathbf{\Psi}}) \, + \, b)\bar{\varphi} \, d\mathbf{r}\,, \tag{3.38}$$

where

$$F(\rho) = \epsilon_{xc}(\rho)\rho \ .$$

Proposition III.1. *In the neighborhood of ($\bar{\mathbf{\Psi}}, \bar{\varphi}\,, \bar{\epsilon}$), the finite-element approximation error in the ground-state energy can be bounded as follows:*

$$
\begin{aligned}
|E_h - E| \leq 2\sum_{i=1}^{N}\Big[\frac{1}{2}\int_{\Omega}|\nabla\delta\psi_i|^2\,d\mathbf{r} + \left|\,\bar{\epsilon}_i\int_{\Omega}(\delta\psi_i)^2\,d\mathbf{r}\right| + \left|\int_{\Omega}F'(\rho(\bar{\mathbf{\Psi}}))(\delta\psi_i)^2\,d\mathbf{r}\right| \\
+ \left|\int_{\Omega}(\delta\psi_i)^2\bar{\varphi}\,d\mathbf{r}\right| + 2\left|\int_{\Omega}\bar{\psi}_i\;\delta\psi_i\;\delta\varphi\,d\mathbf{r}\right|\Big] + \frac{1}{8\pi}\int_{\Omega}|\nabla\delta\varphi|^2\,d\mathbf{r} \qquad (3.39)\\
+ 8\left|\int_{\Omega}F''(\rho(\bar{\mathbf{\Psi}}))\left(\sum_i\bar{\psi}_i\delta\psi_i\right)^2\,d\mathbf{r}\right| \;.
\end{aligned}
$$

Proof. We first expand $E_h(\bar{\mathbf{\Psi}}^h, \bar{\varphi}^h)$ about the solution of the continuous problem, i.e $\bar{\mathbf{\Psi}}^h = \bar{\mathbf{\Psi}} + \delta\mathbf{\Psi}$ and $\bar{\varphi}^h = \bar{\varphi} + \delta\varphi$, and we get

$$
\begin{aligned}
E_h(\bar{\mathbf{\Psi}} + \delta\mathbf{\Psi}, \bar{\varphi} + \delta\varphi) = 2\sum_{i=1}^{N}\int_{\Omega}\frac{1}{2}|\nabla(\bar{\psi}_i + \delta\psi_i)|^2\,d\mathbf{r} + \int_{\Omega}F\left(\rho(\bar{\mathbf{\Psi}} + \delta\mathbf{\Psi})\right)\,d\mathbf{r} \\
- \frac{1}{8\pi}\int_{\Omega}|\nabla(\bar{\varphi} + \delta\varphi)|^2\,d\mathbf{r} + \int_{\Omega}\left(\rho(\bar{\mathbf{\Psi}} + \delta\mathbf{\Psi}) \;+\; b\right)(\bar{\varphi} + \delta\varphi)\,d\mathbf{r}\,,
\end{aligned}
$$

which can then be simplified, using the Taylor series expansion, to

$$
\begin{aligned}
&E_h(\bar{\mathbf{\Psi}}^h, \bar{\varphi}^h) = 2\sum_{i=1}^{N}\int_{\Omega}\frac{1}{2}(|\nabla\bar{\psi}_i|^2 + |\nabla\delta\psi_i|^2 + 2\nabla\bar{\psi}_i\cdot\nabla\delta\psi_i)\,d\mathbf{r} + \int_{\Omega}F(\rho(\bar{\mathbf{\Psi}}))\,d\mathbf{r} \\
&+ 4\sum_{i=1}^{N}\int_{\Omega}F'(\rho(\bar{\mathbf{\Psi}}))\bar{\psi}_i\;\delta\psi_i\,d\mathbf{r} + 8\int_{\Omega}F''(\rho(\bar{\mathbf{\Psi}}))\left(\sum_{i=1}^{N}\bar{\psi}_i\;\delta\psi_i\right)^2\,d\mathbf{r} + 2\sum_{i=1}^{N}\int_{\Omega}F'(\rho(\bar{\mathbf{\Psi}}))(\delta\psi_i)^2\,d\mathbf{r} \\
&- \frac{1}{8\pi}\int_{\Omega}\left(|\nabla\bar{\varphi}|^2 + |\nabla\delta\varphi|^2 + 2\nabla\bar{\varphi}\cdot\nabla\delta\varphi\right)\,d\mathbf{r} + \int_{\Omega}(\rho(\bar{\mathbf{\Psi}}) + b)\bar{\varphi}\;\,d\mathbf{r} + 4\sum_{i=1}^{N}\int_{\Omega}\bar{\psi}_i\;\delta\psi_i\;\bar{\varphi}\;\,d\mathbf{r} \\
&+ \int_{\Omega}\left[(\rho(\bar{\mathbf{\Psi}}) + b)\delta\varphi\;\; + 2\sum_{i=1}^{N}(\delta\psi_i)^2\bar{\varphi}\;\; + 4\sum_{i=1}^{N}\bar{\psi}_i\;\delta\psi_i\;\delta\varphi\;\right]\,d\mathbf{r} + O(\delta\psi_i^3, \delta\psi_i^2\delta\varphi)\,.
\end{aligned}
\qquad (3.40)
$$

We note that $(\bar{\mathbf{\Psi}}, \bar{\varphi}\,, \bar{\epsilon})$ satisfy Euler-Lagrange equations for each $i = 1, \ldots, N$,

$$\frac{1}{2}\int\limits_{\Omega} \nabla\bar{\psi}_i \cdot \nabla\delta\psi_i \, d\mathbf{r} + \int\limits_{\Omega} F'(\rho(\bar{\mathbf{\Psi}}))\bar{\psi}_i \; \delta\psi_i \, d\mathbf{r} + \int\limits_{\Omega} \bar{\psi}_i \; \delta\psi_i \; \bar{\varphi} \;\; d\mathbf{r} = \bar{\epsilon}_i \int\limits_{\Omega} \;\; \bar{\psi}_i \; \delta\psi_i \, d\mathbf{r} \;\; , \tag{3.41a}$$

$$-\frac{1}{4\pi}\int\limits_{\Omega} \nabla\bar{\varphi} \cdot \nabla\delta\varphi \;\; d\mathbf{r} + \int\limits_{\Omega} (\rho(\bar{\mathbf{\Psi}}) + b)\delta\varphi \;\; d\mathbf{r} = 0 \;\; . \tag{3.41b}$$

Using (3.40) and the Euler-Lagrange equations (3.41), we get

$$\begin{aligned} E_h - E = 2\sum_{i=1}^{N} \int\limits_{\Omega} & \left[\frac{1}{2}|\nabla\delta\psi_i|^2 + 2\;\bar{\epsilon}_i\;\bar{\psi}_i\;\delta\psi_i + F'(\rho(\bar{\mathbf{\Psi}}))(\delta\psi_i)^2\right] \, d\mathbf{r} \\ & + 8\int\limits_{\Omega} F''(\rho(\bar{\mathbf{\Psi}}))\left(\sum_{i=1}^{N}\bar{\psi}_i\delta\psi_i\right)^2 \, d\mathbf{r} - \frac{1}{8\pi}\int\limits_{\Omega}|\nabla\delta\varphi|^2\, d\mathbf{r} \\ & + 2\sum_{i=1}^{N}\left[\int\limits_{\Omega}(\delta\psi_i)^2\bar{\varphi} \;\; d\mathbf{r} + 2\int\limits_{\Omega}\bar{\psi}_i \;\delta\psi_i\;\delta\varphi \;\; d\mathbf{r}\right] + O(\delta\psi_i^3, \delta\psi_i^2\delta\varphi) \;\; . \end{aligned} \tag{3.42}$$

The orthonormality constraint functional in the discrete form is given by

$$c(\mathbf{\Psi}^h) = \int\limits_{\Omega} \psi_i^h\psi_j^h \, d\mathbf{r} - \delta_{ij} \;\; , \tag{3.43}$$

and upon expanding about the solution $\bar{\mathbf{\Psi}}$, we get

$$c(\bar{\mathbf{\Psi}}^h) = \int\limits_{\Omega} (\bar{\psi}_i + \delta\psi_i)(\bar{\psi}_j + \delta\psi_j)\, d\mathbf{r} - \delta_{ij} \tag{3.44}$$

$$= \int\limits_{\Omega} \left[\bar{\psi}_i\bar{\psi}_j + \delta\psi_i\bar{\psi}_j + \delta\psi_j\bar{\psi}_i + \delta\psi_i\delta\psi_j\right] \, d\mathbf{r} - \delta_{ij} \;\; . \tag{3.45}$$

Using

$$\int\limits_{\Omega} \bar{\psi}_i\bar{\psi}_j \, d\mathbf{r} = \delta_{ij} \;\; , \tag{3.46}$$

and $c(\bar{\mathbf{\Psi}}^h) = 0$ in (3.45), we get for $i = j$

$$2\int_{\Omega} \bar{\psi}_i \delta\psi_i \, d\mathbf{r} = -\int_{\Omega} (\delta\psi_i)^2 \, d\mathbf{r} \qquad i = 1, 2, \ldots, N \; . \tag{3.47}$$

Using equations (3.42) and (3.47), we arrive at the following error bound in energy

$$\begin{aligned} |E_h - E| \leq 2\sum_{i=1}^{N} \Big[\frac{1}{2}\int_{\Omega} |\nabla\delta\psi_i|^2 \, d\mathbf{r} + \left| \bar{\epsilon}_i \int_{\Omega} (\delta\psi_i)^2 \, d\mathbf{r} \right| + \left| \int_{\Omega} F'(\rho(\bar{\mathbf{\Psi}}))(\delta\psi_i)^2 \, d\mathbf{r} \right| \\ + \left| \int_{\Omega} (\delta\psi_i)^2 \bar{\varphi} \; d\mathbf{r} \right| + 2 \left| \int_{\Omega} \bar{\psi}_i \; \delta\psi_i \; \delta\varphi \; \; d\mathbf{r} \right| \Big] + \frac{1}{8\pi} \int_{\Omega} |\nabla\delta\varphi|^2 \, d\mathbf{r} \\ + 8 \left| \int_{\Omega} F''(\rho(\bar{\mathbf{\Psi}})) \left(\sum_i \bar{\psi}_i \delta\psi_i \right)^2 \; d\mathbf{r} \right| . \end{aligned}$$

□

Proposition III.2. *The finite-element approximation error in proposition III.1 expressed in terms of the approximation errors in electronic wave-functions and electrostatic potential is given by*

$$|E_h - E| \leq C \left(\sum_i \| \; \bar{\psi}_i - \bar{\psi}_i^h \; \|_{1,\Omega}^2 + |\bar{\varphi} - \bar{\varphi}^h|_{1,\Omega}^2 + \sum_i \| \; \bar{\psi}_i - \bar{\psi}_i^h \; \|_{0,\Omega} \| \; \bar{\varphi} - \bar{\varphi}^h \; \|_{1,\Omega} \right) \tag{3.48}$$

Proof. We use the following norms: $|\cdot|_{1,\Omega}$ represents the semi-norm in H^1 space, $\|\cdot\|_{1,\Omega}$ denotes the H^1 norm, $\|\cdot\|_{0,\Omega}$ and $\|\cdot\|_{0,p,\Omega}$ denote the standard L^2 and L^p norms respectively. All the constants to appear in the following estimates are positive and bounded. Firstly, we note that

$$\sum_i \frac{1}{2}\int_{\Omega} |\nabla\delta\psi_i|^2 \, d\mathbf{r} \leq C_1 \sum_i |\bar{\psi}_i - \bar{\psi}_i^h|_{1,\Omega}^2 \, , \tag{3.49}$$

$$\sum_i |\bar{\epsilon}_i| \int_\Omega (\delta\psi_i)^2 \, d\mathbf{r} = \sum_i |\bar{\epsilon}_i| \int_\Omega (\bar{\psi}_i - \bar{\psi}_i^h)^2 \, d\mathbf{r} \leq C_2 \sum_i \| \bar{\psi}_i - \bar{\psi}_i^h \|_{0,\Omega}^2 \ . \tag{3.50}$$

Using Cauchy-Schwartz and Sobolev inequalities, we arrive at the following estimate

$$\begin{aligned}
\sum_i \left| \int_\Omega F'(\rho(\bar{\mathbf{\Psi}}))(\delta\psi_i)^2 \, d\mathbf{r} \right| &\leq \sum_i \int_\Omega \left| F'(\rho(\bar{\mathbf{\Psi}}))(\bar{\psi}_i - \bar{\psi}_i^h)^2 \right| \, d\mathbf{r} \\
&\leq C_3 \sum_i \| \ F'(\rho(\bar{\mathbf{\Psi}})) \ \|_{0,\Omega} \| \ (\bar{\psi}_i - \bar{\psi}_i^h)^2 \ \|_{0,\Omega} \\
&= C_3 \sum_i \| \ F'(\rho(\bar{\mathbf{\Psi}})) \ \|_{0,\Omega} \| \ \bar{\psi}_i - \bar{\psi}_i^h \ \|_{0,4,\Omega}^2 \\
&\leq \bar{C}_3 \sum_i \| \ \bar{\psi}_i - \bar{\psi}_i^h \ \|_{1,\Omega}^2 \ .
\end{aligned} \tag{3.51}$$

Further, we note

$$\frac{1}{8\pi} \int_\Omega |\nabla(\bar{\varphi} - \bar{\varphi}^h)|^2 \, d\mathbf{r} \leq C_4 |\bar{\varphi} - \bar{\varphi}^h|_{1,\Omega}^2 \, . \tag{3.52}$$

Using Cauchy-Schwartz and Sobolev inequalities we arrive at

$$\begin{aligned}
\sum_i \left| \int_\Omega (\delta\psi_i)^2 \bar{\varphi} \ d\mathbf{r} \right| \leq \sum_i \int_\Omega \left| (\bar{\psi}_i - \bar{\psi}_i^h)^2 \ \bar{\varphi} \right| \, d\mathbf{r} &\leq \sum_i \| \ \bar{\varphi} \ \|_{0,\Omega} \| \ (\bar{\psi}_i - \bar{\psi}_i^h)^2 \ \|_{0,\Omega} \\
&\leq C_5 \sum_i \| \ \bar{\psi}_i - \bar{\psi}_i^h \ \|_{0,4,\Omega}^2 \\
&\leq \bar{C}_5 \sum_i \| \ \bar{\psi}_i - \bar{\psi}_i^h \ \|_{1,\Omega}^2 \ .
\end{aligned} \tag{3.53}$$

Also, we note that

$$\begin{aligned}
\sum_i \left| \int_\Omega \bar{\psi}_i \ \delta\psi_i \ \delta\varphi \ d\mathbf{r} \right| &\leq \sum_i \int_\Omega \left| \bar{\psi}_i (\bar{\psi}_i - \bar{\psi}_i^h)(\bar{\varphi} - \bar{\varphi}^h) \right| \, d\mathbf{r} \\
&\leq \ \sum_i \| \ \bar{\psi}_i \ \|_{0,6,\Omega} \| \ \bar{\psi}_i - \bar{\psi}_i^h \ \|_{0,\Omega} \| \ \bar{\varphi} - \bar{\varphi}^h \ \|_{0,3,\Omega} \\
&\leq \sum_i C_6 \ \| \ \bar{\psi}_i - \bar{\psi}_i^h \ \|_{0,\Omega} \| \ \bar{\varphi} - \bar{\varphi}^h \ \|_{1,\Omega} \ ,
\end{aligned} \tag{3.54}$$

where we made use of the generalized Hölder inequality in the first step and Sobolev inequality in the next. Finally, we use Cauchy-Schwartz inequality to arrive at

$$\left| \int_{\Omega} F''(\rho(\bar{\mathbf{\Psi}})) \left(\sum_i \bar{\psi}_i \delta\psi_i \right)^2 d\mathbf{r} \right| \leq \int_{\Omega} \left| F''(\rho(\bar{\mathbf{\Psi}})) \right| \left(\sum_i |\bar{\psi}_i|^2 \right) \left(\sum_i |\delta\psi_i|^2 \right) d\mathbf{r} \tag{3.55}$$

$$= \sum_i \int_{\Omega} \left| F''(\rho(\bar{\mathbf{\Psi}})) \rho(\bar{\mathbf{\Psi}}) (\delta\psi_i)^2 \right| d\mathbf{r} \tag{3.56}$$

$$\leq C_7 \sum_i \| \bar{\psi}_i - \bar{\psi}_i^h \|_{0,\Omega}^2 \ . \tag{3.57}$$

Using the bounds derived above, it follows that

$$|E_h - E| \leq C \left(\sum_i \| \bar{\psi}_i - \bar{\psi}_i^h \|_{1,\Omega}^2 + |\bar{\varphi} - \bar{\varphi}^h|_{1,\Omega}^2 + \sum_i \| \bar{\psi}_i - \bar{\psi}_i^h \|_{0,\Omega} \| \bar{\varphi} - \bar{\varphi}^h \|_{1,\Omega} \right) \tag{3.58}$$

□

We now bound the finite-element discretization error with interpolation errors, which in turn can be bounded with the finite-element mesh size h. This requires a careful analysis in the case of Kohn-Sham DFT and has been discussed in [68]. Using the results from the proof of Theorem 4.3 in [68], we bound the estimates in equation (3.58) using the following inequalities (cf. [79])

$$|\bar{\psi}_i - \bar{\psi}_i^h|_{1,\Omega} \leq \bar{C}_0 |\bar{\psi}_i - \psi_i^I|_{1,\Omega} \leq \tilde{C}_0 \sum_e h_e^k |\bar{\psi}_i|_{k+1,\Omega_e} \ , \tag{3.59a}$$

$$\| \bar{\psi}_i - \bar{\psi}_i^h \|_{0,\Omega} \leq \bar{C}_1 \| \bar{\psi}_i - \psi_i^I \|_{0,\Omega} \leq \tilde{C}_1 \sum_e h_e^{k+1} |\bar{\psi}_i|_{k+1,\Omega_e} \ , \tag{3.59b}$$

$$|\bar{\varphi} - \bar{\varphi}^h|_{1,\Omega} \leq \bar{C}_2 |\bar{\varphi} - \varphi^I|_{1,\Omega} \leq \tilde{C}_2 \sum_e h_e^k |\bar{\varphi}|_{k+1,\Omega_e} \ , \tag{3.59c}$$

$$\| \bar{\varphi} - \bar{\varphi}^h \|_{0,\Omega} \leq \bar{C}_2 \| \bar{\varphi} - \varphi^I \|_{0,\Omega} \leq \tilde{C}_3 \sum_e h_e^{k+1} |\bar{\varphi}|_{k+1,\Omega_e} \ , \tag{3.59d}$$

where k is the order of the polynomial interpolation, and e denotes an element in the

regular family of finite-elements [79] with mesh-size h_e covering a domain Ω_e. Using the above estimates, the error estimate to $O(h^{2k+1})$ is given by

$$|E_h - E| \leq \mathcal{C} \sum_e h_e^{2k} \left[\sum_i |\bar{\psi}_i|^2_{k+1,\Omega_e} + |\bar{\varphi}|^2_{k+1,\Omega_e} \right] . \tag{3.60}$$

3.2.2 Optimal coarse-graining rate

Following the approach in [63], we seek to determine the optimal mesh-size distribution by minimizing the approximation error in energy for a fixed number of elements. Using the definition of the semi-norms, we rewrite equation (3.60) as

$$|E_h - E| \leq \mathcal{C} \sum_{e=1}^{N_E} \Big[h_e^{2k} \int_{\Omega_e} \Big[\sum_i |D^{k+1} \bar{\psi}_i(\mathbf{r})|^2 + |D^{k+1} \bar{\varphi}(\mathbf{r})|^2 \Big] \, d\mathbf{r} \Big] , \tag{3.61}$$

where N_E denotes the total number of elements in the finite-element triangulation, and D^{k+1} denotes the $(k+1)^{th}$ derivative of any function. An element size distribution function $h(\mathbf{r})$ is introduced so that the target element size is defined at all points $\mathbf{r}$ in Ω, and we get

$$|E_h - E| \leq \mathcal{C} \sum_{e=1}^{N_E} \int_{\Omega_e} \Big[h_e^{2k} \Big[\sum_i |D^{k+1} \bar{\psi}_i(\mathbf{r})|^2 + |D^{k+1} \bar{\varphi}(\mathbf{r})|^2 \Big] \, d\mathbf{r} \Big] \tag{3.62}$$

$$\leq \mathcal{C}' \int_{\Omega} h^{2k}(\mathbf{r}) \Big[\sum_i |D^{k+1} \bar{\psi}_i(\mathbf{r})|^2 + |D^{k+1} \bar{\varphi}(\mathbf{r})|^2 \Big] \, d\mathbf{r} \, . \tag{3.63}$$

Further, the number of elements in the mesh is in the order of

$$N_E \propto \int_{\Omega} \frac{d\mathbf{r}}{h^3(\mathbf{r})} \, . \tag{3.64}$$

The optimal mesh-size distribution is then determined by the following variational problem which minimizes the approximation error in energy subject to a fixed number

of elements:

$$\min_{h} \int_{\Omega} \Big\{ h^{2k}(\mathbf{r}) \Big[\sum_{i} |D^{k+1}\bar{\psi}_i(\mathbf{r})|^2 + |D^{k+1}\bar{\varphi}(\mathbf{r})|^2 \Big] \Big\} \, d\mathbf{r} \quad \text{subject to :} \int_{\Omega} \frac{d\mathbf{r}}{h^3(\mathbf{r})} = N_E \,. \tag{3.65}$$

The Euler-Lagrange equation associated with the above problem is given by

$$2kh^{2k-1}(\mathbf{r}) \Big[\sum_{i} |D^{k+1}\bar{\psi}_i(\mathbf{r})|^2 + |D^{k+1}\bar{\varphi}(\mathbf{r})|^2 \Big] - \frac{3\eta}{h^4(\mathbf{r})} = 0 \,, \tag{3.66}$$

where η is the Lagrange multiplier associated with the constraint. Thus, we obtain the following distribution

$$h(\mathbf{r}) = A \Big(\sum_{i} |D^{k+1}\bar{\psi}_i(\mathbf{r})|^2 + |D^{k+1}\bar{\varphi}(\mathbf{r})|^2 \Big)^{-1/(2k+3)} , \tag{3.67}$$

where the constant A is computed from the constraint that the total number of elements in the finite-element discretization is N_E.

The coarse-graining rate derived in equation (3.67) has been employed to construct the finite-element meshes by using the *a priori* knowledge of the asymptotic solutions of $\bar{\psi}_i(\mathbf{r})$ and $\bar{\varphi}(\mathbf{r})$ for different kinds of problems we study in the subsequent sections.

3.3 Numerical implementation

We now turn to the numerical implementation of the discrete formulation of the Kohn-Sham eigenvalue problem described in Section 3.1. We first discuss the higher-order finite-elements used in our study with specific focus on spectral finite-elements, which are important in developing an efficient numerical solution procedure.

3.3.1 Higher-order finite-element discretizations

Linear finite-element basis has been extensively employed for a wide variety of applications in engineering involving complex geometries and moderate levels of accuracy. On the other hand, much higher levels of accuracy (chemical accuracy) is desired in electronic structure computations of materials properties. To achieve the desired chemical accuracy, a linear finite-element basis is computationally inefficient since it requires a large number of basis functions per atom [31, 23]. Hence, we investigate if higher-order finite-element basis functions can possibly be used to efficiently achieve the desired chemical accuracy. To this end, we employ in our study C^0 basis functions comprising of linear tetrahedral element (TET4) and spectral hexahedral elements up to degree eight (HEX27, HEX125SPECT, HEX343SPECT, HEX729SPECT). The numbers following the words 'TET' and 'HEX' denote the number of nodes in the element, and the suffix 'SPECT' denotes that the element is a spectral finite-element. We note that spectral finite-elements [80, 81] have been employed in a previous work in electronic structure calculations [61], but the computational efficiency afforded by these elements has not been thoroughly studied. We first briefly discuss spectral finite-elements (also referred to as spectral-elements) employed in the present work and the role they play in improving the computational efficiency of the Kohn-Sham DFT eigenvalue problem.

3.3.2 Spectral finite-element basis

The spectral-element basis functions employed in the present work are constructed as Lagrange polynomials interpolated through an optimal distribution of nodes corresponding to the roots of derivatives of Legendre polynomials, unlike conventional finite-elements which use equispaced nodes in an element. Such a distribution does not have nodes on the boundaries of an element, and hence it is common to append nodes on the element boundaries which guarantees C^0 basis functions. These

set of nodes are usually referred to as Gauss-Lobatto-Legendre points. Furthermore, we note that conventional finite-elements result in a poorly conditioned discretized problem for a high order of interpolation, whereas spectral-elements provide better conditioning [81]. The improved conditioning of the spectral-element basis was observed to provide a 2-3 fold computational advantage over conventional finite-elements in a recent benchmark study [64] conducted to assess the computational efficiency of higher-order elements in the solution of the orbital-free DFT problem.

A significant advantage of the aforementioned spectral-elements is realized when we conjoin their use with specialized Gaussian quadrature rules that have quadrature points coincident with the nodes of the spectral-element, which in the present case corresponds to the Gauss-Lobatto-Legendre (GLL) quadrature rule [82]. Importantly, the use of such a quadrature rule will result in a diagonal overlap matrix (mass matrix) $\mathbf{M}$. To elaborate, consider the elemental mass matrix $\mathbf{M}^e$ given by

$$\int_{\Omega_e} N_i(\mathbf{r}) N_j(\mathbf{r})\, d\mathbf{r} = \int_{-1}^{1}\int_{-1}^{1}\int_{-1}^{1} N_i(\xi,\eta,\zeta) N_j(\xi,\eta,\zeta)\ \ det(J_e)\ d\xi\ d\eta\ d\zeta \tag{3.68}$$

$$= \sum_{p,q,r=0}^{n_q} w_{p,q,r} N_i(\xi_p,\eta_q,\zeta_r) N_j(\xi_p,\eta_q,\zeta_r)\ \ det(J_e) \tag{3.69}$$

where (ξ,η,ζ) represents the barycentric coordinates, J_e represents the elemental jacobian matrix of an element Ω_e, and n_q denotes the number of quadrature points in each dimension in a tensor product quadrature rule. Since the quadrature points are coincident with nodal points, the above expression is non-zero only if $i = j$, thus resulting in a diagonal elemental mass matrix and subsequently a diagonal global mass matrix. A diagonal mass matrix makes the transformation of the generalized Kohn-Sham eigenvalue problem (3.30) to a symmetric standard eigenvalue problem (3.36) trivial. As discussed and demonstrated subsequently, the transformation to a standard eigenvalue problem allows us to use efficient solution procedures to compute the

eigenspace in the self-consistent field iteration. We note that, while the use of the GLL quadrature rule is important in efficiently transforming the generalized eigenvalue problem to a standard eigenvalue problem, this quadrature rule is less accurate in comparison to Gauss quadrature rules. An n point Gauss-Lobatto rule can integrate polynomials exactly up to degree $2n-3$, while an n point Gauss quadrature rule can integrate polynomials exactly up to degree $2n-1$. Thus, in the present work, we use the GLL quadrature rule only in the evaluation of the overlap matrix, while using the more accurate Gauss quadrature rule to evaluate the discrete Hamiltonian matrix $\mathbf{H}$. The accuracy and sufficiency of this reduced-order GLL quadrature for the evaluation of overlap matrix is demonstrated in the Appendix C.

3.3.3 Self-consistent field iteration

As noted in Section 3.1, the Kohn-Sham eigenvalue problem represents a nonlinear eigenvalue problem and must be solved self-consistently to compute the ground-state electron density and energy. We use computationally efficient schemes to evaluate the occupied eigenspace of the Kohn-Sham Hamiltonian (discussed below) in conjunction with finite temperature Fermi-Dirac distribution and charge density mixing to develop an efficient and robust solution scheme for the self-consistent field iteration of Kohn-Sham problem. Algorithm 1 depicts the typical steps involved in the self-consistent field (SCF) iteration. An initial guess of the electron density field is used to start the computation. A reasonable choice of such an initial guess is the superposition of atomic charge densities, and is used in the present study unless otherwise mentioned. The input charge density ($\rho^h_{\text{in}}(\mathbf{r})$) to a self-consistent iteration is used to compute the total electrostatic potential $\varphi(\mathbf{r}, \mathbf{R})$ by solving the following discrete Poisson equation using a preconditioned conjugate gradient method provided by the

Algorithm 1 Self Consistent Field Iteration

1. Provide initial guess for electron density $\rho_0^h(\mathbf{r})$ on the finite-element mesh. This will be the input electron density for the first self-consistent iteration ($\rho_{\text{in}}^h(\mathbf{r}) = \rho_0^h(\mathbf{r})$).

2. Compute the total electrostatic potential $\varphi^h(\mathbf{r}, \mathbf{R})$ and the self potential for each nuclei $\nu_I^h(\mathbf{r})$ by solving the respective discrete Poisson equations with appropriate boundary conditions.

3. Compute the effective potential, $V_{\text{eff}}(\rho_{\text{in}}^h, \mathbf{R})$ using equation (3.20) or (3.24) based on type of the simulation (all-electron or pseudopotential).

4. Solve for the occupied subspace spanned by the eigenfunctions $\psi_i^h(\mathbf{r})$, $i = 1, 2 \cdots N$ corresponding to N ($N > N_e/2$) smallest eigenvalues of the Kohn-Sham eigenvalue problem (3.30).

5. Calculate the fractional occupancy factors (f_i) using the Fermi-Dirac distribution (Section (3.3.3.2))

6. Compute the new output charge densities ρ_{out}^h from the eigenfunctions:

$$\rho_{\text{out}}^h(\mathbf{r}) = 2 \sum_i f(\epsilon_i, \epsilon_F) |\psi_i^h(\mathbf{r})|^2, \tag{3.70}$$

7. If $||\rho_{\text{out}}^h(\mathbf{r}) - \rho_{\text{in}}^h(\mathbf{r})|| \leq$ tolerance, *stop*; Else, compute new ρ_{in}^h using a mixing scheme (Section 3.3.3.3) and go to step 2.

PETSc [83] package using a Jacobi preconditioner

$$\sum_{k=1}^{M} \Big[\frac{1}{4\pi} \int_{\Omega} \nabla N_j(\mathbf{r}) \,.\nabla N_k(\mathbf{r}) \, d\mathbf{r} \Big] \varphi^k = \int_{\Omega} \left(\rho_{\text{in}}^h(\mathbf{r}) + b(\mathbf{r}, \mathbf{R}) \right) N_j(\mathbf{r}) \, d\mathbf{r} \ . \tag{3.71}$$

Subsequently, the effective potential V_{eff} is evaluated to set up the discrete Kohn-Sham eigenvalue problem (3.30). We now discuss the different strategies we have investigated to compute the occupied eigenspace of the Kohn-Sham Hamiltonian $\mathbf{H}$, and their relative merits.

3.3.3.1 Solver strategies for finding the occupied eigenspace

We examined two different solution strategies to compute the occupied subspace: (i) explicit computation of eigenvectors at every self-consistent field iteration; (ii) A

Chebyshev filtering approach.

Explicit computation of eigenvectors: We first discuss the methods examined in the present work that involve an explicit computation of eigenvectors at a given self-consistent iteration. We recall that the discrete Kohn-Sham eigenvalue problem is a generalized Hermitian eigenvalue problem (GHEP) (3.30). As mentioned previously, by using the GLL quadrature rules for the evaluation of the overlap matrix $\mathbf{M}$, which results in a diagonal overlap matrix, the generalized eigenvalue problem can be trivially transformed into a standard Hermitian eigenvalue problem (SHEP). We have explored both approaches in the present work, i.e. (i) solving the generalized eigenvalue problem employing conventional Gauss quadrature rules; (ii) solving the transformed standard eigenvalue problem by using GLL quadrature rules in the computation of overlap matrix.

We have employed the Jacobi-Davidson (JD) method [84] to solve the GHEP. The JD method falls into the category of iterative orthogonal projection methods where the matrix is orthogonally projected into a lower dimensional subspace and one seeks an approximate eigenpair of the original problem in the subspace. The basic idea in JD method is to arrive at better approximations to eigenpairs by a systematic expansion of the subspace realized by solving a "Jacobi-Davidson correction equation" that involves the solution of a linear system. In the present work, a Jacobi preconditioner has been employed in the solution of the correction equation. The correction equation is solved only approximately, and this approximate solution is used for the expansion of the subspace. Though the JD method has significant advantages in computing the interior eigenvalues and closely spaced eigenvalues, we found the JD method to be computationally expensive for systems involving the computation of eigenvectors greater than 50, due to the increase in the number of times the correction equation is solved.

On the other hand, we employed the Krylov-Schur (KS) method [85] for solving the SHEP. In practice, one could also use the JD method to solve the SHEP, but, as previously mentioned, the JD method is expensive to solve systems involving few hundreds of electrons and beyond. The KS method can be viewed as an improvement over traditional Krylov subspace methods such as Arnoldi and Lanczos methods [86, 87]. The KS method is based on Krylov-Schur decomposition where the Hessenberg matrix has the Schur form. The key idea of the KS method is to iteratively construct the Krylov-subspace using Arnoldi iteration and subsequently filter the unwanted spectrum from the Krylov-Schur decomposition. This results in a robust restarting scheme with faster convergence in most cases.

We now demonstrate the computational efficiency realized by solving the discrete Kohn-Sham eigenvalue problem as a transformed SHEP in comparison to GHEP. To this end, we consider an all-electron simulation of a graphene sheet containing 16 atoms with 96 electrons ($N_e = 96$) and a local pseudopotential simulation (cf. section 3.4.1.2 for details on the pseudopotentials employed) of $3 \times 3 \times 3$ face-centered-cubic aluminum nano-cluster containing 172 atoms with 516 electrons ($N_e = 516$) as benchmark systems. The relative error in the ground-state energy for the finite-element mesh used in the case of graphene is around 1.2×10^{-5} ($0.0004\ Ha/atom$) while it is around 3.6×10^{-6} ($0.0002\ eV/atom$) in the case of aluminum cluster. The reference ground-state energy is obtained using the commercial code GAUSSIAN in the case of the all-electron simulation of the graphene system, while it is obtained using the convergence study presented in Section 3.4 for the aluminum cluster. Table 3.1 shows the computational time taken for the first SCF iteration in each of the above cases. All the times reported in the present work represent the total CPU times. The Jacobi-Davidson method for GHEP and Krylov-Schur method for SHEP provided by the SLEPc package [88] have been employed in the present study. We remark that, in employing the Jacobi-Davidson method, eigenvectors from the pre-

Table 3.1: Comparison of Generalized vs Standard eigenvalue problems.

Element Type	DOFs	Problem Type	N_e	Time (GHEP)	Time (SHEP)
HEX125SPECT	1,368,801	graphene	96	1786 CPU-hrs	150 CPU-hrs
HEX343SPECT	2,808,385	Al $3 \times 3 \times 3$ cluster	516	2084 CPU-hrs	80 CPU-hrs

vious SCF iterations have been supplied as input approximations for the subsequent SCF iteration. The Krylov-Schur method, on the other hand, allows for one only vector to be supplied as the input approximation to a given SCF iteration. Hence, the eigenvector corresponding to smallest eigenvalue from the previous SCF iteration has been supplied as the input approximation for the subsequent SCF iteration. It is interesting to note that a 10-fold speedup is realized by transforming the Kohn-Sham eigenvalue problem to a SHEP in the case of graphene, while a 25-fold speedup was obtained in the case of aluminum cluster. We note that a similar observation was recently reported in [27] where the GHEP was transformed to SHEP via the mass-lumping approximation. Further, other simulations conducted as part of the present study suggest that this speedup increases with increasing system size.

Chebyshev filtering: We now examine the alternate approach of Chebyshev filtering proposed in [66], which is designed to iteratively compute the occupied eigenspace at every SCF iteration. We note that the Chebyshev filtering approach is only valid for standard eigenvalue problems. To this end, we use the aforementioned approach to convert the GHEP to a SHEP by employing the GLL quadrature rules in computing the overlap matrix, and remark that the use of spectral elements in conjunction with the GLL quadrature is crucial in using the Chebyshev filtering technique to solve the Kohn-Sham eigenvalue problem in a finite-element basis. The Chebyshev filtering approach is based on a subspace iteration technique, where an initial subspace is acted upon by a Chebyshev filter constructed from the Kohn-Sham Hamiltonian that transforms the subspace to the occupied eigenspace.

In the present work, at any given SCF iteration, we begin with the initial subspace

V formed from the eigenvectors of the previous SCF iteration. We note that, as is the case with all subspace iteration techniques, we choose the dimension of the subspace V, N, to be larger than the number of filled ground-state orbitals. Typically, we choose $N \sim \frac{N_e}{2} + 20$. This is also necessary to employ the finite temperature Fermi-Dirac smearing, discussed in Section 3.3.3.2, to stabilize the SCF iterations in materials systems that have very small band-gaps or have degenerate states at the Fermi energy. As proposed in [66], the Chebyshev filter is constructed from a shifted and scaled Hamiltonian, $\overline{\mathbf{H}} = c_1\widetilde{\mathbf{H}} + c_2$, where $\widetilde{\mathbf{H}}$ is the transformed Hamiltonian in the SHEP (cf. equation (3.36)). The constants c_1 and c_2 which correspond to the scaling and shifting are determined such that the unwanted eigen-spectrum is mapped into $[-1, 1]$ and the wanted spectrum into $(-\infty, -1)$. In order to compute these constants, we need estimates of the upper bounds of the wanted and unwanted spectrums. The upper bound of the unwanted spectrum, which corresponds to the largest eigenvalue of $\widetilde{\mathbf{H}}$, can be obtained inexpensively by using a small number of iterations of the Lanczos algorithm. The upper bound of the wanted spectrum is chosen as largest Rayleigh quotient of $\widetilde{\mathbf{H}}$ in the space V from the previous SCF iteration. Subsequently, the degree-m Chebyshev filter, $p_m(\overline{\mathbf{H}})$, which magnifies the spectrum of $\overline{\mathbf{H}}$ in $(-\infty, -1)$—the wanted eigen-spectrum of $\widetilde{\mathbf{H}}$—transforms the initial subspace V to the occupied eigenspace of $\widetilde{\mathbf{H}}$. The degree of the Chebyshev filter is chosen such that the obtained space is a close approximation of the occupied space. We note that the action of the Chebyshev filter on V can be performed recursively, similar to the recursive construction of the Chebyshev polynomials [89]. After obtaining the occupied eigenspace, we orthogonalize the basis functions, and subsequently project $\widetilde{\mathbf{H}}$ into the eigenspace to compute the eigenvalues that are used in the Fermi-Dirac smearing discussed in the next subsection.

We remark that the degree of the polynomial required for the Chebyshev filter depends on the separation between eigenvalues of $\overline{\mathbf{H}}$ in $(-\infty, -1)$, which in turn

depends on: (i) the ratio between the wanted and unwanted eigenspectrums of $\widetilde{\mathbf{H}}$; (ii) the separation between the eigenvalues in the wanted spectrum of $\widetilde{\mathbf{H}}$. The size of the unwanted spectrum is primarily governed by the largest eigenvalue of $\widetilde{\mathbf{H}}$, which, in turn, is related to the finite-element discretization—increases with decrease in the element-size of the finite-element mesh. In general, all-electron calculations require locally refined meshes near the nuclei as they involve Coulomb-singular potential fields and highly oscillatory core wavefunctions. Hence, a very high degree of Chebyshev polynomial—of the order of $10^2 - 10^3$ for the problems studied in this work—needs to be employed to effectively filter the unwanted spectrum. On the other hand, simulations performed on systems with smooth pseudopotential required Chebyshev polynomial degrees between 10 to 50 for the range of problems studied in the present work. Further, qualitatively speaking, a larger degree Chebyshev filter is required for larger systems as the separation between eigenvalues in the wanted spectrum of $\widetilde{\mathbf{H}}$ reduces with increasing number of electrons.

We now compare the computational times (cf. table 3.2) taken for a single SCF iteration solved using an eigenvalue solver based on Krylov-Schur method and the Chebyshev filter using the aforementioned benchmark problems comprising of a 16-atom graphene sheet and 172-atom aluminum cluster. We use a Chebyshev polynomial of degree 800 for the graphene all-electron calculation and a polynomial degree of 12 for aluminum cluster pseudopotential calculation respectively. As is evident from the results, we clearly see a factor of 12 speedup that is obtained in the case of graphene, and a factor of around 6 speedup that is obtained in the case of aluminum cluster. The speedup obtained was even greater for larger materials systems.

Table 3.2: Comparison of Standard eigenvalue problem vs Chebyshev filtered subspace iteration (ChFSI).

Element Type	DOFs	Problem Type	N	Time (SHEP)	Time (ChFSI)
HEX125SPECT	1,368,801	graphene	96	150 CPU-hrs	12.5 CPU-hrs
HEX343SPECT	2,808,385	Al $3 \times 3 \times 3$ cluster	512	80 CPU-hrs	13 CPU-hrs

The use of spectral finite-elements in conjunction with Chebyshev filtered subspace iteration presents an efficient and robust approach to solve the Kohn-Sham problem using the finite-element basis. Thus, for subsequent simulations reported in the present work that use hexahedral elements, we employ the Krylov-Schur method for the first SCF iteration to generate a good initial subspace and use the Chebyshev filtering approach for all subsequent iterations to compute the occupied eigenspace. However, for simulations that use tetrahedral elements, we solve the GHEP using Jacobi-Davidson method as a transformation to SHEP is non-trivial and involves the inversion of overlap matrix using iterative techniques.

3.3.3.2 Finite temperature smearing: Fermi-Dirac distribution

For materials systems with very small band gaps or those with degenerate energy levels at the Fermi energy, the SCF iteration may exhibit *charge sloshing*—a phenomenon where large deviations in spatial charge distribution are observed between SCF iterations with different degenerate (or close to degenerate) levels being occupied in different SCF iterations. In such a scenario, the SCF exhibits convergence in the ground-state energy, but not in the spatial electron density. As discussed in Chapter II, it is common in electronic structure calculations to introduce an orbital occupancy function [58] allowing fractional occupancies based on the energy levels and a smearing function to remove charge sloshing in SCF iterations. A common choice for the smearing function is the finite temperature Fermi-Dirac distribution, and the orbital occupancy factor f_i corresponding to an energy level ϵ_i is given by

$$f_i \equiv f(\epsilon_i, \epsilon_F) = \frac{1}{1 + \exp(\frac{\epsilon_i - \epsilon_F}{\sigma})} \ , \tag{3.72}$$

where the smearing factor $\sigma = k_B T$ with k_B denoting the Boltzmann constant and T denoting the temperature in Kelvin. In the above expression, ϵ_F denotes the Fermi

energy, which is computed from the constraint on the total number of electrons given by $\sum_i 2f_i = N_e$. We note that the convergence of ground-state energy is quadratic in the smearing parameter σ [58].

3.3.3.3 Mixing scheme:

The convergence of the SCF iteration is crucially dependent on the mixing scheme, and many past works in the development of electronic structure methods have focused on this aspect [90, 67, 91, 92, 93]. In the present work, we employ an n-stage Anderson mixing scheme [67], which is briefly described below for the sake of completeness. Let $\rho_{\text{in}}^{h^{(n)}}(\mathbf{r})$ and $\rho_{\text{out}}^{h^{(n)}}(\mathbf{r})$ represent the input and output electron densities of the n^{th} self-consistent iteration. The input to the $(n+1)^{\text{th}}$ self-consistent iteration, $\rho_{\text{in}}^{h^{(n+1)}}(\mathbf{r})$, is computed as follows

$$\rho_{\text{in}}^{h^{(n+1)}} = \gamma_{\text{mix}}\, \bar{\rho}_{\text{out}}^{h} + (1 - \gamma_{\text{mix}})\, \bar{\rho}_{\text{in}}^{h} \tag{3.73}$$

where

$$\bar{\rho}_{\text{in(out)}}^{h} = c_n\, \rho_{\text{in(out)}}^{h^{(n)}} + \sum_{k=1}^{n-1} c_k\, \rho_{\text{in(out)}}^{h^{(n-k)}} \tag{3.74}$$

and the sum of all the constants c_i is equal to one, i.e.,

$$c_1 + c_2 + c_3 + \cdots + c_n = 1\ . \tag{3.75}$$

Using the above constraint, equation (3.74) can be written as

$$\bar{\rho}_{\text{in(out)}}^{h} = \rho_{\text{in(out)}}^{h^{(n)}} + \sum_{k=1}^{n-1} c_k \left(\rho_{\text{in(out)}}^{h^{(n-k)}} - \rho_{\text{in(out)}}^{h^{(n)}} \right)\ . \tag{3.76}$$

Denoting $F = \rho_{\text{out}}^{h} - \rho_{\text{in}}^{h}$, the above equation can be written as

$$\bar{F} = F^{\,(n)} + \sum_{k=1}^{n-1} c_k \left(F^{\,(n-k)} - F^{\,(n)} \right)\ . \tag{3.77}$$

The unknown constants c_1 to c_{n-1} are determined by minimizing $R = ||\bar{F}||_2^2 = ||\bar{\rho}_{\text{in}}^h - \bar{\rho}_{\text{out}}^h||_2^2$, which amounts to solving the following system of $(n-1)$ linear equations given by:

$$\sum_{k=1}^{n-1} \left(F^{(n)} - F^{(n-m)}, F^{(n)} - F^{(n-k)}\right) c_k = \left(F^{(n)} - F^{(n-m)}, F^{(n)}\right) \quad m = 1 \cdots n-1 \tag{3.78}$$

where the notation (F, G) stands for the L_2 inner product between functions $F(\mathbf{r})$ and $G(\mathbf{r})$ and is given by

$$(F, G) = \int F(\mathbf{r}) G(\mathbf{r})\, d\mathbf{r} \ . \tag{3.79}$$

The value of the parameter γ_{mix} in equation (3.73) is chosen to be 0.5 in the present work. All the integrals involved in the linear system (3.78) are evaluated using Gauss quadrature rules, and the values of $\rho_{\text{in(out)}}^{h^{(n)}}(\mathbf{r})$ are stored as quadrature point values after every n^{th} self consistent iteration. In all the simulations conducted in the present work, the Anderson mixing scheme is used with full history.

3.4 Numerical results

3.4.1 Rates of convergence

We begin with the examination of convergence rates of the finite-element approximation using a sequence of meshes with decreasing mesh sizes for various polynomial orders of interpolation. The benchmark problems used in this study, include: (i) all-electron calculations performed on boron atom and methane molecule, which represent non-periodic problems with a Coulomb-singular nuclear potential; (ii) local pseudopotential calculations performed on a barium cluster that represents a non-periodic problem with a smooth external potential, and a bulk calculation of face-centered-cubic (FCC) calcium crystal. In the case of all-electron calculations,

the nuclear charges are treated as point charges on the nodes of the finite-element triangulation and the discretization provides a regularization for the electrostatic potential. We note that the self-energy of the nuclei in this case is mesh-dependent and diverges upon mesh refinement. Thus, the self energy is also computed on the same mesh that is used to compute the total electrostatic potential, which ensures that the divergent components of the variational problem on the right hand side of equation (3.12) and the self energy exactly cancel owing to the linearity of the Poisson equation (cf. Appendix A for a detailed discussion).

We conduct the convergence study by adopting the following procedure. Using the *a priori* knowledge of the asymptotic solutions of the atomic wavefunctions [65], we determine the coarsening rate from equation (3.67) which is used to construct the coarsest mesh. Though the computed coarsening rates use the far-field asymptotic solutions instead of the exact ground-state wavefunctions that are *a priori* unknown, the obtained meshes nevertheless provide a systematic way for the discretization of vacuum in non-periodic calculations as opposed to using an arbitrary coarse-graining rate or uniform discretization. In the case of periodic pseudopotential calculations, a finite-element discretization with a uniform mesh-size is used. A uniform subdivision of the initial coarse-mesh is carried out to generate a sequence of refined meshes, which represents a systematic refinement of the finite-element approximation space. The ground-state energies from the discrete formulation, E_h, obtained from the sequence of meshes constructed using the HEX125SPECT element and containing N_e elements are used to obtain a least squares fit of the form

$$|E_h - E_0| = \mathcal{C}(1/N_E)^{2k/3}\,, \tag{3.80}$$

to determine the constants E_0, $\mathcal{C}$ and k. The obtained value of E_0, which represents the extrapolated continuum ground-state energy computed using the HEX125SPECT

element, is used as the reference energy to compute the relative error $\frac{|E_h - E_0|}{|E_0|}$ in the convergence study of various orders of finite-elements reported in subsequent subsections.

3.4.1.1 All-electron calculations

We first begin with all-electron calculations by studying two examples: (i) boron atom (ii) methane molecule.

Boron atom: This is one of the simplest systems displaying the full complexity of an all-electron calculation. For the present case, we use a Chebyshev filter of order 500 to compute the occupied eigenspace. As discussed in Section 3.3.3.2, we use a finite-temperature smearing to avoid instability in the SCF iteration due to charge sloshing from the degenerate states at the Fermi energy. A smearing factor $\sigma = 0.0003168\ Ha$ (T=100K) is used in the present study. The simulation domain used is a spherical domain of radius 20 $a.u.$ with Dirichlet boundary conditions employed on electronic wavefunctions and total electrostatic potential. We first determine the mesh coarse-graining rate by noting that the asymptotic decay of atomic wavefunctions is exponential, and an upper bound to this decay under the Hartree-Fock approximation is given by [65]

$$\psi(r) \sim \exp\Big[-\sqrt{2\,\tilde{\epsilon}}\,r\Big] \quad \text{for} \quad r \to \infty\,, \tag{3.81}$$

where $-\tilde{\epsilon}$ denotes the energy of the highest occupied atomic/molecular orbital. While the above estimate has been derived for the Hartree-Fock formulation, it nevertheless provides a good approximation to the asymptotic decay of wavefunctions computed using the Kohn-Sham formulation. We use the aforementioned estimate, though not optimal, for all the wavefunctions in the atomic system, and adopt this approach for

all systems considered subsequently. Hence, in equation (3.67), we consider $\bar{\psi}_i$ to be

$$\bar{\psi}(r) = \sqrt{\frac{\xi^3}{\pi}} \exp\Big[-\xi\, r\Big] \quad \text{where} \quad \xi = \sqrt{2\,\tilde{\epsilon}}\,. \tag{3.82}$$

The electrostatic potential governed by the Poisson equation with a total charge density being equal to the sum of $5\bar{\psi}^2(r)$ and $-5\delta(r)$ is given by

$$\bar{\varphi}(r) = -5 \exp\left(-2\xi\, r\right) \left(\xi + \frac{1}{r}\right) . \tag{3.83}$$

Using the above equations, the mesh coarse-graining rate from equation (3.67) is given by

$$h(r) = A \left[\frac{5}{\pi}\xi^{2k+5} \exp\left(-2\,\xi\, r\right) + 25 \exp\left(-4\,\xi\, r\right) \left[\xi^{k+2} 2^{k+1} + \sum_{n=0}^{k+1} \binom{k+1}{n} \frac{2^n \xi^n (k+1-n)!}{r^{k-n+2}}\right]^2\right]^{-1/(2k+3)} . \tag{3.84}$$

Since $\tilde{\epsilon}$ in the above equation is unknown *a priori*, the value of $\tilde{\epsilon}^h$ determined on a coarse mesh is used in the above equation to obtain $h(r)$ away from the atom. The finite-elements around the boron atom has been subdivided to get local refinement near the boron atom. We now perform the numerical convergence study with tetrahedral and hexahedral spectral elements up to eighth order using this coarse-graining rate, and the results are shown in figure 3.1. The value of E_0 computed from equation (3.80) is $-24.3431910234\ Ha$, which is used to compute the relative errors in the energies. The ground-state energy computed by performing an all-electron calculation using APE (Atomic Pseudopotential Engine) software [94] is found to be $-24.34319112\ Ha$.

We observe that all the elements studied show close to optimal rates of convergence, $O(h^{2k})$, where k is the degree of the polynomial. An interesting point to note is that, although the governing equations are non-linear in nature and the nuclear potential approaches a Coulomb-singular solution upon mesh refinement, optimal rates

of convergence are obtained. Recent mathematical analysis [68] shows that the finite-element approximation for the Kohn-Sham DFT problem does provide optimal rates of convergence for pseudopotential calculations. To the best of our knowledge, mathematical analysis of higher-order finite-element approximations of the Kohn-Sham DFT problem with Coulomb-singular nuclear potentials is still an open problem.

We note that, in the case of linear finite-elements, a large number of elements are required to even achieve modest relative errors. In fact, close to five million linear TET4 elements are required for a single boron atom to obtain a relative error of 10^{-2}, while relative errors up to 10^{-4} are achieved with just few hundreds of HEX125SPECT and HEX343SPECT elements, and even higher accuracies are achieved with a few thousands of these elements.

Methane molecule: The next example we study is methane with a C-H bond length of 2.07846 a.u. and a C-H-C tetrahedral angle of 109.4712°. For the present case, we use a Chebyshev filter of order 500 to compute the occupied eigenspace, and a smearing factor $\sigma = 0.0003168\ Ha$ (T=100K) for the Fermi-Dirac smearing. The simulation domain used is a cubical domain of side 50 $a.u.$ with Dirichlet boundary conditions employed on electronic wavefunctions and total electrostatic potential. As in the case of boron atom, the finite-element mesh for this molecule is constructed to be locally refined around the atomic sites, while coarse-graining away. A uniform mesh is first constructed near the methane molecule and the finite-elements around each nuclei are then subdivided to obtain local refinements around each nuclei. The mesh coarsening rate in the outer region is determined numerically by employing the asymptotic solution of the far-field electronic fields, estimated as a superposition of single atom far-field asymptotic fields, in equation (3.67). To this end, asymptotic

behavior of the atomic wavefunctions in carbon atom ($\bar{\psi}^C(r)$) is chosen to be

$$\bar{\psi}^C(r) = \sqrt{\frac{\xi^3}{\pi}} \exp\Big[-\xi\, r\Big] \quad \text{where} \quad \xi = \sqrt{2\,\tilde{\epsilon}}\,, \tag{3.85}$$

where $\tilde{\epsilon}$ (negative of the eigenvalue of the highest occupied eigenstate) is determined from a coarse mesh calculation of single carbon atom. The corresponding electrostatic potential is governed by the Poisson equation, with total charge density being equal to the sum of $6|\bar{\psi}^C(r)|^2$ and $-6\delta(r)$, and is given by

$$\bar{\varphi}(r) = -6 \exp\left(-2\xi\, r\right) \left(\xi + \frac{1}{r}\right). \tag{3.86}$$

In the case of hydrogen atom, the analytical solution is given by

$$\bar{\psi}^H(r) = \sqrt{\frac{1}{\pi}} \exp\Big[-\,r\Big]\,, \tag{3.87}$$

and the corresponding electrostatic potential is given by

$$\bar{\varphi}(r) = -\exp\left(-2\,r\right) \left(1 + \frac{1}{r}\right). \tag{3.88}$$

We now perform the numerical convergence study with both tetrahedral and hexahedral elements with the meshes constructed as explained before. Figure 3.2 shows the convergence results for the various elements, and figure 3.3 shows the isocontours of electron density for methane molecule. The value of E_0 computed from equation (3.80), the reference ground-state energy per atom of the methane molecule which is used to compute the relative errors in the energies, is found to be $-8.023988150\ Ha$. The ground-state energy per atom computed using the GAUSSIAN package [72] with polarization consistent 4 DFT basis set (pc-4) is found to be $-8.0239855633\ Ha$. As in the case of boron atom, we obtain close to optimal convergence rates, and sig-

nificantly higher relative accuracies in ground-state energies are observed by using higher-order elements.

3.4.1.2 Local Pseudopotential calculations

We now turn to pseudopotential calculations in multi-electron systems. A pseudopotential constitutes the effective potential of the nucleus and core electrons experienced by the valence electrons. Pseudopotentials are constructed such that the wavefunctions of valence electrons outside the core and their corresponding eigenvalues are close to those computed using all-electron calculations. We note that, in the present work, we have restricted our investigation to local pseudopotential calculations as the present focus of this work is the demonstration of the computational efficiency afforded by adaptive higher-order finite-element discretizations. We note that the use of non-local pseudopotentials—for instance, the Troullier Martins pseudopotential in the Kleinman-Bylander form [78]—results in an additional sparse matrix in the discrete Hamiltonian whose sparsity is dependent on the extent of the non-local projectors. We expect that the consideration of non-local pseudopotentials will only have a marginal effect on the demonstrated performance of the algorithms and the scalability results, and a careful study of this aspect will be undertaken in our future investigations. In the present work, we use the local evanescent core pseudopotential [95] as a model pseudopotential to demonstrate our ideas. This pseudopotential has the following form

$$V_{ion}^{I} = -\frac{Z}{R_c}\left(\frac{1}{y}(1-(1+\beta y)e^{-\alpha y}) - Ae^{-y}\right) \ , \tag{3.89}$$

where Z denotes the number of valence electrons and $y = |\mathbf{r} - \mathbf{R}_I|/R_c$. The core decay length R_c and $\alpha \geq 0$ are atom-dependent constants [95]. The constants β and

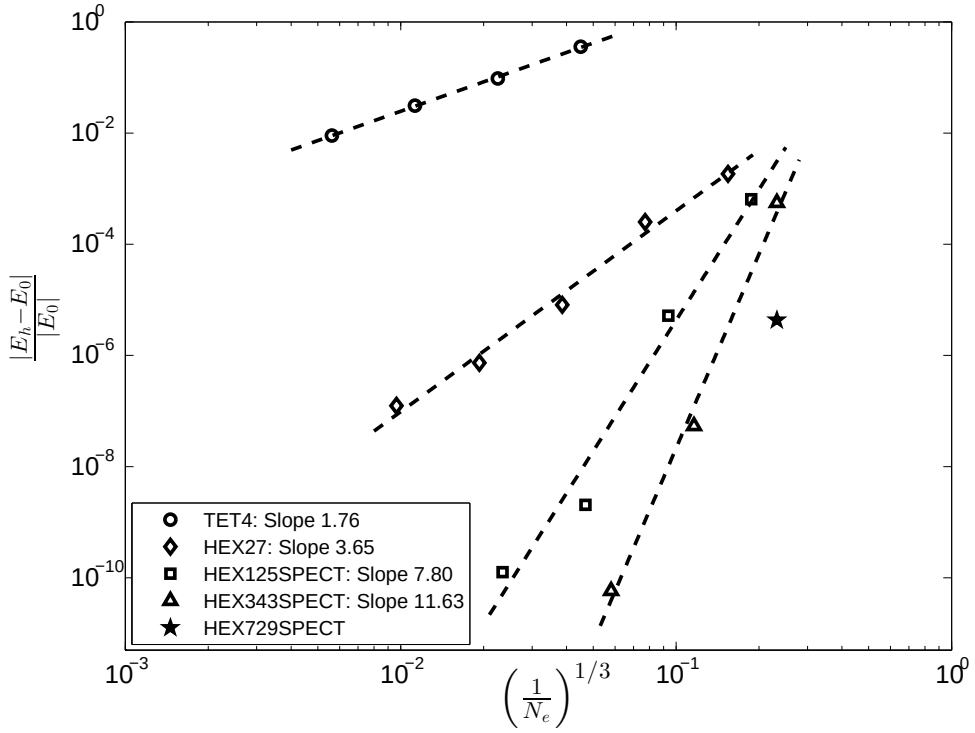

Figure 3.1: Convergence rates for the finite-element approximation of boron atom.

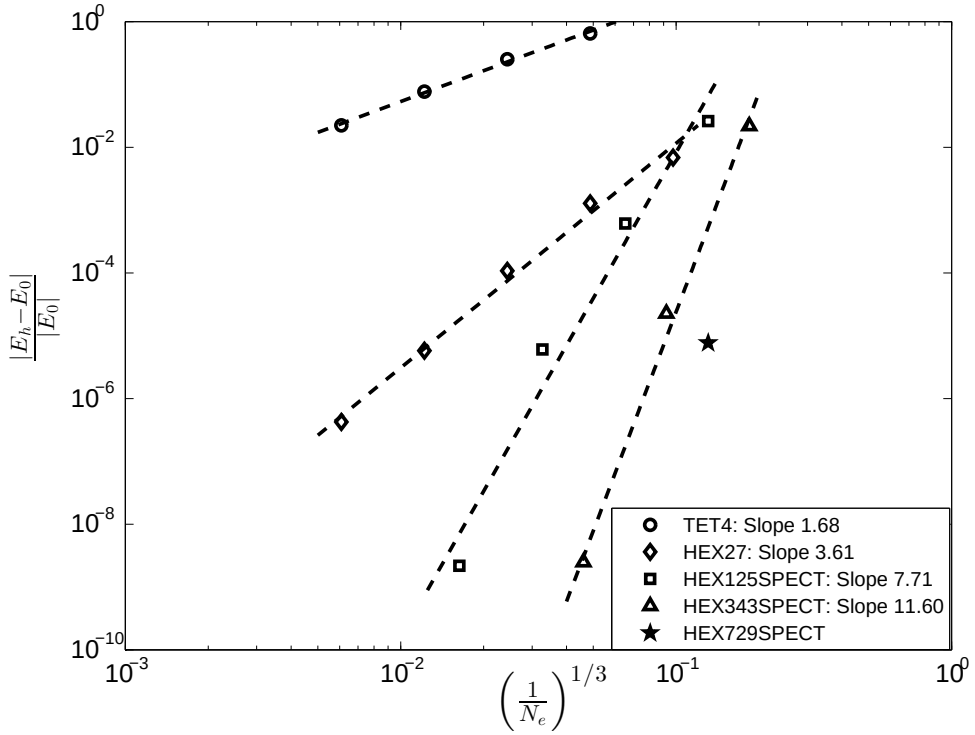

Figure 3.2: Convergence rates for the finite-element approximation of methane molecule.

A are evaluated by the following relations:

$$\beta = \frac{\alpha^3 - 2\,\alpha}{4(\alpha^2 - 1)}\,, \quad A = \frac{1}{2}\alpha^2 - \alpha\beta. \tag{3.90}$$

Barium cluster: The first local pseudopotential calculation we present is a barium $2 \times 2 \times 2$ body-centered cubic (BCC) cluster with a lattice parameter of 9.5 $a.u.$. A Chebyshev filter of order 16 is employed to compute the occupied eigenspace, and a smearing factor $\sigma = 0.000634\ Ha$ (T=200K) is used for the Fermi-Dirac smearing. The simulation domain used is a cubical domain of side 100 $a.u.$ with Dirichlet boundary conditions employed on electronic wavefunctions and total electrostatic potential. The finite-element mesh for this molecule is constructed to be uniform in the cluster region where barium atoms are present, while coarse-graining away. The mesh coarsening rate in the vacuum is determined numerically by employing the asymptotic solution of the far-field electronic fields, estimated as a superposition of single atom far-field asymptotic fields, in equation (3.67). To this end, asymptotic behavior of the atomic wavefunctions in barium atom ($\bar{\psi}(r)$) is chosen to be

$$\bar{\psi}(r) = \sqrt{\frac{\xi^3}{\pi}} \exp\Big[-\xi\, r\Big] \quad \text{where} \quad \xi = \sqrt{2\,\tilde{\epsilon}}\,, \tag{3.91}$$

where $\tilde{\epsilon}$ (negative of the eigenvalue of the highest occupied eigenstate) is estimated from a coarse mesh calculation. The corresponding electrostatic potential is determined by the Poisson equation, with total charge density being equal to the sum of $2\bar{\psi}^2(r)$ and $-2\delta(r)$, and is given by

$$\bar{\varphi}(r) = -2 \exp\left(-2\xi\, r\right) \left(\xi + \frac{1}{r}\right)\,. \tag{3.92}$$

The numerical convergence study is conducted with both tetrahedral and hexahedral elements. Figure 3.5 shows the rates of convergence for the various elements consid-

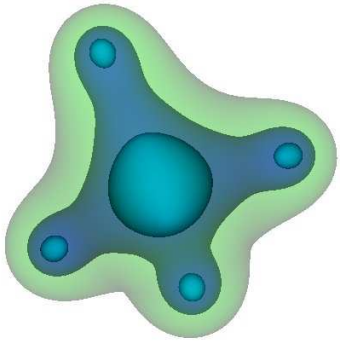

Figure 3.3: Electron density contours of methane molecule.

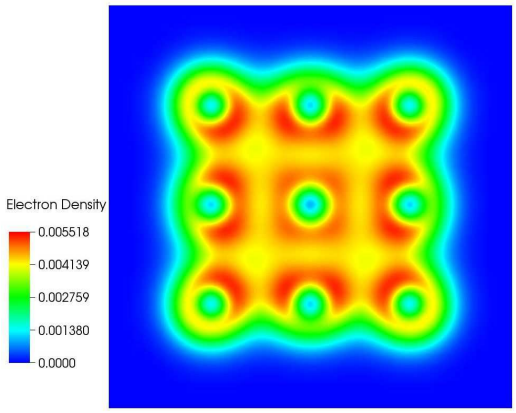

Figure 3.4: Electron density contours of barium $2 \times 2 \times 2$ BCC cluster.

ered that are close to optimal rates of convergence and figure 3.4 show the relevant electron-density contours. The value of E_0 computed from equation (3.80), the reference ground-state energy per atom which is used to compute the relative errors in the energies, is found to be $-0.6386307998\ Ha$. The energy per atom obtained with plane-wave basis using ABINIT with a cutoff energy 30 Ha and cell-size 80 $a.u.$ is $-0.638627743\ Ha$. The main observation that distinguishes this study from the all-electron study is that all orders of interpolation provide much greater accuracies for the local pseudopotential calculations in comparison to all-electron calculations. Linear basis functions are able to approximate the ground-state energies up to relative errors of 10^{-3}, whereas relative errors of 10^{-6} can be achieved with higher-order elements with polynomial degrees of four and above.

Perfect crystal with periodic boundary conditions: The next example considered is that of a perfect calcium face-centered cubic (FCC) crystal with lattice constant 10.55 $a.u.$. Bloch theorem [57] is used in the simulation with 10 k-points (high symmetry) to sample the first Brillouin zone, which represents a quadrature rule of order 2 [96]. The eigenspace is computed using the Krylov-Schur method, and a smearing parameter of 0.003168 Ha (T=1000K) is used in these simulations. Figure 3.6 shows the rates of convergence for the various higher-order finite-elements

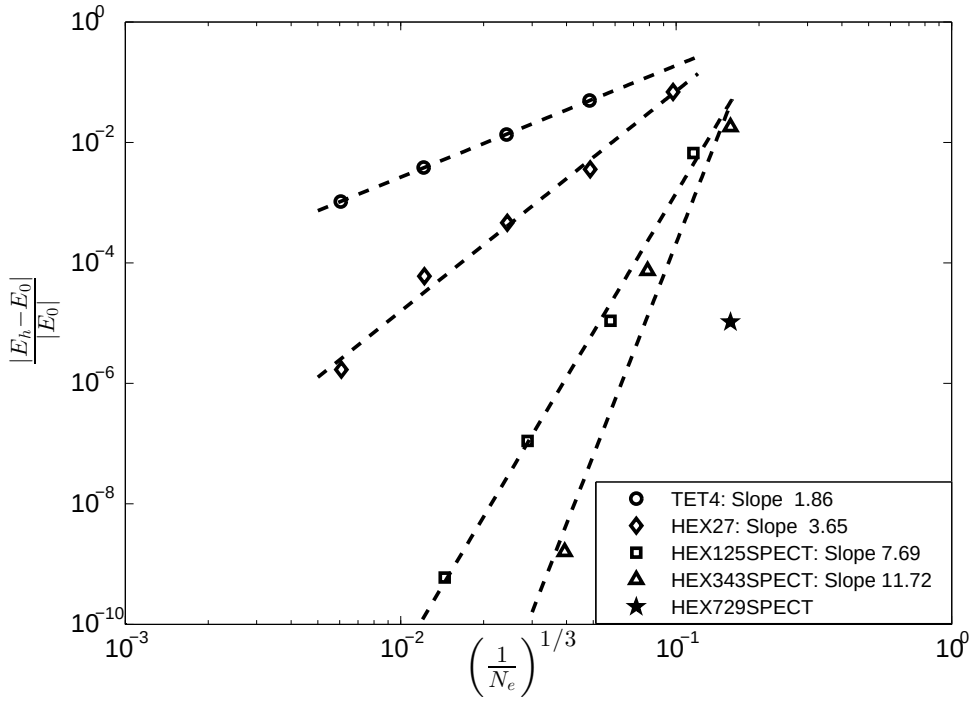

Figure 3.5: Convergence rates for the finite-element approximation of barium cluster.

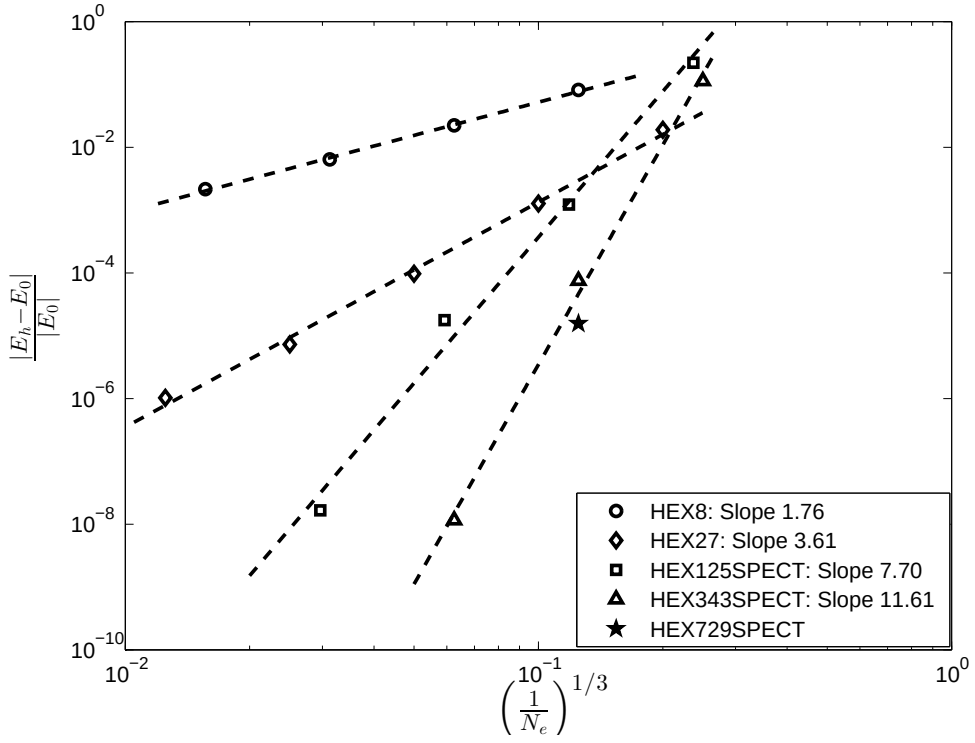

Figure 3.6: Convergence rates for the finite-element approximation of bulk FCC calcium.

considered in the present work. The value of E_0 computed from equation (3.80), the reference bulk energy per atom, is computed to be $-0.729027041\ Ha$. The bulk energy per atom obtained using ABINIT with a cutoff energy of 40 Ha is found to be $-0.72902775\ Ha$. We note that the results are qualitatively similar to the local pseudopotential calculations carried on barium cluster.

3.4.2 Computational cost

We now examine the key aspect of computational efficiency afforded by the use of higher-order finite-element approximations in the Kohn-Sham DFT problem. As seen from the results in Section 3.4.1, higher-order finite-element discretizations provide significantly higher accuracies with far fewer elements in comparison to linear finite-elements. However, the use of higher-order elements increases the per-element computational cost due to an increase in the number of nodes per element, which also results in an increase in the bandwidth of the Hamiltonian matrix. Further, higher-order elements require a higher-order accurate quadrature rule, which again increases the per-element computational cost. Thus, in order to unambiguously determine the computational efficiency afforded by higher-order finite-element discretizations, we measured the CPU-time taken for the simulations conducted on the aforementioned benchmark problems for a wide range of meshes providing different relative accuracies. All the simulations are conducted using meshes with the coarse-graining rates determined by the approach outlined in Section 3.2.2. All the numerical simulations reported in this work are conducted using a parallel implementation of the code based on MPI(message-passing interface), and are executed on a parallel computing cluster with the following specifications: dual-socket six-core Intel Core I7 CPU nodes with 12 total processors (cores) per node, 48 GB memory per node, and 40 Gbps Infiniband networking between all nodes for fast MPI communication. The various benchmark calculations were executed using 1 to 12 processors, while the results for

the larger problems discussed subsequently were executed on 48 to 96 processors. It was verified (see Section 3.4.3) that our implementation scales linearly on this parallel computing platform for the range of processors used, and hence the total CPU-times reported for the calculation are close to the wall-clock time on a single processor. The number of processors used to conduct ABINIT and GAUSSIAN simulations for the comparative studies, discussed subsequently, are carefully chosen to ensure scalability of these codes, and are typically less than 20 processors.

3.4.2.1 Benchmark systems

We first consider the benchmark systems comprising of boron atom, methane molecule, barium cluster and bulk calcium crystal. The mesh coarsening rates for these benchmark systems derived in Section 3.4.1 are employed in the present study. The number of elements are varied to obtain finite-element approximations with varying accuracies that target relative energy errors in the range of $10^{-1} - 10^{-7}$. We employ the same numerical algorithms and algorithmic parameters—order of Chebyshev filter, finite-temperature smearing parameter—as discussed in Section 3.4.1 for the present study. The total CPU-time is measured for each of these simulations on the series of meshes constructed for varying finite-element interpolations and normalized with the longest time in the series of simulations for a given material system. The relative error in ground-state energy is then plotted against this normalized CPU-time. Figures 3.7, 3.8, 3.9 and 3.10 show these results for boron, methane molecule, barium cluster and bulk calcium crystal, respectively.

Our results show that the computational efficiency of higher-order interpolations improves as the desired accuracy of the computations increases, in particular for errors commensurate with chemical accuracy—order of 1 meV per atom error for pseudopotential calculations and 1 mHa per atom error for all-electron calculations. We note that a thousand-fold computational advantage is obtained with higher-order

elements over linear TET4 element even for modest accuracies corresponding to relative errors of 10^{-2}. For relative errors of 10^{-3}, quadratic HEX27 element performance is similar to other finite-elements with quartic interpolation and beyond, and sometimes marginally better. However, all higher-order elements significantly outperform linear TET4 element. Considering relative errors of 10^{-5}, quartic HEX125SPECT element performs better in comparison to quadratic HEX27 element almost by a factor of 10, while hexic HEX343SPECT element is computationally more efficient than HEX125SPECT element by a factor greater than three and this factor improves further for lower relative errors. The octic HEX729SPECT element performs only marginally better than the hexic element for relative errors lower than 10^{-5}. Comparing the results across different materials systems, we observe that the performance of lower-order elements is inferior in the case of all-electron systems in comparison to systems with smooth local pseudopotentials. For instance, at a relative error of 10^{-2}, the solution time using TET4 is more than three orders of magnitude larger than HEX343SPECT for the case of methane molecule. However, the solution time is three orders of magnitude larger for TET4 over HEX343SPECT for the case barium cluster at a relative error of 10^{-3}.

In summary, for chemical accuracies, the computational efficiency improves significantly with the order of the element up to sixth-order, with diminishing returns beyond. Further, the relative performance of higher-order elements with respect to linear TET4 element in the case of all-electron calculations is significantly better in comparison to local pseudopotential calculations. Lastly, qualitatively speaking, the sequence of graphs of relative error vs. normalized CPU-time for the various elements tend towards increasing accuracy and computational efficiency with increasing order of finite-element interpolation. However, we note that, for the systems studied, the point of diminishing returns in terms of computational efficiency of higher-order elements for relative errors commensurate with chemical accuracy is around sixth-order.

As demonstrated in Appendix B , the primary reason for the diminishing returns is the increase in the cost of computing the Hamiltonian matrix which also increasingly dominates the total time with increasing order of the element.

3.4.2.2 Large materials systems

In this section, we further investigate the computational efficiency afforded by higher-order finite-elements by considering larger material systems involving both local pseudopotential and all-electron calculations. As a part of this investigation, we demonstrate the effectiveness of the higher-order finite-elements by comparing the solution times of calculations with local pseudopotentials against plane-wave basis set and solution times of all-electron calculations against a Gaussian basis set providing similar relative accuracy in the ground-state energy. The systems chosen as a part of this study are aluminum clusters containing $3 \times 3 \times 3$, $5 \times 5 \times 5$, $7 \times 7 \times 7$ FCC unit cells for the case of pseudopotential calculations. A graphene sheet containing 100 atoms and a coordination complex, tris (bipyridine) ruthenium, containing 61 atoms are chosen in the case of all-electron calculations.

Local pseudopotential calculations: The pseudopotential calculations on aluminum clusters are conducted using the evanescent core pseudopotential [95]. All the simulations in the case studies involving local pseudopotentials use superposition of single-atom electron densities as the initial guess for the electron density in the first SCF iteration. We used the Krylov-Schur iteration for solving the eigenvalue problem in the first SCF iteration and used Chebyshev filtered subspace iteration for the subsequent SCF iterations. The order of Chebyshev filters used for the $3 \times 3 \times 3$, $5 \times 5 \times 5$ and $7 \times 7 \times 7$ aluminum clusters are 12, 30 and 50 respectively. All simulations are conducted using a finite temperature Fermi-Dirac smearing parameter of 0.0003168 Ha (T=100K). In order to conduct a one-to-one comparison, the

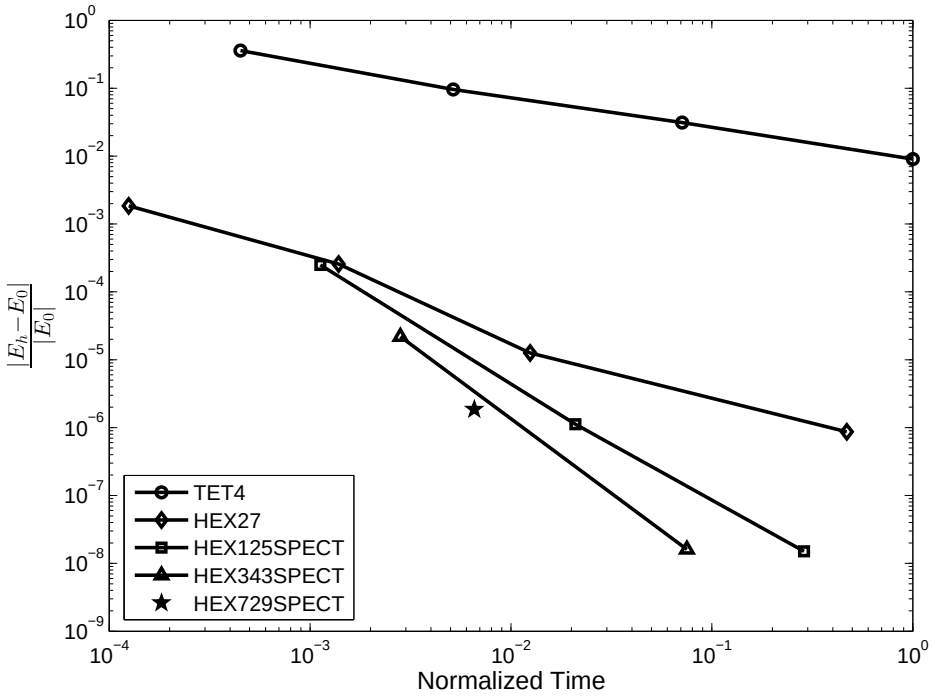

Figure 3.7: Computational efficiency of various orders of finite-element approximations. Case study: boron atom.

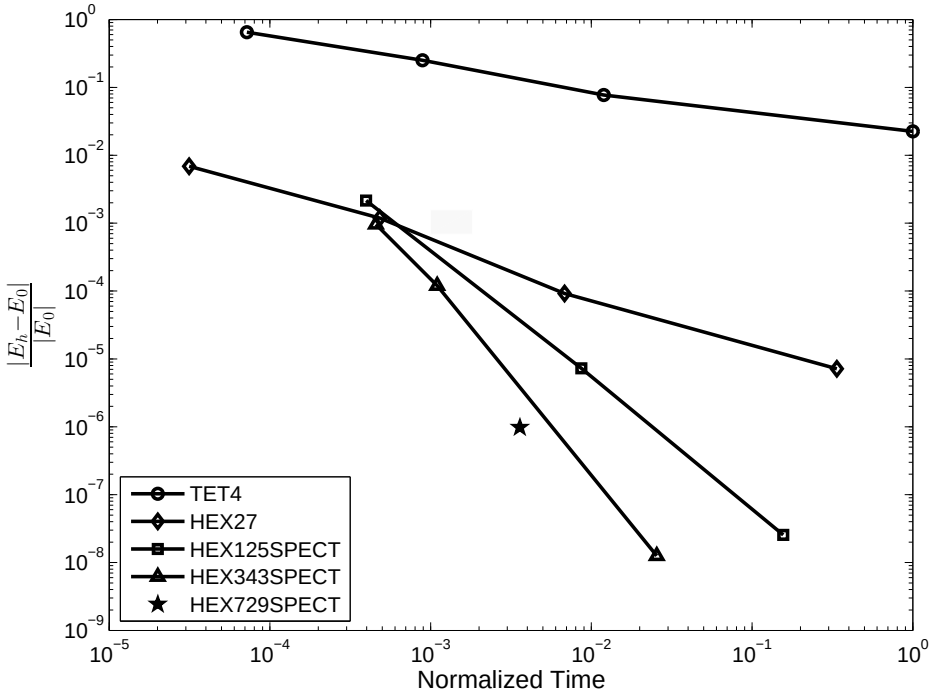

Figure 3.8: Computational efficiency of various orders of finite-element approximations. Case study: methane molecule.

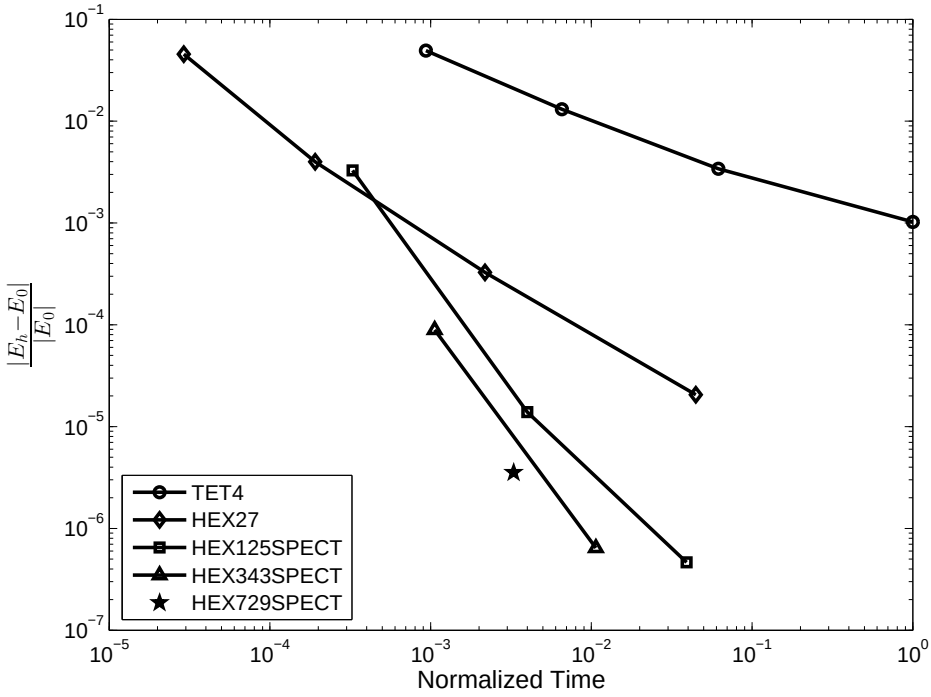

Figure 3.9: Computational efficiency of various orders of finite-element approximations. Case study: barium $2 \times 2 \times 2$ BCC cluster.

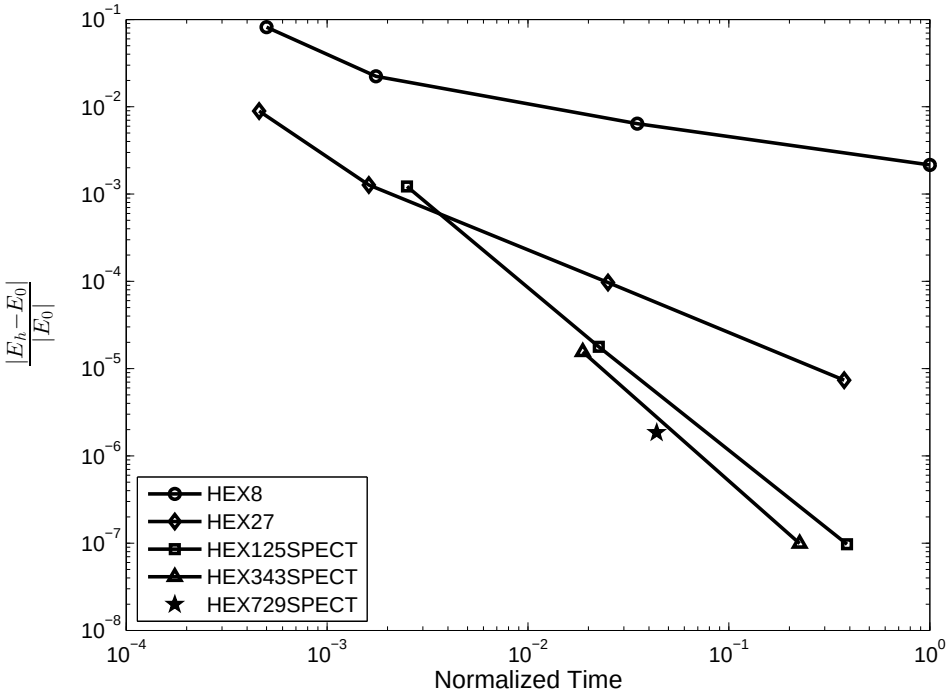

Figure 3.10: Computational efficiency of various orders of finite-element approximations. Case study: bulk calcium FCC crystal.

plane-wave simulations are also conducted using the same pseudopotential and finite temperature Fermi-Dirac smearing used in the finite-element simulations.

Aluminum $3 \times 3 \times 3$ cluster: We first consider an aluminum cluster containing $3 \times 3 \times 3$ FCC unit cells with a lattice spacing of 7.45 $a.u.$. The system comprises of 172 atoms with 516 electrons. The finite-element mesh for this calculation is chosen to be uniform in the cluster region containing aluminum atoms, while coarse-graining away. The mesh coarsening rate in the vacuum is determined numerically by employing the asymptotic solution of the far-field electronic fields, estimated as a superposition of single atom far-field asymptotic fields, in equation (3.67). To this end, the asymptotic behavior of atomic wavefunctions in an aluminum atom ($\bar{\psi}(r)$) is chosen to be

$$\bar{\psi}(r) = \sqrt{\frac{\xi^3}{\pi}} \exp\Big[-\xi\, r\Big] \quad \text{where} \quad \xi = \sqrt{3\,\tilde{\epsilon}}\,, \tag{3.93}$$

where $\tilde{\epsilon}$ (negative of the eigenvalue of the highest occupied eigenstate) is determined from a single aluminum atom coarse mesh calculation. The corresponding total electrostatic potential, governed by the Poisson equation with total charge density being equal to the sum of $3\bar{\psi}^2(r)$ and $-3\delta(r)$, is given by

$$\bar{\varphi}(r) = -3 \exp\left(-2\xi\, r\right) \left(\xi + \frac{1}{r}\right) . \tag{3.94}$$

Table 3.3: Convergence with finite-element basis for a $3 \times 3 \times 3$ FCC aluminum cluster using HEX125SPECT element.

Degrees of freedom	Energy per atom (eV)	Relative error
$184,145$	-54.1076597	3.4×10^{-2}
$1,453,089$	-56.0076146	1.8×10^{-4}
$11,546,177$	-56.01788889	1.3×10^{-6}

We obtain the converged value of the ground-state energy by following the procedure outlined in Section 3.4.1. We use a sequence of increasingly refined HEX125SPECT

finite-element meshes on a cubic simulation domain of side 400 $a.u.$, and compute the ground-state energy E_h for these meshes which are tabulated in Table 3.3. Using the extrapolation procedure discussed in Section 3.4.1 (equation (3.80)), we compute the reference ground-state energy (energy per atom) to be $E_0 = -56.0179603\ eV$. The relative errors reported in Table 3.3 are with respect to this reference energy, and this reference energy will be used to compute the relative errors for all subsequent finite-element and plane-wave basis simulations for this material system.

Table 3.4: Comparison of higher-order finite-element (FE) basis with plane-wave basis for a $3 \times 3 \times 3$ FCC aluminum cluster.

Type of basis set	Energy (eV) per atom	Abs. error (eV) per atom	Rel. error	Time (CPU-hrs)
Plane-wave basis (cut-off 30 Ha; cell-size of 60 $a.u.$; $847,348$ plane waves)	-56.0181429	0.00018	3.3×10^{-6}	646
FE basis (HEX343SPECT; $2,808,385$ nodes; domain size: 200 $a.u.$)	-56.0177597	0.0002	3.6×10^{-6}	371

In order to assess the performance of higher-order finite-elements on this material system, we conduct the finite-element simulation with a mesh containing HEX343SPECT elements and compare the computational CPU-time against a plane-wave basis code ABINIT [60] solved to a similar relative accuracy in the ground-state energy with respect to reference value E_0 obtained above. The finite-element simulation has been performed on a cubic domain size of 200 $a.u.$ with a mesh coarsening rate away from the cluster of atoms as determined using equations (3.67), (3.93), (3.94). The resulting mesh contains $12,800$ HEX343SPECT elements with $2,808,385$ nodes. The plane-wave basis simulation has been performed by using a cell-size of 60 $a.u.$ and a cut-off energy of 30 Ha with one k-point to obtain the ground-state energy of similar relative accuracy(0.0002 eV/atom) as the finite-element simulation. The computational times for the finite-element basis and the plane-wave basis for the full self-consistent solution are tabulated in Table 3.4. These results demonstrate that the performance

of higher-order finite-element discretization is comparable, in fact better by a two-fold factor, to the plane-wave basis for this material system. Figure 3.11 shows the electron density contours on the mid-plane of the $3 \times 3 \times 3$ aluminum cluster from the finite-element simulation.

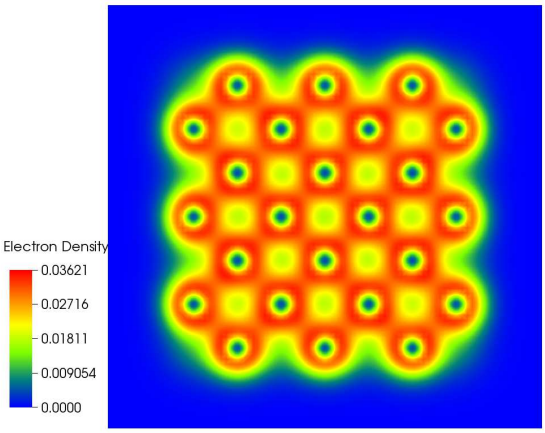

Figure 3.11: Electron density contours of $3 \times 3 \times 3$ FCC aluminum cluster.

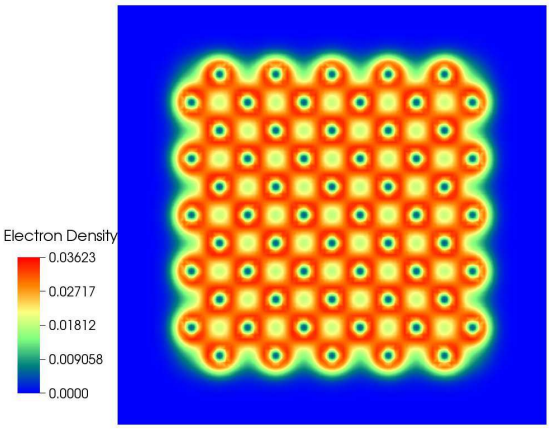

Figure 3.12: Electron density contours of $5 \times 5 \times 5$ FCC aluminum cluster.

Aluminum $5 \times 5 \times 5$ cluster: We next consider an aluminum cluster containing $5 \times 5 \times 5$ FCC unit cells with a lattice spacing of 7.45 $a.u.$. This material system comprises of 666 atoms with 1998 electrons. The finite-element mesh is constructed along similar lines as the $3 \times 3 \times 3$ cluster, where a uniform mesh resolution is chosen in the cluster region containing aluminum atoms and coarse-graining away into the vacuum with a numerically determined coarsening rate as discussed earlier. As before, we first obtain the reference ground-state energy by using a sequence of increasingly refined HEX125SPECT finite-element meshes with a cubic simulation domain of side 800 $a.u.$ and extrapolating the computed ground-state energies on these meshes (cf. Table 3.5). The reference ground-state energy (energy per atom), thus determined, is $E_0 = -56.0495071\ eV$.

We now assess the performance of higher-order finite-elements on this material system in comparison to a plane-wave basis. The finite-element simulation in this

Table 3.5: Convergence with finite-element basis for a $5 \times 5 \times 5$ FCC cluster using HEX125SPECT element.

Degrees of freedom	Energy per atom(eV)	Relative error
$394,169$	-54.8536312	2.1×10^{-2}
$3,124,593$	-56.0425334	1.2×10^{-4}
$24,883,937$	-56.0494500	1.01×10^{-6}

case has been performed on a simulation domain size of 400 $a.u.$ containing $36,064$ HEX343SPECT elements with $7,875,037$ nodes. The plane-wave basis simulation conducted using the ABINIT package has been performed on a cell-size of 80 $a.u.$ and a cut off energy of 30 Ha with one k-point to sample the Brillouin zone to obtain the ground-state energy of similar accuracy with respect to the reference value E_0 obtained above. The solution time for the finite-element basis and the plane-wave basis are tabulated in Table 3.6, which shows that using higher-order finite-elements one can achieve similar computational efficiencies as afforded by a plane-wave basis, at least in the case of non-periodic calculations. Figure 3.12 shows the electron density contours on the mid-plane of the $5 \times 5 \times 5$ FCC cluster from the finite-element simulation.

Table 3.6: Comparison of higher-order finite-element (FE) basis with plane-wave basis sets for a $5 \times 5 \times 5$ FCC aluminum cluster.

Type of basis set	Energy (eV) per atom	Abs. error (eV) per atom	Rel. error	Time (CPU-hrs)
Plane-wave basis (cut-off 30 Ha; cell-size of 80 a.u; $2,009,661$ plane waves)	-56.0506841	0.0012	2.1×10^{-5}	7307
FE basis (HEX343SPECT; $7,875,037$ nodes; domain size: 400 $a.u.$)	-56.04906430	0.00044	7.9×10^{-6}	6619

Aluminum $7 \times 7 \times 7$ cluster: As a final example in our case study with local pseudopotential calculations, we study an aluminum cluster containing $7 \times 7 \times 7$ FCC unit cells with a lattice spacing of 7.45 $a.u.$ This material system comprises of 1688

atoms with 5064 electrons. We only use the finite-element basis to simulate this system as the plane-wave basis calculation was beyond reach for this material system with the computational resources at our disposal. The finite-element simulation has been performed on a cubic simulation domain with a side of 800 $a.u.$. The finite-element mesh was constructed as described in the simulation of other aluminum clusters, and comprised of $69,984$ HEX343SPECT elements with $15,257,197$ nodes. The computed energy per atom for this aluminum cluster is $-56.06826762\ eV$, and figure 3.13 shows the electron density contours on the mid-plane of the cluster.

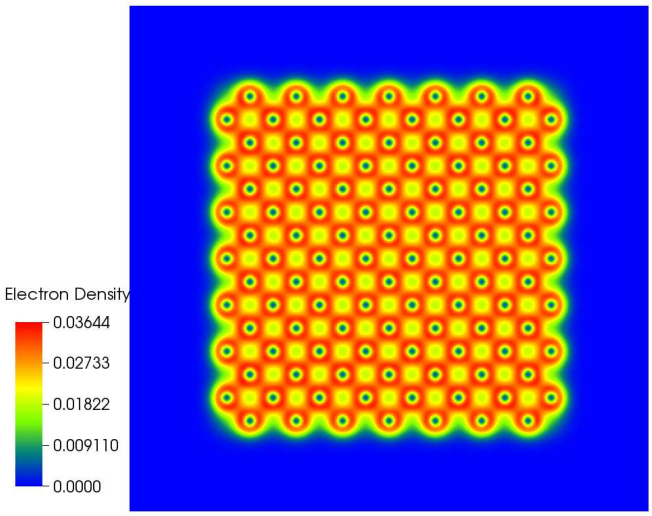

Figure 3.13: Electron density contours of $7 \times 7 \times 7$ FCC aluminum cluster.

All-electron calculations: We now demonstrate the performance of higher-order finite-element discretization in the case of all-electron calculations, by considering a graphene sheet and a transition metal complex, namely, tris (bipyridine) ruthenium as our benchmark problems. In these calculations which employ HEX125SPECT finite-element, the initial guess for electron-density in the first SCF iteration is computed by interpolating the self-consistent solution obtained from a lower-order HEX27 finite-

element mesh. The computational times reported for these calculations include the time taken to generate the initial guess.

Graphene sheet: We begin with a graphene sheet containing 100 atoms (600 electrons) with a C-C bond length of 2.683412 $a.u.$. We first obtain a converged value of the ground-state energy by conducting simulations using the GAUSSIAN package [72] using the polarization consistent DFT basis sets (pc-n), which have been demonstrated to provide a systematic convergence in Kohn-Sham DFT calculations [97]. Since these basis sets are not directly available in the GAUSSIAN package, we introduce them as an external basis set for conducting these simulations. The ground-state energy value obtained for triple-zeta pc-3 basis set is taken as the reference value (E_0) in this study, which is computed to be $E_0 = -37.7619141\ Ha$ per atom. We note that we did not use the extrapolation procedure outlined in Section 3.4.1, as it was computationally beyond reach with our resources.

We assess the performance of higher-order finite-elements on this material system by comparing the computational CPU-time against the pc-2 basis set, which provides similar relative accuracy in the ground-state energy with respect to the E_0 determined above. The finite-element mesh for this problem is chosen to be uniform in the region containing carbon atoms with local refinement around each atom while coarse-graining away into vacuum. The mesh coarsening rate in the vacuum is determined numerically by employing the asymptotic solution of the far-field electronic fields, estimated as a superposition of single atom far-field asymptotic fields, in equation (3.67). To this end, the asymptotic behavior of the atomic wavefunctions in carbon atom ($\bar{\psi}(r)$) is chosen to be as in equation (3.85). Since the GAUSSIAN package does not account for partial occupancy of energy levels, we suppress the Fermi-Dirac smearing in the finite-element simulations for the present case in order to conduct a one-to-one comparison. A Chebyshev filter of order 500 is used in

this simulation. The simulation domain used is a cubical domain of side 300 $a.u.$ with Dirichlet boundary conditions employed on electronic wavefunctions and total electrostatic potential. Table 3.7 shows the relevant results of the simulation with figure 3.14 showing the electron density contours of the graphene sheet. We remark that the finite-element simulation with HEX125SPECT elements is around ten-fold slower than the GAUSSIAN simulation with pc basis set.

Table 3.7: 100 atom graphene sheet (600 electrons).

Type of basis set	Energy (Ha) per atom	Abs. error (Ha) per atom	Rel. error	Time (CPU-hrs)
pc2 (Gaussian; $3,000$ basis functions)	-37.757954	0.00396	1.06×10^{-4}	666
FE basis (HEX125SPECT; $8,004,003$ nodes)	-37.757382	0.00452	1.2×10^{-4}	7461

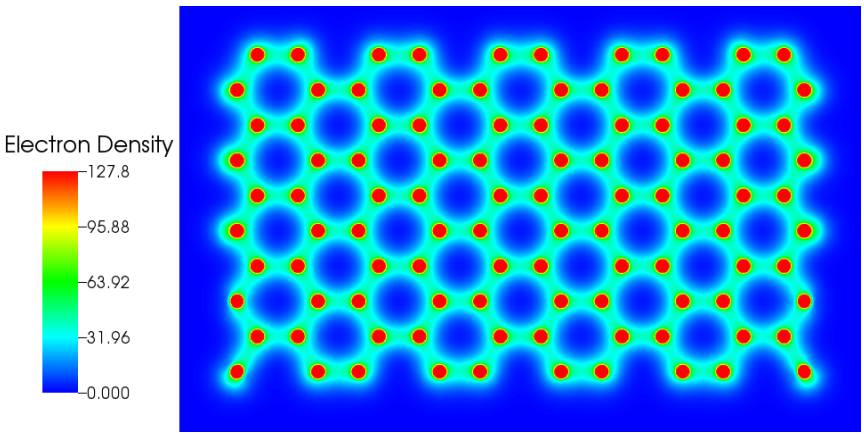

Figure 3.14: Electron density contours of a graphene sheet containing 100 atoms.

Tris (bipyridine) ruthenium: We now demonstrate the performance of our numerical algorithms on a compound involving a moderately heavy metal. We choose Tris (bipyridine) ruthenium complex (TBR) as our benchmark problem, which belongs to the class of transition metal complexes that has attracted significant attention because of its distinctive optical properties [98]. Though the prototype complex TBR is extensively studied as a di-cation, we consider the charge neutral complex in this

case study. The geometric structure of this compound was determined using the geometry optimization option in the GAUSSIAN package. The resulting compound consists of a central ruthenium atom bonded to nitrogen atoms (ligands) of the three bipyridine rings as shown in Figure 3.15. The compound contains a total of 61 atoms (290 electrons) comprising of 30 carbon atoms, 24 hydrogen atoms, 6 nitrogen atoms and 1 ruthenium atom.

We conducted the simulations using GAUSSIAN package in the following manner. Polarized consistent DFT basis sets provide a series of improved basis sets for carbon, hydrogen and nitrogen atoms, but are not suited for the ruthenium atom. Hence, we first conducted the GAUSSIAN simulation using the most refined polarized consistent basis set namely pc-4 basis functions for carbon, hydrogen and nitrogen, and used the polarized valence double zeta basis function designed for DFT (DZDFTO) for ruthenium. However, the self-consistent iteration did not converge for this choice of basis sets. Hence, we conducted the GAUSSIAN simulation with a coarser polarized consistent quadruple zeta basis (pc-3) functions for carbon, hydrogen and nitrogen atoms, and used the DZDFTO basis for ruthenium. The self-consistent iteration did converge for this choice, and the ground-state energy and solution time for this case are tabulated in Table 3.8.

We now assess the performance of higher-order finite-elements on this material system. The finite-element mesh for this problem is chosen to be uniform in the region where the molecule is present with local refinement around each atom while coarse-graining away into the vacuum. The mesh coarsening rate in the vacuum is determined numerically by employing the asymptotic solution of far-field asymptotic fields, estimated as a superposition of single atom far-field asymptotic fields in equation 3.67. The finite-element simulation is conducted using HEX125SPECT elements with a Chebyshev filter of order 500 and a Fermi-Dirac smearing parameter of 0.00158 Ha (T=500K). The simulation domain used is a cubical domain of side

200 $a.u.$ with Dirichlet boundary conditions employed on electronic wavefunctions and total electrostatic potential. Table 3.8 demonstrates the relevant results for the finite-element simulation with figure 3.16 showing the electron-density contours. We remark that the ground-state energy per atom obtained from finite-element simulation differs by 0.00146 Ha in comparison with aforementioned GAUSSIAN simulation. As observed in the case of graphene sheet, the finite-element simulation is ten-fold slower than the GAUSSIAN simulation.

Table 3.8: Tris(bipyridine)ruthenium (290 electrons).

Type of basis set	Energy (Ha) per atom	Time (CPU-hrs)
pc3 (Gaussian; $3,156$ basis functions)	-96.923328	311
FE basis (HEX125SPECT; $10,054,041$ nodes)	-96.924636	3927

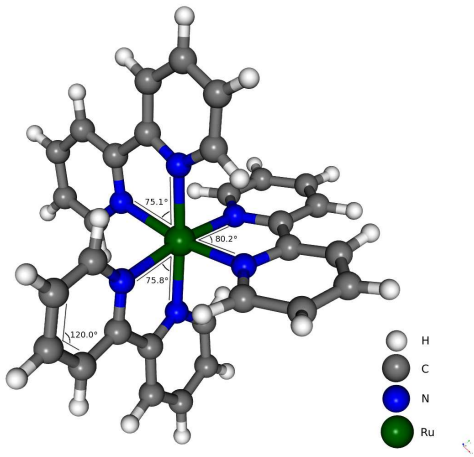

Figure 3.15: Schematic of Tris(bipyridine) ruthenium complex.

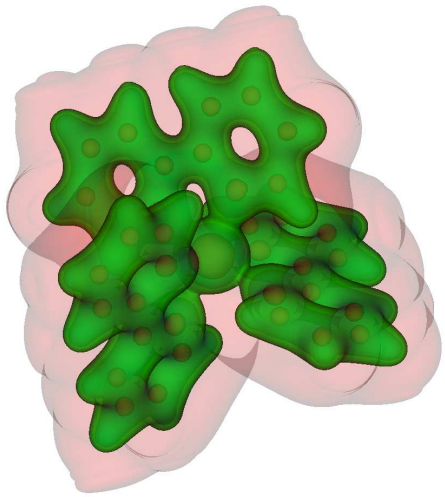

Figure 3.16: Electron density contours of Tris (bipyridine) ruthenium complex.

We note that the Gaussian basis sets employed in these benchmark studies are highly optimized for specific material systems, which is reflected in the far fewer basis functions required for the above calculations. We believe this is the main reason for the superior performance of Gaussian basis. We also note that the computational

time using finite-element basis functions can possibly be reduced significantly by enriching the finite-element shape functions with single atom wavefunctions using the partitions-of-unity approach [99, 100]. The degree of freedom advantage of the partitions-of-unity approach for Kohn-Sham calculations has been first demonstrated in [101], and presents a promising future direction for all-electron Kohn-Sham DFT calculations.

3.4.3 Scalability of finite-element basis:

The parallel scalability of our numerical implementation is demonstrated in Figure 3.17. We study the strong scaling behavior by measuring the relative speedup with increasing number of processors on a fixed problem of constant size, which is chosen to be the aluminum $3 \times 3 \times 3$ cluster discretized with HEX125SPECT elements containing 3.91 million degrees of freedom. The speedup is measured relative to the computational CPU-time taken on 2 processors, as a single processor run was beyond reach due to memory limitations. It is evident from the figure, that the scaling is almost linear. The relative speedup corresponding to 96-fold increase in the number of processors is 87.82, which translates into an efficiency of 91.4%.

3.5 Summary

The prospect of using higher-order spectral finite-elements as basis functions, in conjunction with the proposed solution strategies, for Kohn-Sham DFT electronic structure calculations is indeed very promising. While finite-elements have the advantages of handling complex geometries and boundary conditions and exhibit good scalability on massively parallel computing platforms, their use has been limited in electronic structure calculations as their computational efficiency compared unfavorably to plane-wave and Gaussian basis functions. The results presented in this chapter shows that the use of higher-order discretizations can alleviate this problem, and

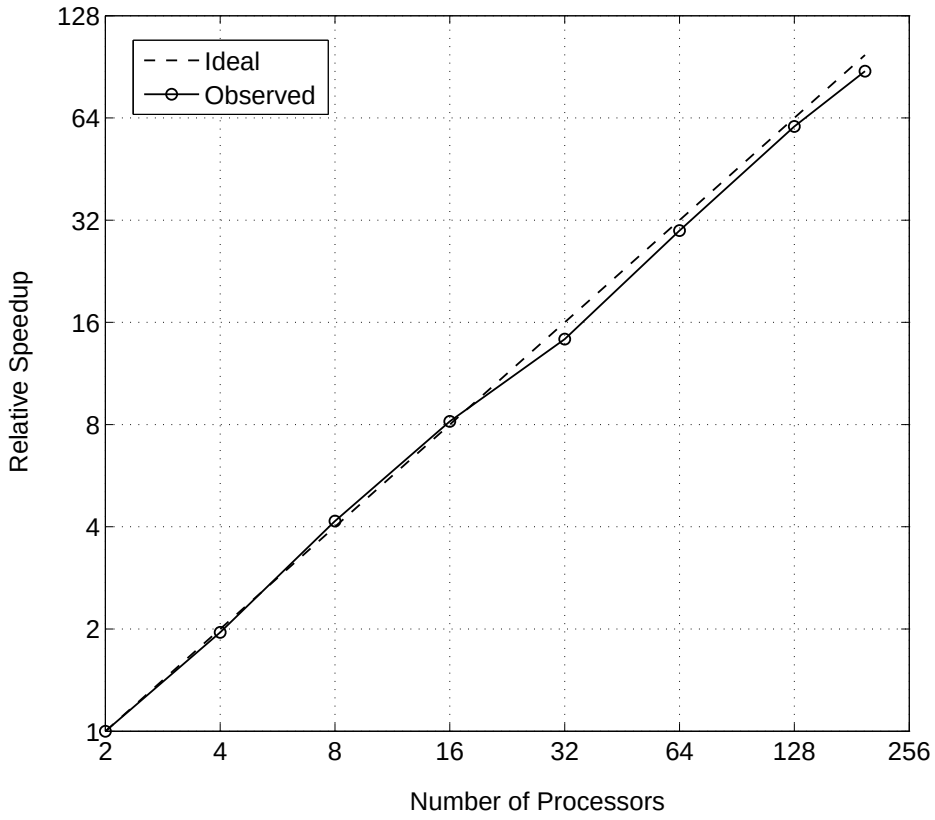

Figure 3.17: Relative speedup as a function of the number of processors.

presents a useful direction for electronic structure calculations using finite-element discretization. Further, the computational cost in the case of all-electron calculations can be further reduced by enriching the finite-element shape functions with single-atom wavefunctions, and is a worthwhile subject for future investigation. The implications of using higher-order spectral finite-element approximations in the development of a reduced scaling Kohn-Sham DFT formulation is explored in Chapter IV.

CHAPTER IV

Subquadratic-scaling subspace projection method for Kohn-Sham density functional theory

The traditional self-consistent approach to solving the discretized nonlinear Kohn-Sham eigenvalue problem involves the diagonalization of the Hamiltonian to obtain orthonormal eigenvectors, the computational complexity of which typically scales as $\mathcal{O}(M\,N^2)$ where M denotes the number of basis functions and N denotes the system size (number of atoms or number of electrons). This cost becomes prohibitively expensive, approaching cubic-scaling, as the system size becomes larger. To this end, numerous efforts have focused on either reducing the prefactor [66, 102] associated with the computational cost of the Kohn-Sham DFT calculations or reducing the computational complexity to have improved-scaling behavior for DFT calculations. The latter methods usually exploit locality in the wavefunctions [103] directly or indirectly, and can be broadly categorized [32] into two types: one which calculate the single-electron density matrix, and another which work with its representation in terms of localized Wannier functions. The divide and conquer method [104, 105, 106], Fermi-operator expansion [34, 107, 108, 35], density-matrix minimization [109, 110] approach belong to the former category, whereas, the Fermi-operator projection method [111, 112] and the orbital minimization approach [113, 114, 115, 36] belong to the latter category. A comprehensive review of these methods has been provided by Göedecker [32], and

more recently by Bowler and Miyazaki [33]. These methods, which rely on the locality of the Wannier functions or the exponential decay of the density matrix in real-space, have been demonstrated to work well for insulating systems, exhibiting linear-scaling with system size. However, for metallic systems, due to the slower decay of the density matrix, the computational complexity of these approaches can deviate significantly, in practice, from linear-scaling. Further, we note that, some of the developed techniques [109, 111, 112, 36] assume the existence of a band-gap, thus restricting these techniques solely to insulating systems. The Fermi-operator expansion method [34, 35, 32], which is equally applicable to both insulating and metallic systems, computes the finite-temperature density-matrix through a Chebyshev polynomial approximation of the Fermi distribution function (also referred to as Fermi function) of the Kohn-Sham Hamiltonian. The accuracy of such an expansion depends on the smearing parameter ($\sigma = k_B T$) in the Fermi distribution and the width of the eigenspectrum (ΔE) of the discretized Hamiltonian. In fact, the number of polynomial terms required to achieve a prescribed accuracy [35] is $\mathcal{O}(\frac{\Delta E}{\sigma})$. Numerous recent efforts [116, 117, 118, 119, 120] have focused towards developing alternate approximations to the Fermi function, or approximations to its spectral representation [121]. A majority of these methods aim to reduce the number of terms used in the expansion to approximate the Fermi function. However, a major drawback with these methods is that they are not efficient for local real-space basis functions like finite-elements, where, typically, more refined discretizations are needed. In a recent study [1], it was observed that the width of the eigenspectrum of the finite-element discretized Hamiltonian (using higher-order finite-elements) is $\mathcal{O}(10^3)$ Ha for pseudopotential calculations, and $\mathcal{O}(10^5)$ Ha for all-electron calculations. In this chapter, building on our earlier work [1] described in the previous chapter, we propose a reduced-scaling subspace projection technique in the framework of spectral finite-element discretization. To this end, we borrow localization ideas from Garcia et.

al. [36] and develop a subspace iteration technique that treats both metallic and insulating systems on a similar footing. Further, besides pseudopotential calculations, the proposed technique is also applicable to all-electron calculations, as demonstrated in our benchmark studies. The main ideas used in our approach are: (i) employ Chebyshev filtered subspace iteration to compute the occupied eigenspace; (ii) employ a localization procedure to generate non-orthogonal localized wavefunctions spanning the Chebyshev filtered subspace; (iii) use adaptive tolerances to truncate the wavefunctions, with looser tolerances being employed in initial self-consisted field (SCF) iterations and progressively tightening as the SCF iteration approaches convergence, and (iv) employ Fermi-operator expansion in terms of the projected Hamiltonian expressed in the non-orthogonal localized basis to compute the density matrix, electron density and band energy.

We first present an abstract mathematical framework in which the projection of the Hamiltonian into a subspace, corresponding to the occupied eigenspace, and the associated density matrix are expressed in a non-orthogonal basis spanning the subspace. We then derive expressions for the computation of electron density, constraint on the number of electrons and the band energy in terms of the projected Hamiltonian, which are subsequently used to formulate the subspace projection technique within the framework of finite-element discretization. To this end, the Kohn-Sham Hamiltonian and the corresponding wave-functions are represented in the Löwdin orthonormalized finite-element basis constructed using spectral finite-elements in conjunction with Gauss-Lobatto-Legendre quadrature rules. The SCF iteration begins with an initial subspace spanned by the localized single-atom wavefunctions, and a Chebyshev filter is applied on this subspace to compute an approximation to the occupied eigenspace. Next, we employ a localization procedure to construct non-orthogonal localized wavefunctions spanning the Chebyshev filtered subspace. The localized wavefunctions are then truncated using a truncation tolerance, below which

the localized wavefunctions are set to zero. We note that the proposed approach of providing a compact support for the wavefunctions by using a truncation tolerance on the wavefunctions differs from commonly employed approach of using truncation radius, and presents a more efficient approach as the localized wavefunctions may not necessarily be spherically symmetric about the localization center. The Kohn-Sham Hamiltonian is then projected into the localized basis, and a Fermi-operator expansion in terms of the projected Hamiltonian is employed to compute the finite-temperature density matrix and the electron density. If the truncated wavefunctions are sufficiently sparse, the computational cost of each of the above steps is shown to scale linearly with number of atoms.

The proposed approach is implemented in a parallel computing framework, and the performance of the algorithm is investigated on representative benchmark atomic systems involving metallic aluminum nano-clusters (pseudopotential calculations), insulating alkane chains (pseudopotential calculations), and semi-conducting silicon nano-clusters (all-electron calculations). The scaling behavior is assessed on these materials systems with varying system sizes up to 3430 atoms in the case of aluminum nano-clusters, up to 7052 atoms in the case of alkane chains, and up to 3920 electrons in the case of all-electron silicon nano-clusters. The scaling of the computational time per SCF iteration with the system size is computed to be $\mathcal{O}(N^{1.46})$ for aluminum nano-clusters, $\mathcal{O}(N^{1.18})$ for the alkane chains, and $\mathcal{O}(N^{1.75})$ for the all-electron silicon nano-clusters. One factor contributing to the deviation from linearity is the use of adaptive tolerances—using looser tolerances in the initial SCF iterations and progressively tightening the tolerances as the SCF approaches convergence—which partially sacrifices the scaling for good accuracy in the ground-state energies. We note that the computed ground-state energies using the proposed approach are within 5 meV per atom for pseudopotential calculations and are within 5 mHa per atom for all-electron calculations with respect to the reference ground-state energies. Further, in our im-

plementation, we switch from using sparse data-structures to dense data-structures when the density fraction of the localized wavefunctions exceeds 2%, as the computational cost of using parallel sparse data-structures is observed to exceed that of dense data-structures beyond this point. This is another factor contributing to the deviation from linear-scaling as discussed in the Appendix D. Our results suggest that significant computational savings can be realized using the proposed approach, where $\sim 10-$fold speedups are obtained with respect to reference benchmark calculations for the largest systems.

The remainder of the chapter is organized as follows. Section 4.1 briefly recalls the real-space formulation of the Kohn-Sham DFT problem described in Chapter III, followed by the presentation of the mathematical formulation of the subspace projection technique in an abstract setting. Section 4.2 describes the various steps involved in the subspace projection technique within the framework of spectral finite-element discretization. Section 4.3 presents the numerical study on three representative materials systems demonstrating the accuracy, computational efficiency and scaling of our approach. We finally conclude with a summary and outlook in Section 4.4.

4.1 Mathematical Formulation

In this section, we first recall the system of equations corresponding to the Kohn-Sham self-consistent formulation described in Chapter III and then discuss some mathematical preliminaries in an abstract setting to present an expression for the projection of the Hamiltonian operator into a subspace spanned by a non-orthogonal basis. Subsequently, we derive the density matrix corresponding to the projected Hamiltonian, and present the expressions for the computation of electron density, constraint on the number of electrons and the band energy in terms of the projected Hamiltonian. This constitutes the mathematical formulation for the subspace projection technique within the framework of spectral finite-element discretization,

described in the next section.

We recall from Chapter III that the system of equations corresponding to the self-consistent formulation of the Kohn-Sham eigenvalue problem are:

$$\left(-\frac{1}{2}\nabla^2 + V_{\text{eff}}(\rho, \mathbf{R})\right)\psi_i = \epsilon_i \psi_i, \tag{4.1a}$$

$$2\sum_i f(\epsilon_i, \mu) = N_e; \quad \rho(\mathbf{r}) = 2\sum_{i=1}^{N} f(\epsilon_i, \mu)|\psi_i(\mathbf{r})|^2, \tag{4.1b}$$

$$-\frac{1}{4\pi}\nabla^2\varphi(\mathbf{r}, \mathbf{R}) = \rho(\mathbf{r}) + b(\mathbf{r}, \mathbf{R}); \quad -\frac{1}{4\pi}\nabla^2\nu_I(\mathbf{r}, \mathbf{R}) = b_I(\mathbf{r}, \mathbf{R}). \tag{4.1c}$$

where $\psi_i(\mathbf{r})$ denotes the spatial part of canonical wavefunctions. In the case of all-electron calculations, $V_{\text{eff}}(\rho, \mathbf{R}) = \varphi(\mathbf{r}, \mathbf{R}) + V_{\text{xc}}(\rho)$ with φ denoting the total electrostatic potential comprising both Hartree and nuclear contributions and V_{xc} denoting the exchange-correlation potential while the pseudopotential case has $V_{\text{eff}}(\rho, \mathbf{R}) = \varphi(\mathbf{r}, \mathbf{R}) + V_{\text{xc}}(\rho) + V_{\text{loc}}(\mathbf{R}) + V_{nl}(\mathbf{R}) - \sum_{J=1}^{N_a}\nu_J(\mathbf{r})$. Here V_{loc} denotes the local part of pseudopotential and V_{nl} denotes the nonlocal contribution of the pseudopotential and further only the wavefunctions corresponding to the valence electrons are computed. ν_I denotes the self-potential corresponding to the I^{th} nuclei.

4.1.1 Projection of the Hamiltonian into a finite-dimensional subspace

If $\mathcal{H}$ denotes the Hermitian operator representing the Hamiltonian of interest (c.f equation (4.1a)) defined on the infinite dimensional Hilbert space $\mathbb{H}$ equipped with the inner product $\langle .|. \rangle$ and a norm $\| \ . \ \|$ derived from the inner product and $\mathbb{V}_h^M \subset \mathbb{H}$ denotes a finite-dimensional subspace of $\mathbb{H}$ with dimension M as defined in Chapter III, then we define the projection operator into the subspace $\mathbb{V}_h^M$ to be $\mathcal{P}^q : \mathbb{H} \to \mathbb{V}_h^M$ given by

$$\mathcal{P}^q = \sum_{i=1}^{M} |q_i\rangle \langle q_i| \ . \tag{4.2}$$

where $\{|q_i\rangle\}$ denote an orthonormal basis for $\mathbb{V}_h^M$. In the present case, the representation of $|q_i\rangle$ in the real space, $\langle \mathbf{r}|\, q_i\rangle = q_i(\mathbf{r})$, denotes the Löwdin orthonormalized finite-element basis employed in this study, as discussed subsequently in section 4.2. The projection of the Hamiltonian into $\mathbb{V}_h^M$ is given by $\mathcal{P}^q\mathcal{H} : \mathbb{V}_h^M \to \mathbb{V}_h^M$, or equivalently $\mathcal{P}^q\mathcal{H}\mathcal{P}^q : \mathbb{H} \to \mathbb{V}_h^M$. We denote the operator corresponding to the projected Hamiltonian to be $\widetilde{\mathcal{H}} \equiv \mathcal{P}^q\mathcal{H}\mathcal{P}^q$, and the matrix corresponding to $\widetilde{\mathcal{H}}$ expressed in $\{|q_i\rangle\}$ basis by $\widetilde{\mathbf{H}}$ with the matrix element given by $\widetilde{\mathrm{H}}_{ij} = \left\langle q_i \middle| \widetilde{\mathcal{H}} \middle| q_j \right\rangle$.

4.1.2 Reprojection into a non-orthogonal basis

We now consider a subspace $\mathbb{V}^N \subset \mathbb{V}_h^M$, which approximates the occupied eigenspace of $\widetilde{\mathcal{H}}$ that can be computed, for instance, using a Chebyshev filtering approach [66, 1] (discussed in chapter III). Let $\{|\phi_\alpha\rangle\}$ represent a non-orthonormal basis which spans $\mathbb{V}^N$. We denote by $\mathcal{P}^\phi : \mathbb{V}_h^M \to \mathbb{V}^N$ the projection operator into the space $\mathbb{V}^N$, and is given by

$$\mathcal{P}^\phi = \sum_{\alpha,\beta=1}^{N} |\phi_\alpha\rangle\, S^{-1}_{\alpha\beta}\, \langle\phi_\beta| \,, \tag{4.3}$$

where $\mathbf{S}$ denotes the overlap matrix with matrix elements $S_{\alpha\beta} = \langle\phi_\alpha|\, \phi_\beta\rangle$. We denote the projection of $\widetilde{\mathcal{H}}$ into $\mathbb{V}^N$ by $\mathcal{H}^\phi$, and is given by $\mathcal{H}^\phi \equiv \mathcal{P}^\phi\widetilde{\mathcal{H}}\mathcal{P}^\phi : \mathbb{V}_h^M \to \mathbb{V}^N$. Denoting the matrix corresponding to $\mathcal{H}^\phi$ expressed in $\{|q_i\rangle\}$ basis to be $\mathbf{H}^q$ and in $\{|\phi_\alpha\rangle\}$ basis to be $\mathbf{H}^\phi$, we derive the expressions for the corresponding matrix elements H^q_{ij} and $\mathrm{H}^\phi_{\alpha\beta}$ using equations (4.2) and (4.3) as follows:

$$\begin{aligned}
\mathrm{H}^q_{ij} &= \left\langle q_i \middle| \mathcal{H}^\phi \middle| q_j \right\rangle = \left\langle q_i \middle| \mathcal{P}^\phi\widetilde{\mathcal{H}}\mathcal{P}^\phi \middle| q_j \right\rangle \\
&= \sum_{\substack{\alpha,\beta=1 \\ \gamma,\delta=1}}^{N} \langle q_i|\, \phi_\alpha\rangle\, S^{-1}_{\alpha\beta} \left\langle \phi_\beta \middle| \widetilde{\mathcal{H}} \middle| \phi_\gamma \right\rangle S^{-1}_{\gamma\delta}\, \langle\phi_\delta|\, q_j\rangle \,.
\end{aligned} \tag{4.4}$$

Since $\mathcal{P}^q$ is idempotent ($\mathcal{P}^q\mathcal{P}^q = \mathcal{P}^q$), we note that $\widetilde{\mathcal{H}} = \mathcal{P}^q\widetilde{\mathcal{H}}\mathcal{P}^q$. Hence, equation (4.4) can be written as

$$\begin{aligned}
\mathrm{H}^{q}_{ij} &= \sum_{\substack{\alpha,\beta=1\\ \gamma,\delta=1}}^{N} \langle q_i|\, \phi_\alpha\rangle\, S^{-1}_{\alpha\beta} \left\langle \phi_\beta \right| \mathcal{P}^q \widetilde{\mathcal{H}} \mathcal{P}^q \left| \phi_\gamma \right\rangle S^{-1}_{\gamma\delta}\, \langle \phi_\delta|\, q_j\rangle \\
&= \sum_{\substack{\alpha,\beta=1\\ \gamma,\delta=1}}^{N} \sum_{k,\,l=1}^{M} \phi_{i\alpha}\, S^{-1}_{\alpha\beta}\, \phi^{*}_{k\beta}\, \widetilde{\mathrm{H}}_{kl}\, \phi_{l\gamma}\, S^{-1}_{\gamma\delta}\, \phi^{*}_{j\delta}\,, \qquad (4.5)
\end{aligned}$$

where $\phi_{i\alpha} = \langle q_i|\, \phi_\alpha\rangle$ and $\phi^{*}_{k\beta}$ denotes the complex conjugate of $\phi_{k\beta}$. The above equation can be conveniently recast in terms of matrices as:

$$\mathbf{H}^{q} = \mathbf{\Phi}\mathbf{\Phi}^{+}\widetilde{\mathbf{H}}\mathbf{\Phi}\mathbf{\Phi}^{+} \qquad (4.6)$$

where $\mathbf{\Phi}$ denotes a matrix whose column vectors are the components of $|\phi_\alpha\rangle$ in $|q_i\rangle$ basis, and $\mathbf{\Phi}^{+}$ denotes the Moore-Penrose pseudo-inverse of $\mathbf{\Phi}$ given by

$$\mathbf{\Phi}^{+} = \mathbf{S}^{-1}\mathbf{\Phi}^{\dagger} \qquad (4.7)$$

with $\mathbf{\Phi}^{\dagger}$ denoting the conjugate transpose of the matrix $\mathbf{\Phi}$. We now derive the expression for the matrix element corresponding to the operator $\mathcal{H}^{\phi}$ expressed in the non-orthonormal basis $\{|\phi_\alpha\rangle\}$:

$$\begin{aligned}
\mathrm{H}^{\phi}_{\alpha\beta} &= \sum_{\gamma=1}^{N} S^{-1}_{\alpha\gamma} \left\langle \phi_\gamma \right| \mathcal{H}^{\phi} \left| \phi_\beta \right\rangle = \sum_{\gamma=1}^{N} S^{-1}_{\alpha\gamma} \left\langle \phi_\gamma \right| \mathcal{P}^{\phi} \widetilde{\mathcal{H}} \mathcal{P}^{\phi} \left| \phi_\beta \right\rangle \\
&= \sum_{\gamma=1}^{N} S^{-1}_{\alpha\gamma} \left\langle \phi_\gamma \right| \widetilde{\mathcal{H}} \left| \phi_\beta \right\rangle = \sum_{\gamma=1}^{N} S^{-1}_{\alpha\gamma} \left\langle \phi_\gamma \right| \mathcal{P}^{q} \widetilde{\mathcal{H}} \mathcal{P}^{q} \left| \phi_\beta \right\rangle \\
&= \sum_{\gamma=1}^{N} \sum_{k,\,l=1}^{M} S^{-1}_{\alpha\gamma}\, \langle \phi_\gamma|\, q_k\rangle \left\langle q_k \right| \widetilde{\mathcal{H}} \left| q_l \right\rangle \langle q_l|\, \phi_\beta\rangle \\
&= \sum_{\gamma=1}^{N} \sum_{k,\,l=1}^{M} S^{-1}_{\alpha\gamma}\, \phi^{*}_{k\gamma}\, \widetilde{\mathrm{H}}_{kl}\, \phi_{l\beta}\,. \qquad (4.8)
\end{aligned}$$

Using matrices, the above equation (4.8) can be conveniently expressed as

$$\mathbf{H}^{\phi} = \mathbf{\Phi}^{+}\widetilde{\mathbf{H}}\mathbf{\Phi}\,. \tag{4.9}$$

We also note the following relation between $\mathbf{H}^{\phi}$ and $\mathbf{H}^{q}$ using equations (4.6) and (4.9):

$$\mathbf{H}^{q} = \mathbf{\Phi}\mathbf{H}^{\phi}\mathbf{\Phi}^{+}\,. \tag{4.10}$$

4.1.3 Density Matrix

We now consider the single particle density operator ($\mathit{\Gamma}$) corresponding to $\mathcal{H}^{\phi}$ given by

$$\begin{aligned}\mathit{\Gamma} &= \sum_{i=1}^{N} f(\epsilon_i^{\phi}) \left|\psi_i^{\phi}\right\rangle \left\langle\psi_i^{\phi}\right| \\ &= f(\mathcal{H}^{\phi})\,,\end{aligned} \tag{4.11}$$

where ϵ_i^{ϕ} and $\left|\psi_i^{\phi}\right\rangle$ denote the eigenvalues and the corresponding eigenvectors of $\mathcal{H}^{\phi}$, and we note that the relation $\mathit{\Gamma} = f(\mathcal{H}^{\phi})$ follows from the spectral decomposition of the Hermitian operator $\mathcal{H}^{\phi}$. Denoting the matrix representation of $\mathit{\Gamma}$ in $\{|q_i\rangle\}$ basis by $\mathbf{\Gamma}$, we have the following relation between the matrices $\mathbf{\Gamma}$ and $\mathbf{H}^{q}$ from equation (4.11):

$$\mathbf{\Gamma} = f(\mathbf{H}^{q})\,. \tag{4.12}$$

We now derive the expression for $\mathbf{\Gamma}$ in terms of the matrices $\mathbf{H}^{\phi}$ and $\mathbf{\Phi}$. To this end, we note that the function $f(\epsilon)$ represents the Fermi distribution (c.f equations (2.54) and (3.72)), which is an analytic function. Hence, this admits a power series representation given by

$$f(\mathbf{H}^{q}) = \sum_{k=0}^{\infty} a_k \left(\mathbf{H}^{q}\right)^{k}\,. \tag{4.13}$$

Using equation (4.6) and the relation $\mathbf{\Phi}^{+}\mathbf{\Phi} = \mathbf{I}_N$, where $\mathbf{I}_N$ denotes an identity matrix of dimension N, we have

$$\begin{aligned}
\mathbf{\Gamma} &= \sum_{k=0}^{\infty} a_k \left(\mathbf{H}^q\right)^k = \sum_{k=0}^{\infty} a_k \left(\mathbf{\Phi}\mathbf{\Phi}^{+}\widetilde{\mathbf{H}}\mathbf{\Phi}\mathbf{\Phi}^{+}\right)^k \\
&= \sum_{k=0}^{\infty} a_k \, \mathbf{\Phi}(\mathbf{\Phi}^{+}\widetilde{\mathbf{H}}\mathbf{\Phi})^k\mathbf{\Phi}^{+} = \mathbf{\Phi}\left(\sum_{k=0}^{\infty} a_k(\mathbf{H}^{\phi})^k\right)\mathbf{\Phi}^{+} \\
&= \mathbf{\Phi} f(\mathbf{H}^{\phi})\mathbf{\Phi}^{+} \,. \qquad (4.14)
\end{aligned}$$

We note that the electron density $\rho(\mathbf{r})$ is related to the diagonal of the density operator $\mathit{\Gamma}$ expressed in the real space, and is given by

$$\rho(\mathbf{r}) = 2 \, \langle \mathbf{r} | \, \mathit{\Gamma} \, | \mathbf{r} \rangle = 2 \sum_{i,j=1}^{M} \Gamma_{ij} \, q_i(\mathbf{r}) \, q_j(\mathbf{r}) \,, \qquad (4.15)$$

where Γ_{ij} denote the matrix elements of $\mathbf{\Gamma}$. We note that factor 2 in the above equation represents the case of a spin independent system, where each orbital is occupied by two electrons. We now derive an expression for the constraint on the total number of electrons i.e. $\int \rho(\mathbf{r}) \, d\mathbf{r} = N_e$. To this end, we have

$$\begin{aligned}
\int \rho(\mathbf{r}) \, d\mathbf{r} &= 2 \int \sum_{i,j=1}^{M} \Gamma_{ij} \, q_i(\mathbf{r}) \, q_j(\mathbf{r}) \, d\mathbf{r} = 2 \sum_{i=1}^{M} \Gamma_{ii} \,, \\
&= 2 \, \mathrm{tr} \left(\mathbf{\Gamma}\right) = 2 \, \mathrm{tr} \left(\mathbf{\Phi} f(\mathbf{H}^{\phi})\mathbf{\Phi}^{+}\right) \\
&= 2 \, \mathrm{tr} \left(f(\mathbf{H}^{\phi})\mathbf{\Phi}^{+}\mathbf{\Phi}\right) = 2 \, \mathrm{tr} \left(f(\mathbf{H}^{\phi})\right) \,. \qquad (4.16)
\end{aligned}$$

Hence, the constraint on the total number of electrons can be reformulated as

$$2 \, \mathrm{tr} \left(f(\mathbf{H}^{\phi})\right) = N_e \,. \qquad (4.17)$$

Finally, the band-energy (E_b), which is required in the calculation of the ground-state energy, is given by

$$\begin{aligned} E_b &= 2 \text{ tr } (\mathbf{\Gamma}\, \mathbf{H}^q) = 2 \text{ tr } \left(\mathbf{\Phi} f(\mathbf{H}^\phi) \mathbf{\Phi}^+ \mathbf{\Phi} \mathbf{H}^\phi \mathbf{\Phi}^+\right) \\ &= 2 \text{ tr } \left(\mathbf{\Phi} f(\mathbf{H}^\phi) \mathbf{H}^\phi \mathbf{\Phi}^+\right) = 2 \text{ tr } \left(\mathbf{\Phi}^+ \mathbf{\Phi} f(\mathbf{H}^\phi) \mathbf{H}^\phi\right) \\ &= 2 \text{ tr } \left(f(\mathbf{H}^\phi) \mathbf{H}^\phi\right) \ . \end{aligned} \tag{4.18}$$

4.2 Subspace-projection algorithm using finite-element basis

In this section, we recall the finite-element discretization of the Kohn Sham eigenvalue problem from Chapter III, and subsequently present the subspace projection algorithm used to reduce the computational complexity involved in the solution of the Kohn-Sham problem.

4.2.1 Eigenvalue problem in orthonormalized FE basis

If $\mathbb{V}_h^M$ represents the finite-dimensional subspace with dimension M and $N_j^h : 1 \leq j \leq M$ denotes the non-orthogonal finite-element basis spanning $\mathbb{V}_h^M$, we recall from previous chapter that the discretization of the Kohn-Sham eigenvalue problem (4.1a) results in a generalized eigenvalue problem given by:

$$\mathbf{H} \hat{\mathbf{\Psi}}_i = \epsilon_i^h \mathbf{M} \hat{\mathbf{\Psi}}_i \ , \tag{4.19}$$

where $\mathbf{H}$ denotes the discrete Hamiltonian matrix with matrix elements H_{jk}, $\mathbf{M}$ denotes the overlap matrix (or commonly referred to as the mass matrix in the finite-element literature) with matrix elements M_{jk}, and ϵ_i^h denotes the i^{th} eigenvalue corresponding to the discrete eigenvector $\hat{\mathbf{\Psi}}_i$ (see equations 3.31, 3.32, 3.33 and 3.35 in Chapter III for the relevant expressions). As discussed in the previous chapter it is convenient to transform the generalized eigenvalue problem in equation (4.19) to the

following standard eigenvalue problem:

$$\widetilde{\mathbf{H}}\widetilde{\boldsymbol{\Psi}}_i = \epsilon_i^h \widetilde{\boldsymbol{\Psi}}_i \tag{4.20}$$

where

$$\widetilde{\boldsymbol{\Psi}}_i = \mathbf{M}^{1/2}\hat{\boldsymbol{\Psi}}_i$$
$$\widetilde{\mathbf{H}} = \mathbf{M}^{-1/2}\mathbf{H}\mathbf{M}^{-1/2}\,.$$

We note that $\widetilde{\mathbf{H}}$ is a Hermitian matrix, and (3.36) represents a standard Hermitian eigenvalue problem. The actual eigenvectors are recovered by the transformation $\hat{\boldsymbol{\Psi}}_i = \mathbf{M}^{-1/2}\tilde{\boldsymbol{\Psi}}_i$. We remark that $\tilde{\boldsymbol{\Psi}}_i$ is a vector containing the expansion coefficients of the discretized eigenfunction $\psi_i^h(\mathbf{r})$ expressed in Löwdin orthonormalized finite-element basis $q_j(\mathbf{r}) : 1 \leq j \leq M$ spanning the finite-element space. We note the following relation between $q_j(\mathbf{r})$ and $N_j(\mathbf{r})$:

$$q_j(\mathbf{r}) = \sum_{k=1}^{M} \mathrm{M}_{jk}^{-1/2} N_k(\mathbf{r})\,. \tag{4.21}$$

Using a spectral finite-element basis in conjunction with Gauss-Lobatto-Legendre(GLL) quadratures for the evaluation of integrals in the mass-matrix, an efficient and a scalable approach using adaptive higher-order spectral finite-element discretization of the Kohn-Sham DFT problem has been proposed and discussed in Chapter III. In the latter approach, the self-consistent field (SCF) iteration consists of employing a Chebyshev filtering approach [66] to compute the occupied eigenspace of the spectral finite-element discretized Hamiltonian $\widetilde{\mathbf{H}}$. The computational complexity of the Chebyshev filtering scales as $\mathcal{O}(M\,N)$, where N denotes the number of eigenstates of interest. Upon computing the approximate eigenspace, the Chebyshev filtered vectors spanning the eigenspace are orthonormalized, and the projection of the Hamiltonian

into this orthonormal basis is computed. The computational complexity of this orthonormalization and projection scales as $\mathcal{O}(M\,N^2)$. Finally, the projected Hamiltonian is diagonalized to compute the eigenvalues and eigenvectors, which, in turn, are used in the computation of the electron density. The computational complexity of this step scales as $\mathcal{O}(N^3)$. Hence, the solution approach described in Chapter III, subsequently referred to as the Chebyshev filtered subspace iteration for the finite-element basis (ChFSI-FE), scales as $\mathcal{O}(N^3)$ asymptotically (as $M \propto N$), thus limiting accessible systems to a few thousand atoms. In order to address this significant limitation, we build on our prior work to develop a subspace projection technique that reduces the computational complexity of solving the Kohn-Sham problem. The proposed approach treats both insulating and metallic systems under a single framework, and is applicable for both pseudopotential and all-electron calculations. The key ideas involved in the method for a single self-consistent field (SCF) iteration are discussed below.

4.2.2 Chebyshev filtered subspace iteration

We recall from Chapter III that Chebyshev filtered subspace iteration (ChFSI) [122] belongs to the class of subspace iteration techniques that are generalizations of the power method applied to a subspace. As the ground-state electron density, and subsequently the ground-state energy, depends solely on the occupied eigenspace—the vector space spanned by the eigenfunctions corresponding to the occupied states—the ChFSI technique exploits the fast growth property of Chebyshev polynomial in $(-\infty, -1)$ to magnify the relevant spectrum and thereby providing an efficient approach for the solution of the Kohn-Sham eigenvalue problem. We refer to [66] and [1](c.f Chapter III) for the application of this technique to electronic structure calculations in the context of finite-difference and finite-element discretizations, respectively. We also refer to [36] for a linear-scaling subspace iteration technique based

on Chebyshev filtering for insulating systems. In the present work, we also adopt the Chebyshev filtering procedure to find the occupied eigenspace at any given SCF iteration. We start with an initial subspace $\overline{\mathbb{V}}^N$ of dimension N ($N > N_e/2$) spanned by the set of localized wavefunctions $\{\psi_1(\mathbf{r}), \psi_2(\mathbf{r}), \cdots, \psi_N(\mathbf{r})\}$ obtained from the previous SCF iteration (cf. section 4.2.3 for details on the construction of the localized wavefunctions). We note that, here, and subsequently, all the electronic fields (wavefunctions and electron density) denote finite-element discretized fields, and we have dropped the superscript h for notational simplicity. We denote by $\mathbf{X}$ the matrix whose column vectors are the coefficients of expansion of these localized wavefunctions in the Löwdin orthonormalized spectral finite-element basis ($q_j : 1 \leq j \leq M$). The Chebyshev filtered subspace iteration then proceeds as follows:

Construction of shifted and scaled Hamiltonian: The discretized Hamiltonian $\widetilde{\mathbf{H}}$ is scaled and shifted to construct $\bar{\mathbf{H}}$ such that the unwanted (unoccupied) spectrum of $\widetilde{\mathbf{H}}$ is mapped to $[-1, 1]$ and the wanted (occupied) spectrum into $(-\infty, -1)$. Hence

$$\bar{\mathbf{H}} = \frac{1}{e}(\widetilde{\mathbf{H}} - c\mathbf{I}) \text{ where } e = \frac{b-a}{2} \quad c = \frac{a+b}{2}\,. \tag{4.22}$$

Here a and b denote the upper bound of the wanted and unwanted spectrum of $\widetilde{\mathbf{H}}$, respectively. The upper bound b is obtained inexpensively using a small number of Lanczos iterations [123] whose computational complexity scales as $\mathcal{O}(M)$. The upper bound of the wanted spectrum is chosen as the largest Rayleigh quotient of $\widetilde{\mathbf{H}}$ in the occupied eigenspace computed in the previous SCF iteration.

Construction of Chebyshev filter: In a given SCF iteration, the action of a Chebyshev filter on $\mathbf{X}$ is given by

$$\mathbf{Y} = T_m(\bar{\mathbf{H}})\mathbf{X}\,, \tag{4.23}$$

where $\mathbf{Y}$ denotes the matrix whose column vectors are the coefficients of expansion of the Chebyshev filtered wavefunctions $\{\psi_1^f(\mathbf{r}), \psi_2^f(\mathbf{r}), \cdots, \psi_N^f(\mathbf{r})\}$ expressed in the Löwdin orthonormalized finite-element basis. We note that the subspace $\mathbb{V}^N$ spanned by these Chebyshev filtered wavefunctions is a close approximation to the occupied eigenspace. In the above, the filter $T_m(\bar{\mathbf{H}})$ is constructed using a Chebyshev polynomial $T_m(x)$ of degree m, and the action of the filter on $\mathbf{X}$ can be recursively computed [124] as

$$T_m(\bar{\mathbf{H}})\mathbf{X} = \left[2\bar{\mathbf{H}}\, T_{m-1}(\bar{\mathbf{H}}) - T_{m-2}(\bar{\mathbf{H}})\right] \mathbf{X}\,, \tag{4.24}$$

with $T_0(\bar{\mathbf{H}})\mathbf{X} = \mathbf{X}$ and $T_1(\bar{\mathbf{H}})\mathbf{X} = \bar{\mathbf{H}}\mathbf{X}$. It is evident from equation (4.24) that the application of Chebyshev filter on $\mathbf{X}$ involves matrix-vector multiplications between the discretized Hamiltonian $\widetilde{\mathbf{H}}$ and the vectors obtained during the course of recursive iteration (4.24). Further, we note that the finite-element basis functions $N_j : 1 \leq j \leq M$ are local. Hence, the discretized Hamiltonian $\widetilde{\mathbf{H}}$ expressed in the Löwdin orthonormalized spectral finite-element basis $q_j : 1 \leq j \leq M$ is sparse, and has the exact same sparsity as $\mathbf{H}$ if the matrix $\mathbf{M}$ is evaluated using the GLL quadrature. Thus, if the vectors obtained during the process of recursive iteration of Chebyshev filtering procedure are sparse, the computational complexity of the relevant matrix-vector multiplications scales as $\mathcal{O}(M)$.

In practice, we exploit the locality of finite-element basis to construct the elemental-matrices corresponding to $\mathbf{H}^{\text{loc}}$ (c.f equation (3.32)), i.e. the individual contributions from each finite-element to $\mathbf{H}^{\text{loc}}$, without explicitly assembling the global matrix. We note that building these elemental-matrices scales as $\mathcal{O}(M)$. In the case of pseudopotential calculations, we compute $C^J_{lm,j}$(c.f equation (3.33)) at the finite-element level only for those elements in the compact support of ΔV_l^J. Further, the vectors obtained during the course of the recursive iteration (4.24) are truncated using a truncation tol-

erance δ_c, below which the values are set to zero. The matrix-vector multiplications in the Chebyshev filtering procedure are performed at the finite-element level only if the vector has a non-zero value in the finite-element considered. This leads to the computation of only the non-trivial elemental matrix-vector products, thereby rendering the computational complexity of the Chebyshev filtering procedure to $\mathcal{O}(M)$. The resulting element-level vectors are then assembled to form the global vectors $\mathbf{Y}$. We choose δ_c to be in the range of 10^{-4} to 10^{-14} in our subsequent numerical simulations (cf. section 4.3) with looser tolerances being employed in the intial SCF iterations, where the solution is far away from the ground-state solution, and, adaptively employing tighter tolerances in later iterations as the SCF approaches convergence.

4.2.3 Localization and truncation

Various procedures have been employed in the literature to achieve linear-scaling (cf. [33, 32] for a comprehensive review) for pseudopotential calculations, and the use of localized functions spanning the occupied eigenspace (or an approximation to this space) has been one of the ideas exploited in developing linear-scaling algorithms for materials systems with a band-gap. In this regard, we remark that Wannier functions [125, 126, 127, 128] have played an important role. In particular, the maximally localized Wannier functions [129] have been effectively used as an orthogonal localized basis for Kohn-Sham DFT calculations, specifically in periodic systems. However, techniques employing non-orthogonal localized functions have also been proposed [130, 113, 114, 131], which have better localization properties than orthogonal functions. A discussion on general localization properties of bases spanning the eigenspace is provided in [132] and [133]. In the present work, we adopt the technique proposed in [36] to construct a localized basis for the subspace $\mathbb{V}^N$ spanned by Chebyshev filtered wavefunctions $\{\psi_1^f(\mathbf{r}), \psi_2^f(\mathbf{r}), \cdots, \psi_N^f(\mathbf{r})\}$. Here, the localized

basis is obtained as

$$\arg \min_{\psi \in \mathbb{V}^N, ||\psi||=1} \int w(\mathbf{r}) |\psi(\mathbf{r})|^2 \, d\mathbf{r} \,, \tag{4.25}$$

where $w(\mathbf{r}) \geq 0$ is chosen to be a smooth weighting function $|\mathbf{r} - \boldsymbol{b}_I|^{2p}$, with p being a positive integer and $\boldsymbol{b}_I$ denoting a localization center. Such a choice of $w(\mathbf{r})$ minimizes the spread of the wavefunctions from a localization center, similar in spirit to the construction of maximally localized Wannier functions [129]. In the present work, we choose p to be 1 and $\boldsymbol{b}_I$ to be an atom center $\mathbf{R}_I$. Let n_I denote the number of localized functions we desire to compute at every atom center $\mathbf{R}_I$. Also, letting

$$\psi(\mathbf{r}) = \sum_i \alpha_i \psi_i^f(\mathbf{r}) \quad \in \quad \mathbb{V}^N \,, \tag{4.26}$$

the minimization problem (4.25) is equivalent to solving the following generalized eigenvalue problem for the smallest n_I eigenvalues

$$\mathbf{W}^I \boldsymbol{\alpha} = \lambda \mathbf{S} \boldsymbol{\alpha} \,, \tag{4.27}$$

where

$$\mathrm{W}_{ij}^I = \int |\mathbf{r} - \mathbf{R}_I|^2 \, \psi_i^f(\mathbf{r}) \, \psi_j^f(\mathbf{r}) \, d\mathbf{r} \quad i, j = 1 \cdots N \tag{4.28a}$$

$$\mathrm{S}_{ij} = \int \psi_i^f(\mathbf{r}) \, \psi_j^f(\mathbf{r}) \, d\mathbf{r} \,. \tag{4.28b}$$

In the present work, we choose n_I to be equal to the number of occupied single-atom orbitals corresponding to the I^{th} atom. If $\sum_I n_I < N$, then we randomly pick some atoms to compute additional localized functions. We note that we can rewrite $\mathbf{W}^I$ in (4.28a) using matrix notation to be

$$\mathbf{W}^I = \mathbf{L}^T \mathbf{K}^I \mathbf{L} \,, \tag{4.29}$$

where columns of the matrix $\mathbf{L}$ correspond to the nodal values of the wavefunctions $\{\psi_1^f(\mathbf{r}), \psi_2^f(\mathbf{r}), \cdots, \psi_N^f(\mathbf{r})\}$ obtained after Chebyshev filtering, and

$$\mathrm{K}_{ij}^I = \int |\mathbf{r} - \mathbf{R}_I|^2 \, N_i(\mathbf{r}) N_j(\mathbf{r}) \, d\mathbf{r} \,. \tag{4.30}$$

We note that the computational complexity of computing the matrix $\mathbf{W}^I$ for an atom I scales as $\mathcal{O}(MN^2)$ as the wavefunctions $\{\psi_1^f, \psi_2^f, \cdots, \psi_N^f\}$ obtained after Chebyshev filtering need not be sparse. Hence the total computational complexity for N_a atoms ($N_a \propto N$) in a given materials system scales as $\mathcal{O}(MN^3)$. We propose the following procedure in order to reduce the computational complexity to $\mathcal{O}(M)$. We first expand $\mathbf{K}^I$ in terms of atom $I = 0$ as follows:

$$\begin{aligned}
\mathrm{K}_{ij}^I &= \int |\mathbf{r} - \mathbf{R}_0 + \mathbf{R}_0 - \mathbf{R}_I|^2 \, N_i(\mathbf{r}) N_j(\mathbf{r}) \, d\mathbf{r} \\
&= \int \Big[|\mathbf{r} - \mathbf{R}_0|^2 \, N_i(\mathbf{r}) N_j(\mathbf{r}) + |\mathbf{R}_0 - \mathbf{R}_I|^2 \, N_i(\mathbf{r}) N_j(\mathbf{r}) \\
&\quad + 2 \, (\mathbf{r} - \mathbf{R}_0) \, . \, (\mathbf{R}_0 - \mathbf{R}_I) \, N_i(\mathbf{r}) N_j(\mathbf{r}) \Big] \, d\mathbf{r} \\
&= \mathrm{K}_{ij}^0 + |\mathbf{R}_0 - \mathbf{R}_I|^2 \, \mathrm{M}_{ij} + 2 \, (R_{0x} - R_{Ix}) \mathrm{B}_{ij}^x \\
&\quad + 2 \, (R_{0y} - R_{Iy}) \mathrm{B}_{ij}^y + 2 \, (R_{0z} - R_{Iz}) \mathrm{B}_{ij}^z
\end{aligned}$$

where

$$\mathrm{K}_{ij}^0 = \int |\mathbf{r} - \mathbf{R}_0|^2 \, N_i(\mathbf{r}) N_j(\mathbf{r}) \, d\mathbf{r} \,, \tag{4.31a}$$

$$\mathrm{M}_{ij} = \int N_i(\mathbf{r}) N_j(\mathbf{r}) \, d\mathbf{r} \,, \tag{4.31b}$$

$$\mathrm{B}_{ij}^x = \int (x - R_{0x}) \, N_i(\mathbf{r}) N_j(\mathbf{r}) \, d\mathbf{r} \,, \tag{4.31c}$$

$$\mathrm{B}_{ij}^y = \int (y - R_{0y}) \, N_i(\mathbf{r}) N_j(\mathbf{r}) \, d\mathbf{r} \,, \tag{4.31d}$$

$$\mathrm{B}_{ij}^z = \int (z - R_{0z}) \, N_i(\mathbf{r}) N_j(\mathbf{r}) \, d\mathbf{r} \,. \tag{4.31e}$$

We use Gauss-Lobatto-Legendre quadrature rules to evaluate each of the above integrals which renders the matrices in (4.31) diagonal. Further, the matrix $\mathbf{W}^I$ for any atom I is constructed as a linear combination of five matrices, and is given by

$$\begin{aligned}\mathbf{W}^I = \mathbf{L}^T\mathbf{K}^0\mathbf{L} + |\mathbf{R}_0 - \mathbf{R}_I|^2\mathbf{L}^T\mathbf{M}\mathbf{L} + \\ 2\,(R_{0x} - R_{Ix})\mathbf{L}^T\mathbf{B}^x\mathbf{L} + 2\,(R_{0y} - R_{Iy})\mathbf{L}^T\mathbf{B}^y\mathbf{L} + \\ 2\,(R_{0z} - R_{Iz})\mathbf{L}^T\mathbf{B}^z\mathbf{L}\,. \end{aligned} \tag{4.32}$$

We note that the five matrices $\mathbf{L}^T\mathbf{K}^0\mathbf{L}$, $\mathbf{L}^T\mathbf{M}\mathbf{L}$, $\mathbf{L}^T\mathbf{B}^x\mathbf{L}$, $\mathbf{L}^T\mathbf{B}^y\mathbf{L}$ and $\mathbf{L}^T\mathbf{B}^z\mathbf{L}$ are independent of I, and can be computed *a priori*. Further, in order to reduce the computational complexity of computing these five matrices, we introduce a truncation tolerance $\delta_w > \delta_c$ ($\delta_w \sim 10^{-4} - 10^{-8}$) to truncate the Chebyshev filtered wavefunctions used in the construction of matrices $\mathbf{L}$ and $\mathbf{S}$. We note that this truncation in the Chebyshev filtered wavefunctions is introduced only in the construction of $\mathbf{L}$ and $\mathbf{S}$, and not in other operations involving the Chebyshev filtered wavefunctions, in particular, the linear combination in (4.26). Introducing the truncation δ_w renders a sparse structure to both $\mathbf{L}$ and $\mathbf{S}$, and thus the computation of $\mathbf{W}^I$ for all the atoms $I = 1 \cdots N_a$ scales as $\mathcal{O}(M)$. We note that the use of GLL quadrature rules in the evaluation of matrix elements in (4.31), as well as, the use of truncation tolerance δ_w in the construction of $\mathbf{L}$ and $\mathbf{S}$ introduces approximation errors in the solution of the eigenvectors $\boldsymbol{\alpha}$ in the generalized eigenvalue problem (4.27). However, we note that these approximations errors do not alter the space $\mathbb{V}^N$ spanned by the localized wavefunctions (cf. equation (4.26)), as the vector space remains invariant under any linear combination.

Using the eigenvectors $\boldsymbol{\alpha}$ from the solution of the eigenvalue problem in (4.27) for each atom I, and the linear combination in (4.26), the non-orthogonal localized wavefunctions are computed and are denoted by $\{\phi_1^L(\mathbf{r}), \phi_2^L(\mathbf{r}), \cdots, \phi_N^L(\mathbf{r})\}$ which span $\mathbb{V}^N$.

In order to provide a compact support for these non-orthogonal localized wavefunctions, we introduce a truncation tolerance δ_l, where the nodal values of these functions that are below this tolerance are set to zero. We note that, upon truncating these wavefunctions, the space spanned by these functions is only an approximation to $\mathbb{V}^N$, where the approximation error in the subspace depends on the choice of δ_l. As in the case of δ_c, the truncation tolerance introduced during the Chebyshev filtering, δ_l is also chosen adaptively with looser tolerances in the initial SCF iterations and progressively employing tighter tolerances as the SCF approaches convergence (see section 4.3 for details). We denote by $\mathbf{\Phi}_L$ the matrix whose column vectors are the expansion coefficients of these compactly-supported non-orthogonal localized wavefunctions expressed in the Löwdin orthonormalized finite-element basis. We note that the locality of the non-orthogonal wavefunctions $\phi_i^L(\mathbf{r}) : 1 \leq i \leq N$ renders sparsity to the matrix $\mathbf{\Phi}_L$.

4.2.4 Subspace projection in the non-orthogonal basis

We now discuss the steps involved in the subspace projection of the Hamiltonian into the non-orthogonal localized basis represented by $\mathbf{\Phi}_L$.

Computation of overlap matrix: The overlap matrix $\mathbf{S}$ resulting from the non-orthogonal localized wavefunctions is given by

$$\mathbf{S} = \mathbf{\Phi}_L^T \mathbf{\Phi}_L \,. \tag{4.33}$$

We note that the computational complexity of evaluating $\mathbf{S}$ scales as $\mathcal{O}(N)$ if $\mathbf{\Phi}_L$ is a sparse matrix.

Computation of projected Hamiltonian: We recall from the discussion in section 4.1 that the projection of the Hamiltonian into a non-orthogonal localized basis

is given by

$$\mathbf{H}^{\phi} = \mathbf{S}^{-1}\mathbf{\Phi}_L^T\widetilde{\mathbf{H}}\mathbf{\Phi}_L\,. \tag{4.34}$$

The above equation involves the inverse of the overlap matrix $\mathbf{S}^{-1}$, which can be evaluated using scaled third-order Newton-Schulz iteration [134, 36]. If $\mathbf{S}$ and $\mathbf{S}^{-1}$are exponentially localized, $\mathbf{S}^{-1}$ can be computed in $\mathcal{O}(N)$ complexity [135]. Since the discretized Hamiltonian $\widetilde{\mathbf{H}}$ is sparse, and if the matrix $\mathbf{\Phi}_L$ is sparse with a bandwidth independent of N, $\mathbf{H}^{\phi}$ can be computed in $\mathcal{O}(N)$ complexity.

4.2.5 Electron density computation

The Fermi-operator expansion techniques [32, 33] have been widely adopted to avoid explicit diagonalization of the discretized Hamiltonian in order to compute the electron density. One of the widely used Fermi-operator expansion technique [107, 108], which works for both insulating as well as metallic systems, approximates the Fermi distribution (cf. equation (2.54)) by means of a Chebyshev polynomial expansion. The accuracy of such an expansion depends on the smearing parameter in the Fermi distribution, σ, and the width of the eigenspectrum (spectral width) of discretized Hamiltonian denoted by ΔE. In particular, the degree of polynomial required to achieve a desired accuracy in the approximation [35] of the Fermi distribution is $\mathcal{O}(\frac{\Delta E}{\sigma})$, and is $\mathcal{O}(\sqrt{\Delta E})$ for a given σ and the occupied spectrum [136]. We also note that numerous recent efforts have focused on developing alternate approximations to the Fermi distribution [116, 117, 119, 118, 120] with reduced computational complexity.

One of the major challenges in employing the Fermi-operator expansion technique on a finite-element discretized Hamiltonian is the large spectral width of the Hamiltonian—$\mathcal{O}(10^3)$ Ha for pseudopotential calculations and $\mathcal{O}(10^5)$ Ha for all-electron calculations [1]—that deteriorates the accuracy of the Fermi-operator expansion. To circumvent this, we employ the Fermi-operator expansion in terms of

the subspace projected Hamiltonian $\mathbf{H}^{\phi}$ whose spectral width is commensurate with that of the occupied eigenspectrum. We recall from equation (4.15) that the electron density in terms of the density matrix is given by

$$\rho(\mathbf{r}) = 2 \sum_{i,j=1}^{M} \Gamma_{ij} q_i(\mathbf{r}) q_j(\mathbf{r}) \,. \tag{4.35}$$

Using equations (4.21) and (4.14) in the above equation, we have

$$\begin{aligned} \rho(\mathbf{r}) &= 2 \, \boldsymbol{N}^T(\mathbf{r}) \, \mathbf{M}^{-1/2} \, \boldsymbol{\Phi}_L \, f(\mathbf{H}^{\phi}) \, \boldsymbol{\Phi}_L^{+} \, \mathbf{M}^{-1/2} \boldsymbol{N}(\mathbf{r}) \\ &= 2 \, \boldsymbol{N}^T(\mathbf{r}) \, \mathbf{M}^{-1/2} \, \boldsymbol{\Phi}_L \, f(\mathbf{H}^{\phi}) \, \mathbf{S}^{-1} \, \boldsymbol{\Phi}_L^{T} \mathbf{M}^{-1/2} \boldsymbol{N}(\mathbf{r}) \,, \end{aligned} \tag{4.36}$$

where $\boldsymbol{N}^T(\mathbf{r}) = [N_1(\mathbf{r}) \,, N_2(\mathbf{r}) \,, N_3(\mathbf{r}), \, \cdots \,, N_M(\mathbf{r})]$ and

$$f(\mathbf{H}^{\phi}) = \frac{1}{1 + \exp\left(\frac{\mathbf{H}^{\phi} - \mu \mathbf{I}}{\sigma}\right)} \tag{4.37}$$

with μ being the chemical potential and $\sigma = k_B \, T$. We note that as the self-consistent field iteration converges, $f(\mathbf{H}^{\phi})$ represents the finite-temperature density matrix expressed in the non-orthogonal localized basis. We remark that, for a jellium approximation (a simplified representation for a metallic system), it was shown that the finite-temperature density operator exhibits an exponential decay in real-space [137, 138]. However, this remains an open question beyond the jellium approximation for metallic systems. For an insulating system with a band-gap, the density operator, even at zero temperature, has an exponential decay in real-space [32]. Assuming that the density operator decays in real-space, and recalling that $\boldsymbol{\Phi}_L$ represents a localized basis, we note that $f(\mathbf{H}^{\phi})$ will have a sparse structure with the extent of sparsity depending on the decay properties of the density operator.

We use Chebyshev polynomial expansion to approximate $f(\mathbf{H}^{\phi})$, and compute the electron density. To this end, we begin by scaling and shifting $\mathbf{H}^{\phi}$ to obtain $\mathbf{H}_s^{\phi}$

such that its spectrum lies in $[-1, 1]$ and then $f(\mathbf{H}^{\phi})$ is approximated using a finite number of Chebyshev polynomials [35] as

$$f(\mathbf{H}^{\phi}) = \sum_{n=0}^{R} a_n(\sigma_s, \mu_s) T_n(\mathbf{H}_s^{\phi}), \tag{4.38}$$

where

$$\mathbf{H}_s^{\phi} = \frac{\mathbf{H}^{\phi} - \bar{\epsilon}\mathbf{I}}{\Delta\epsilon} \quad ; \quad \sigma_s = \frac{\Delta\epsilon}{\sigma} \quad ; \quad \mu_s = \frac{\mu - \bar{\epsilon}}{\Delta\epsilon}, \tag{4.39}$$

$$\Delta\epsilon = \frac{\epsilon_{\max} - \epsilon_{\min}}{2} \quad ; \quad \bar{\epsilon} = \frac{\epsilon_{\max} + \epsilon_{\min}}{2}, \tag{4.40}$$

and

$$a_n(\sigma_s, \mu_s) = \frac{2 - \delta_{n\,0}}{\pi} \int_{-1}^{1} \frac{T_n(x)}{\sqrt{1 - x^2}} \frac{1}{1 + e^{\sigma_s(x - \mu_s)}} dx \,, \tag{4.41}$$

where δ_{ij} denotes the Kronecker delta. In the above, $\epsilon_{\max}$ and $\epsilon_{\min}$ denote the upper and lower bounds for the spectrum of $\mathbf{H}^{\phi}$. Estimates for $\epsilon_{\max}$ and $\epsilon_{\min}$ are computed using the Krylov-Schur method [85]. As $\mathbf{H}^{\phi}$ is the projection of the Hamiltonian into a localized basis, $\mathbf{H}^{\phi}$ is a sparse matrix, and these estimates for the spectral width can be computed in $\mathcal{O}(N)$ complexity. We also remark that if $\mathbf{H}^{\phi}$ is sufficiently sparse, $f(\mathbf{H}^{\phi})$ can be computed in $\mathcal{O}(N)$ complexity [35]. Further, we note that the degree R of the Chebyshev expansion in equation (4.38) is proportional to the spectral width $\Delta E = \epsilon_{\max} - \epsilon_{\min}$ of $\mathbf{H}^{\phi}$. As discussed earlier, since $\mathbf{H}^{\phi}$ is the projected Hamiltonian in the space containing the occupied eigenstates and only a few unoccupied eigenstates, the spectral width of $\mathbf{H}^{\phi}$ is $\mathcal{O}(1)$ Ha for pseudopotential calculations and $\mathcal{O}(10)$ Ha for all-electron calculations for low atomic numbers. Thus, the Fermi-operator expansion can be computed efficiently and accurately using a Chebyshev polynomial expansion of $\mathcal{O}(100)$ for pseudopotential calculations and $\mathcal{O}(1000)$ for all-electron calculations for moderate temperatures ($\sim 500K$) used in the smearing parameter. The Fermi-energy (μ), which is required in the computation of the Fermi-operator expansion for

$f(\mathbf{H}^{\phi})$ and the electron density, is evaluated using the constraint in (4.17)

$$2 \text{ tr} \left(f(\mathbf{H}^{\phi}) \right) = N_e \,, \tag{4.42}$$

where N_e is the number of electrons in the given system. The above equation is solved using the Newton-Raphson method [139] and an initial guess to the Newton-Raphson method is computed using the bisection algorithm [139]. It is evident from equation (4.38) that the dependence of the expansion on the Fermi-energy is only in the coefficients of the expansion. Exploiting this fact, the Fermi-energy can be efficiently computed using methods described in Baer et. al. [35], which scales as $\mathcal{O}(N)$. To this end, the m^{th} column of $f(\mathbf{H}^{\phi})$ is obtained by the application of the expansion in (4.38) on a unit column vector $\boldsymbol{v}^m$ containing all zeros except at the m^{th} position. Hence,

$$\left[f(\mathbf{H}^{\phi}) \right]_m = \sum_{n=0}^{R} a_n(\sigma_s, \mu_s) \boldsymbol{v}_n^m, \tag{4.43}$$

where $\boldsymbol{v}_n^m = T_n(\mathbf{H}_s^{\phi}) \boldsymbol{v}^m$ denotes the m^{th} column of $T_n(\mathbf{H}_s^{\phi})$. We note that $\boldsymbol{v}_n^m$ can be computed efficiently using the Chebyshev polynomial recursion given by

$$\begin{aligned} \boldsymbol{v}_0^m &= \boldsymbol{v}^m \\ \boldsymbol{v}_1^m &= \mathbf{H}^{\phi} \boldsymbol{v}^m \\ \boldsymbol{v}_{n+1}^m &= 2\, \mathbf{H}^{\phi} \boldsymbol{v}_n^m - \boldsymbol{v}_{n-1}^m \,. \end{aligned}$$

As the vectors $\boldsymbol{v}_n^m$ can be precomputed and stored, the evaluation of $\text{tr} \left(f(\mathbf{H}^{\phi}) \right)$ for every trial Fermi-energy results in a trivial computational cost.

Upon evaluating the Fermi energy, the band energy (E_b) can also be expressed in terms of $\mathbf{H}^{\phi}$ as

$$E_b = 2 \text{ tr} \left(f(\mathbf{H}^{\phi}) \mathbf{H}^{\phi} \right) \,. \tag{4.44}$$

Finally, we note that the computational complexity of computing the electron density at a quadrature point $\mathbf{r}$ is independent of the system size. This can be seen by rewriting the expression (4.36) as

$$\rho(\mathbf{r}) = 2\, \boldsymbol{c}^T(\mathbf{r})\, f(\mathbf{H}^{\phi})\, \mathbf{S}^{-1}\, \boldsymbol{c}(\mathbf{r})\,, \tag{4.45}$$

where $\boldsymbol{c}(\mathbf{r}) = \boldsymbol{\Phi}_L^T \mathbf{M}^{-1/2} \boldsymbol{N}(\mathbf{r})$ is a sparse vector if $\boldsymbol{\Phi}_L$ is sparse. As $f(\mathbf{H}^{\phi})\mathbf{S}^{-1}$ can be pre-computed *a priori*, the computation of $\rho(\mathbf{r})$ is independent of the system size. Since the total number of quadrature points scales linearly with system size, computation of electron density for a given material system is $\mathcal{O}(M)$ complexity.

4.3 Results and discussion

In this section, we investigate the accuracy, performance, and scaling of the proposed subspace projection technique. As benchmark systems, we consider non-periodic three dimensional systems involving metallic, insulating and semi-conducting materials systems. The benchmark metallic systems chosen for this study include aluminum nano-clusters of varying sizes, containing $3\times3\times3$ (172 atoms), $5\times5\times5$ (666 atoms), $7\times7\times7$ (1688 atoms) and $9\times9\times9$ (3430 atoms) face-centered-cubic (fcc) unit-cells. The benchmark insulating systems chosen for this study include alkane chains of varying lengths, containing 101, 302, 902, 2702 and 7058 atoms. Silicon nano-clusters containing $1\times1\times1$ (252 electrons), $2\times1\times1$ (434 electrons), $2\times2\times1$ (756 electrons), $2\times2\times2$ (1330 electrons) and $3\times3\times3$ (3920 electrons) diamond-cubic (dia) unit-cells are chosen for the benchmark semi-conducting materials systems. Norm-conserving Troullier-Martins pseudopotentials [77] have been employed in the case of aluminum nano-clusters and alkane chains, whereas all-electron calculations have been performed in the case of silicon nano-clusters. In all our simulations, we use the n-stage Anderson [67] mixing scheme on the electron density in self-consistent field it-

eration of the Kohn-Sham problem. Further, all the numerical simulations reported in this section are conducted using a parallel implementation of the code based on MPI, and are executed on a parallel computing cluster with the following specifications: dual-socket eight-core Intel Core Sandybridge CPU nodes with 16 processors (cores) per node, 64 GB memory per node, and 40 Gbps Infiniband networking between all nodes for fast MPI communications.

As discussed in section 4.2, the linear-scaling of the proposed subspace projection technique relies on the locality of the finite-element basis ($q_i : 1 \leq i \leq M$) as well as the localized wavefunctions ($\phi_j^L : 1 \leq j \leq N$), and subsequently, the sparsity of the various matrices involved in our formulation ($\widetilde{\mathbf{H}}, \mathbf{H}^{\phi}, \mathbf{\Phi}_L, \mathbf{S}, \mathbf{W}^I$). We recall that the compact support of localized wavefunctions and the sparsity in various matrices is achieved by introducing truncation tolerances δ_c (in Chebyshev filtering) and δ_l (for localized wavefunctions). Further, as mentioned in section 4.2 , and elaborated subsequently, the truncation tolerances are chosen adaptively with looser tolerances being employed in the initial SCF iterations and progressively tightening these during the course of the SCF convergence. As demonstrated in our benchmark studies, such an adaptive tolerance provides significant computational efficiency while retaining the accuracy of the solution to the Kohn-Sham DFT problem. We note that the sparsity of various matrices is governed by the eigenspectrum of discrete Hamiltonian as well as the values of the truncation tolerances employed, which changes with each SCF iteration. In the present implementation of the subspace projection technique, we employ efficient parallel data-structures provided by PETSc package [83], where necessary, to represent various matrices and perform arithmetic operations between them. We observe in our simulations that the operations involving sparse data-structures provided by PETSc are efficient only when the fraction of non-zero entries (density fraction) in the matrix is $< 1 - 2\%$. Beyond this density-fraction, the overhead cost of using a sparse data-structure is prohibitively expensive, and it is more efficient to

use dense data-structures. To maximize the computational efficiency, in the present work, we employ sparse data-structures only when the density fraction is $< 2\%$, beyond which we switch to dense data-structures. This is the main source of deviation from linear-scaling, in practice, in the present implementation.

In order to assess the accuracy, performance and scaling of the proposed approach, we use as reference the recently developed Chebyshev filtered subspace iteration for the finite-element basis [1] (ChFSI-FE). The ChFSI-FE involves the projection of the Hamiltonian into an orthogonal basis spanning the Chebyshev filtered space, and an explicit computation of the eigenvalues and eigenvectors of the projected Hamiltonian to estimate the electron density. It was demonstrated [1] that ChFSI-FE technique with the use of higher-order finite-element discretization presents a computationally efficient real-space approach for Kohn-Sham DFT calculations, which can handle both pseudopotential and all-electron calculations. We also note that the accuracy of ChFSI-FE was ascertained, on benchmark problems of varying sizes, using ABINIT software [60] for pseudopotential calculations and GAUSSIAN software [72] for all-electron calculations. In the present work, we use ChFSI-FE as our reference to assess the accuracy and performance of the proposed approach.

4.3.1 Aluminum nano-clusters: Pseudopotential study

We consider aluminum nano-clusters formed from fcc unit cells with lattice spacing of 7.45 $a.u.$. The norm-conserving Troullier-Martins pseudopotential in the Kleinman-Bylander form [77, 78] is employed in these simulations. We consider the $3s$ and $3p$ components to compute the projector, while the $3d$ component is chosen to be the local component of the pseudopotential. The pseudopotentials are generated using the fhi98pp [140] software and the default cut-off radii are used for $3s$, $3p$ and $3d$ components, which are 1.8 $a.u.$, 2.0 $a.u.$ and 2.15 $a.u.$, respectively. In order to choose finite-element meshes which provide a discretization error of less than 5 meV

per atom for the various nano-clusters considered in the present study, we first obtain the converged ground-state energy for the aluminum cluster containing $3 \times 3 \times 3$ fcc unit cells which comprises of 172 atoms with 516 electrons. To this end, we use a sequence of increasingly refined fourth-order spectral finite-element (HEX125SPECT) meshes on a cubic simulation domain of side 400 *a.u.* employing Dirichlet boundary conditions. Here, and subsequently, we use the *a priori* mesh adaption techniques developed in Motamarri et. al [1] to construct the finite-element meshes, and refer to this prior work for details. For these sequence of meshes, the ground-state energy is computed using ChFSI-FE with a Chebyshev filter of degree 20 and employing a Fermi smearing parameter of 0.00158 Ha (T=500K). The computed discrete ground-state energies (E_h) for these meshes are tabulated in Table 4.1, where h denotes a measure of the finite-element mesh-size. The extrapolation procedure proposed in Motamarri et. al [1] allows us to estimate the ground-state energy in the limit as $h \to 0$, denoted by E_0. Using this extrapolation procedure, we computed the ground-state energy per atom to be $E_0 = -56.6966935\ eV$. In order to ascertain the accuracy of this extrapolated ground-state energy, we conducted a plane wave simulation with ABINIT using a cell-size of 80 *a.u.* and an energy cut-off of 30 Ha with one k-point (the most refined calculation possible within our memory limitations). In the case of ABINIT, the ground-state energy per atom was found to be $-56.6966719\ eV$, which only differs from E_0 by 0.02 meV.

Table 4.1: Convergence of the finite-element discretization (HEX125SPECT element) for a $3 \times 3 \times 3$ fcc aluminum cluster.

Degrees of freedom (DoF)	Energy per atom (eV)	Relative error $\left\lvert \frac{E_h - E_0}{E_0} \right\rvert$
$222,553$	-55.5622017	2.0×10^{-2}
$1,760,305$	-56.6677104	5.1×10^{-4}
$14,003,809$	-56.6966331	1.06×10^{-6}

We next choose a finite-element mesh with fifth-order spectral finite-elements (HEX216SPECT) for the $3 \times 3 \times 3$ aluminum nano-cluster, where the mesh-size is chosen such that the discretization error, measured with respect to E_0, is less than 5 meV per atom. Using the same characteristic mesh-size, which is expected to result in a similar discretization error, we construct the finite-element meshes for the varying sizes of aluminum clusters containing $5 \times 5 \times 5$ (666 atoms), $7 \times 7 \times 7$ (1688 atoms) and $9 \times 9 \times 9$ (3430 atoms) fcc unit-cells. Using a Chebyshev filter of degree 20 and a Fermi smearing parameter of 0.00158 Ha (T=500K), we compute the reference ground-state energies using ChFSI-FE. These are tabulated in Table 4.2.

We next compute the ground-state energies using the proposed subspace projection algorithm (cf. section 4.2) with identical meshes and parameters (Chebyshev filter degree, Fermi smearing parameter) employed in our reference calculations. The polynomial degree R used in the Chebyshev expansion of the Fermi-function of the projected Hamiltonian (4.38) is chosen to be 400. We recall that we use truncation tolerances (δ_c, δ_l) to achieve compact support for the non-orthogonal localized wavefunctions ($\mathbf{\Phi}_L$) and sparsity in the various matrices involved in our formulation. In the initial SCF iterations we use looser truncation tolerances, and employ tighter tolerances as the self-consistent iteration proceeds towards convergence. In particular, we choose $\delta_c = \delta_l$ and vary the truncation tolerance as a function of the relative change in the ground-state energy between two successive SCF iterations (δE_r). The specific choice of the truncation tolerance employed in the present study is

$$\delta_c = \begin{cases} C_1 & \text{if } \delta E_r \geq 1, \\ C_1(\delta E_r)^p & \text{if } 10^{-1.5} \leq \delta E_r < 1, \\ C_2(\delta E_r)^q & \text{otherwise}\,. \end{cases} \tag{4.46}$$

Here, we use a truncation tolerance of $C_1 = 10^{-4}$ when δE_r is greater than 1, then

use a power law (cf. equation (4.46)), subsequently, with $p = \frac{2}{3}$ and $q = \frac{3}{2}$. In order to ensure continuity in δ_c, C_2 is chosen to be 0.00178. We note that the choice of this truncation tolerance is arbitrary, however, this form of the truncation tolerance has provided robust convergence of the SCF for all benchmark calculations, where the number of SCF iterations using the subspace projection approach is only marginally ($\sim 4-5$ iterations) greater than those using ChFSI-FE. In all our simulations, using the proposed method as well as ChFSI-FE, the SCF is terminated when $\delta E_r < 10^{-7}$ for three successive iterations.

The ground-state energies computed using the proposed subspace projection algorithm for the range of nano-clusters considered in this work are tabulated in Table 4.2. The above results show that the proposed subspace projection technique provides good accuracies in the ground-state energies, where the computed energies are within 5 meV per atom of the reference energies computed using ChFSI-FE. The computational times for the full SCF convergence for the range of nano-clusters are plotted in figure 4.1 for the proposed method, as well as, the reference calculations using ChFSI-FE. In this plot, the computational time denoted on the Y-axis is the total computational CPU time in hours (CPU time = Number of cores $\times$ wall-clock time in hours). These results show that the proposed approach is computationally efficient, compared to ChFSI-FE, for system sizes beyond 172 atoms. Further, we note that the subspace projection technique provides a factor of $\sim$ 8.5 speedup for the nano-cluster containing 3430 atoms. Using these computational times, we estimated the scaling of the proposed approach and our reference calculations using ChFSI-FE as a function of system size (number of atoms). The scaling for the proposed approach is found to be approximately $\mathcal{O}(N^{1.66})$, while the scaling in the case of ChFSI-FE is $\mathcal{O}(N^{2.37})$. The deviation from linear-scaling of the proposed method, in practice, is primarily due to two factors. Firstly, we observe that the number of SCF iterations increase with increasing system size. For instance, the number of SCF iterations in-

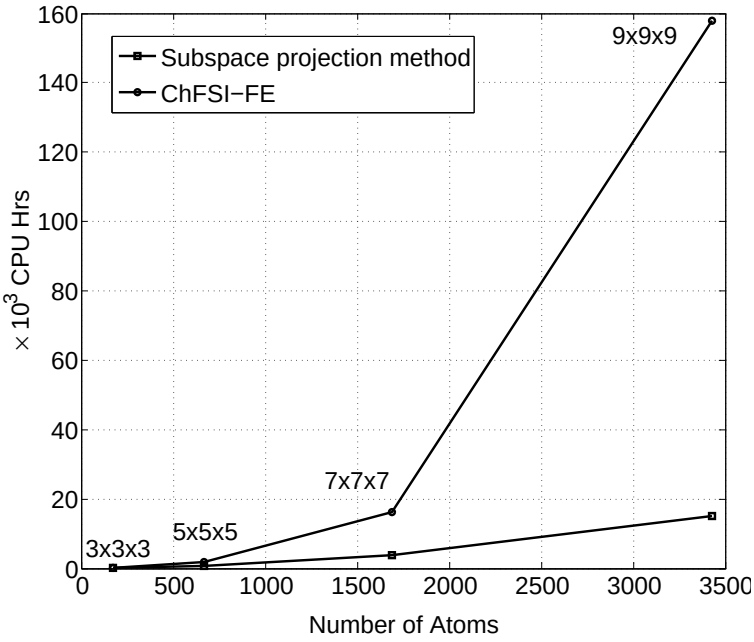

Figure 4.1: Total computational times for the proposed method and ChFSI-FE. Case study: Aluminum nano-clusters.

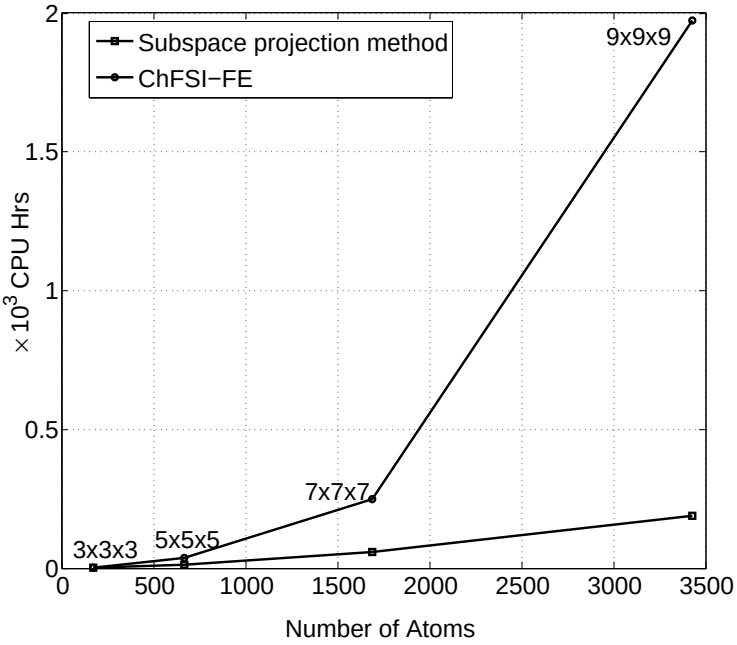

Figure 4.2: Average computational times per SCF iteration for the proposed method and ChFSI-FE. Case study: Aluminum nano-clusters.

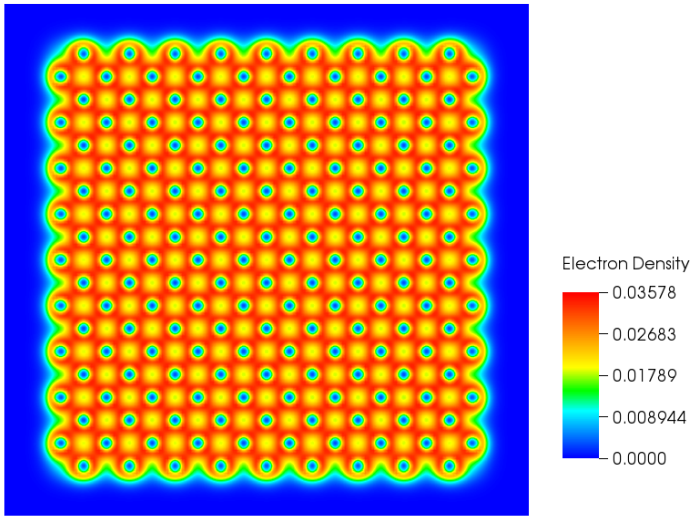

Figure 4.3: Electron density contours on the mid-plane of $9 \times 9 \times 9$ fcc aluminum nano-cluster.

crease from 45 SCF iterations for the $3 \times 3 \times 3$ nano-cluster to 80 iterations for the $9 \times 9 \times 9$ nano-cluster. This issue of increasing SCF iterations with system size can potentially be mitigated using improved mixing schemes [141]. Figure 4.2 shows the computational time per SCF iteration, and the scaling with system size is found to be $\mathcal{O}(N^{1.46})$ for the proposed subspace projection method and $\mathcal{O}(N^{2.17})$ for ChFSI-FE. The second factor which results in the deviation of the proposed subspace projection approach from being linear-scaling is due to the use of dense data-structures when the density fraction is above 2%. Although the use of dense data-structure affects the overall scaling, it is still computationally efficient in comparison to using sparse data-structures for density fractions greater than 2%. We refer to the Appendix D for the scaling of various components of the subspace projection algorithm and a discussion. Figure 4.3 shows the electron density contours on the mid-plane of $9 \times 9 \times 9$ nano-cluster computed using the proposed subspace projection technique.

Table 4.2: Ground-state energies per atom (eV) for the various sizes of aluminum nano-clusters computed using the proposed subspace projection algorithm technique and ChFSI-FE [1].

Cluster	DoF	Proposed Method	ChFSI-FE
3x3x3	$1,107,471$	-56.694963	-56.6949697
5x5x5	$4,363,621$	-56.876491	-56.876518
7x7x7	$11,085,371$	-56.959021	-56.9623511
9x9x9	$22,520,721$	-57.010587	-57.0145334

4.3.2 Alkane chains: Pseudopotential study

We next consider three-dimensional alkane chains with individual repeating units of CH_2 with C-C and C-H bond lengths to be 2.91018 a.u. and 2.0598 a.u., respectively. The H-C-H and C-C-C bond angles are taken to be 109.47^0. Norm-conserving Troullier-Martins pseudopotential in the Kleinman-Bylander form [77, 78] has been employed in these simulations. In the case of carbon, we consider the 2s component to compute the projector in the Kleinman-Bylander form, while the 2p component is chosen to be the local component of the pseudopotential. We consider the local pseudopotential for hydrogen corresponding to the 1s component. The pseudopotentials are generated using the software package fhi98PP [140] using the default cut-off radii, which is 1.5 a.u. for both 2s and 2p components of carbon and 1.3 a.u. for the 1s component of hydrogen. In order to choose finite-element meshes with discretization errors less than 5 meV per atom for various alkane chains, we first consider the case of $C_{33}H_{68}$ containing 101 atoms with 200 valence electrons and obtain the converged value of the ground-state energy. To this end, as in the case of aluminum nano-clusters (cf. section 4.3.1), we use a sequence of increasingly refined fourth-order spectral finite-elements (HEX125SPECT) on a cuboidal simulation domain of dimensions 100 $a.u.$ $\times$ 100 $a.u.$ $\times$ 220 $a.u.$. For these sequence of meshes, the ground-state energy E_h is computed using ChFSI-FE with a Chebyshev filter of degree 35 and em-

ploying a Fermi smearing parameter of 0.00158 Ha (T=500K), and these results are tabulated in Table 4.3. Using the extrapolation procedure described in Chapter III, we find the reference ground-state energy per atom to be $E_0 = -61.44173873\ eV$. Further, we also compared our reference ground-state energy with ABINIT using a cuboidal simulation of size 40 $a.u.$ × 40 $a.u.$ × 160 $a.u.$ and an energy cut-off of 30 Ha with one k-point (the most refined calculation possible within our memory limitations). In the case of ABINIT, the ground-state energy per atom was found to $-61.44219366\ eV$, which differs from E_0 by $\sim 0.4\ meV$.

Table 4.3: Convergence of the finite-element discretization for $C_{33}H_{68}$ using HEX125SPECT element.

Deg. of freedom	Energy per atom (eV)	Relative error
$391,893$	-61.31623538	2.0×10^{-3}
$3,096,585$	-61.43711471	7.5×10^{-5}
$24,621,969$	-61.44173469	5.01×10^{-8}

We next choose a finite-element mesh with fifth-order spectral finite-elements (HEX216SPECT) for $C_{33}H_{68}$, where the mesh-size is chosen such that the discretization error, measured with respect to E_0, is less than 5 meV per atom. Using the same characteristic mesh-size which is expected to result in a similar discretization error, we construct finite-element meshes for varying lengths of alkane chains, namely $C_{100}H_{202}$ (302 atoms), $C_{300}H_{602}$ (902 atoms), $C_{900}H_{1802}$ (2702 atoms) and $C_{2350}H_{4702}$ (7052 atoms). Using a Chebyshev filter of degree 35 and a Fermi smearing parameter of 0.00158 Ha (T=500K), we compute the reference ground-state energies using ChFSI-FE for these systems, and are tabulated in Table 4.4.

The subspace projection algorithm is then used to compute the ground-state energies using identical meshes and parameters (Chebyshev filter degree, Fermi smearing parameter) employed in our reference calculations. The polynomial degree R used in

the Chebyshev expansion of the Fermi function of the projected Hamiltonian (4.38) is chosen to be 400. Just as in the case of aluminum nano-clusters, we use adaptive truncation tolerances (δ_c, δ_l). In particular, we choose $\delta_c = \delta_l$ and use the specific choice of truncation tolerance given in equation (4.46) with identical values of C_1, p and q as employed in the case of our previous benchmark calculations involving aluminum nano-clusters. In all our simulations, using the proposed method as well as ChFSI-FE, the SCF is terminated when $\delta E_r < 10^{-7}$ for three successive iterations.

Table 4.4: Comparison of ground-state energies (eV per atom) for various alkane chains.

Alkane Chain	DoF	Proposed Method	ChFSI-FE
C_{33} H_{68}	$870,656$	-61.438671	-61.438680
C_{100} H_{202}	$2,491,616$	-62.041530	-62.041532
C_{300} H_{602}	$7,354,496$	-62.240148	-62.240277
C_{900} H_{1802}	$21,943,138$	-62.303101	-62.303608

The ground-state energies computed using the proposed subspace projection algorithm for different lengths of alkane chains considered in this work are tabulated in Table 4.4. These results indicate that the proposed method provides good accuracies in the ground-state energies, where the computed energies are within 1 meV per atom of the reference energies computed using ChFSI-FE. The computational times for the full SCF convergence for varying lengths of alkane chains are plotted in figure 4.4 for the proposed method, as well as, the reference calculations using ChFSI-FE. These results indicate that the proposed approach is computationally efficient, compared to ChFSI-FE, for system sizes beyond 101 atoms and provides a factor of ~ 8 speedup for the alkane chain containing 2702 atoms. Using these computational times, the estimated scaling for the proposed approach is found to be approximately $\mathcal{O}(N^{1.33})$, while scaling in the case of ChFSI-FE is $\mathcal{O}(N^{2.13})$. The average computational time per SCF iteration is shown in figure 4.5, and the scaling with system size

is found to be $\mathcal{O}(N^{1.18})$ for the proposed subspace projection method and $\mathcal{O}(N^{1.98})$ for ChFSI-FE. We refer to the Appendix D for the scaling of various components of the subspace projection algorithm and a discussion. We note that the proposed subspace projection technique exhibits better scaling behavior for the alkane chains, which is an insulating system, in comparison to the aluminum nano-clusters, which is a metallic system. This is due to the better localization of the wavefunctions in the insulating system in comparison to the metallic system (cf. Appendix D). Figure 4.6 shows the isocontours of electron density of the alkane chain containing 2702 atoms.

4.3.3 Silicon nano-clusters: All-electron study

We consider silicon nano-clusters comprising of diamond-cubic unit cells with a lattice constant of 10.26 $a.u.$ and conduct all-electron calculations to test the performance of the subspace projection method. In order to choose finite-element meshes which provide a discretization error of less than 5 mHa per atom for various nano-clusters, we first obtain a converged value of the ground state energy by conducting a very refined simulation using the GAUSSIAN package [72] on silicon nano-cluster containing $1 \times 1 \times 1$ unit-cell which comprises of 18 atoms with 252 electrons. To this end, we employ the polarization consistent DFT basis sets (pc-n) and introduce them as an external basis set in GAUSSIAN package. Using the most refined pc-4 basis set, the computed ground-state energy per atom (E_0) is -288.3179669 Ha.

We next chose a finite-element mesh with fifth-order spectral finite-elements for the $1\times1\times1$ silicon nano-cluster, where the discretization error, measured with respect to E_0, is less than 3 mHa. Using the same characteristic mesh-size, we construct the finite-element meshes for the varying sizes of silicon nano-clusters containing $1\times1\times1$ (252 electrons), $2 \times 1 \times 1$ (434 electrons), $2 \times 2 \times 1$ (756 electrons), $2 \times 2 \times 2$ (1330 electrons) and $3\times3\times3$ (3920 electrons) diamond-cubic unit cells. The finite-element mesh is locally refined near the nuclei since all-electron calculations involve highly

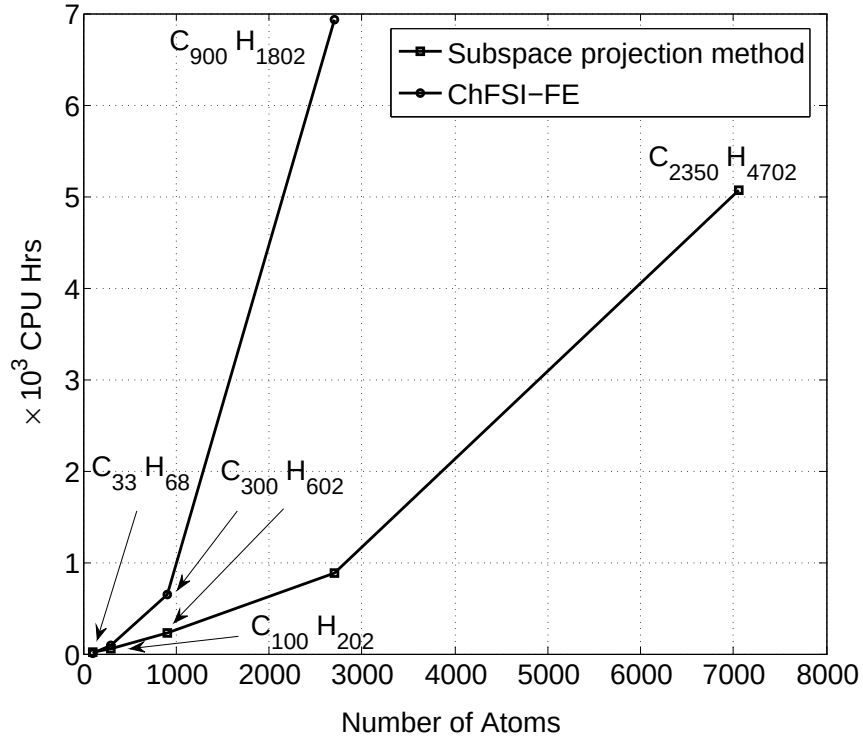

Figure 4.4: Total computational times for the proposed method and ChFSI-FE. Case study: Alkane chains.

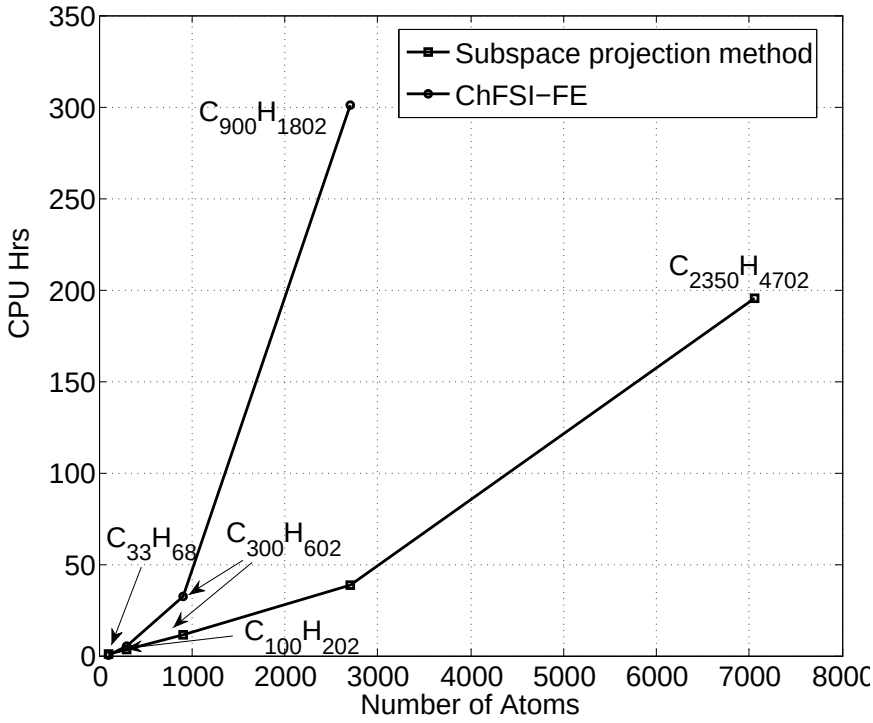

Figure 4.5: Average computational times per SCF iteration for the proposed method and ChFSI-FE. Case study: Alkane chains.

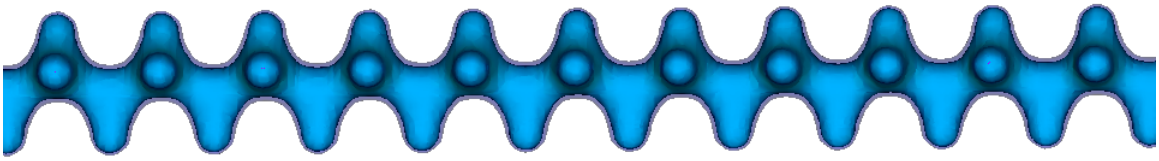

Figure 4.6: Electron density isocontours of $C_{900}H_{1802}$.

oscillatory wavefunctions near the nuclei. The order of the Chebyshev filter thus required in these simulations is around 1000 to effectively filter out the unwanted spectrum. Using a Chebyshev filter of degree 1000, and a Fermi smearing parameter of 0.00475 Ha (T=1500K), we compute the reference ground-state energies using ChFSI-FE which are tabulated in Table 4.5.

The subspace projection algorithm is then used to compute the ground-state energies with identical meshes and parameters employed in our reference calculations. The polynomial degree R used in the Chebyshev expansion of the Fermi-operator of the projected Hamiltonian (4.38) is chosen to be 1250 since the width of the occupied spectrum is larger than that of a pseudopotential calculation. Just as in the case of the previous benchmark calculations, we use adaptive truncation tolerances (δ_c, δ_l) with $\delta_l = 10^4\delta_c$ and vary δ_c as a function of relative change in the ground-state energy between two successive iterations (δE_r). We use the specific choice of truncation tolerance given in equation (4.46) with $C_1 = 10^{-11}$, $p = 2/3$ and $q = 3/2$. We note that much tighter tolerances have been used for δ_c in comparison to pseudopotential calculations in order to control the accumulation of truncation errors in applying a very high degree Chebyshev filter. In all our simulations, using the proposed method as well as ChFSI-FE, the SCF is terminated when $\delta E_r < 10^{-6}$ for three successive iterations.

The ground-state energies computed using the proposed subspace projection algorithm for varying sizes of silicon nano-clusters considered in this work are tabulated

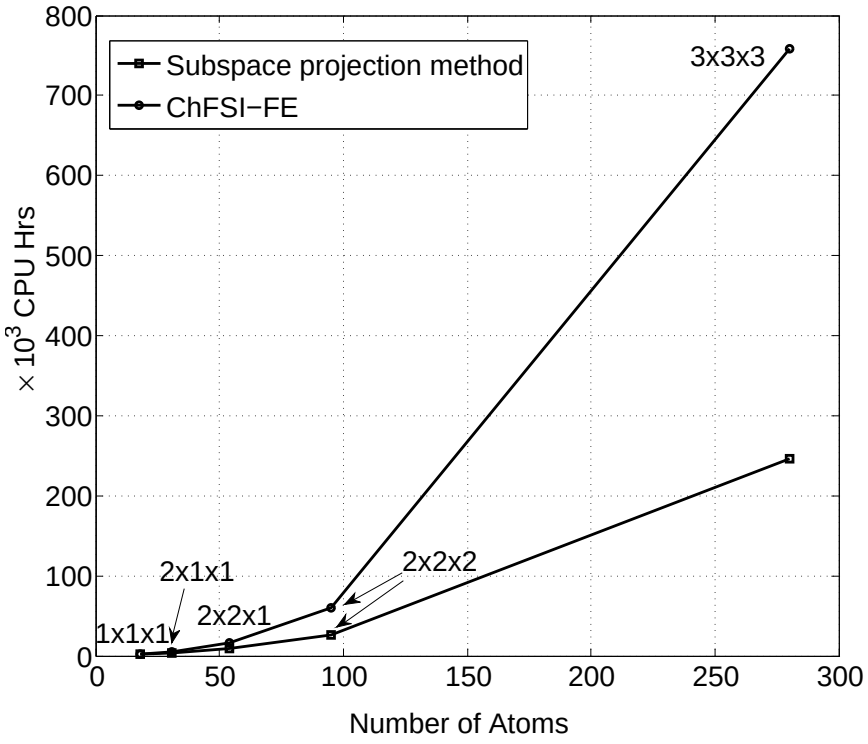

Figure 4.7: Total computational times for the proposed method and ChFSI-FE. Case study: Silicon nano-clusters.

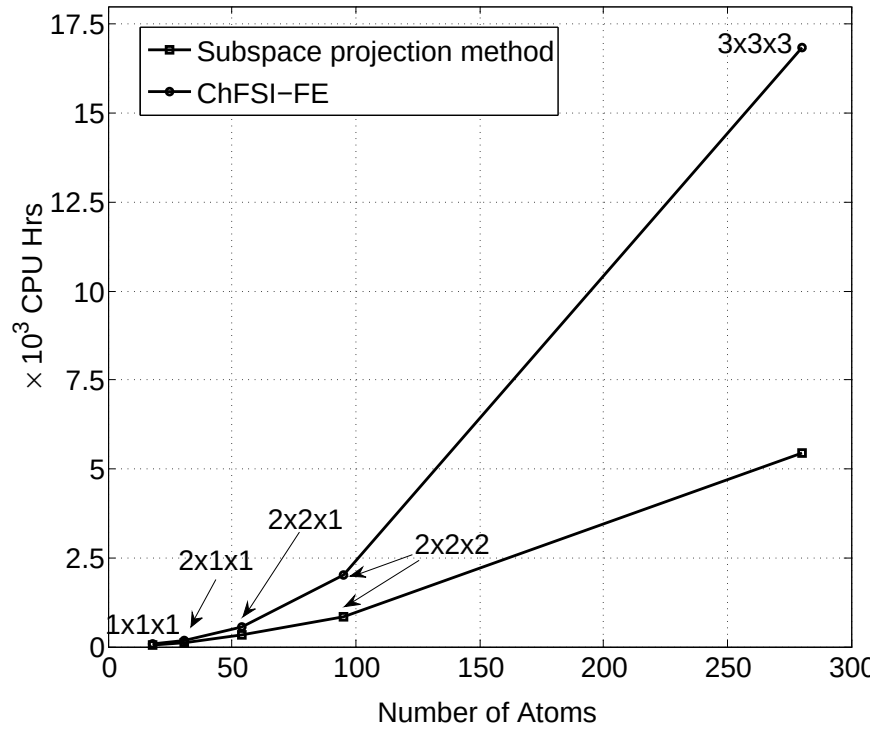

Figure 4.8: Average computational times per SCF iteration for the proposed method and ChFSI-FE. Case study: Silicon nano-clusters.

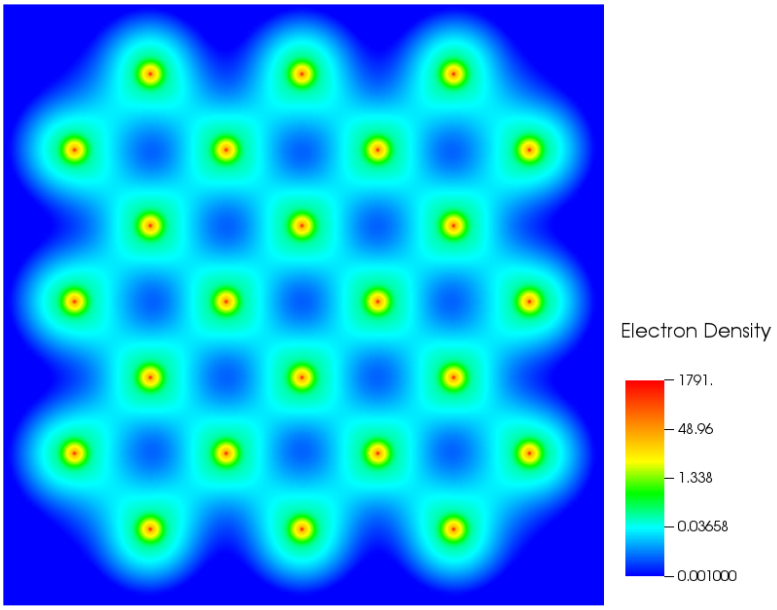

Figure 4.9: Electron density contours on the mid-plane of $3 \times 3 \times 3$ silicon nano-cluster.

in Table 4.5. These results indicate that the proposed method provides good accuracies in the ground-state energies, where the computed energies are within 3 mHa per atom of the reference energies computed using ChFSI-FE. The computational times for the full SCF convergence for varying sizes of silicon nano-clusters are plotted in figure 4.7 for the proposed method, as well as, the reference calculations using ChFSI-FE. These results indicate that the proposed approach is computationally efficient, compared to ChFSI-FE, for system sizes beyond 18 atoms and provides a factor of ~ 3 speedup for the $3 \times 3 \times 3$ nano-cluster containing 280 atoms. Using these computational times, the estimated scaling for the proposed approach is found to be approximately $\mathcal{O}(N^{1.85})$, while scaling in the case of ChFSI-FE is $\mathcal{O}(N^{2.21})$. The average computational time per SCF iteration is shown in figure 4.8, and the scaling is computed to be $\mathcal{O}(N^{1.75})$ for the proposed subspace projection method and $\mathcal{O}(N^{2.11})$ for ChFSI-FE. The deterioration in the scaling for all-electron calculations in comparison to pseudopotential calculations is due to tighter truncation tolerances employed in order to control the accumulation of the truncation errors during the ap-

Table 4.5: Comparison of ground-state energies (Ha per atom) for various sizes of silicon clusters.

Cluster	DoF	Proposed Method	ChFSI-FE
1x1x1	$5,136,901$	-288.32016	-288.32046
2x1x1	$9,676,481$	-288.33380	-288.33411
2x2x1	$16,358,791$	-288.34715	-288.34791
2x2x2	$27,208,731$	-288.35985	-288.36140
3x3x3	$79,226,681$	-288.37132	-288.37341

plication of a very high degree Chebyshev filter. Nevertheless, the proposed approach provides significant savings, which will increase with increasing system size. We refer to the Appendix D for the scaling of various components of the subspace projection algorithm in the case of all-electron calculations and a discussion. Figure 4.9 shows the electron density contours on the mid-plane of $3 \times 3 \times 3$ nano-cluster computed using the proposed subspace projection technique.

4.4 Summary

The present chapter demonstrates a methodology to conduct large scale electronic structure calculation using spectral finite-element discretizations at reduced scaling and presents an important direction for electronic structure calculations employing the finite-element basis. The computational efficiency as well as scaling in the case of all-electron calculations can be further improved by using a finite-element basis enriched with single-atom wavefunctions, or, alternately, the partitions-of-unity finite-element approach [101] which forms an important future direction.

CHAPTER V

Configurational force approach to atomic relaxations using Kohn-Sham density functional theory

We have so far considered the problem of computing the ground-state electron density for a fixed set of atom positions in the previous chapters and now we turn to the computation of forces on atoms. An important aspect of electronic structure calculations using DFT is the efficient computation of forces on atoms to find the geometry of a given materials system in the most stable state and this forms the subject of the chapter. A crucial step to evaluate forces on atoms in most DFT codes is to use Hellmann-Feynman (HF) theorem [37] which relates the derivatives of the total energy with respect to position of atoms to the expectation value of the derivative of the Hamiltonian with respect to position of atoms. However these atomic forces are usually corrected for incomplete-basis-set error [38, 39, 40], non-self-consistency error [40, 41] which are not accounted for, when using the HF theorem. Furthermore, HF theorem fails to capture stress in a periodic-unit cell as it produces the zero force for any affine deformation of the system and these Pulay stress contributions are later explicitly accounted in the DFT calculations [42, 43]. The computation of atomic forces within the framework of the real-space finite-element formulation proposed in

this thesis must account for all the above three errors often unaccounted using HF theorem and thus needs a careful approach. In this chapter, we propose the use of configurational force (Eshelby) approach for efficient computation of atomic forces and derive the relevant expressions for forces in a more general setting by using the non-orthogonal formulation of Kohn-Sham DFT, taking into account the fractional occupancies. We refer to [25] for computation of atomic forces in the restricted case of orthogonal formulation of Kohn-Sham DFT. Though the Eshelby approach of computing the atomic forces is relatively new in the context of Kohn-Sham DFT calculations, the approach is based on ideas widely used in mechanics [142] following Eshelby's formulation of force on a defect [143]. We note that the proposed Eshelby formulation for atomic relaxations provides a unified framework that captures atomic forces due to Hellmann-Feynman theorem, incomplete-basis-sets and the non-self-consistency, and furthermore accounts for elastic stresses on periodic unit-cells on a single footing.

We first begin with the proof of the well-known Hellmann-Feynman theorem and explain the origin of errors discussed previously and subsequently derive the expression for the configurational force in the context of the non-orthogonal formulation of the Kohn-Sham DFT functional.

5.1 Hellmann-Feynman theorem

Using the expression for energy as the expectation value of the Hamiltonian $\mathcal{H}_e$ from equation (2.12) of Chapter II, we evaluate the force acting on an atom I using Hellmann-Feynman theorem [37] as:

$$\boldsymbol{f}_I = -\frac{\partial J}{\partial \mathbf{R}_I} = -\frac{\partial}{\partial \mathbf{R}_I} \langle \Psi_e | \mathcal{H}_e | \Psi_e \rangle = -\left\langle \Psi_e \middle| \frac{\partial \mathcal{H}_e}{\partial \mathbf{R}_I} \middle| \Psi_e \right\rangle \tag{5.1}$$

and the proof uses that wavefunction Ψ_e is an eigenfunction of the Hamiltonian under consideration and is normalized.

$$\mathcal{H}_e \left|\Psi_e\right\rangle = E_e \left|\Psi_e\right\rangle \tag{5.2}$$

$$\left\langle\Psi_e\right| \Psi_e\rangle = 1 \implies \frac{\partial}{\partial \mathbf{R}_I} \left\langle\Psi_e\right| \Psi_e\rangle = 0 \tag{5.3}$$

Hellmann-Feynman theorem is easy to show by applying the derivative product rule to the above expectation value of Hamiltonian viewed as a function of position of atoms $\{\mathbf{R}_I\}$:

$$\begin{aligned}
\frac{\partial J}{\partial \mathbf{R}_I} &= -\frac{\partial}{\partial \mathbf{R}_I} \left\langle\Psi_e\right| \mathcal{H}_e \left|\Psi_e\right\rangle \\
&= -\left[\left\langle \frac{\partial \Psi_e}{\partial \mathbf{R}_I} \right| \mathcal{H}_e \left| \Psi_e \right\rangle + \left\langle \Psi_e \right| \mathcal{H}_e \left| \frac{\partial \Psi_e}{\partial \mathbf{R}_I} \right\rangle + \left\langle \Psi_e \right| \frac{\partial \mathcal{H}_e}{\partial \mathbf{R}_I} \left| \Psi_e \right\rangle\right] \\
&= -\left[E_e \left\langle \frac{\partial \Psi_e}{\partial \mathbf{R}_I} \right| \Psi_e \right\rangle + E_e \left\langle \Psi_e \right| \frac{\partial \Psi_e}{\partial \mathbf{R}_I} \right\rangle + \left\langle \Psi_e \right| \frac{\partial \mathcal{H}_e}{\partial \mathbf{R}_I} \left| \Psi_e \right\rangle\right] \\
&= -\left[E_e \frac{\partial}{\partial \mathbf{R}_I} \left\langle\Psi_e\right| \Psi_e\rangle + \left\langle \Psi_e \right| \frac{\partial \mathcal{H}_e}{\partial \mathbf{R}_I} \left| \Psi_e \right\rangle\right] \\
&= -\left\langle \Psi_e \right| \frac{\partial \mathcal{H}_e}{\partial \mathbf{R}_I} \left| \Psi_e \right\rangle
\end{aligned} \tag{5.4}$$

We proceed further and use Slater determinant to express Ψ_e to be $1/\sqrt{N!}\det\{\psi_i\}$ of orbitals ψ_i with the one-particle Kohn-Sham approximation(c.f Chapter II) in conjunction with the real space formulation described in equation 3.16 of Chapter III, then the Hellmann-Feynman theorem simply results in the following expression for the force on an atom $\boldsymbol{f}_I$:

$$\boldsymbol{f}_I = -\frac{\partial}{\partial \mathbf{R}_I} \sum_{K=1}^{N_a} \int_{\Omega} Z_K \widetilde{\delta}(\mathbf{r} - \mathbf{R}_K) \varphi(\mathbf{r})\, d\mathbf{r} + \frac{\partial}{\partial \mathbf{R}_I} \sum_{K=1}^{N_a} \int_{\Omega_K} Z_K \widetilde{\delta}(\mathbf{r} - \mathbf{R}_K) \nu_K(\mathbf{r})\, d\mathbf{r} \tag{5.5}$$

which can be simplified as:

$$\begin{aligned}
\boldsymbol{f}_I &= \int_{\Omega} Z_I \frac{\partial}{\partial \mathbf{r}} \widetilde{\delta}(\mathbf{r}-\mathbf{R}_I)\varphi(\mathbf{r})\, d\mathbf{r} - \int_{\Omega_I} Z_I \frac{\partial}{\partial \mathbf{r}} \widetilde{\delta}(\mathbf{r}-\mathbf{R}_I)\nu_I(\mathbf{r})\, d\mathbf{r} \\
&= -\int_{\Omega} Z_I \widetilde{\delta}(\mathbf{r}-\mathbf{R}_I) \frac{\partial}{\partial \mathbf{r}} \varphi(\mathbf{r})\, d\mathbf{r} + \int_{\Omega_I} Z_I \widetilde{\delta}(\mathbf{r}-\mathbf{R}_I) \frac{\partial}{\partial \mathbf{r}} \nu_I(\mathbf{r})\, d\mathbf{r} \\
&= -Z_I \nabla\varphi(\mathbf{R}_I) + Z_I \nabla\nu_I(\mathbf{R}_I) \qquad (5.6)
\end{aligned}$$

However, the computation of atomic forces using equation (5.6) has significant drawbacks. First we recall from the derivation in equation (5.4) that HF theorem assumes the electronic wavefunction to be an exact eigenfunction (or stationary state wavefunction) of the particular Hamiltonian under consideration and is normalized to unity and hence, the terms involving the variations of the wavefunctions with respect to positions of atoms vanish. However this is true only if complete (infinite) basis-sets are used to express the electronic wavefunctions ($\{\psi_i\}$ after making the Kohn-Sham approximation) which can never be true in any numerical calculation. The error resulting from the incomplete basis-sets used to expand the electronic-wavefunctions is referred to as incomplete basis-set error or the Pulay force [37] and often needs to be explicitly accounted when the basis functions themselves depend on atomic positions (for e.g., atomic-orbital basis). Though this force does not arise in the case of numerical calculations with basis functions independent of positions of atoms (like for e.g., plane waves), the finite-element discretization presented in this thesis deals with atomic nuclei coincident with finite-element nodes and hence has to account for incomplete basis-set error when computing the atomic forces. Furthermore, the expression in (5.6) does not capture the stress in a periodic unit-cell as it produces zero force for any affine deformation on the materials system, and fails to capture elastic effects corresponding to the affine deformation on the crystal. We therefore employ Eshelby approach of calculating the configurational force on the system which pro-

vides us a single expression to capture HF forces, Pulay forces and the elastic stresses on the crystal in the context of Kohn-Sham DFT.

5.2 Configurational force approach

We now consider a system with N_a nuclei with position vectors denoted by $\mathbf{R} = \{\mathbf{R}_1, \mathbf{R}_2, \mathbf{R}_3, \cdots\}$. Let $\{\phi_i(\mathbf{r})\}$ for $i = 1 \cdots N$ with $N > N_e/2$ denote a non-orthogonal basis functions spanning the occupied eigensubspace of the Kohn-Sham Hamiltonian (c.f equation (3.25a)) with $\mathbf{S}$ denoting the overlap matrix associated with $\{\phi_i(\mathbf{r})\}$ and $\mathbf{\Gamma}^{\phi}$ be the corresponding density matrix expressed in the non-orthogonal basis with matrix element Γ^{ϕ}_{ij}. Further, let $\bar{\varphi}(\mathbf{x})$, $\bar{\boldsymbol{\nu}} = \{\bar{\nu}_1(\mathbf{r}), \bar{\nu}_2(\mathbf{r}), \bar{\nu}_3(\mathbf{r}), \cdots\}$ denote the solutions of the Poisson problems given in equation (3.25c) and $\rho(\mathbf{r})$ denote the electron-density distribution, then the expression for Helmholtz free energy in terms of the finite temperature counterpart of Kohn-Sham ground state energy(E_σ) and the entropy term (E_{ent}) is

$$\mathcal{F} = E_{\text{KS}} - E_{\text{ent}}\,, \tag{5.7}$$

with
$$\begin{aligned} E_{\text{KS}} &= E_{\text{KS}}(\{\phi_i\}, \bar{\varphi}, \bar{\boldsymbol{\nu}}, \Gamma^{\phi}_{ij}, \mathbf{R})\,, \\ &= E_{\text{b}}(\Gamma^{\phi}_{ij}, \{\phi_i\}, \mathbf{R}) + E_{\text{veff}}(\rho, \mathbf{R}) + E_{\text{xc}}(\rho) + E_{\bar{\varphi}}(\rho, \mathbf{R}) + E_{\bar{\boldsymbol{\nu}}}(\mathbf{R})\,, \end{aligned} \tag{5.8}$$

where
$$E_{\text{xc}} = \int_{\Omega} F(\rho(\mathbf{r}))\, d\mathbf{r}\,, \tag{5.9a}$$

$$E_{\text{veff}} = -\int_{\Omega} \rho(\mathbf{r}) V_{\text{eff}}(\rho(\mathbf{r}), \mathbf{R})\, d\mathbf{r}\,, \tag{5.9b}$$

$$S_{jk} = \int_{\Omega} \phi^*_j(\mathbf{r})\phi_k(\mathbf{r})\, d\mathbf{r} \quad , \quad \rho(\mathbf{r}) = 2\,\Gamma^{\phi}_{ij}\, S^{-1}_{jk}\, \phi^*_k(\mathbf{r})\, \phi_i(\mathbf{r}) \tag{5.9c}$$

$$E_{\text{b}} = 2\int_{\Omega} \Gamma^{\phi}_{ij}\, S^{-1}_{jk}\, \phi^*_k(\mathbf{r}) \left(-\frac{1}{2}\nabla^2 + V_{\text{eff}}(\rho(\mathbf{r}), \mathbf{R})\right) \phi_i(\mathbf{r})\, d\mathbf{r}\,, \tag{5.9d}$$

$$E_{\bar{\varphi}} = \sup_{\varphi} \left\{ -\frac{1}{8\pi}\int_{\Omega} |\nabla\varphi(\mathbf{r})|^2\, d\mathbf{r} + \int_{\Omega} (\rho(\mathbf{r}) + b(\mathbf{r}, \mathbf{R}))\varphi(\mathbf{r})\, d\mathbf{r} \right\}, \tag{5.9e}$$

$$E_{\bar{\boldsymbol{\nu}}} = \inf_{\boldsymbol{\nu}} \Big(\sum_{I=1}^{N_a} \Big[\frac{1}{8\pi} \int\limits_{\Omega_I} |\nabla \nu_I(\mathbf{r})|^2 \, d\mathbf{r} - \int\limits_{\Omega_I} b_I(\mathbf{r}) \nu_I(\mathbf{r}) \, , \, d\mathbf{r} - \frac{1}{8\pi} \int\limits_{\partial\Omega_I} \bar{\nu_I}(\mathbf{r}) (\nabla \bar{\nu_I}(\mathbf{r}).\boldsymbol{n}) \, d\mathbf{S}_I \Big] \Big) \tag{5.10a}$$

$$E_{\text{ent}} = -2\,\sigma \, \text{tr} \left[\boldsymbol{\Gamma}^{\phi} \ln \boldsymbol{\Gamma}^{\phi} + (\boldsymbol{I} - \boldsymbol{\Gamma}^{\phi}) \ln(\boldsymbol{I} - \boldsymbol{\Gamma}^{\phi}) \right] . \tag{5.10b}$$

σ in the above equation denotes the smearing parameter $k_B\,T$ as defined in equation (3.72). Further, summation from 1 to N is implied over the repeated indices i, j, k in (5.9d) and we note the use of Einstein summation convention in the subsequent equations to follow. We now use the Lagrange multiplier μ to enforce the constraint on the number of electrons and the constrained energy functional $\mathcal{E}_c$ is

$$\mathcal{E}_c = \mathcal{F} - \mu \left[2\,\text{tr}(\boldsymbol{\Gamma}^{\phi}) - N_e \right] . \tag{5.11}$$

A bijective mapping $\chi_\varepsilon(\mathbf{r})$ is now defined for every point in space with the following properties:

$$\begin{aligned} &\chi_\varepsilon(\mathbf{r}) \, : \Omega \to \Omega', \;\; \chi_0 = \mathbf{I} \\ &\mathbf{r}' = \; \chi_\varepsilon(\mathbf{r}) \; = \mathbf{r} + \varepsilon \boldsymbol{\Upsilon}(\mathbf{r}) \\ &\frac{d}{d\varepsilon} \; \chi_\varepsilon(\mathbf{r}) \Big|_{\varepsilon=0} = \boldsymbol{\Upsilon}(\mathbf{r}) \end{aligned} \tag{5.12}$$

The bijective map $\chi_\varepsilon(\mathbf{r})$ defined above can be viewed as a perturbation created at every material point $\mathbf{r}$ in space to a new point $\mathbf{r}'$ along some direction $\boldsymbol{\Upsilon}(\mathbf{r})$ related by $\mathbf{r}' = \mathbf{r} + \varepsilon \boldsymbol{\Upsilon}(\mathbf{r})$. However this mapping should preserve the nuclear charge distribution and hence the mapping is constrained to rigid body motions on the compact support of the nucleus, i.e. $\chi_\varepsilon(\mathbf{r}) \; = \boldsymbol{Q}^I_\varepsilon \mathbf{r} + \boldsymbol{T}^I_\varepsilon$ for $I = 1 \cdots N_a$ in the compact support of $b_I(\mathbf{r}, \mathbf{R})$. Here $\boldsymbol{Q}^I_\varepsilon$ is unitary and $\boldsymbol{Q}^I_\varepsilon$, $\boldsymbol{T}^I_\varepsilon$ are independent of $\mathbf{r}$. Before deriving the

expressions for configurational force, we first define the following identities:

$$
\begin{aligned}
\frac{d}{d\varepsilon}\left\{\frac{\partial r_i'}{\partial r_j}\right\}\Big|_{\varepsilon=0} &= \frac{\partial \Upsilon_i(\mathbf{r})}{\partial r_j}\,, \\
\frac{d}{d\varepsilon}\left\{\frac{\partial r_i}{\partial r_j'}\right\}\Big|_{\varepsilon=0} &= -\frac{\partial r_i}{\partial r_k'}\left(\frac{d}{d\varepsilon}\frac{\partial r_k'}{\partial r_l}\right)\frac{\partial r_l}{\partial r_j'}\Big|_{\varepsilon=0} = -\frac{\partial \Upsilon_i(\mathbf{r})}{\partial r_j}\,, \\
\frac{d}{d\varepsilon}\left\{\det\left(\frac{\partial x_i'}{\partial x_j}\right)\right\}\Big|_{\varepsilon=0} &= \frac{d}{d\varepsilon}\left\{\det\left(\delta_{ij}+\varepsilon\frac{\partial \Upsilon_i(\mathbf{r})}{\partial x_j}\right)\right\}\Big|_{\varepsilon=0} \\
&= \frac{d}{d\varepsilon}\left\{1+\frac{\partial \Upsilon_j(\mathbf{r})}{\partial x_j}\varepsilon+\mathcal{O}(\varepsilon^2)\right\}\Big|_{\varepsilon=0} = \frac{\partial \Upsilon_j(\mathbf{r})}{\partial r_j}\,, \\
\det\left\{\frac{\partial r_i'}{\partial r_j}\right\}\Big|_{\varepsilon=0} &= 1\,, \qquad \frac{\partial r_i}{\partial r_j'}\Big|_{\varepsilon=0} = \delta_{ij}\,, \qquad \frac{\partial r_i'}{\partial r_j}\Big|_{\varepsilon=0} = \delta_{ij}\,.
\end{aligned}
\tag{5.13}
$$

Due to the infinitesimal variations introduced by the mapping $\chi_\varepsilon(\mathbf{r})$, $\mathcal{E}_c$ is now

$$
\begin{aligned}
\mathcal{E}_c &= \mathcal{E}_c(\,\chi_\varepsilon(\mathbf{r})\,)\,, \\
\mathcal{E}_c(\,\chi_\varepsilon(\mathbf{r})\,) &= \mathcal{F}(\,\chi_\varepsilon(\mathbf{r})\,) - \mu\left[2\,\mathrm{tr}(\widetilde{\mathbf{\Gamma}}^{\phi}) - N_e\right]\,,
\end{aligned}
$$

where $\widetilde{\mathbf{\Gamma}}^{\phi}$ denotes the perturbed density matrix corresponding to infinitesimal variations introduced by the mapping $\chi_\varepsilon(\mathbf{r})$. We thus have $\mathcal{F}(\,\chi_\varepsilon(\mathbf{r})\,) = E_{\mathrm{KS}}(\,\chi_\varepsilon(\mathbf{r})\,) - E_{\mathrm{ent}}(\,\chi_\varepsilon(\mathbf{r})\,)$ with each term of $E_{\mathrm{KS}}(\,\chi_\varepsilon(\mathbf{r})\,)$ carefully treated below. Thus

$$
E_b(\,\chi_\varepsilon(\mathbf{r})\,) = 2\int\limits_{\Omega'} \widetilde{\Gamma}_{ij}^{\phi}\,\widetilde{S}_{jk}^{-1}\,\phi_k^*(\mathbf{r}')\left(-\frac{1}{2}\nabla_{\mathbf{r}'}^2 + V_{\mathrm{eff}}(\rho(\mathbf{r}'))\right)\phi_i(\mathbf{r}')\,d\mathbf{r}'\,. \tag{5.14}
$$

Transforming the integrals back onto Ω, we obtain in indicial notation

$$
E_b(\,\chi_\varepsilon(\mathbf{r})\,) = 2\int\limits_{\Omega} \widetilde{\Gamma}_{ij}^{\phi}\,\widetilde{S}_{jk}^{-1}\,\phi_k^*(\,\chi_\varepsilon(\mathbf{r})\,)\left(-\frac{1}{2}\nabla_{\mathbf{r}'}^2 + V_{\mathrm{eff}}(\rho(\,\chi_\varepsilon(\mathbf{r})\,))\right)\phi_i(\,\chi_\varepsilon(\mathbf{r})\,)\,\det\left(\frac{\partial \mathbf{r}'}{\partial \mathbf{r}}\right)\,d\mathbf{r}\,.
$$

We note that $\widetilde{S}_{jk}^{-1}$ denotes the perturbed inverse overlap matrix corresponding to infinitesimal variations introduced by the mapping $\chi_\varepsilon(\mathbf{r})$ and its functional dependence

can be written as

$$\widetilde{S}^{-1}_{jk} = \widetilde{S}^{-1}_{jk}\left(\,\chi_\varepsilon(\mathbf{r})\,,\,\det\left(\frac{\partial \mathbf{r}'}{\partial \mathbf{r}}\right)\right)\,. \tag{5.15}$$

The configurational force arising out of the term E_b is obtained by evaluating the generalized directional derivative of $E_b(\,\chi_\varepsilon(\mathbf{r})\,)$ and is given by

$$\frac{d}{d\varepsilon}E_b(\,\chi_\varepsilon(\mathbf{r})\,)\Big|_{\varepsilon=0} = I_1 + I_2 + I_3 + I_4 + I_5\,, \tag{5.16}$$

where

$$\begin{aligned}
I_1 &= 2\int_\Omega \left[\frac{d}{d\varepsilon}\left(\widetilde{\Gamma}^\phi_{ij}\right)\widetilde{S}^{-1}_{jk}\,\phi^*_k(\,\chi_\varepsilon(\mathbf{r})\,)\left(-\frac{1}{2}\nabla^2_{\mathbf{r}'} + V_{\text{eff}}(\rho(\,\chi_\varepsilon(\mathbf{r})\,))\right)\phi_i(\,\chi_\varepsilon(\mathbf{r})\,)\,\det\left(\frac{\partial \mathbf{r}'}{\partial \mathbf{r}}\right)\right]\Bigg|_{\varepsilon=0} d\mathbf{r}\,,\\
I_2 &= 2\int_\Omega \left[\widetilde{\Gamma}^\phi_{ij}\,\frac{d}{d\varepsilon}\left(\widetilde{S}^{-1}_{jk}\right)\,\phi^*_k(\,\chi_\varepsilon(\mathbf{r})\,)\left(-\frac{1}{2}\nabla^2_{\mathbf{r}'} + V_{\text{eff}}(\rho(\,\chi_\varepsilon(\mathbf{r})\,))\right)\phi_i(\,\chi_\varepsilon(\mathbf{r})\,)\,\det\left(\frac{\partial \mathbf{r}'}{\partial \mathbf{r}}\right)\right]\Bigg|_{\varepsilon=0} d\mathbf{r}\,,\\
I_3 &= 2\int_\Omega \left[\widetilde{\Gamma}^\phi_{ij}\,\widetilde{S}^{-1}_{jk}\frac{d}{d\varepsilon}\left(\phi^*_k(\,\chi_\varepsilon(\mathbf{r})\,)\right)\left(-\frac{1}{2}\nabla^2_{\mathbf{r}'} + V_{\text{eff}}(\rho(\,\chi_\varepsilon(\mathbf{r})\,))\right)\phi_i(\,\chi_\varepsilon(\mathbf{r})\,)\,\det\left(\frac{\partial \mathbf{r}'}{\partial \mathbf{r}}\right)\right]\Bigg|_{\varepsilon=0} d\mathbf{r}\,,\\
I_4 &= 2\int_\Omega \left[\widetilde{\Gamma}^\phi_{ij}\,\widetilde{S}^{-1}_{jk}\,\phi^*_k(\,\chi_\varepsilon(\mathbf{r})\,)\frac{d}{d\varepsilon}\left[\left(-\frac{1}{2}\nabla^2_{\mathbf{r}'} + V_{\text{eff}}(\rho(\,\chi_\varepsilon(\mathbf{r})\,))\right)\phi_i(\,\chi_\varepsilon(\mathbf{r})\,)\right]\,\det\left(\frac{\partial \mathbf{r}'}{\partial \mathbf{r}}\right)\right]\Bigg|_{\varepsilon=0} d\mathbf{r}\,,\\
I_5 &= 2\int_\Omega \left[\widetilde{\Gamma}^\phi_{ij}\,\widetilde{S}^{-1}_{jk}\,\phi^*_k(\,\chi_\varepsilon(\mathbf{r})\,)\left(-\frac{1}{2}\nabla^2_{\mathbf{r}'} + V_{\text{eff}}(\rho(\,\chi_\varepsilon(\mathbf{r})\,))\right)\phi_i(\,\chi_\varepsilon(\mathbf{r})\,)\frac{d}{d\varepsilon}\left[\det\left(\frac{\partial \mathbf{r}'}{\partial \mathbf{r}}\right)\right]\right]\Bigg|_{\varepsilon=0} d\mathbf{r}\,.
\end{aligned} \tag{5.17}$$

Each term in the above set of equations can be simplified using the relations in (5.13). To evaluate $\frac{d}{d\varepsilon}\widetilde{S}^{-1}_{jk}$ in I_2, consider the variational derivative of the relation $\widetilde{\boldsymbol{S}}\widetilde{\boldsymbol{S}}^{-1} = \boldsymbol{I}$ giving rise to

$$\frac{d}{d\varepsilon}\left(\widetilde{\boldsymbol{S}}\right)\widetilde{\boldsymbol{S}}^{-1} + \widetilde{\boldsymbol{S}}\frac{d}{d\varepsilon}\left(\widetilde{\boldsymbol{S}}^{-1}\right) = 0 \implies \frac{d}{d\varepsilon}\widetilde{\boldsymbol{S}}^{-1} = -\widetilde{\boldsymbol{S}}^{-1}\left(\frac{d}{d\varepsilon}\widetilde{\boldsymbol{S}}\right)\widetilde{\boldsymbol{S}}^{-1}\,. \tag{5.18}$$

$$\frac{d}{d\varepsilon}\widetilde{S}^{-1}_{jk}\bigg|_{\varepsilon=0} = \left[-\widetilde{S}^{-1}_{jp} \int\limits_{\Omega} \left(\frac{d}{d\varepsilon} \left[\phi^*_p(\,\chi_\varepsilon(\mathbf{r})\,)\phi_q(\,\chi_\varepsilon(\mathbf{r})\,)\,\det\left(\frac{\partial \mathbf{r}'}{\partial \mathbf{r}}\right)\right]\,d\mathbf{r}\right)\,\widetilde{S}^{-1}_{qk}\right]\bigg|_{\varepsilon=0}. \tag{5.19}$$

We further simplify the above using chain rule to get

$$\begin{aligned}\frac{d}{d\varepsilon}\widetilde{S}^{-1}_{jk}\bigg|_{\varepsilon=0} = -\widetilde{S}^{-1}_{jp}\bigg|_{\varepsilon=0} \int\limits_{\Omega} \frac{d}{d\varepsilon}\Big[\phi^*_p(\,\chi_\varepsilon(\mathbf{r})\,)\phi_q(\,\chi_\varepsilon(\mathbf{r})\,)\Big]\bigg|_{\varepsilon=0} d\mathbf{r}\;\; \widetilde{S}^{-1}_{qk}\bigg|_{\varepsilon=0} \\ - \widetilde{S}^{-1}_{jp}\bigg|_{\varepsilon=0} \int\limits_{\Omega} \left(\phi^*_p(\mathbf{r})\phi_q(\mathbf{r})\frac{\partial \Upsilon_s(\mathbf{r})}{\partial r_s}\right)\,d\mathbf{r}\;\; \widetilde{S}^{-1}_{qk}\bigg|_{\varepsilon=0}.\end{aligned} \tag{5.20}$$

Hence the expression for I_2 can be simplified to be

$$\begin{aligned}I_2 = 2\int\limits_{\Omega} \Gamma^{\phi}_{ij}\,\frac{d}{d\varepsilon}\left(S^{-1}_{jk}(\,\chi_\varepsilon(\mathbf{r})\,)\right)\bigg|_{\varepsilon=0} \phi^*_k(\mathbf{r})\left(-\frac{1}{2}\nabla^2_{\mathbf{r}} + V_{\text{eff}}(\rho(\mathbf{r}))\right)\phi_i(\mathbf{r})\,d\mathbf{r} \\ - 2\int\limits_{\Omega} \Gamma^{\phi}_{ij}\,S^{-1}_{jp}\,\left(\int\limits_{\Omega}\phi_p(\mathbf{r})\,\phi_q(\mathbf{r})\,\nabla.\boldsymbol{\Upsilon}\;d\mathbf{r}\right)\,S^{-1}_{qk}\,\phi^*_k(\mathbf{r})\left(-\frac{1}{2}\nabla^2_{\mathbf{r}} + V_{\text{eff}}(\rho(\mathbf{r}))\right)\phi_i(\mathbf{r})\,d\mathbf{r}\,.\end{aligned}$$

Consider the term I_4 in which we evaluate the term

$$\frac{d}{d\varepsilon}\left[\left(-\frac{1}{2}\nabla^2_{\mathbf{r}'}\phi_i(\,\chi_\varepsilon(\mathbf{r})\,) + V_{\text{eff}}(\rho(\,\chi_\varepsilon(\mathbf{r})\,))\phi_i(\,\chi_\varepsilon(\mathbf{r})\,)\right)\right]\bigg|_{\varepsilon=0} \tag{5.21}$$

by first evaluating $\frac{d}{d\varepsilon}\left(-\frac{1}{2}\nabla^2_{\mathbf{r}'}\phi_i(\,\chi_\varepsilon(\mathbf{r})\,)\right)\Big|_{\varepsilon=0}$ as

$$\frac{d}{d\varepsilon}\left(-\frac{1}{2}\frac{\partial}{\partial r'_p}\left(\frac{\partial\phi_i(\,\chi_\varepsilon(\mathbf{r})\,)}{\partial r'_p}\right)\right)\bigg|_{\varepsilon=0} = \frac{d}{d\varepsilon}\left(-\frac{1}{2}\frac{\partial}{\partial r_m}\left(\frac{\partial\phi_i(\,\chi_\varepsilon(\mathbf{r})\,)}{\partial r_l}\frac{\partial r_l}{\partial r'_p}\right)\frac{\partial r_m}{\partial r'_p}\right)\bigg|_{\varepsilon=0}$$

$$= \frac{d}{d\varepsilon}\left(-\frac{1}{2}\frac{\partial}{\partial r_p}\left(\frac{\partial\phi_i(\,\chi_\varepsilon(\mathbf{r})\,)}{\partial r_p}\right)\right)\bigg|_{\varepsilon=0} + \left(\frac{\partial^2\phi_i(\mathbf{r})}{\partial r_m\,\partial r_l}\right)\frac{\partial\Upsilon_m(\mathbf{r})}{\partial r_l} + \frac{1}{2}\left(\frac{\partial\phi_i(\mathbf{r})}{\partial r_l}\right)\frac{\partial^2\Upsilon_l}{\partial r_p\,\partial r_p},$$

using the expressions in (5.13) in conjunction with chain rules and product rules for derivatives. Finally we have

$$\frac{d}{d\varepsilon}\left(-\frac{1}{2}\nabla^2_{\mathbf{r}'}\phi_i(\,\chi_\varepsilon(\mathbf{r})\,)\right)\Big|_{\varepsilon=0} = \frac{d}{d\varepsilon}\left(-\frac{1}{2}\nabla^2_{\mathbf{r}}\phi_i(\,\chi_\varepsilon(\mathbf{r})\,)\right)\Big|_{\varepsilon=0} + \nabla(\nabla\phi_i) : \nabla\boldsymbol{\Upsilon} + \frac{1}{2}\nabla\phi_i \,.\, \nabla^2\boldsymbol{\Upsilon}\,.$$

Hence the expression for I_4 can be simplified to be

$$\begin{aligned} I_4 = {} & 2\int_\Omega \Gamma^\phi_{ij}\, S^{-1}_{jk}\, \phi^*_k(\mathbf{r})\left(-\frac{1}{2}\nabla^2_{\mathbf{r}} + V_{\text{eff}}(\rho(\mathbf{r}))\right)\frac{d}{d\varepsilon}\left[\phi_i(\,\chi_\varepsilon(\mathbf{r})\,)\right]\Big|_{\varepsilon=0} d\mathbf{r} \\ & + 2\int_\Omega \Gamma^\phi_{ij}\, S^{-1}_{jk}\, \phi^*_k(\mathbf{r})\,\frac{d}{d\varepsilon}\left[V_{\text{eff}}(\rho(\,\chi_\varepsilon(\mathbf{r})\,)\right]\Big|_{\varepsilon=0}\phi_i(\mathbf{r})\, d\mathbf{r} \\ & + 2\int_\Omega \Gamma^\phi_{ij}\, S^{-1}_{jk}\, \phi^*_k(\mathbf{r})\left[\nabla(\nabla\phi_i) : \nabla\boldsymbol{\Upsilon} \;+\; \frac{1}{2}\nabla\phi_i \,.\, \nabla^2\boldsymbol{\Upsilon}\right]\, d\mathbf{r}\,. \end{aligned} \tag{5.22}$$

Using the relation between $\rho(\mathbf{r})$ and $\{\phi_i\mathbf{r})\}$ from (5.9c), we have

$$\begin{aligned} I_4 = {} & 2\int_\Omega \Gamma^\phi_{ij}\, S^{-1}_{jk}\, \phi^*_k(\mathbf{r})\left(-\frac{1}{2}\nabla^2_{\mathbf{r}} + V_{\text{eff}}(\rho(\mathbf{r}))\right)\frac{d}{d\varepsilon}\left[\phi_i(\,\chi_\varepsilon(\mathbf{r})\,)\right]\Big|_{\varepsilon=0} d\mathbf{r} \\ & + \int \rho(\mathbf{r})\frac{d}{d\varepsilon}\left[V_{\text{eff}}(\rho(\,\chi_\varepsilon(\mathbf{r})\,)\right]\Big|_{\varepsilon=0} d\mathbf{r} \;+\; 2\int_\Omega \Gamma^\phi_{ij}\, S^{-1}_{jk}\, \phi^*_k(\mathbf{r})\left[\nabla(\nabla\phi_i) : \nabla\boldsymbol{\Upsilon} \;+\; \frac{1}{2}\nabla\phi_i \,.\, \nabla^2\boldsymbol{\Upsilon}\right]\, d\mathbf{r}\,. \end{aligned}$$

Using the relation

$$\nabla \,.\, \left[\phi^*_k(\mathbf{r})\,\nabla\boldsymbol{\Upsilon}^T\,\nabla\phi_i(\mathbf{r})\right] = \phi^*_k(\mathbf{r})\,[\nabla(\nabla\phi_i) : \nabla\boldsymbol{\Upsilon}] + \phi^*_k(\mathbf{r})\left[\nabla\phi_i \,.\, \nabla^2\boldsymbol{\Upsilon}\right] + \nabla\boldsymbol{\Upsilon} : (\nabla\phi_i \otimes \nabla\phi_k)\,,$$

the third term in I_4 can be written as

$$\begin{aligned} & 2\int_\Omega \Gamma^\phi_{ij}\, S^{-1}_{jk}\, \phi^*_k(\mathbf{r})\left[\nabla(\nabla\phi_i) : \nabla\boldsymbol{\Upsilon} \;+\; \frac{1}{2}\nabla\phi_i \,.\, \nabla^2\boldsymbol{\Upsilon}\right]\, d\mathbf{r} \\ & = \int_\Omega \Gamma^\phi_{ij}\, S^{-1}_{jk}\, \phi^*_k(\mathbf{r})\,[\nabla(\nabla\phi_i) : \nabla\boldsymbol{\Upsilon}]\; d\mathbf{r} + \int_\Omega \Gamma^\phi_{ij}\, S^{-1}_{jk}\, \nabla \,.\, \left[\phi^*_k(\mathbf{r})\,\nabla\boldsymbol{\Upsilon}^T\,\nabla\phi_i(\mathbf{r})\right]\, d\mathbf{r} \\ & - \int_\Omega \Gamma^\phi_{ij}\, S^{-1}_{jk}\; [(\nabla\phi_i \otimes \nabla\phi_k) : \nabla\boldsymbol{\Upsilon}]\, d\mathbf{r}\,. \end{aligned}$$

Using the divergence theorem and setting the boundary terms involving wavefunctions to zero, we have the final simplified expression for I_4 to be

$$\begin{aligned} I_4 = & 2 \int_{\Omega} \Gamma^{\phi}_{ij} \, S^{-1}_{jk} \, \phi^*_k(\mathbf{r}) \left(-\frac{1}{2}\nabla^2_{\mathbf{r}} + V_{\text{eff}}(\rho(\mathbf{r})) \right) \frac{d}{d\varepsilon} \left[\phi_i(\, \chi_\varepsilon(\mathbf{r}) \,) \right] \Big|_{\varepsilon=0} d\mathbf{r} \\ & + \int \rho(\mathbf{r}) \frac{d}{d\varepsilon} \left[V_{\text{eff}}(\rho(\, \chi_\varepsilon(\mathbf{r}) \,)) \right] \Big|_{\varepsilon=0} d\mathbf{r} + \int_{\Omega} \Gamma^{\phi}_{ij} \, S^{-1}_{jk} \, \phi^*_k(\mathbf{r}) \left[\nabla(\nabla\phi_i) : \nabla \boldsymbol{\Upsilon} \right] \, d\mathbf{r} \\ & - \int_{\Omega} \Gamma^{\phi}_{ij} \, S^{-1}_{jk} \, \left[(\nabla\phi_i \otimes \nabla\phi_k) : \nabla \boldsymbol{\Upsilon} \right] \, d\mathbf{r} \end{aligned} \tag{5.23}$$

Finally I_5 can be easily evaluated as

$$I_5 = 2 \int_{\Omega} \Gamma^{\phi}_{ij} \, S^{-1}_{jk} \, \phi^*_k(\mathbf{r}) \left(-\frac{1}{2}\nabla^2_{\mathbf{r}} + V_{\text{eff}}(\rho(\mathbf{r})) \right) \phi_i(\mathbf{r}) \, (\boldsymbol{I} : \nabla \boldsymbol{\Upsilon}) \, d\mathbf{r} \tag{5.24}$$

Collecting all the terms from I_1 to I_5, we can write the generalized directional derivative of $E_b(\, \chi_\varepsilon(\mathbf{r}) \,)$ as

$$\frac{d}{d\varepsilon} E_b(\, \chi_\varepsilon(\mathbf{r}) \,) \Big|_{\varepsilon=0} = J_1 + J_2 + J_3 + J_4 \tag{5.25}$$

where

$$\begin{aligned} J_1 = & 2 \int_{\Omega} \left(\frac{d}{d\varepsilon} \left(\widetilde{\Gamma}^{\phi}_{ij} \right) \Big|_{\varepsilon=0} S^{-1}_{jk} \, \phi^*_k(\mathbf{r}) \left(-\frac{1}{2}\nabla^2_{\mathbf{r}} + V_{\text{eff}}(\rho(\mathbf{r})) \right) \phi_i(\mathbf{r}) \right) \, d\mathbf{r} \\ J_2 = & 2 \int_{\Omega} \Gamma^{\phi}_{ij} \, \frac{d}{d\varepsilon} \left[S^{-1}_{jk}(\, \chi_\varepsilon(\mathbf{r}) \,) \right] \Big|_{\varepsilon=0} \phi^*_k(\mathbf{r}) \left(-\frac{1}{2}\nabla^2_{\mathbf{r}} + V_{\text{eff}}(\rho(\mathbf{r})) \right) \phi_i(\mathbf{r}) \, d\mathbf{r} \\ & + 2 \int_{\Omega} \Gamma^{\phi}_{ij} \, S^{-1}_{jk} \, \frac{d}{d\varepsilon} \left[\phi^*_k(\, \chi_\varepsilon(\mathbf{r}) \,) \right] \Big|_{\varepsilon=0} \left(-\frac{1}{2}\nabla^2_{\mathbf{r}} + V_{\text{eff}}(\rho(\mathbf{r})) \right) \phi_i(\mathbf{r}) \, d\mathbf{r} \\ & + 2 \int_{\Omega} \Gamma^{\phi}_{ij} \, S^{-1}_{jk} \, \phi^*_k(\mathbf{r}) \left(-\frac{1}{2}\nabla^2_{\mathbf{r}} + V_{\text{eff}}(\rho(\mathbf{r})) \right) \frac{d}{d\varepsilon} \left[\phi_i(\, \chi_\varepsilon(\mathbf{r}) \,) \right] \Big|_{\varepsilon=0} d\mathbf{r} \end{aligned}$$

$$J_3 = -2\int_{\Omega}\Gamma^{\phi}_{ij}\,S^{-1}_{jp}\,\left(\int_{\Omega}\phi_p(\mathbf{r})\,\phi_q(\mathbf{r})\,\nabla.\boldsymbol{\Upsilon}\;d\mathbf{r}\right)S^{-1}_{qk}\,\phi^{*}_{k}(\mathbf{r})\left(-\frac{1}{2}\nabla^2_{\mathbf{r}}+V_{\text{eff}}(\rho(\mathbf{r}))\right)\phi_i(\mathbf{r})\,d\mathbf{r}$$
$$+\int_{\Omega}\Gamma^{\phi}_{ij}\,S^{-1}_{jk}\,\phi^{*}_{k}(\mathbf{r})\,[\nabla(\nabla\phi_i):\nabla\boldsymbol{\Upsilon}]\;d\mathbf{r}-\int_{\Omega}\Gamma^{\phi}_{ij}\,S^{-1}_{jk}\;[(\nabla\phi_i\otimes\nabla\phi_k):\nabla\boldsymbol{\Upsilon}]\;d\mathbf{r}$$
$$+2\int_{\Omega}\Gamma^{\phi}_{ij}\,S^{-1}_{jk}\,\phi^{*}_{k}(\mathbf{r})\left(-\frac{1}{2}\nabla^2_{\mathbf{r}}+V_{\text{eff}}(\rho(\mathbf{r}))\right)\phi_i(\mathbf{r})\,(\boldsymbol{I}:\nabla\boldsymbol{\Upsilon})\,d\mathbf{r}$$
$$J_4 = \int_{\Omega}\rho(\mathbf{r})\frac{d}{d\varepsilon}\left[V_{\text{eff}}(\rho(\,\chi_\varepsilon(\mathbf{r})\,)\right]\Big|_{\varepsilon=0}d\mathbf{r}$$

Using a similar procedure one can evaluate the generalized directional derivative of $E_{\text{veff}}(\,\chi_\varepsilon(\mathbf{r})\,)$ to be

$$\frac{d}{d\varepsilon}E_{\text{veff}}(\,\chi_\varepsilon(\mathbf{r})\,)\Big|_{\varepsilon=0} = K_1+K_2+K_3$$

where

$$K_1 = -\int_{\Omega}\frac{d}{d\varepsilon}\rho(\,\chi_\varepsilon(\mathbf{r})\,)\Big|_{\varepsilon=0}V_{\text{eff}}(\rho(\mathbf{r}))\,d\mathbf{r}$$
$$K_2 = -\int_{\Omega}\rho(\mathbf{r})\,\frac{d}{d\varepsilon}\left[V_{\text{eff}}(\rho(\,\chi_\varepsilon(\mathbf{r})\,)\right]\Big|_{\varepsilon=0}d\mathbf{r}$$
$$K_3 = -\int_{\Omega}\rho(\mathbf{r})\,V_{\text{eff}}(\rho(\mathbf{r}))\,(\boldsymbol{I}:\nabla\boldsymbol{\Upsilon})\,d\mathbf{r}$$

Similarly

$$\frac{d}{d\varepsilon}E_{\text{xc}}(\,\chi_\varepsilon(\mathbf{r})\,)\Big|_{\varepsilon=0} = L_1+L_2$$

where

$$L_1 = \int_{\Omega}\frac{d}{d\varepsilon}\rho(\,\chi_\varepsilon(\mathbf{r})\,)\Big|_{\varepsilon=0}V_{\text{xc}}(\rho(\mathbf{r}))\,d\mathbf{r}$$
$$L_2 = \int_{\Omega}F(\rho(\mathbf{r}))(\boldsymbol{I}:\nabla\boldsymbol{\Upsilon})\,d\mathbf{r}$$

We now consider the generalized directional derivatives of $E_{\bar{\varphi}}(\rho,\mathbf{R})$ and $E_{\bar{\nu}}(\mathbf{R})$.

To this end, we recall that the mapping $\chi_\varepsilon(\mathbf{r})$ in the compact support of the nucleus is restricted to rigid body motion and we have $\chi_\varepsilon(\mathbf{r}) = \boldsymbol{Q}_\varepsilon^I \mathbf{r} + \boldsymbol{T}_\varepsilon^I$ for $I = 1 \cdots N_a$ in the compact support of $b_I(\mathbf{r}, \mathbf{R})$ with $b_I(\mathbf{r}, \mathbf{R}) = b_I(|\mathbf{r} - \mathbf{R}|)$. Hence

$$b(|\mathbf{r}' - \mathbf{R}'|) = \sum_{I=1}^{N_a} Z_I \widetilde{\delta}(|\mathbf{r}' - \mathbf{R}'_I|) = \sum_{I=1}^{N_a} Z_I \widetilde{\delta}(|\boldsymbol{Q}_\varepsilon^I \mathbf{r} - \boldsymbol{Q}_\varepsilon^I \mathbf{R}_I|)$$
$$= \sum_{I=1}^{N_a} Z_I \widetilde{\delta}(|\mathbf{r} - \mathbf{R}_I|) = b(|\mathbf{r} - \mathbf{R}|)$$

Also we note that in the regions where $b \neq 0$, we have $\boldsymbol{Q}_0 = \boldsymbol{I}$, the identity matrix and hence $\nabla \cdot \boldsymbol{\Upsilon} = \operatorname{tr}\left(\frac{d}{d\varepsilon}\boldsymbol{Q}_\varepsilon\Big|_{\varepsilon=0}\right) = \operatorname{tr}\left(-\frac{d}{d\varepsilon}\boldsymbol{Q}_\varepsilon^T\Big|_{\varepsilon=0}\right) \implies \nabla \cdot \boldsymbol{\Upsilon} = 0$. Using the fact that (i) $b(\mathbf{r}, \mathbf{R})$ is independent of ε, (ii) $\nabla \cdot \boldsymbol{\Upsilon} = 0$ in the region when $b \neq 0$ and (iii) $\bar{\varphi}$ satisfies the Euler-Lagrange equations in (3.25c), we have

$$\frac{d}{d\varepsilon} E_{\bar{\varphi}}(\, \chi_\varepsilon(\mathbf{r})\,)\Big|_{\varepsilon=0} = M_1 + M_2$$

where

$$M_1 = \int_\Omega \left(-\frac{1}{8\pi}|\nabla\bar{\varphi}|^2 + \rho\bar{\varphi}\right)(\boldsymbol{I} : \nabla\boldsymbol{\Upsilon})\, d\mathbf{r} + \frac{1}{4\pi}\int_\Omega (\nabla\bar{\varphi} \otimes \nabla\bar{\varphi}) : \nabla\boldsymbol{\Upsilon}\, d\mathbf{r}$$
$$M_2 = \int_\Omega \frac{d}{d\varepsilon}\rho(\, \chi_\varepsilon(\mathbf{r})\,)\Big|_{\varepsilon=0} \bar{\varphi}(\mathbf{r})\, d\mathbf{r}$$

To compute the directional derivation of $E_{\bar{\boldsymbol{\nu}}}$, we make an additional assumption that the simulation domain is large enough to make the surface contributions to $E_{\bar{\boldsymbol{\nu}}}$ lower order. Using the same procedure as above, we obtain

$$\frac{d}{d\varepsilon} E_{\bar{\boldsymbol{\nu}}}(\, \chi_\varepsilon(\mathbf{r})\,)\Big|_{\varepsilon=0} = N_1$$

$$N_1 = \sum_{I=1}^{N_a} \int_{\Omega_I} \frac{1}{8\pi}|\nabla\bar{\nu}^I|^2 (\boldsymbol{I} : \nabla\boldsymbol{\Upsilon})\, d\mathbf{r} - \frac{1}{4\pi}\int_{\Omega_I} \left(\nabla\bar{\nu}^I \otimes \nabla\bar{\nu}^I\right) : \nabla\boldsymbol{\Upsilon}\, d\mathbf{r}$$

The directional derivative in the case of E_{ent} is given by

$$\left.\frac{d}{d\varepsilon}E_{\text{ent}}\right|_{\varepsilon=0} = -2\,\sigma\,\text{tr}\left[\left.\frac{d}{d\varepsilon}\widetilde{\mathbf{\Gamma}^{\phi}}\right|_{\varepsilon=0}\ln\left(\frac{\mathbf{\Gamma}^{\phi}}{\boldsymbol{I}-\mathbf{\Gamma}^{\phi}}\right)\right]$$

Finally, the directional derivative of $\mathcal{E}_c(\,\chi_\varepsilon(\mathbf{r})\,)$ is given by

$$\left.\frac{d}{d\varepsilon}\mathcal{E}_c(\,\chi_\varepsilon(\mathbf{r})\,)\right|_{\varepsilon=0} = \left.\frac{d}{d\varepsilon}\mathcal{F}(\,\chi_\varepsilon(\mathbf{r})\,)\right|_{\varepsilon=0} - 2\,\mu\,\text{tr}\left(\left.\frac{d}{d\varepsilon}\widetilde{\mathbf{\Gamma}^{\phi}}\right|_{\varepsilon=0}\right)$$

Collecting the directional derivatives of all the energy terms involved in $\mathcal{E}_c(\,\chi_\varepsilon(\mathbf{r})\,)$:

$$\begin{aligned}\left.\frac{d}{d\varepsilon}\mathcal{E}_c(\,\chi_\varepsilon(\mathbf{r})\,)\right|_{\varepsilon=0} =& J_1 + J_2 + J_3 + J_4 + K_1 + K_2 + K_3 + L_1 + L_2 + M_1 + M_2 + N_1 \\ &+ 2\,\sigma\,\text{tr}\left[\left.\frac{d}{d\varepsilon}\widetilde{\mathbf{\Gamma}^{\phi}}\right|_{\varepsilon=0}\ln\left(\frac{\mathbf{\Gamma}^{\phi}}{\boldsymbol{I}-\mathbf{\Gamma}^{\phi}}\right)\right] - 2\,\mu\,\text{tr}\left(\left.\frac{d}{d\varepsilon}\widetilde{\mathbf{\Gamma}^{\phi}}\right|_{\varepsilon=0}\right) \qquad (5.26)\end{aligned}$$

Now we make the following observations:

- Since $\{\phi_i(\mathbf{r})\}$ span the occupied eigensubspace of the Kohn-Sham Hamiltonian, one can easily show that $J_2 = 0$.
- The term J_4 equals negative of K_2 and hence $J_4 + K_2 = 0$.
- The terms $L_1 + M_2$ equals negative of K_1 and hence $K_1 + L_1 + M_2 = 0$.
- The term J_1 along with the last two terms of equation (5.26) equals zero since $\mathbf{\Gamma}^{\phi}$ satisfies the Fermi-Dirac distribution in equation (4.37).

Hence the full configurational force for the Kohn-Sham DFT problem is given by

$$\left.\frac{d}{d\varepsilon}\mathcal{E}_c(\,\chi_\varepsilon(\mathbf{r})\,)\right|_{\varepsilon=0} = J_3 + K_3 + L_2 + M_1 + N_1 \qquad (5.27)$$

$$
\begin{aligned}
J_3 = &-2\int_{\Omega}\Gamma^{\phi}_{ij}\,S^{-1}_{jp}\left(\int_{\Omega}\phi_p(\mathbf{r})\,\phi_q(\mathbf{r})\,(\boldsymbol{I}:\nabla\boldsymbol{\Upsilon})\,d\mathbf{r}\right)S^{-1}_{qk}\,\phi^{*}_{k}(\mathbf{r})\left(-\frac{1}{2}\nabla^2_{\mathbf{r}}+V_{\text{eff}}(\rho(\mathbf{r}))\right)\phi_i(\mathbf{r})\,d\mathbf{r}\\
&+\int_{\Omega}\Gamma^{\phi}_{ij}\,S^{-1}_{jk}\,\phi^{*}_{k}(\mathbf{r})\,[\nabla(\nabla\phi_i):\nabla\boldsymbol{\Upsilon}]\;d\mathbf{r}-\int_{\Omega}\Gamma^{\phi}_{ij}\,S^{-1}_{jk}\;[(\nabla\phi_i\otimes\nabla\phi_k):\nabla\boldsymbol{\Upsilon}]\;d\mathbf{r}\\
&+2\int_{\Omega}\Gamma^{\phi}_{ij}\,S^{-1}_{jk}\,\phi^{*}_{k}(\mathbf{r})\left(-\frac{1}{2}\nabla^2_{\mathbf{r}}+V_{\text{eff}}(\rho(\mathbf{r}))\right)\phi_i(\mathbf{r})\,(\boldsymbol{I}:\nabla\boldsymbol{\Upsilon})\,d\mathbf{r}\\
K_3 = &-\int_{\Omega}\rho(\mathbf{r})\,V_{\text{eff}}(\rho(\mathbf{r}))\,(\boldsymbol{I}:\nabla\boldsymbol{\Upsilon})\,d\mathbf{r}\,,\\
L_2 = &\int_{\Omega}F(\rho(\mathbf{r}))(\boldsymbol{I}:\nabla\boldsymbol{\Upsilon})\,d\mathbf{r}\,,\\
M_1 = &\int_{\Omega}\left(-\frac{1}{8\pi}|\nabla\bar{\varphi}|^2+\rho\bar{\varphi}\right)(\boldsymbol{I}:\nabla\boldsymbol{\Upsilon})\,d\mathbf{r}+\frac{1}{4\pi}\int_{\Omega}(\nabla\bar{\varphi}\otimes\nabla\bar{\varphi}):\nabla\boldsymbol{\Upsilon}\,d\mathbf{r}\,,\\
N_1 = &\sum_{I=1}^{N_a}\int_{\Omega_I}\frac{1}{8\pi}|\nabla\bar{\nu}^I|^2(\boldsymbol{I}:\nabla\boldsymbol{\Upsilon})\,d\mathbf{r}-\frac{1}{4\pi}\int_{\Omega_I}\left(\nabla\bar{\nu}^I\otimes\nabla\bar{\nu}^I\right):\nabla\boldsymbol{\Upsilon}\,d\mathbf{r}\,.
\end{aligned}
$$

In any numerical calculation involving self-consistent field iteration (SCF), the input electron-density $\rho^{\text{in}}(\mathbf{r})$ for a given iteration is never exactly equal to the output electron-density $\rho(\mathbf{r})$ computed from the wavefunctions till self-consistency is achieved to a very tight numerical tolerance. To this end, we note that $K_1+L_1+M_2$ is not exactly equal to zero and gives rise to non self-consistent force

$$
\begin{aligned}
F_{\text{NSCF}} &= \int_{\Omega}\frac{d}{d\varepsilon}\rho(\,\chi_{\varepsilon}(\mathbf{r})\,)\Big|_{\varepsilon=0}\left(V_{\text{eff}}(\rho)-V_{\text{eff}}(\rho^{\text{in}})\right)\,d\mathbf{r}\,, &(5.28)\\
&= \int_{\Omega}(\nabla\rho(\mathbf{r})\,.\,\boldsymbol{\Upsilon})\left(V_{\text{eff}}(\rho)-V_{\text{eff}}(\rho^{\text{in}})\right)\;d\mathbf{r} &(5.29)
\end{aligned}
$$

which is added to the force in equation (5.27). We also remark that the expression in (5.27) accounts for the change in the volume of the crystal and can hence capture the state of stress in a crystal. It will be zero only when the crystal is in equilibrium and under no externally applied stress.

In a finite-element setting, when the space is discretized with M nodes, we have

the discretized form of $\Upsilon_j(\mathbf{r}) = \Upsilon_j^k N^k(\mathbf{r})$ where $N^k(\mathbf{r})$ is the real space shape function of node k and Υ_j^k is the perturbation of node k in the j^{th} direction. We obtain the configurational force at node i of the discretization in the j^{th} direction (f_j^i) by setting $\Upsilon_j^i = 1$ and 0 otherwise in equation (5.27) and the physical force at node i is the negative of the Eshelbian gradient ($-f_j^i$). We note that this force contains both Hellmann-Feynman force on the atoms along with the incomplete basis-set forces, the latter primarily arising from the need to minimize the energy with respect to the nodal configuration for a fixed number of nodes.

CHAPTER VI

Conclusions

6.1 Summary

The present thesis developed new computationally efficient and robust finite-element based methods (DFT-FE) in a manner that enable large-scale Kohn-Sham DFT calculations on materials systems involving tens of thousands of electrons on parallel computing architectures. The proposed DFT-FE exploits the adaptive nature of the finite-element basis sets and enables both pseudopotential and all-electron DFT calculations on complex geometries and boundary conditions on a single footing, thus paving the way to study more complex systems, than possible heretofore.

The first part of the thesis (Chapter III) developed a real-space adaptive higher-order spectral finite-element based self-consistent framework that enables all-electron, pseudopotential calculations with complex boundary conditions on a single footing. To this end, we first derived error estimates for the finite-element discretization error in the ground-state energy in terms of the ground-state electronic fields (wavefunctions and electrostatic potential) and characteristic mesh-size. These error estimates and the *a priori* knowledge of the asymptotic solutions of far-field electronic fields were used to construct mesh coarsening rates for the various benchmark problems considered. Since the finite-element discretization of the Kohn-Sham problem results in a generalized eigenvalue problem, which is computationally expensive to solve, we

presented an approach to trivially transform this into a standard eigenvalue problem by using spectral finite-elements in conjunction with the Gauss-Lobatto quadrature rules that results in a diagonal overlap matrix. We subsequently examined two different strategies to solve the Kohn-Sham problem: (i) explicit computation of eigenvectors at every self-consistent field iteration; (ii) a Chebyshev filtering approach that directly computes the occupied eigenspace. Our investigations suggest that the use of spectral finite-elements and Gauss-Lobatto rules in conjunction with Chebyshev acceleration techniques to compute the eigenspace gives a $10-20$ fold computational advantage, even for modest materials system sizes, in comparison to traditional methods of solving the standard eigenvalue problem where the eigenvectors are computed explicitly. Further, the proposed approach has been observed to provide a staggering $100-200$ fold computational advantage over the solution of a generalized eigenvalue problem that does not take advantage of the spectral finite-element discretization and Gauss-Lobatto quadrature rules. Using the derived error estimates and the *a priori* knowledge of the asymptotic solutions of far-field electronic fields, we constructed close to optimal finite-element meshes for the various benchmark problems, which include all-electron calculations on systems comprising of boron atom and methane molecule, and local pseudopotential calculations on barium cluster and bulk calcium crystal. We employed the Chebyshev filtering approach on the transformed standard eigenvalue problem in our numerical investigations to study the computational efficiency of higher-order finite-element discretizations. To this end, we first investigated the performance of higher-order elements by studying the convergence rates of linear tetrahedral element and hexahedral spectral-elements up to sixth-order. In all the benchmark problems considered, we observed close to optimal rates of convergence for the finite-element approximation in the ground-state energy. Importantly, we note that optimal rates of convergence were obtained for all orders of finite-element approximations, considered in this work, even for all-electron Kohn-Sham DFT calculations

with Coulomb-singular potentials, the mathematical analysis of which, to the best of our knowledge, is an open question to date and has not been numerically demonstrated elsewhere. We further investigated the computational efficiency afforded by the use of higher-order finite-elements up to eighth-order spectral-elements. To this end, we used the mesh coarsening rates determined from the proposed mesh adaption scheme and studied the CPU time required to solve the benchmark problems. Our results demonstrate that significant computational savings can be realized by using higher-order elements. For instance, a staggering $1000-$fold savings in terms of CPU-time are realized by using sixth-order hexahedral spectral-element in comparison to linear tetrahedral element. We also note that the point of diminishing returns in terms of computational efficiency was determined to be around sixth-order for the benchmark systems we examined. The degree of freedom advantage of higher-order finite-elements is nullified by the increasing per basis-function costs beyond this point. To further assess the performance of higher-order finite-elements, we extended our investigations to study large materials systems and compared the computational CPU-time with commercially available plane-wave and Gaussian basis codes. We first conducted simulations on aluminium clusters with local pseudopotential containing 172 atoms and 666 atoms using sixth-order spectral-element in our implementation, as well as, the plane-wave basis in ABINIT package solved to a similar relative accuracy in the ground-state energy. These studies showed that the computational CPU-time required for the finite-element simulations is lesser in comparison to plane-wave basis sets underscoring the fact that higher-order finite-elements can compete with plane-waves, at least in non-periodic settings, when employed in conjunction with efficient solution strategies. Furthermore, we were able to compute the electronic structure of an aluminium cluster containing $1,688$ atoms by employing the sixth-order spectral-element, which was not possible using ABINIT due to large memory requirements. Next, we examined the computational efficiency in the case of all-electron calculations

on a graphene sheet containing 100 atoms and tris (bipyridine) ruthenium complex containing 61 atoms. The all-electron calculations were conducted using Gaussian DFT basis sets and the fourth-order spectral-element basis, and we observed that the computational time for the finite-element basis was $10-$fold greater than the Gaussian basis. Good scalability of the implementation up to a few hundred processors is also demonstrated.

The second part of the thesis (Chapter IV) formulated a subspace projection technique in the framework of higher-order spectral finite-element discretization of the Kohn-Sham DFT problem in order to reduce the computational complexity involved in traditional solution approaches that compute the canonical orthonormal Kohn-Sham eigenfunctions. The proposed approach provides a single unified framework to handle both insulating and metallic materials system. Further, both pseudopotential as well as all-electron calculations can be conducted using the proposed methodology. The development of the proposed approach involved bringing together four main ideas. Firstly, we took advantage of the representation of Kohn-Sham Hamiltonian and the corresponding wave-functions in Löwdin orthonormalized finite-element basis constructed using spectral finite-elements in conjunction with Gauss-Lobatto-Legendre quadrature rules. The adaptive nature of the finite-element basis was crucial for efficiently handling all-electron DFT calculations. Secondly, we employed the Chebyshev filtering approach [66] to directly compute an approximation of the occupied eigenspace in each SCF iteration. In this Chebyshev filtering step, we effectively exploited the finite-element structure to conduct matrix-vector products, associated with the action of the Chebyshev filter on a space of localized trial wavefunctions from previous SCF iteration, in linear-scaling complexity. We subsequently employed the localization procedure proposed by Garcia et al. [36] to compute atom-centered non-orthogonal localized basis (localized wavefunctions) spanning the Chebyshev filtered subspace. We employed an adaptive tolerance, where looser tolerances are used in

initial iteration and progressively become tighter as the SCF approaches convergence, to provide a compact support for the localized wavefunctions. The use of adaptive tolerance provides strict control on the accuracy of the calculation, which is reflected in our benchmark calculations. Finally, we computed the projection of the Hamiltonian into the non-orthogonal localized basis, and used the Fermi-operator expansion [35] to compute the relevant quantities, including the finite-temperature density matrix, electron density and the band energy. We note that as the Fermi-operator expansion is computed in the projected subspace, the spectral width of the projected Hamiltonian is bounded—$\mathcal{O}(1\,Ha)$ for pseudopotential calculations and $\mathcal{O}(10\,Ha)$ for all-electron calculations—and can efficiently be computed for both pseudopotential and all-electron calculations. We demonstrated from complexity estimates that, for well-localized wavefunctions with a compact support, all operations in the proposed algorithm are linear-scaling in complexity. The accuracy and performance of the proposed method was investigated on three different materials system: (i) a series of aluminum nano-clusters up to 3430 atoms representing a metallic system; (ii) a series of alkane chains up to 7052 atoms representing an insulating system; (iii) a series of silicon nano-clusters up to 3920 electrons representing a semiconducting system. Pseudopotential calculations were conducted on aluminum nano-clusters and alkane chains, whereas all-electron calculations were performed on silicon nano-clusters. In all the cases, the proposed method provided ground-state energies that are in excellent agreement with reference calculations, with accuracies commensurate with chemical accuracy. From these benchmark calculations, the computational complexity of the proposed approach was computed to be $\mathcal{O}(N^{1.46})$ for aluminum nano-clusters, $\mathcal{O}(N^{1.18})$ for the alkane chains, and $\mathcal{O}(N^{1.75})$ for the all-electron silicon nano-clusters. The deviation from linear-scaling, in practice, is due to the use of adaptive tolerances with tighter tolerances in the later SCF iterations in order to ensure strict control on the accuracy of the calculations. This affects the scaling due to reduced sparsity

in the localized wavefunctions. We further note that using the proposed approach $\sim 10-$fold speedups were obtained with respect to reference benchmark calculations for the largest systems.

The third part of the thesis (Chapter V) developed configurational force approach for efficient computation of forces on atoms in Kohn-Sham DFT calculations. We derived the relevant expressions in a more general setting by using the non-orthogonal formulation of Kohn-Sham DFT, taking into account fractional occupancies via density matrix expressed in the non-orthogonal basis. We finally showed that the proposed configurational force approach for atomic relaxations provides a unified framework that captures atomic forces due to Hellmann-Feynman theorem, incomplete-basis-sets and non-self-consistency, and furthermore accounts for elastic stresses on periodic-cells on a single footing.

6.2 Future work and directions

The prospect of using higher-order spectral finite-elements as basis functions, in conjunction with the proposed solution methods, for Kohn-Sham DFT electronic structure calculations is indeed very promising. While finite-elements have the advantages of handling complex geometries and boundary conditions and exhibit good scalability on massively parallel computing platforms, their use has been limited in electronic structure calculations as their computational efficiency compared unfavorably to plane-wave and Gaussian basis functions. However, the proposed DFT-FE presents a useful direction for large-scale electronic structure calculations using finite-element discretization, thus opening up the possibility of studying large range of materials properties using DFT. However, this work leaves a number of interesting challenges/problems which could be worthwhile subjects for future investigation.

A posteriori mesh adaption: An *a priori* mesh-adaption technique was used to construct a optimal finite-element discretization of the DFT problem in this thesis. However, the error estimates derived in Chapter III can be modified in the spirit of [63] to develop an *a posteriori* mesh adaption scheme. This might result in increased computational efficiency of finite-element basis sets in simulations where *a priori* knowledge of electronic fields and region of interest is lacking. Further, the configurational force approach discussed in Chapter V can also be effectively used for *a posteriori* mesh adaption since the configurational force is obtained from the necessity of minimizing the energy with respect to the nodal configuration for a fixed number of nodes.

Enriched finite-elements: The locally refined meshes employed in all-electron calculations of the current work result in a very high upper bound of the spectrum of the Kohn-Sham Hamiltonian ($\sim \mathcal{O}(10^5)\ Ha$). This in turn demands a very high degree of Chebyshev polynomial to filter the occupied eigen-subspace, thus increasing its computational cost. One way to mitigate this issue is to explore the possibility of enriching the classical finite-element basis functions with single-atom wavefunctions obtained from a radial solution of the Kohn-Sham DFT problem. This can potentially allow us to use coarse finite-element meshes with mesh size close to that of a pseudopotential calculation thus improving the computational efficiency of all-electron calculations. Further reduced scaling behavior might be possible in the case of all-electron calculations by using enriched finite-elements.

Electronic structure in a bulk environment: An accurate understanding of the energetics of an isolated defect core in its bulk or exploring the nature of quantum-transport in an organic molecule in the presence of bulk electrodes in a nano-electronic device requires simulating the electronic structure of a given materials system in its bulk environment. The finite-element discretization readily offers this flexibility

of handling arbitrary boundary conditions and is exploited in a recent study [144] which is first of it kind, to quantify the dislocation core-energy solely from electronic-structure using orbital-free DFT theory(a theory in which electron-density is explicitly computed). However, simulating the electronic structure of a materials system in the presence of bulk environment in the context of Kohn-Sham DFT is not a straightforward problem as it is formulated in terms of single-particle wavefunctions and requires a careful approach. The ideas of localization and subspace projection proposed in this thesis can play a crucial role in formulating a solution to the problem. Efforts to formulate an elegant approach to this problem can assist in studying wide variety of problems in material science. These include estimating the dislocation core-energy of transition metals, its dependence on macroscopic strain, computation of Peierls barrier to dislocation glide, dislocation-solute interactions and their response to external strains and many more.

Quasi-continuum approach to Kohn-Sham DFT: The development of coarse-graining methodology for Kohn-Sham DFT along the lines of QC orbital-free DFT [145] is a very important problem for future investigations which would then enable study of defects generating long-range fields in transition metals, that are characterized by strongly localized core effects. The non-orthogonal localized real space finite-element formulation of Kohn-Sham DFT would be a natural starting point for developing a coarse graining strategy for Kohn-Sham DFT and forms a very important future research direction.

We also remark that incorporation of hybrid exchange correlation functionals into the existing real space finite-element framework and extensions of the current real-space finite-element formulation to time-dependent density functional theory would be of obvious interest for future investigations.

APPENDICES

APPENDIX A

Discrete formulation of electrostatic interactions in all-electron calculations

The electrostatic interaction energy in the discrete formulation is given by

$$E^h_{\text{electrostatic}} = \left[-\frac{1}{8\pi} \int\limits_{\Omega} |\nabla \varphi_h(\mathbf{r})|^2 \, d\mathbf{r} + \int\limits_{\Omega} (\rho_h(\mathbf{r}) + b(\mathbf{r})) \varphi_h(\mathbf{r}) \, d\mathbf{r} \right] - E^h_{\text{self}} \quad \text{where} \tag{A.1}$$

$$E^h_{\text{self}} = \frac{1}{2} \sum_{I=1}^{N_a} \int\limits_{\Omega} Z_I \delta(\mathbf{r} - \mathbf{R}_I) V_{h_I}(\mathbf{r}) \, d\mathbf{r} \ , \tag{A.2}$$

where φ_h denotes the total electrostatic potential field, corresponding to the electron-density ρ_h and nuclear charge distribution $b(\mathbf{r})$, computed in the finite-element basis. The nuclear potential corresponding to the I^{th} nuclear charge, i.e $Z_I \delta(\mathbf{r} - \mathbf{R}_I)$, computed in the finite-element basis is denoted by V_{h_I}. The nuclear charges located on the nodes of the finite-element triangulation are treated as point charges and the discreteness of the finite-element triangulation provides a regularization of the potential fields. However, the self-energy of the nuclei in this case is mesh-dependent and diverges upon mesh refinement. Thus, care must be taken to evaluate the total electrostatic potential φ_h and the nuclear potentials V_{h_I}, $I = 1, \ldots N_a$ on the same

finite-element mesh. The electrostatic interaction energy in equation (A.1) can be simplified to

$$E^h_{\text{electrostatic}} = \frac{1}{2}\int_{\Omega} \rho(\mathbf{r})\varphi_h(\mathbf{r})\, d\mathbf{r} + \underbrace{\frac{1}{2}\int_{\Omega} b(\mathbf{r})\varphi_h(\mathbf{r})\, d\mathbf{r}}_{(a)} - \underbrace{\frac{1}{2}\sum_{I=1}^{N_a}\int_{\Omega} \delta(\mathbf{r}-\mathbf{R}_I)V_{h_I}(\mathbf{r})\, d\mathbf{r}}_{(b)} . \tag{A.3}$$

In the above expression, the first term on the righthand side contains the contribution of electron-electron interaction energy and half contribution of the electron-nuclear interaction energy. The term (a) contains the other half of the electron-nuclear interaction energy, nuclear-nuclear repulsion energy, and the self energy of the nuclei. The term (b) represents the self energy of the nuclei. By evaluating all the electrostatic potentials on the same finite-element mesh, the divergent self energy contribution in term (a) equals the sum of separately evaluated divergent self-energy terms in (b) owing to the linearity of the Poisson problem. The boundary conditions used for the computation of the discrete potential fields are homogeneous Dirichlet boundary conditions for total electrostatic potential (φ_h) and Dirichlet boundary conditions with the prescribed Coulomb potential for nuclear potentials (V_{h_I}), applied on a large enough domain where the boundary conditions become realistic. The numerical results we present below show that the diverging components of self energy in terms (a) and (b) indeed cancel. To this end, we present the case study of the electrostatic interaction energy computed for a methane molecule with the geometry as described in section 3.4 of Chapter III. The electron-density $\rho(\mathbf{r})$ is chosen to be the superposition of the distributions computed from equation (3.85) with ξ equal to 0.83235 and equation (3.87), and normalized to the number of electrons in the system. We choose a sequence of refined meshes obtained by uniform subdivision of initial coarse mesh with HEX27 and HEX125SPECTRAL elements. The results in tables (A.1) and (A.2) show that while terms (a) and (b) diverge upon mesh refinement, the electrostatic en-

ergy nevertheless converges suggesting the cancelation of divergent self energy terms. Furthermore the convergence rates for the electrostatic energy is close to optimal [1]. The value of E_0 obtained using the extrapolation procedure as discussed in section 3.4 of Chapter III and is found to be -23.79671760794.

Table A.1: Convergence of $E^h_{\text{electrostatic}}$ for "HEX27" element

Degrees of Freedom	Term (a)	Term (b)	$E^h_{electrostatic}$
13059	1637.011830893	1665.4003185717	-22.77175242597
96633	3641.626361382	3657.972341778	-23.7628285436
765,041	7299.84650294	7316.0488206578	-23.7936738766
6,090,465	14534.01973132	14550.219757955	-23.7964615239
48,608,705	29248.01834776	29264.218261189	-23.7966991925

Table A.2: Convergence of $E^h_{\text{electrostatic}}$ for "HEX125SPECTRAL" element

Degrees of Freedom	Term (a)	Term (b)	$E^h_{electrostatic}$
64841	1995.473107	2011.773736	-23.5282153593
510,993	4003.728396	4019.928861	-23.7965792134
4,058,657	8023.635544	8039.835447	-23.79670460619
32,355,393	16063.4709881	16079.670897	-23.79671759075

APPENDIX B

Trade-offs in higher-order elements: Source of diminishing returns with increasing order

We observed in section 3.4.2 of Chapter III that for relative errors commensurate with chemical accuracies, the computational efficiency improves significantly with the order of element up to sixth order, but with diminishing returns beyond this for the benchmark problems considered. Here we identify the source of diminishing returns on $2 \times 2 \times 2$ barium cluster. To this end, we choose three finite-element meshes containing HEX125SPECT, HEX343SPECT and HEX729SPECT elements which give a relative discretization error in the ground-state energy of the order of 10^{-5}. Table (B.1) shows the computational cost (measured in terms of CPU-mins) incurred in building the Hamiltonian matrix and the matrix-vector multiplications involved in a single SCF iteration.

Table B.1: Computational cost per iteration. Case study: Barium

Type of element	Degrees of freedom	Hamiltonian matrix construction (t_1 mins)	Matrix vector multiplication (t_2 mins)	Total time ($t_1 + t_2$ mins)
HEX125SPECT	667,873	18.83	15.03	33.86
HEX343SPECT	143,989	21.91	3.79	25.70
HEX729SPECT	41,825	25.99	1.64	27.63

We observe from the table (B.1) that while there is significant reduction in the number of basis functions with increasing polynomial degree to achieve the same relative accuracy, there is no computational savings obtained by using octic element over hexic element due to the increase in the computational cost involved in building the Hamiltonian matrix which increasingly dominates the total time with increasing order of the element. The cost of computing the Hamiltonian matrix depends on the number of basis functions per element and the order of the quadrature rule, both of which increase with increasing order and cannot be mitigated. However, we remark that, for large enough systems (in terms of number of electrons) the orthogonalization of the Chebyshev filtered vectors will become the dominant cost in a SCF iteration, at which point the order of the polynomial beyond which diminishing returns will be observed can move to a polynomial order beyond the sixth order. But, in the present study, for the range of systems considered, this point has not been reached where the orthogonalization step is the dominant cost in a SCF iteration.

APPENDIX C

Accuracy of Gauss-Lobatto-Legendre quadrature

As presented in section 3.3 of Chapter III, employing the Gauss-Lobatto-Legendre (GLL) quadrature—a reduced-order quadrature rule—for the overlap matrix corresponding to spectral elements results in a standard eigenvalue problem which can be very effectively solved using the Chebyshev filtering technique. Here, we present the results from benchmark problems to establish the accuracy of this reduced-order quadrature employed in the computation of the overlap matrix. To begin with, we consider the Hydrogen atom which represents the simplest example in the all-electron Kohn-Sham DFT problem. We consider a sequence of finite-element meshes on a spherical domain of radius 20 $a.u.$ employing HEX125SPECTRAL elements that are uniform subdivisions of the coarsest mesh. The ground-state energies obtained by employing the GLL quadrature rule for the overlap matrix are presented in table C.1, which demonstrates the convergence of the ground-state energies. Further, close to optimal rate of convergence of the ground-state energies is observed [1].

We subsequently used two benchmark problems—methane molecule (all-electron calculation) and $2 \times 2 \times 2$ barium cluster (local pseudopotential calculation)—to compare the ground-state energies obtained by employing GLL quadrature rules for the overlap matrix with those obtained by employing Gauss quadrature rules. For each of

these benchmark systems, we considered a coarse and a relatively fine mesh discretization for different orders of discretization. These results are tabulated in table C.2. We note that the absolute difference in ground-state energies per atom between GLL and Gauss quadrature (GQ) rules, for both the systems and for the different meshes considered, is about an order of magnitude smaller than the discretization error (reference values in sections 5.1.1.2 and 5.1.2.1). These results demonstrate the accuracy and sufficiency of GLL quadrate rules for the computation of the overlap matrix.

We further note a recent numerical analysis [146] which investigates the error in the eigenspectrum of second-order linear differential operators due to discretization and reduced-order quadrature. While this analysis was not the main objective of this work, it comprises of results that presents a qualitative understanding of the sufficiency of reduced-order quadrature rules for the Kohn-Sham DFT problem. The results in figure A2 in [146] demonstrate that reduced-order quadratures introduce errors in the higher-end of the spectrum, where C^0 finite-elements are anyway no longer accurate even with exact integration and result in spurious optical modes, but are accurate for the lower-end of the eigenspectrum. The ground-state properties in the Kohn-Sham DFT are solely governed by the lower-end of the eigenspectrum, which provides a qualitative explanation for the observed accuracy of the GLL quadrature.

Table C.1: Computed ground-state energies of Hydrogen atom by employing GLL quadrature rules for overlap matrix.

Degrees of freedom (DoF)	Ground state energy (Ha)
17,713	-0.499894312878
140,257	-0.499999964823
1,117,634	-0.4999999999076
8,926,245	-0.50000000000912

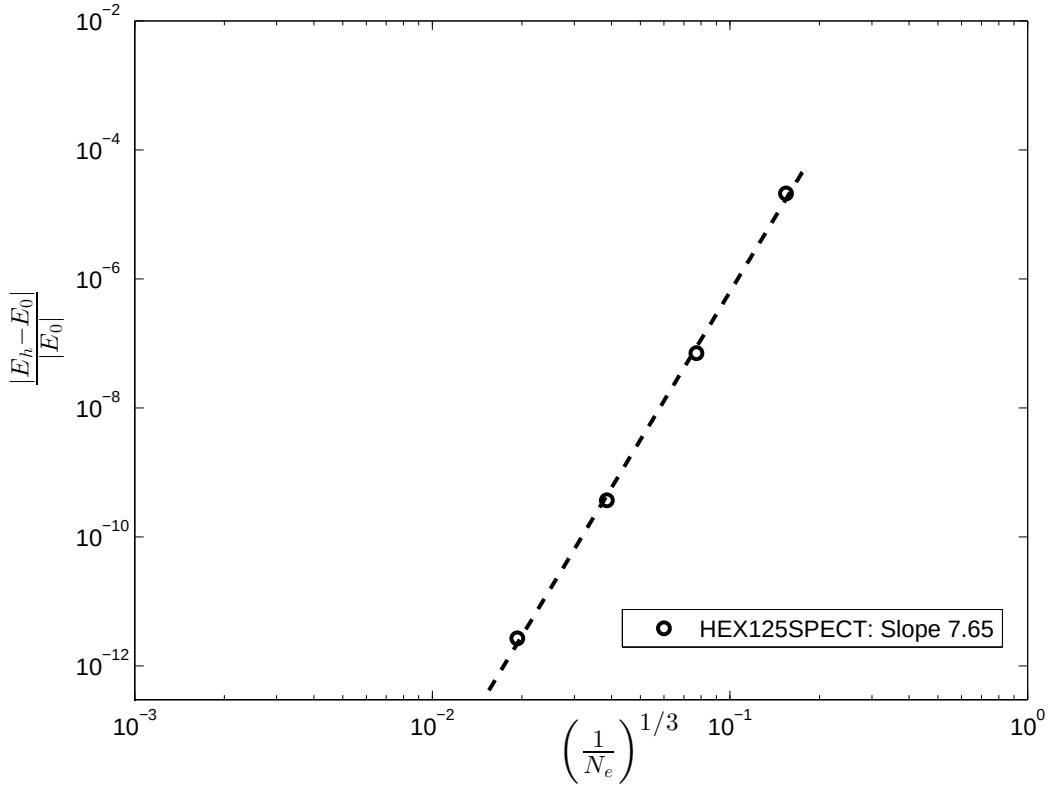

Figure C.1: Convergence of the finite-element approximation for Hydrogen atom using GLL quadrature rule for overlap matrix.

Table C.2: Comparison between GLL rule and GQ rule

Type of System	Element Type	DoF	Energy/atom (GLL)	Energy/atom (GQ)
Methane	HEX27	18,509	-7.9989600253Ha	-8.0030290831 Ha
Methane	HEX27	317,065	-8.0215895393Ha	-8.0220114249 Ha
Methane	HEX125SPECT	43,289	-8.0065360952 Ha	-8.0044564654Ha
Methane	HEX125SPECT	289,401	-8.0239636665 Ha	-8.0239659379 Ha
Barium 2x2x2 cluster	HEX27	175,101	-0.64013198302 Ha	-0.6403673302 Ha
Barium 2x2x2 cluster	HEX27	2,379,801	-0.63858359722 Ha	-0.6385901453 Ha
Barium 2x2x2 cluster	HEX343SPECT	57,121	-0.6373331092Ha	-0.6374840072Ha
Barium 2x2x2 cluster	HEX343SPECT	449,473	-0.6386270069 Ha	-0.6386263119 Ha

APPENDIX D

Scaling performance of individual components of the subspace projection technique

Case study: Pseudopotential calculations

We report scaling of individual components of the proposed subspace projection algorithm with system size for the benchmark calculations involving aluminum nano-clusters and alkane chains reported in section 4.3. The average CPU-times per SCF iteration of the various components involved in the proposed technique (cf. section 4.2)—namely: a) Chebyshev filtered subspace iteration (ChFSI) b) Localization procedure (Loc) c) Subspace projection in the non-orthogonal basis (SubProj) and d) Electron-density computation (ElecDen)—have been recorded and are plotted against number of atoms.

Aluminum nano-clusters: Figure D.1 shows the average computational CPU-times per SCF iteration for individual components of the subspace projection technique in the case of aluminum nano-clusters. These results indicate a computational complexity of $\mathcal{O}(N^{1.34})$ for the Chebyshev filtered subspace iteration, $\mathcal{O}(N^{1.91})$ for the localization procedure, $\mathcal{O}(N^{1.93})$ for the subspace projection and $\mathcal{O}(N^{1.94})$ for the

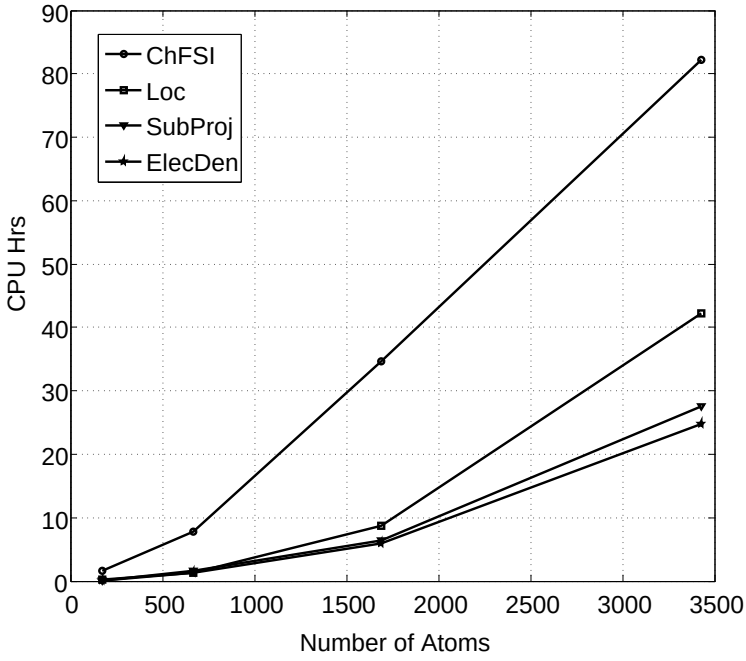

Figure D.1: Average computational times per SCF iteration for individual components of the proposed method. Case Study: Aluminum nano-clusters.

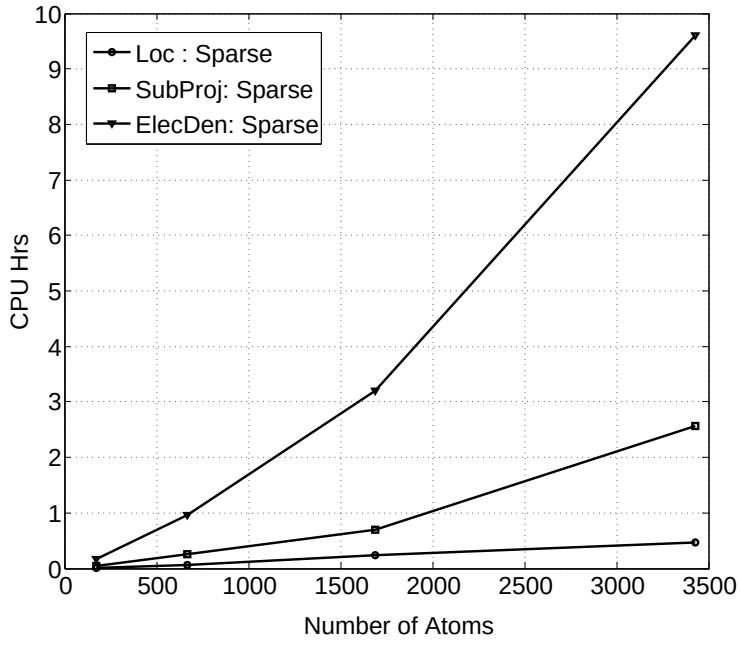

Figure D.2: Average computational times per SCF iteration for individual components when sparse data-structures are active. Case Study: Aluminum nano-clusters.

computation of electron-density. The deviation of the scaling behaviour from linearity for the individual components of the algorithm is primarily due to the use of an adaptive tolerance (cf. equation (4.46)) to truncate the localized wavefunctions, which is important to ensure the accuracy of the subspace projection technique. We recall that looser truncation tolerances are employed in the initial SCF iterations with progressive tightening of the tolerances during the course of SCF convergence. We note that the Chebyshev filtering procedure has the dominant computational cost, and also exhibits better scaling in comparison to the other components of the subspace projection algorithm. The better scaling behaviour of Chebyshev filtering procedure can be attributed to the matrix-vector multiplications performed at the finite-element level only if the relevant wave-functions have a non-zero value in the finite-element considered (cf. Section 4.2.2). This allows us to naturally exploit the sparsity of the wavefunctions at the finite-element level even with tight tolerances. The higher scaling observed for the other components of the subspace projection algorithm is due to the use of dense data-structures of PETSc when the density fraction of the relevant matrices is above 2%, as sparse PETSc data-structures have been observed to be efficient only when the density fraction is $< 1 - 2\%$. Figure D.2 shows the average computational CPU-times per SCF iteration when the sparse data-structures are active. The results indicate a computational complexity of $\mathcal{O}(N^{1.20})$ for the localization procedure, $\mathcal{O}(N^{1.32})$ for the subspace projection and $\mathcal{O}(N^{1.34})$ for the computation of electron-density. We remark that the scaling exponents of these individual components are closer to linearity when the sparse data-structures are active, but still deviate from linearity. We attribute this deviation from linearity to the delocalized nature of the wavefunctions for a metallic system. This delocalized nature of wavefunctions results in a higher density fraction (lesser sparsity) of truncated wavefunctions ($\mathbf{\Phi}_L$) for any given truncation tolerance in comparison to the insulating alkane chains (see discussion below on alkane chains). We also note that, as expected, the scaling of

the individual components of the subspace projection technique (Loc, SubProj, Elec-Den) is close to cubic-scaling ($\sim \mathcal{O}(N^{2.8})$) when dense data-structures are employed. Figure D.5 shows the variation of density fraction of $\mathbf{\Phi}_L$ with SCF iteration in the case of aluminum nano-cluster (7x7x7 cluster with 1688 atoms) highlighting the SCF iterations in which sparse data-structures are active. Figure D.6 shows the variation of relative error in ground-state energy with SCF iteration for the same benchmark problem.

Alkane Chains: Figure D.3 shows the average computational CPU-times per SCF iteration for individual components of the subspace projection technique in the case of alkane chains. These results indicate a computational complexity of $\mathcal{O}(N^{1.15})$ for the Chebyshev filtered subspace iteration, $\mathcal{O}(N^{1.80})$ for the localization procedure, $\mathcal{O}(N^{1.85})$ for the subspace projection and $\mathcal{O}(N^{1.91})$ for the computation of electron-density. As in the case of aluminum clusters, the Chebyshev filtering procedure comprises the dominant computational cost of the subspace projection algorithm, and is almost linear-scaling for this system. The improved scaling of the Chebyshev filtering procedure in comparison to aluminum nano-clusters can be attributed to better localization of wavefunctions in the case of alkane chains, an insulating material system. The higher scaling of other components of the subspace projection algorithm is once again due to the use of dense data-structures of PETSc when density fraction of the relevant matrices is above 2%, while sparse data-structures are employed only when the density fraction is $< 2\%$. Figure D.4 shows the average computational CPU-times per SCF iteration when sparse data-structures are active. The results indicate a computational complexity of $\mathcal{O}(N^{1.13})$ for the localization procedure, $\mathcal{O}(N^{1.25})$ for the subspace projection and $\mathcal{O}(N^{1.29})$ for the computation of electron-density. We remark that these scaling exponents are smaller in comparison to those of aluminum nano-cluster (metallic nature) due to the localized nature of the wavefunctions, thus

resulting in smaller density fractions (greater sparsity) of the truncated wavefunctions ($\mathbf{\Phi}_L$). Figure D.5 shows the variation of density fraction with SCF iteration in the case of $C_{900}H_{1802}$ (2702 atoms) highlighting the SCF iterations in which sparse data-structures are active. Figure D.6 shows the variation of relative error in ground-state energy with SCF iterations for the same problem.

Case study: All-electron calculations

Silicon nano-clusters: Figure D.7 shows the average computational CPU-times per SCF iteration for individual components of the subspace projection technique in the case of all-electron calculations performed on silicon nano-clusters. These results indicate a computational complexity of $\mathcal{O}(N^{1.74})$ for the Chebyshev filtered subspace iteration, $\mathcal{O}(N^{2.72})$ for the localization procedure, $\mathcal{O}(N^{2.55})$ for the subspace projection and $\mathcal{O}(N^{2.51})$ for the computation of electron density. In comparison to the pseudopotential calculations, the scaling of the individual components deviate significantly from linearity. The main reason for this significant deviation is due to the tighter adaptive tolerances employed in all-electron calculations. These tighter tolerances were necessary to avoid error accumulations during the Chebyshev filtering procedure as a very high order Chebyshev filter is needed in all-electron calculations to filter the large unwanted spectrum. For these tighter tolerances, the density fractions for the various relevant matrices were greater than 2% even during the initial SCF iterations, which explains the observed close to cubic-scaling of the localization procedure, subspace projection, and computation of electron density. However, we note that the significantly dominant cost for all-electron calculations is the Chebyshev filtering step, which naturally exploits the sparsity in truncated wavefunctions, even for high density fractions, by computing the matrix-vector products at the finite-element level only if the relevant wave-functions have a non-zero value in the finite-element being considered (cf. Section 4.2.2). Thus, the overall scaling of the proposed technique

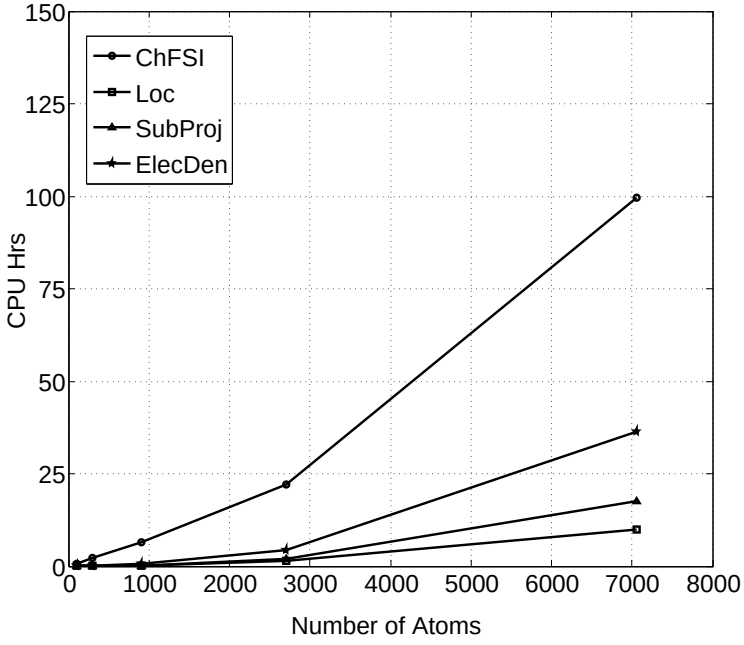

Figure D.3: Average computational times per SCF iteration for individual components of the proposed method. Case Study: Alkane chain.

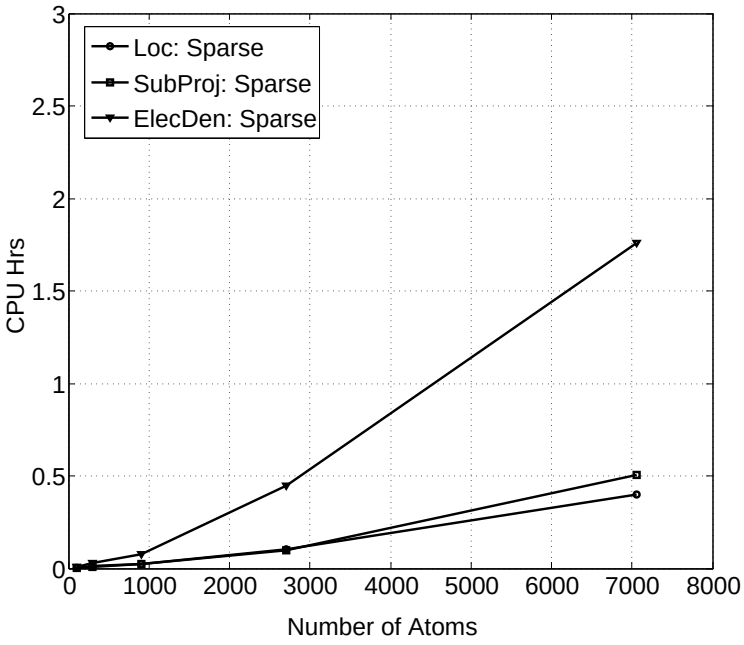

Figure D.4: Average computational times per SCF iteration for individual components when sparse data-structures are active. Case Study: Alkane chain.

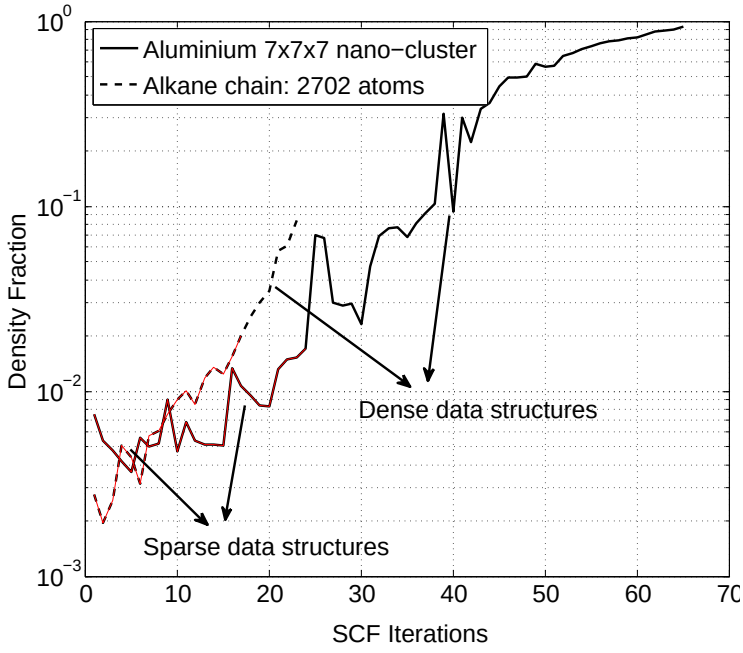

Figure D.5: Variation of density fraction with SCF iteration showing where the sparse data-structures (brown line) and dense data-structures are used. Case Study: Aluminum 7x7x7 nano-cluster and Alkane chain $C_{900}H_{1802}$.

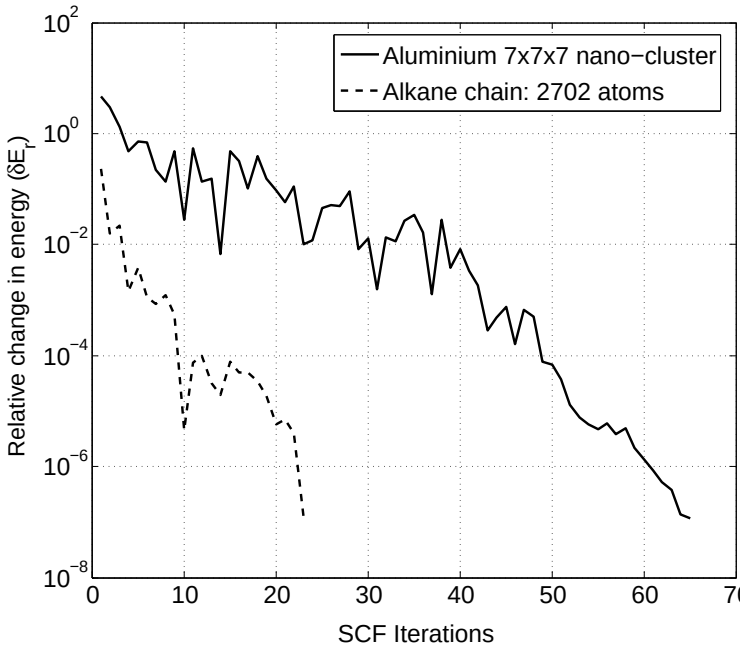

Figure D.6: Relative change in ground-state energy with SCF iteration. Case Study:Aluminum 7x7x7 nano-cluster and Alkane chain $C_{900}H_{1802}$.

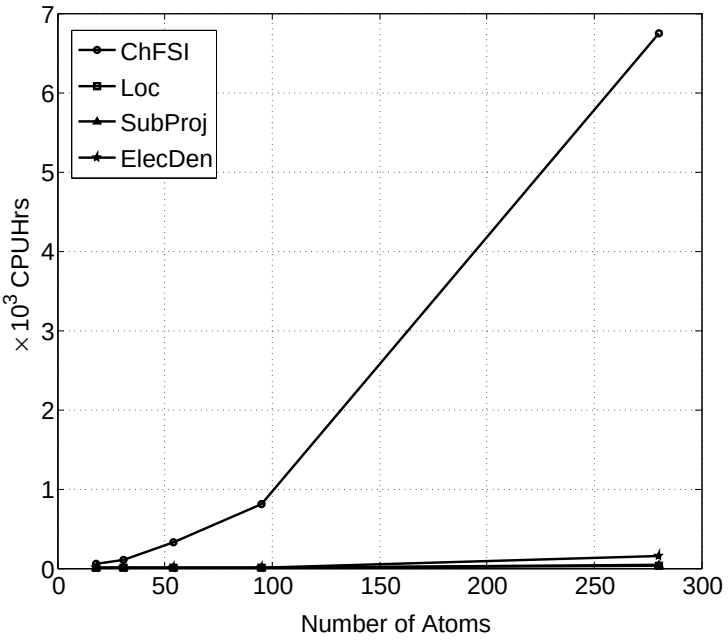

Figure D.7: Average computational times per SCF iteration for individual components of the proposed method. Case Study: Silicon nano-clusters.

for all-electron calculations is determined by the scaling of the Chebyshev filtering step, even for modestly sized systems. While, the performance of the proposed approach for all-electron calculations is not as good as the performance for pseudopotential calculations, the proposed approach does offer significant computational savings (~ 3 fold in comparison to ChFSI-FE for the silicon nano-cluster containing ~ 4000 electrons). Further, we note that the need of a very high degree Chebyshev filter for all-electron calculations can be mitigated by employing an enriched finite-element basis, where the finite-element basis functions are enriched by numerically computed single-atom wavefunctions, and this can potentially lead to better overall scaling of the method for all-electron calculations.

BIBLIOGRAPHY

BIBLIOGRAPHY

[1] P. Motamarri, M. Nowak, K. Leiter, J. Knap, and V. Gavini. Higher-order adaptive finite-element methods for Kohn-Sham density functional theory. *J. Comput. Phys.*, 253:308–343, 2013.

[2] W. Kohn and L. J. Sham. Self-consistent equations including exchange and correlation effects. *Phys. Rev.*, 140(4A):A1133, 1965.

[3] P. Hohenberg and W. Kohn. Inhomogeneous electron gas. *Phys. Rev.*, 136(3B):B864, 1964.

[4] W. J. Hehre, R. F. Stewart, and J. A. Pople. Self-consistent molecular-orbital methods. i. Use of Gaussian expansions of Slater-type atomic orbitals. *J. Chem. Phys.*, 51(6):2657–2664, 1969.

[5] J. M. Wills and B. R. Cooper. Synthesis of band and model hamiltonian theory for hybridizing cerium systems. *Phys. Rev. B*, 36(7):3809–3823, 1987.

[6] F. Jensen. *Introduction to Computational Chemistry*. Wiley Publishers, West Sussex, UK, 1999.

[7] T. L. Beck. Real-space mesh techniques in density-functional theory. *Rev. Mod. Phys.*, 72(4):1041–1080, 2000.

[8] J. M. Soler, E. Artacho, J. D. Gale, A. García, J. Junquera, P. Ordejón, and D. Sánchez-Portal. The SIESTA method for ab initio order-N materials simulation. *J. Phys.: Condens. Matter*, 14(11):2745–2779, 2002.

[9] J. R Chelikowsky, N. Troullier, and Y. Saad. Finite-difference-pseudopotential method: electronic structure calculations without a basis. *Phys. Rev. Lett*, 72(8):1240–1243, 1994.

[10] A. Castro, H. Appel, M. Oliveira, C. A. Rozzi, X. Andrade, F. Lorenzen, M. A. L. Marques, E. K. U. Gross, and A. Rubio. OCTOPUS: a tool for the application of time-dependent density functional theory. *Phys. Status Solidi B*, 243(11):2465–2488, 2006.

[11] L. Genovese, B. Videau, M. Ospici, T. Deutsch, S. Goedecker, and J.-F Méhaut. Daubechies wavelets for high performance electronic structure calculations: The BigDFT project. *Comptes Rendus Mécanique*, 339(2):149–164, 2011.

[12] D. R. Bowler, R. Choudhury, M. J. Gillan, and T. Miyazaki. Recent progress with large-scale ab initio calculations: the CONQUEST code. *Phys. Status Solidi B*, 243(5):989–1000, 2006.

[13] C.-K. Skylaris, P. D. Haynes, A. A. Mostofi, and M. C. Payne. Introducing onetep: Linear-scaling density functional simulations on parallel computers. *J. Chem. Phys.*, 122(8):084–119, 2005.

[14] N. A. Modine, G. Zumbach, and E. Kaxiras. Adaptive-coordinate real-space electronic-structure calculations for atoms, molecules, and solids. *Phys. Rev. B*, 55(16):289–301, 1997.

[15] S. R. White, J. W. Wilkins, and M. P. Teter. Finite-element method for electronic structure. *Phys. Rev. B*, 39(9):5819–5830, 1989.

[16] E. Tsuchida and M. Tsukada. Electronic-structure calculations based on the finite-element method. *Phys. Rev. B*, 52(8):5573–5578, 1995.

[17] E. Tsuchida and M. Tsukada. Adaptive finite-element method for electronic-structure calculations. *Phys. Rev. B*, 54(11):7602–7605, 1996.

[18] E. Tsuchida and M. Tsukada. Large-scale electronic-structure calculations based on the adaptive finite-element method. *J. Phys. Soc. Jpn*, 67(11):3844–3858, 1998.

[19] J. E. Pask, B. M. Klein, C. Y. Fong, and P. A. Sterne. Real-space local polynomial basis for solid-state electronic-structure calculations: A finite-element approach. *Phys. Rev. B*, 59(19):12352–12358, 1999.

[20] J. E. Pask, B. M Klein, P. A Sterne, and C. Y Fong. Finite-element methods in electronic-structure theory. *Comp. Phys. Comm*, 135(1):1–34, 2001.

[21] J. E. Pask and P. A. Sterne. Finite element methods in ab initio electronic structure calculations. *Mod. Sim. Mat. Sci. Eng.*, 13(3):R71–R96, 2005.

[22] D. Zhang, L. Shen, A. Zhou, and X.-G. Gong. Finite element method for solving Kohn–Sham equations based on self-adaptive tetrahedral mesh. *Phys. Lett. A*, 372(30):5071–5076, 2008.

[23] E. J. Bylaska, M. Holst, and J. H. Weare. Adaptive finite element method for solving the exact Kohn-Sham equation of density functional theory. *J. Chem. Theory. Comput.*, 5(4):937–948, 2009.

[24] L. Lehtovaara, V. Havu, and M. Puska. All-electron density functional theory and time-dependent density functional theory with high-order finite elements. *J. Chem. Physics*, 131(5):054103, 2009.

[25] P. Suryanarayana, V. Gavini, T. Blesgen, K. Bhattacharya, and M. Ortiz. Non-periodic finite-element formulation of Kohn–Sham density functional theory. *J. Mech. Phys. Solids*, 58(2):256–280, 2010.

[26] L. Lin, J. Lu, L. Ying, et al. Adaptive local basis set for Kohn–Sham density functional theory in a discontinuous Galerkin framework I: Total energy calculation. *J. Comp. Phys.*, 231(4):2140–2154, 2012.

[27] J. Fang, X. Gao, and A. Zhou. A Kohn–Sham equation solver based on hexahedral finite elements. *J. Comp. Phys.*, 231(8):3166–3180, 2012.

[28] B. Gang, H. Guanghui, and L. Di. An h-adaptive finite element solver for the calculations of the electronic structures. *J. Comp. Phys.*, 231(8):4967–4979, 2012.

[29] A. Masud and R. Kannan. B-splines and NURBS based finite element methods for Kohn–Sham equations. *Comput. Methods Appl. Mech. Engrg*, 241–244:112–127, 2012.

[30] V. Schauer and C. Linder. All-electron Kohn-Sham density functional theory on hierarchic finite element spaces. *J. Comput. Phys.*, 250:644–664, 2013.

[31] B. Hermansson and D. Yevick. Finite-element approach to band-structure analysis. *Phys. Rev. B*, 33(10):7241, 1986.

[32] S. Goedecker. Linear scaling electronic structure methods. *Rev. Mod. Phys.*, 71:1085–1123, 1999.

[33] D. R. Bowler and T. Miyazaki. $\mathcal{O}$(N) methods in electronic structure calculations. *Rep. Prog. Phys.*, 75:036503, 2009.

[34] S. Goedecker. Integral representation of the Fermi distribution and its applications in electronic-structure calculations. *Phys. Rev. B*, 48:17573–17575, 1993.

[35] R. Baer and M. Head-Gordon. Chebyshev expansion methods for electronic structure calculations on large molecular systems. *J. Chem. Phys.*, 107(23):10003–10013, 1997.

[36] C. J. García-Cervera, J. Lu, Y. Xuan, and W. E. Linear-scaling subspace-iteration algorithm with optimally localized nonorthogonal wave functions for Kohn-Sham density functional theory. *Phys. Rev. B*, 79:115110, 2009.

[37] R. M. Martin. *Electronic structure: basic theory and practical methods*. Cambridge university press, Cambridge, UK, 2004.

[38] P. Pulay. Analytical derivative methods in quantum chemistry. *Adv. Chem. Phys.*, pages 241–286, 1987.

[39] M. Fähnle, C. Elsässer, and H. Krimmel. The basic strategy behind the derivation of various ab-initio force formulae. *phys. stat. sol. (b)*, 191(1):9–19, 1995.

[40] P. Bendt and A. Zunger. Simultaneous relaxation of nuclear geometries and electric charge densities in electronic structure theories. *Phys. Rev. Lett.*, 50(21):1684, 1983.

[41] C. T. Chan, K. P. Bohnen, and K. M. Ho. Accelerating the convergence of force calculations in electronic-structure computations. *Phys. Rev. B*, 47:4771–4774, 1993.

[42] P. G. Dacosta, O. H. Nielsen, and K. Kunc. Stress theorem in the determination of static equilibrium by the density functional method. *J. Phys. C: Solid State Phys.*, 19(17):3163, 1986.

[43] P. Focher, G. L. Chiarotti, M. Bernasconi, E. Tosatti, and M. Parrinello. Structural phase transformations via first-principles simulation. *Europhys. Lett.*, 26(5):345, 1994.

[44] Mike. Finnis. *Interatomic forces in condensed matter*. Oxford University Press, Oxford, UK, 2003.

[45] J. M. Ziman. *Principles of the Theory of Solids*. Cambride University Press, Cambridge, UK, 1972.

[46] P. A. M. Dirac. Quantum mechanics of many-electron systems. *Proc. R. Soc. A.*, 123:714, 1929.

[47] A. Szabo and N. S. Ostlund. *Modern quantum chemistry: Introduction to advanced electronic structure theory*. MacMillan Publishing Co, New York, US, 1982.

[48] G. Friesecke. The multiconfiguration equations for atoms and molecules: Charge quantization and existence of solutions. *Arch. Rational Mech. Anal.*, 169:35, 2003.

[49] M. Lewin. Solutions of the multiconfiguration equations in quantum chemistry. *Arch. Rational Mech. Anal.*, 171:83, 2004.

[50] R. G. Parr and W. Yang. *Density functional theory of atoms and molecules*. Oxford University Press, New York, US, 2003.

[51] E. H. Lieb. Density functional for coulomb systems. *Int, J. Quantum. Chem*, 24(3):243–277, 1983.

[52] G. E. Scuseria and V. N Staroverov. Progress in the development of exchange-correlation functionals, 2005.

[53] D. C. Langreth and M. J. Mehl. Beyond the local-density approximation in calculations of ground-state electronic properties. *Phys. Rev. B*, 28:1809–1834, 1983.

[54] J. P. Perdew, K. Burke, and M. Ernzerhof. Generalized gradient approximation made simple. *Phys. Rev. Lett.*, 77:3865–3868, 1996.

[55] A. D. Becke. A new mixing of Hartree-Fock and local density-functional theories. *The Journal of Chemical Physics*, 98(2):1372–1377, 1993.

[56] W. E. Pickett. Pseudopotential methods in condensed matter applications. *Comput. Phys. Rep.*, 9(3):115–197, 1989.

[57] N. W. Ashcroft and N. D. Mermin. *Solid State Physics*. Hartcourt College Publishers, San Diego, US, 1976.

[58] G. Kresse and J. Furthmüller. Efficient iterative schemes for ab initio total-energy calculations using a plane-wave basis set. *Phys. Rev. B*, 54(16):11169–11186, 1996.

[59] M. D. Segall, Philip J. D. Lindan, M. J. Probert, C. J. Pickard, P. J. Hasnip, S. J. Clark, and M. C. Payne. First-principles simulation: ideas, illustrations and the CASTEP code. *J. Phys.: Condens. Matter*, 14(11):2717–2744, 2002.

[60] X. Gonze, J. M. Beuken, R. Caracas, F. Detraux, M. Fuchs, G. M. Rignanese, L. Sindic, M. Verstraete, G. Zerah, F. Jollet, M. Torrent, A. Roy, M. Mikami, Ph. Ghosez, J. Y. Raty, and D. C. Allan. First-principles computation of material properties: the abinit software project. *Comp. Mat. Sci*, 25(3):478–492, 2002.

[61] P. F. Batcho. Computational method for general multicenter electronic structure calculations. *Phys. Rev. E*, 61(6):7169–7183, 2000.

[62] Z. H. Levine and J. W. Wilkins. An energy-minimizing mesh for the Schrödinger equation. *J. Comput. Phys.*, 83(2):361–372, 1989.

[63] R. Radovitzky and M. Ortiz. Error estimation and adaptive meshing in strongly nonlinear dynamic problems. *Comput. Methods Appl. Mech. Engrg.*, 172(1):203–240, 1999.

[64] P. Motamarri, M. Iyer, J. Knap, and V. Gavini. Higher-order adaptive finite-element methods for orbital-free density functional theory. *J. Comput. Phys.*, 231(20):6596–6621, 2012.

[65] T. Ishida and K. Ohno. On the asymptotic behavior of Hartree-Fock orbitals. *Theor. Chim. Acta.*, 81(6):355–364, 1992.

[66] Y. Zhou, Y. Saad, M. L. Tiago, and J. R. Chelikowsky. Parallel self-consistent-field calculations via Chebyshev-filtered subspace acceleration. *Phys. Rev. E*, 74(6):066704, 2006.

[67] D. G. Anderson. Iterative procedures for nonlinear integral equations. *J. Assoc. Comput. Mach.*, 12(4):547–560, 1965.

[68] H. Chen, X. Gong, L. He, Z. Yang, and A. Zhou. Numerical analysis of finite dimensional approximations of Kohn–Sham models. *Adv. Comput. Math.*, 38(2):225–256, 2013.

[69] H. Chen, X. Gong, and A. Zhou. Numerical approximations of a nonlinear eigenvalue problem and applications to a density functional model. *Math. Meth. Appl. Sci*, 33(14):1723–1742, 2010.

[70] E. Cancès, R. Chakir, and Y. Maday. Numerical analysis of nonlinear eigenvalue problems. *J. Sci. Comput.*, 45(1-3):90–117, 2010.

[71] H. Chen, L. He, and A. Zhou. Finite element approximations of nonlinear eigenvalue problems in quantum physics. *Comput. Methods Appl. Mech. Engrg.*, 200(21):1846–1865, 2011.

[72] M. J. Frisch, G. W. Trucks, H. B. Schlegel, G. E. Scuseria, M. A. Robb, J. R. Cheeseman, G. Scalmani, V. Barone, B. Mennucci, G. A. Petersson, H. Nakatsuji, M. Caricato, X. Li, H. P. Hratchian, A. F. Izmaylov, J. Bloino, G. Zheng, J. L. Sonnenberg, M. Hada, M. Ehara, K. Toyota, R. Fukuda, J. Hasegawa, M. Ishida, T. Nakajima, Y. Honda, O. Kitao, H. Nakai, T. Vreven, J. A. Montgomery, J. E. Peralta, F. Ogliaro, M. Bearparka, J. J. Heyd, E. Brothers, K. N. Kudin, V. N. Staroverov, R. Kobayashi, J. Normand, K. Raghavachari, A. Rendell, J. C. Burant, S. S. Iyengar, J. Tomasi, M. Cossi, N. Rega, J. M. Millam, M. Klene, J. E. Knox, J. B. Cross, V. Bakken, C. Adamo, J. Jaramillo, R. Gomperts, R. E. Stratmann, O. Yazyev, A. J. Austin, R. Cammi, C. Pomelli, J. W. Ochterski, R. L. Martin, K. Morokuma, V. G. Zakrzewski, G. A. Voth, P. Salvador, J. J. Dannenberg, S. Dapprich, A. D. Daniels, Ö. Farkas, J. B. Foresman, J. V. Ortiz, and J. Cioslowsk. Gaussian 09, Revision a. 1. Wallingford ct: Gaussian, 2009.

[73] D. M. Ceperley and B. J. Alder. Ground state of the electron gas by a stochastic method. *Phys. Rev. Lett.*, 45(7):566, 1980.

[74] J. P. Perdew and A. Zunger. Self-interaction correction to density-functional approximations for many-electron systems. *Phys. Rev. B*, 23(10):5048–5079, 1981.

[75] V. Gavini, J. Knap, K. Bhattacharya, and M. Ortiz. Non-periodic finite-element formulation of orbital-free density functional theory. *J. Mech. Phys. Solids*, 55(4):669–696, 2007.

[76] A. Anantharaman and E. Cancès. Existence of minimizers for Kohn–Sham models in quantum chemistry. In *Annales de l'Institut Henri Poincare (C) Non Linear Analysis*, volume 26, pages 2425–2455. Elsevier, 2009.

[77] N. Troullier and J. L. Martins. Efficient pseudopotentials for plane-wave calculations. *Phys. Rev. B*, 43:1993–2006, 1991.

[78] L. Kleinman and D. M. Bylander. Efficacious form for model pseudopotentials. *Phy. Rev. Lett.*, 48(20):1425, 1982.

[79] P. G. Ciarlet. *The finite element method for elliptic problems*. SIAM, Philadelphia, US, 2002.

[80] A. T. Patera. A spectral element method for fluid dynamics: laminar flow in a channel expansion. *J. Comp. Phys.*, 54(3):468–488, 1984.

[81] J. P. Boyd. *Chebyshev and Fourier spectral methods*. Dover Publications, New York, US, 2001.

[82] C. Canuto, M. Y. Hussaini, A. Quarteroni, and T. A. Zang. *Spectral methods: evolution to complex geometries and applications to fluid dynamics*. Springer, New York, US, 2007.

[83] S. Balay, J. Brown, K. Buschelman, V. Eijkhout, W. Gropp, D. Kaushik, M. Knepley, L. C. McInnes, B. Smith, and H. Zhang. Petsc users manual revision 3.4, 2013.

[84] G. L. G. Sleijpen and H. A Van der Vorst. A Jacobi–Davidson iteration method for linear eigenvalue problems. *SIAM Rev.*, 42(2):267–293, 2000.

[85] G. W. Stewart. A Krylov–Schur algorithm for large eigenproblems. *SIAM J. Matrix Anal.Appl.*, 23(3):601–614, 2002.

[86] L. N Trefethen and Bau. D. *Numerical Linear Algebra*. SIAM, Philadelphia, US, 1997.

[87] Z. Bai, J. Demmel, J. Dongarra, A. Ruhe, and H. van der Vorst. *Templates for the solution of algebraic eigenvalue problems: a practical guide*, volume 11. SIAM, Philadelphia, US, 2000.

[88] V. Hernandez, J. E. Roman, and V. Vidal. Slepc: A scalable and flexible toolkit for the solution of eigenvalue problems. *ACM Transactions on Mathematical Software (TOMS)*, 31(3):351–362, 2005.

[89] T. J. Rivlin. *Chebyshev Polynomials: From approximation theory to Algebra and Number Theory*. Wiley Publishers, New York, US, 1973.

[90] P. Pulay. Convergence acceleration of iterative sequences. the case of SCF iteration. *Chem. Phy. Lett.*, 73(2):393–398, 1980.

[91] C. G. Broyden. A class of methods for solving nonlinear simultaneous equations. *Math. Comput.*, pages 577–593, 1965.

[92] K. N. Kudin, G. E. Scuseria, and E. Cancès. A black-box self-consistent field convergence algorithm: One step closer. *J. Chem. Phys.*, 116(19):8255–8261, 2002.

[93] V. Eyert. A comparative study on methods for convergence acceleration of iterative vector sequences. *J. Comp. Phys*, 124(2):271–285, 1996.

[94] M. J. T. Oliveira and F. Nogueira. Generating relativistic pseudo-potentials with explicit incorporation of semi-core states using APE, the Atomic Pseudopotentials Engine. *Comp. Phys. Comm.*, 178(7):524–534, 2008.

[95] F. Nogueira, C. Fiolhais, J. He, J. P. Perdew, and A. Rubio. Transferability of a local pseudopotential based on solid-state electron density. *J. Phys: Condens. Matter B*, 8(3):287–302, 1996.

[96] Naval Research Laboratory. Pre-defined k-point sets for crystalline calculations.

[97] F. Jensen. Polarization consistent basis sets. ii. estimating the Kohn–Sham basis set limit. *J. Chem. Phys.*, 116(17):7372–7379, 2002.

[98] S. Campagna, F. Puntoriero, F. Nastasi, G. Bergamini, and V. Balzani. Photochemistry and photophysics of coordination compounds: ruthenium. In *Photochemistry and Photophysics of Coordination Compounds I*, pages 117–214. Springer, 2007.

[99] J. M. Melenk and I. Babuška. The partition of unity finite element method: basic theory and applications. *Comput. Meth. Appl. Mech. Engng*, 139(1):289–314, 1996.

[100] I. Babuška and J. M. Melenk. The partition of unity method. *Int. J. Numer. Meth. Engng.*, 40:727–758, 1997.

[101] N. Sukumar and J. E. Pask. Classical and enriched finite element formulations for Bloch-periodic boundary conditions. *Int. J. Numer. Meth. Engng*, 77(8):1121–1138, 2009.

[102] G. Schofield, J. R. Chelikowsky, and Y. Saad. A spectrum slicing method for the Kohn–Sham problem. *Comp. Phys. Comm*, 183(3):497–505, 2012.

[103] W. Kohn. Density functional and density matrix method scaling linearly with the number of atoms. *Phys. Rev. Lett.*, 76:3168–3171, 1996.

[104] W. Yang. Electron density as the basic variable: a divide-and-conquer approach to the ab initio computation of large molecules. *J. Mol. Struc. Theochem*, 255:461–479, 1992.

[105] T. Ozaki. $\mathcal{O}(N)$ Krylov-subspace method for large-scale ab initio electronic structure calculations. *Phys. Rev. B*, 74:245101, 2006.

[106] M. Barrault, E. Cancès, W. W. Hager, and C. Le Bris. Multilevel domain decomposition for electronic structure calculations. *J. Comput. Phys*, 222(1):86–109, 2007.

[107] S. Goedecker and L. Colombo. Efficient linear scaling algorithm for tight-binding molecular dynamics. *Phys. Rev. Lett.*, 73:122–125, 1994.

[108] S. Goedecker and M. Teter. Tight-binding electronic-structure calculations and tight-binding molecular dynamics with localized orbitals. *Phys. Rev. B*, 51:9455–9464, 1995.

[109] X.-P. Li, R. W. Nunes, and D. Vanderbilt. Density-matrix electronic-structure method with linear system-size scaling. *Phys. Rev. B*, 47:10891–10894, 1993.

[110] P. D. Haynes, C.-K. Skylaris, A. A. Mostofi, and M. C. Payne. ONETEP: linear-scaling density-functional theory with local orbitals and plane waves. *Phys. Stat. Sol.(b)*, 243(11):2489–2499, 2006.

[111] O. F. Sankey, D. A. Drabold, and A. Gibson. Projected random vectors and the recursion method in the electronic-structure problem. *Phys. Rev. B*, 50:1376–1381, 1994.

[112] U. Stephan and D. A. Drabold. Order-N projection method for first-principles computations of electronic quantities and Wannier functions. *Phys. Rev. B*, 57:6391–6407, 1998.

[113] F. Mauri, G. Galli, and R. Car. Orbital formulation for electronic-structure calculations with linear system-size scaling. *Phys. Rev. B*, 47:9973–9976, 1993.

[114] J. Kim, F. Mauri, and G. Galli. Total-energy global optimizations using nonorthogonal localized orbitals. *Phys. Rev. B*, 52:1640–1648, 1995.

[115] W. Gao and E. Weinan. Orbital minimization with localization. *Discrete Contin. Dyn. Syst. A*, 23:249–264, 2009.

[116] T. Ozaki. Continued fraction representation of the Fermi-Dirac function for large-scale electronic structure calculations. *Phys. Rev. B*, 75:035123, 2007.

[117] M. Ceriotti, T. D. Kühne, and M. Parrinello. An efficient and accurate decomposition of the Fermi operator. *J. Chem. Phys.*, 129(2):024707, 2008.

[118] L. Lin, J. Lu, L. Ying, and E. Weinan. Pole-based approximation of the Fermi-Dirac function. *Chin. Ann. Math.*, 30B(6):729–742, 2009.

[119] T. Ozaki. Efficient low-order scaling method for large-scale electronic structure calculations with localized basis functions. *Phys. Rev. B*, 82:075131, 2010.

[120] L. Lin, M. Chen, C. Yang, and L. He. Accelerating atomic orbital-based electronic structure calculation via pole expansion and selected inversion. *J. Phys: Condens. Matter*, 25(29):295501, 2013.

[121] P. Suryanarayana, K. Bhattacharya, and M. Ortiz. Coarse-graining Kohn–Sham density functional theory. *J. Mech. Phys. Solids*, 61(1):38–60, 2013.

[122] Y. Saad. *Numerical methods for large eigenvalue problems*, volume 158. SIAM, Philadelphia, US, 1992.

[123] C. Lanczos. An iteration method for the solution of the eigenvalue problem of linear differential and integral operators. *J. Res. Nat. Bureau Standards, Sec. B*, 45:255–282, 1950.

[124] T. J. Rivlin. *Chebyshev Polynomials. From Approximation Theory to Algebra and Number Theory*. John Wiley, New York, US, 1973.

[125] G. H. Wannier. The structure of electronic excitation levels in insulating crystals. *Phys. Rev.*, 52:191–197, 1937.

[126] W. Kohn. Analytic properties of Bloch waves and Wannier functions. *Phys. Rev.*, 115:809–821, 1959.

[127] W. Kohn. Construction of Wannier functions and applications to energy bands. *Phys. Rev. B*, 7:4388–4398, 1973.

[128] W. Kohn. Density functional/Wannier function theory for systems of very many atoms. *Chem. Phys. Lett.*, 208(3):167–172, 1993.

[129] N. Marzari and D. Vanderbilt. Maximally localized generalized Wannier functions for composite energy bands. *Phys. Rev. B*, 56:12847–12865, 1997.

[130] P. W. Anderson. Self-consistent pseudopotentials and ultralocalized functions for energy bands. *Phys. Rev. Lett.*, 21:13–16, 1968.

[131] P. Ordejón, D. A. Drabold, M. P. Grumbach, and R. M. Martin. Unconstrained minimization approach for electronic computations that scales linearly with system size. *Phys. Rev. B*, 48:14646–14649, 1993.

[132] E. Weinan, T. Li, and J. Lu. Localized bases of eigensubspaces and operator compression. *Proc. Nat. Acad. Sci.*, 107(4):1273–1278, 2010.

[133] V. Ozoliņš, R. Lai, R. Caflisch, and S. Osher. Compressed modes for variational problems in mathematics and physics. *Proc. Nat. Acad. Sci.*, 110(46):18368–18373, 2013.

[134] B. Jansík, S. Høst, P. Jørgensen, J. Olsen, and T. Helgaker. Linear-scaling symmetric square-root decomposition of the overlap matrix. *J. Chem. Phys.*, 126(12):124104, 2007.

[135] E. H. Rubensson and P. Sałek. Systematic sparse matrix error control for linear scaling electronic structure calculations. *J. Comput. Chem.*, 26(15):1628–1637, 2005.

[136] P. Suryanarayana. On spectral quadrature for linear-scaling density functional theory. *Chem. Phys. Lett.*, 584:182–187, 2013.

[137] S. Goedecker. Decay properties of the finite-temperature density matrix in metals. *Phys. Rev. B*, 58:3501–3502, 1998.

[138] S. Ismail-Beigi and T. A. Arias. Locality of the density matrix in metals, semiconductors, and insulators. *Phys. Rev. Lett.*, 82:2127–2130, 1999.

[139] K. E. Atkinson. *An Introduction to Numerical Analysis*. John Wiley & Sons, New York, US, 2008.

[140] M. Fuchs and M. Scheffler. Ab initio pseudopotentials for electronic structure calculations of poly-atomic systems using density-functional theory. *Comp. Phys. Comm.*, 119(1):67–98, 1999.

[141] L. Lin and C. Yang. Elliptic preconditioner for accelerating the self-consistent field iteration in Kohn–Sham density functional theory. *SIAM J. Sci. Comput*, 35(5):S277–S298, 2013.

[142] M. E. Gurtin. *Configurational forces as basic concepts of continuum physics*, volume 137. Springer, New York, US, 2000.

[143] J. D. Eshelby. The force on an elastic singularity. *Phil. Trans. Royal Soc. Lond. A*, 244(877):87–112, 1951.

[144] M. Iyer, B. Radhakrishnan, and V. Gavini. Electronic-structure study of an edge dislocation in aluminum and the role of macroscopic deformations on its energetics. *arXiv preprint arXiv:1406.3741*, 2014.

[145] V. Gavini, K. Bhattacharya, and M. Ortiz. Quasi-continuum orbital-free density-functional theory: A route to multi-million atom non-periodic DFT calculation. *J. Mech. Phys. Solids*, 55(4):697–718, 2007.

[146] T. J. R. Hughes, A. Reali, and G. Sangalli. Efficient quadrature for NURBS-based isogeometric analysis. *Comput. Meth. Appl. Mech. Engng*, 199(5):301–313, 2010.